



WELL LOGGING LABORATORY

TECHNICAL REPORT NO. 32

October 2011



**Department of Electrical Engineering
Cullen College of Engineering
University of Houston**



Technical Report No. 32

University of Houston

2011

WELL LOGGING TECHNICAL REPORT NO. 32

October 2011

All rights reserved

Well Logging Laboratory
Department of Electrical and Computer Engineering
University of Houston
Houston, Texas 77204-4005
U. S. A.

Research Staff

Faculty

Dr. Qiming Li, Adjunct Professor
Dr. Kurt M. Strack, Adjunct Professor
Dr. Donald Wilton, Professor
Dr. Richard Liu, Professor
Dr. Ning Yuan, Research Assistant Professor

Post Doctors

Dr. Xiaochun Nie

Research Assistants

Jing Li (Ph. D. Candidate)
Min Wu (Ph.D. Candidate)
Zhijuan Zhang (Ph.D. Candidate)
Fouad Shehab (Master Candidate)
Yajun Kong (M. S. Candidate)
Chang Ming Lin (M. S. Candidate)
Boyuan Yu (Ph.D. Candidate)
Ziting Liu (M. S. Candidate)
Bo Gong (Ph.D. Candidate)
Yinxi Zhang (Ph.D. Candidate)
Jing Wang (Ph.D. Candidate)
Azizuddin Abdul Aziz (Ph.D. Candidate)

Acknowledgment

The authors would like to acknowledge gratefully the financial support and the technical assistance which they have received from the following companies:

BP

Chevron E & P Technology Company

ExxonMobil Upstream Research Company

Great Wall Drilling Company

Halliburton Energy Services

Pathfinder Energy Services

Saudi Aramco

Schlumberger Oilfield Services

Statoil

Weatherford

TECHNICAL REPORT NO. 32 (2011)

Table of Contents

Research Staff	ii
Acknowledgment	iii
Table of Contents	iv
<hr/>	
CHAPTER 1 1D Inversion of Triaxial Induction Tool in Layered Anisotropic Formation, by Zhijuan Zhang, Ning Yuan and Richard Liu.....	1
CHAPTER 2 Parallelization of Forward Modeling Codes using OpenMP, by Ning Yuan, Zhijuan Zhang and Richard Liu.....	32
CHAPTER 3 Simulation of Mandrel Effect on Logging-While-Drilling Propagation Tool, by Yajuan Kong, Qiming Li and Richard Liu.....	83
CHAPTER 4 Fast Finite-Difference Time-Domain Modeling for Marine-Subsurface Electromagnetic Problems using Artificially High Dielectric Constant, by Boyuan Yu and Richard Liu.....	127
CHAPTER 5 New Addition and Modification to Well Logging Forward Modeling and Inversion Interface, by Yajun Kong, Qiming Li and Richard Liu.....	147
CHAPTER 6 Wireless Relay Network: Novel Data Transmission Approach for Measurement-While-Drilling Telemetry, by Bo Gong and Richard Liu.....	162
CHAPTER 7 Wireless MWD Telemetry System Using MEMS Radio, by Ziting Liu and Richard Liu.....	177
APPENDIX A List of Theses and Dissertations.....	208
APPENDIX B List of Technical Paper Publications.....	217

CHAPTER 1

1D Inversion of Triaxial Induction Tool in Layered Anisotropic Formation

Abstract

In this paper, we present a one-dimensional (1-D) inversion algorithm for triaxial induction logging tools in multi-layered transverse isotropic (TI) formation. A non-linear least-square model based on Gauss-Newton algorithm is used in the inversion. Zero-D inversion is conducted at the center of each layer to provide a reasonable initial guess for best efficiency of the inversion procedure. Cross components are used to provide sufficient information for determining the boundaries in the initial guess. It will be illustrated that using all the nine components of the conductivity/resistivity yield more reliable inversion results and faster convergence than using only the diagonal components. The resultant algorithm can be used to obtain various geophysical parameters such as layer boundaries, horizontal and vertical resistivity, dipping angle and rotation angle *etc.* from triaxial logging data automatically without any priori information. Several synthetic examples are presented to demonstrate the capability and reliability of the inversion algorithm. Finally, the present algorithm is applied to a traditional induction field log which is fitted from a published paper to further demonstrate its capability.

1. Introduction

Electrical anisotropy has been recognized as one potential source of error in traditional induction logging analysis [1]. A common case is a thinly laminated sand-shale sequence where the horizontal resistivity is much smaller than the vertical resistivity. When the

well is drilled perpendicular to the bedding planes, conventional induction logging only measures the horizontal resistivity since the tool contain only co-axial transmitter and receiver coils. Thus, the interpretation based on the measured data will either miss the pay-zone or overestimate the water saturation [2]. The emerging triaxial induction tool comprises three mutually perpendicular transmitters and three mutually perpendicular receivers along the x, y and z direction. By collecting sufficient information from multiple directions, the triaxial induction tool is capable of detecting formation anisotropy.

For accurate interpretation of the measured data, an efficient inversion procedure is crucial. Via inversion, we can retrieve various geophysical parameters of the formation, such as location of the boundaries, resistivity of each layer, the dipping angle etc. Then petrophysicists are able to evaluate the hydrocarbon content and water saturation based on these parameters. Nowadays, most inversion algorithms are based on one-dimensional (1-D) modeling for best efficiency since the inversion process requires carrying out the forward modeling repeatedly and thus is usually time consuming [3]. Yu *et. al.* developed an 1-D inversion algorithm based on turbo boosting proposed by Hakvoort [4]. This method describes layered formation using equally thick thin layers with known relative dipping angle and azimuthal angle. In order to stabilize the process, dual frequency data were used. Lu *et. al.* [5] performed a new 1-D inversion algorithm using the method of singular value decomposition (SDV) without calculating the sensitivity matrix. However, robust layer position must be known as priori information. Later, Zhang *et. al.* presented three analytical methods for the determination of the relative dipping angle and azimuthal angle [6]. Wang *et al* introduced an 1-D inversion algorithm by applying Gauss-Newton to retrieve the transverse isotropic formation parameters [7]. But in this algorithm, initial guess must be determined with some prior information. Recently, Abubakar *et. al.* developed a three-dimensional (3-D) inversion for triaxial induction logging based on a

fully anisotropic 3-D finite-difference forward modeling [8,9]. The inversion is based on a constrained, regularized Gauss-Newton minimization scheme proposed by Habashy [10]. This inversion algorithm is very robust in extracting formation and invasion anisotropic resistivities, invasion radii, bed boundary locations, relative dip, and azimuth angle from logging data. However, as a full 3-D inversion, the CPU time is still the bottleneck although a dual grid approach was used to speed up the inversion procedure to some extent.

In this paper, we present a 1-D inversion algorithm based on the nonlinear least-square algorithm and Gauss-Newton algorithm. Zero-D inversion is conducted at the center of each layer to provide a reliable initial model since the efficiency of the entire inversion procedure can be significantly improved by using good initial guess. In the inversion, our previously developed 1-D analytical forward modeling [11] is used as the embedded forward engine. The developed algorithm can simultaneously determine the horizontal resistivity, vertical resistivity, formation dip, and azimuthal angle and bed boundary position from the triaxial induction logging data. The biggest advantage of the present algorithm is that no priori information is required. Synthetic examples will be presented to illustrate the robustness of the algorithm. We will also show that the algorithm can yield reliable inversion results even for field log data.

2. Methodology

2.1 The Triaxial Tool Configuration

A basic triaxial induction tool comprises three pairs of transmitters and receivers oriented at the x , y , and z direction, respectively, as shown in Fig. 1(a). Since the transmitter and receiver coils are infinitely small, we can treat them as magnetic dipoles. The equivalent dipole model is shown in Fig. 1(b). Thus, the magnetic source excitation

of the triaxial tool can be expressed as $\mathbf{M} = (M_x, M_y, M_z)\delta(\mathbf{r})$.

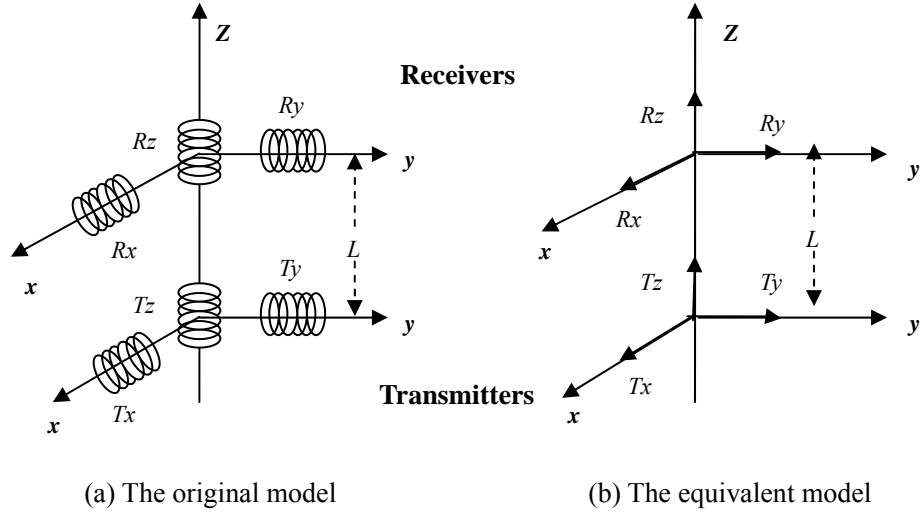


Fig. 1 Basic structure of a triaxial induction tool

The tool is moving along the axis in the borehole and for every logging point, a 3×3 apparent conductivity tensor σ_a is measured at each pair of transmitter-receiver spacing, *i.e.*

$$\sigma_a = \begin{bmatrix} \sigma_{ax}^x & \sigma_{ax}^y & \sigma_{ax}^z \\ \sigma_{ay}^x & \sigma_{ay}^y & \sigma_{ay}^z \\ \sigma_{az}^x & \sigma_{az}^y & \sigma_{az}^z \end{bmatrix}, \quad (1)$$

where σ_{ai}^j is the apparent conductivity measured at the j -directed receiver from the i -directed transmitter.

2.2 Inversion Theory

1) Gauss-Newton Algorithm

Assume the vector \mathbf{M} denote the measured conductivity at NR logging points, \mathbf{M} will be

a $9NR \times 1$ vector since the conductivity has 9 components at each logging point, *i.e.*

$$\mathbf{M} = \begin{bmatrix} m_1 \\ m_2 \\ \vdots \\ m_{NR} \end{bmatrix}^T = \begin{bmatrix} \sigma_{x,1}^x \\ \sigma_{x,1}^y \\ \sigma_{x,1}^z \\ \sigma_{y,1}^x \\ \sigma_{y,1}^y \\ \sigma_{y,1}^z \\ \sigma_{z,1}^x \\ \sigma_{z,1}^y \\ \sigma_{z,1}^z \\ \vdots \\ \sigma_{x,NR}^x \\ \vdots \\ \sigma_{z,NR}^z \end{bmatrix}^T \quad (2)$$

In the framework of the inversion, these measured data is assumed to be borehole corrected but with the invasion effect ignored.

In the 1-D inversion model, each layer is characterized by its horizontal conductivity, vertical conductivity and the bed boundary position, yielding a total of $3 \times L - 1$ parameters for an L -layer formation model. Plus the dipping angle and rotation angle, we will need to determine $N = 3 \times L + 1$ parameters in the 1-D inversion. Assume the parameter vector \mathbf{X} is the vector composed of the unknown parameters given by

$$X = \begin{bmatrix} x_1 \\ x_2 \\ \vdots \\ x_N \end{bmatrix}^T = \begin{bmatrix} \log(\alpha) \\ \log(\gamma) \\ \log(Z_1) \\ \vdots \\ \log(Z_{L/3}) \\ \log(\sigma_{h,1}) \\ \log(\sigma_{v,1}) \\ \vdots \\ \log(\sigma_{h,L/3}) \\ \log(\sigma_{v,L/3}) \end{bmatrix}^T \quad (3)$$

All parameters within the proper magnitude range are rescaled due to the application of logarithm. Then we use the parameter vector X to construct the following objective function (cost function)

$$C(X) = \frac{1}{2} \mathbf{R}(X)^T \mathbf{R}(X) \quad (4)$$

where $\mathbf{R}(X)$ is the residual function defined by $\mathbf{R}(X) = S(X) - M$, $S(X)$ is the simulated tool response corresponding to a particular model in terms of the vector X .

As we can see, the cost function measures the error between the calculated log and the input log. The smaller the cost function is, the more reliable inversion results we may obtain. Hence the most critical procedure in the inversion is to reduce the cost function. We choose the classical nonlinear inversion approach, Gauss-Newton minimization algorithm in our 1-D inversion. According to Taylor expansion, we can approximate the cost function $C(X)$ with a local quadratic model as follows [12]

$$C(X) \approx \frac{1}{2} \mathbf{R}^T(X_c) \mathbf{R}(X_c) + \mathbf{g}^T(X_c) (X - X_c) + \frac{1}{2} (X - X_c)^T \bar{\bar{H}}(X_c) (X - X_c) \quad (5)$$

where $\mathbf{g}(X) = \nabla C(X) = \bar{\bar{J}}^T(X) \mathbf{R}(X)$ is the gradient of the cost function $C(X)$ and $\bar{\bar{H}}(X) = \nabla \nabla C(X)$ is the Hessian of the cost function $C(X)$ which is given by

$$\bar{\bar{\mathbf{H}}}(\mathbf{X}) = \bar{\bar{\mathbf{J}}}^T(\mathbf{X})\bar{\bar{\mathbf{J}}}(\mathbf{X}) + \bar{\bar{\mathbf{S}}}(\mathbf{X}) \approx \bar{\bar{\mathbf{J}}}^T(\mathbf{X})\bar{\bar{\mathbf{J}}}(\mathbf{X}) + \mu\mathbf{I}. \quad (6)$$

where $\bar{\bar{\mathbf{S}}}(\mathbf{X}) = \sum_{i=1}^{9 \times NR} \mathbf{r}_i(\mathbf{X})\nabla^2 \mathbf{r}_i(\mathbf{X})$ denotes the second-order information in $\bar{\bar{\mathbf{H}}}(\mathbf{X})$. In (6),

we apply the Cholesky factorization algorithm to update μ . By determining $\mu > 0$,

$\bar{\bar{\mathbf{H}}}(\mathbf{X}) \approx \bar{\bar{\mathbf{J}}}^T(\mathbf{X})\bar{\bar{\mathbf{J}}}(\mathbf{X}) + \mu\mathbf{I}$ is positive definite, which guarantees the minimum of the cost

function to be found. Then (5) can be rewritten as

$$\mathbf{C}(\mathbf{X}) \approx \frac{1}{2}\mathbf{R}^T(\mathbf{X}_c)\mathbf{R}(\mathbf{X}_c) + \mathbf{R}^T(\mathbf{X}_c)\bar{\bar{\mathbf{J}}}(\mathbf{X}_c)(\mathbf{X} - \mathbf{X}_c) + \frac{1}{2}(\mathbf{X} - \mathbf{X}_c)^T(\bar{\bar{\mathbf{J}}}^T(\mathbf{X}_c)\bar{\bar{\mathbf{J}}}(\mathbf{X}_c) + \mu\mathbf{I})(\mathbf{X} - \mathbf{X}_c) \quad (7)$$

Then the solution of (7) is given by

$$\mathbf{X}_+ \approx \mathbf{X}_c - (\bar{\bar{\mathbf{J}}}^T(\mathbf{X}_c)\bar{\bar{\mathbf{J}}}(\mathbf{X}_c) + \mu\mathbf{I})^{-1}\bar{\bar{\mathbf{J}}}^T(\mathbf{X}_c)\mathbf{R}(\mathbf{X}_c) \quad (8)$$

The details of the Cholesky factorization algorithm can be referred to [13] and is omitted here.

2) Line Search Technique

Equation (8) provides us the Newton direction $\mathbf{P} \approx \mathbf{X}_+ - \mathbf{X}_c$. Usually this step can not guarantee the minimum value of the cost function because of the poor match between the cost function and the quadratic form. Therefore, we incorporate a line search along the Gauss-Newton direction to guarantee a reduced cost function in each iteration until the cost function satisfies:

$$\mathbf{C}(\mathbf{X}_k + \lambda\mathbf{P}_k) \leq \mathbf{C}(\mathbf{X}_k) + \alpha\lambda_k\delta\mathbf{C}_{k+1} \quad (9)$$

where $\alpha \in \{0, 1\}$, λ_k is the kth line search step. In practice, α is a very small value

and we choose $\alpha = 10^{-4}$ in this paper. Starting from $\mathbf{X}_{k+1} = \mathbf{X}_k + \lambda_k\mathbf{P}_k$, the cost function $\mathbf{C}(\mathbf{X})$

can be expressed as a quadratic form of the step length λ

$$\mathbf{C}(\lambda) = \mathbf{C}(\mathbf{X}_k + \lambda\mathbf{P}_k) \approx a + b\lambda + c_2\lambda^2 \quad (10)$$

where a, b and c are constants determined from the current cost function $\mathbf{C}(\lambda)$,

$$a = \mathbf{C}(\lambda = 0) = \mathbf{C}(\mathbf{X}_k) \quad (11)$$

$$b = \left. \frac{d\mathbf{C}(\lambda)}{d\lambda} \right|_{\lambda=0} = \mathbf{g}^T(\mathbf{X}_k) \mathbf{p}_k \quad (12)$$

$$c = \frac{1}{\{\lambda_k^{(m)}\}^2} \left[\mathbf{C}(\mathbf{X}_k + \lambda_k^{(m)} \mathbf{P}_k) - \mathbf{C}(\mathbf{X}_k) - \lambda_k^{(m)} \delta \mathbf{C}_{k+1} \right] \quad (13)$$

Thus, $\lambda_k^{(m+1)}$, which is the minimum of $\mathbf{C}(\lambda)$, for $m=0, 1, 2, \dots$ is given by

$$\lambda_k^{(m+1)} = -\frac{b}{2c} = \frac{\{\lambda_k^{(m)}\}^2 \delta \mathbf{C}_{k+1}}{2 \left[\mathbf{C}(\mathbf{X}_k + \lambda_k^{(m)} \mathbf{P}_k) - \mathbf{C}(\mathbf{X}_k) - \lambda_k^{(m)} \delta \mathbf{C}_{k+1} \right]} \quad (14)$$

Then, we start with $\lambda_k^{(0)} = 1$ and proceed with the backtracking procedure of (10) until (9) is satisfied. In order to take advantage of the newly acquired information of the cost function beyond the first backtrack and improve the accuracy, we replace the quadratic model of Equation (10) with the following cubic form

$$\mathbf{C}(\lambda) = \mathbf{C}(\mathbf{X}_k + \lambda \mathbf{P}_k) \approx a + b\lambda + c_2\lambda^2 + d\lambda^3 \quad (15)$$

where

$$\begin{bmatrix} c \\ d \end{bmatrix} = \frac{1}{\lambda_2 - \lambda_1} \begin{bmatrix} -\lambda_1 / \lambda_2^2 & \lambda_2 / \lambda_1^2 \\ 1 / \lambda_2^2 & -1 / \lambda_1^2 \end{bmatrix} \bullet \begin{bmatrix} \mathbf{C}(\lambda_2) - \lambda_2 b - \mathbf{C}(\mathbf{x}_k) \\ \mathbf{C}(\lambda_1) - \lambda_1 b - \mathbf{C}(\mathbf{x}_k) \end{bmatrix} \quad (16)$$

λ_1, λ_2 are two previous subsequent search steps. Then the final solution to $\lambda_k^{(m+1)}$ is given

by

$$\lambda_k^{(m+1)} = \frac{-c + \sqrt{c^2 - 3db}}{3d} \quad (17)$$

3) The Jacobian Matrix

In (8), the Jacobian matrix is given by

$$\mathbf{J}(\mathbf{X}) = \begin{bmatrix} \partial s_1 / \partial x_1 & \cdots & \partial s_1 / \partial x_i & \cdots & \partial s_1 / \partial x_N \\ \vdots & \ddots & \vdots & \ddots & \vdots \\ \partial s_j / \partial x_1 & \cdots & \partial s_j / \partial x_i & \cdots & \partial s_j / \partial x_N \\ \vdots & \ddots & \vdots & \ddots & \vdots \\ \partial s_{9 \times NR} / \partial x_1 & \cdots & \partial s_{9 \times NR} / \partial x_i & \cdots & \partial s_{9 \times NR} / \partial x_N \end{bmatrix} \quad (18)$$

Every entry of the Jacobian matrix can be estimated through a finite-difference computation,

$$\frac{\partial s_j(x)}{\partial x_i} \approx \frac{s_j[(1+\Delta)x_i] - s_j(x_i)}{\Delta x_i} \quad (19)$$

In our implementation, Δ is chosen to be 10^{-4} . The computation of the Jacobian matrix is the most time-consuming part in the entire inversion procedure since in each Gauss-Newton step we need to solve $9 \times NR \times N$ forward problems to construct the Jacobian matrix.

4) The Constrain Algorithm

For better efficiency, it is necessary to impose a priori maximum and minimum bounds for the unknown parameters. For this purpose, we introduce a nonlinear transformation given by

$$x_i = \frac{x_i^{\max} + x_i^{\min}}{2} + \frac{x_i^{\max} - x_i^{\min}}{2} \sin(c_i), \quad -\infty < c_i < +\infty \quad (20)$$

where x_i^{\max}, x_i^{\min} are the upper and lower bounds on the physical model parameter x_i . It is clear that

$$x_i \rightarrow x_i^{\min}, \text{ as } \sin(c_i) \rightarrow -1 \quad (21)$$

$$x_i \rightarrow x_i^{\max}, \text{ as } \sin(c_i) \rightarrow +1 \quad (22)$$

Theoretically, by using this nonlinear transformation we should update the artificial unknown parameters c_i instead of the physical model parameters x_i . However, it is

straightforward to show that

$$\frac{\partial s_j}{\partial c_j} = \frac{dx_i}{xc_j} \frac{\partial s_j}{\partial x_i} = \sqrt{(x_i^{\max} - x_i)(x_i - x_i^{\min})} \frac{\partial s_j}{\partial x_i} \quad (23)$$

The two successive iterates $x_{i,k+1}$ and $x_{i,k}$ of x_i are related by

$$\begin{aligned} x_{i,k+1} &= \frac{x_i^{\max} + x_i^{\min}}{2} + \frac{x_i^{\max} - x_i^{\min}}{2} \sin(c_{i,k+1}) \\ &= \frac{x_i^{\max} + x_i^{\min}}{2} + \frac{x_i^{\max} - x_i^{\min}}{2} \sin(c_{i,k} + q_{i,k}) \end{aligned} \quad (24)$$

where

$$c_i = \arcsin\left(\frac{2x_{i,k} - x_i^{\max} - x_i^{\min}}{x_i^{\max} - x_i^{\min}}\right) \quad (25)$$

and $q_{i,k} = c_{i,k+1} - c_{i,k}$ is the Gauss-Newton search step in c_i towards the minimum of the cost functional in (10). This Gauss-Newton direction in x_i is related to the Gauss-Newton direction in c_i through the following relation

$$p_i = q_i \frac{dx_i}{dc_i} \quad (26)$$

Therefore, by applying the relationship in (26) to (24), we obtain the following relationship between the two successive iterates $x_{i,k+1}$ and $x_{i,k}$ of x_i (the step-length γ_k along the search direction x_i is assumed to be adjustable):

$$x_{i,k+1} = \frac{x_i^{\max} + x_i^{\min}}{2} + \left(x_{i,k} - \frac{x_i^{\max} + x_i^{\min}}{2}\right) \cos\left(\frac{V_k P_{i,k}}{\gamma_k}\right) + \gamma_k \sin\left(\frac{V_k P_{i,k}}{\gamma_k}\right) \quad (27)$$

where

$$\gamma_k = \sqrt{(x_i^{\max} - x_{i,k})(x_{i,k} - x_i^{\min})} \quad (28)$$

Thus, in the inversion process there is no need to compute either c_i or q_i explicitly. This will reduce the round-off errors caused by the introduction of the nonlinear function.

5) Zero-D Inversion

Next, we will describe the choice of the initial model in the inversion procedure since good initial model can significantly improve the efficiency of the inversion. In practical, we do not know the exact number of the layers, therefore we employ a whole space inversion (also called Zero-D inversion) to get the initial model. Zero-D inversion is receiving increasing interest in the study of inversion [14]. The biggest difference between Zero-D inversion and 1-D inversion is that Zero-D inversion inverts parameters based on each logging point. In Zero-D inversion, at each logging point, we should invert four parameters (the dipping angle, rotation angle, horizontal conductivity and vertical conductivity). In order to be distinguished from the 1-D inversion, the initial guess of the Zero-D inversion is called as starting values. Next, we will explain the choice of the starting values in the zero-D inversion.

Starting Values

In order to get an acceptable starting point for the Zero-D inversion, we use the analytic expressions to compute α , γ , σ_h and σ_v directly [6] [15]:

$$\alpha = a \tan \left(\frac{2H_{xz_i}^t}{H_{xx_i}^t - H_{zz_i}^t} \right) \quad (29)$$

$$\gamma = a \tan \left(\frac{2H_{xy_i}^c}{H_{xx_i}^c - H_{yy_i}^c} \right) \quad (30)$$

$$\sigma_h = \frac{4\pi l}{\omega\mu_0} \left[\operatorname{Im}(H_x^i) + \frac{1}{2} \operatorname{Im}(H_z^i) + \sqrt{\left(\operatorname{Im}(H_x^i) - \frac{1}{2} \operatorname{Im}(H_z^i) \right)^2 + 2 \operatorname{Im}(H_z^i)^2} \right] \quad (31)$$

$$\lambda^2 = 256\pi^2 l^2 \sigma_{ha}^2 / \operatorname{Im}(H_z^i) \left(\operatorname{Im}(H_x^i) + \operatorname{Im}(H_y^i) + \operatorname{Im}(H_z^i) - \frac{\omega\mu_0}{4\pi l} \sigma_h \right) \quad (32)$$

$$\sigma_v = \frac{1}{\lambda^2} \sigma_h \quad (33)$$

where superscripts t and c represent the borehole and the tool coordinates.

With the aid of the Zero-D inversion, the average values of α , γ are assumed as the initial dipping and rotation angle.

Initial Boundary

After the initial dipping and rotation angle are determined, we need to determine the initial boundary. We employ two methods together to determine the initial boundary:

- (1) Variance based method of $2\sigma_v - \sigma_h$
- (2) Horn effect of the cross components σ_{xz}, σ_{zx}

The disadvantage of the first method is its instability. As we know, Zero-D inversion results sometimes have large error. In this case, we can not completely rely on the variance based method. As a good supplement, we use the horn effect of the cross components σ_{xz}, σ_{zx} to determine boundary since σ_{xz}, σ_{zx} have obvious horn effect when crossing the boundary. By combining the two methods, we can assure that no boundary is missed.

The next important issue is how to detect and merge the redundant initial boundaries during the 1-D inversion. In this paper, we employ the golden section search to merge redundant layers.

6) Noise Analysis

According to Anderson [16], we incorporate two types of noises: coherent noise and incoherent noise to simulate borehole noise, which is the main source of the noise. For coherent noise, since the triaxial array is assumed to be co-located, the borehole noise will be correlated in all the measurements. In this case, all coils should have the same noise level. On the other hand, if the x, y, and z coils are not co-located, or if the tool is moving at an irregular speed, the noise will be incoherent. In order to simulate incoherent

noise, an array of different random numbers will be generated for each measure channel and then scaled and added as above [16].

7) *Flow Chart of the Inversion*

Fig. 2 shows the flow chart of the 1-D inversion. One can load the initial guess either from Zero-D inversion or from a predetermined initial files.

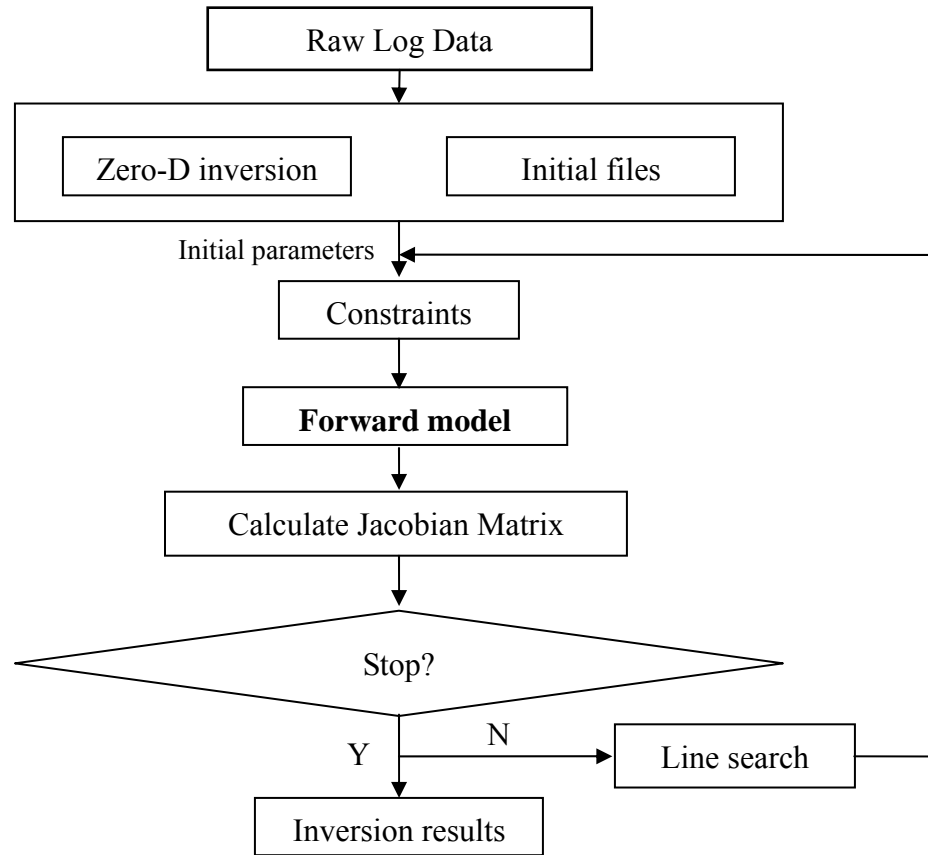


Fig 2. Flow chart of 1-D inversion

3. Examples

Based on the above theory, we develop an 1-D inversion code. In this section, we will demonstrate the capability and robustness of the code by synthetic data and a field log data. If without specific illustration, in all the examples, initial models are provided by

Zero-D inversion. No priori information is required in our inversion procedure. The conductivity σ , dipping angle α , rotation angle γ , and the bed-boundary parameters Z_i are enforced to be within the following range:

$$\begin{aligned} 0.0005 < \sigma < 5 \\ 0.0001 < \alpha < 89^\circ \\ 0.0001 < \gamma < 180^\circ \\ Z_{i-1} < Z_i < Z_{i+1} \quad (2 \leq i \leq L-2) \\ D_0 < Z_1 < Z_2 \\ Z_{L-2} < Z_{L-1} < D_N \end{aligned}$$

It should be noted that limits on boundary are dynamic. D_0 and D_N are the depth of the first and last measured data, respectively. Hence each layer can shift maximum between the adjacent boundaries. The examples were run on a 2-core 2.61 GHz, 1.87 GB PC.

Example 1

In the first example, the formation model is a simple three-layer anisotropic model, as shown in Fig. 3. The formation is characterized by a high-resistivity pay zone surrounded by two symmetric isotropic zones.

The synthetic data used in this example are sampled from 10 ft to 50 ft with a 0.25 ft step. We use the triaxial array as shown in Fig 1 to collect data. The distance between the transmitter and receiver is 40 inches. The working frequency is 20 KHz. In this example, the dipping angle is 30° and the rotation angle is 60° .

We apply the full matrix as well as the diagonal terms of the apparent conductivity tensor as the input log data, respectively. By comparing the inversion results from these two input data, we want to investigate whether reducing input data can still guarantee the accuracy of the 1-D inversion.

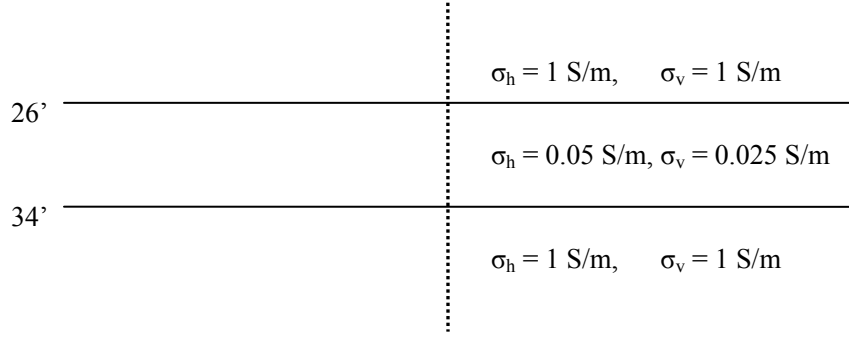


Fig 3. A three-layer anisotropic model

Validation I— raw data

We first apply the raw data without noise to do inversion. The initial guess is provided by the Zero-D inversion with the full matrix. Fig. 4 shows the initial guess and inverted conductivity profile. The maximum relative error of the inverted horizontal and vertical conductivities is less than 0.1%.

Tabel 1 presents the initial guess and inversion results of the dipping angle, rotation angle obtained from the full matrix and the diagonal terms, respectively. We can see that the inversion results from the full matrix and the diagonal terms match well with the true parameters except the rotation angle given by the diagonal terms is different from the true value. The inverted rotation angle (120°) becomes the coangle of the true rotation angle (60°), which is caused by the elimination of all the cross components.

In Fig.5, we compare the raw data and the calculated responses from the inverted formations. As can be seen, the components $\sigma_{xx}, \sigma_{yy}, \sigma_{zz}, \sigma_{yz}$, and σ_{zy} from the inverted formation obtained both the full matrix and diagonal terms coincide with the raw data. Since the inverted rotation angle from the diagonal terms is the coangle of the true value, The cross components $\sigma_{xz}, \sigma_{zx}, \sigma_{yz}$ and σ_{zy} obtained from the diagonal term inversion model are exactly in the reverse direction of the raw log since the inverted rotation angle

is the coangle of the true one. Thus we can conclude that neglecting the cross components in inversion will introduce uncertainty when determining the rotation angle. Table 2 shows the total CPU time cost by the inversions using the full conductivity matrix and the diagonal terms, respectively. We can see that the when using the full matrix to do the inversion, the procedure converges faster and cost less time. In Fig 6 we compare the cost functions of the two inversion models versus the iteration numbers. Compared with the full-matrix model, the diagonal-term model requires more iteration to converge although each iteration cost less computation time, yielding slower behavior than the full-matrix model. Due to the slower behavior and the uncertain effect on the rotation angle of the diagonal-term model, we prefer to do the inversion using the full conductivity matrix.

Table 1. The inverted dipping angle and rotation angle Validation I

Validation I	Initial Guess	Full Matrix	Diagonal Term
α ($^{\circ}$)	32.29	30.00	30.00
γ ($^{\circ}$)	34.63	60.00	120.00

Table 2. The CPU time cost in Validation I

Inversion model	Full Matrix	Diagonal Term
Time (s)	92	106

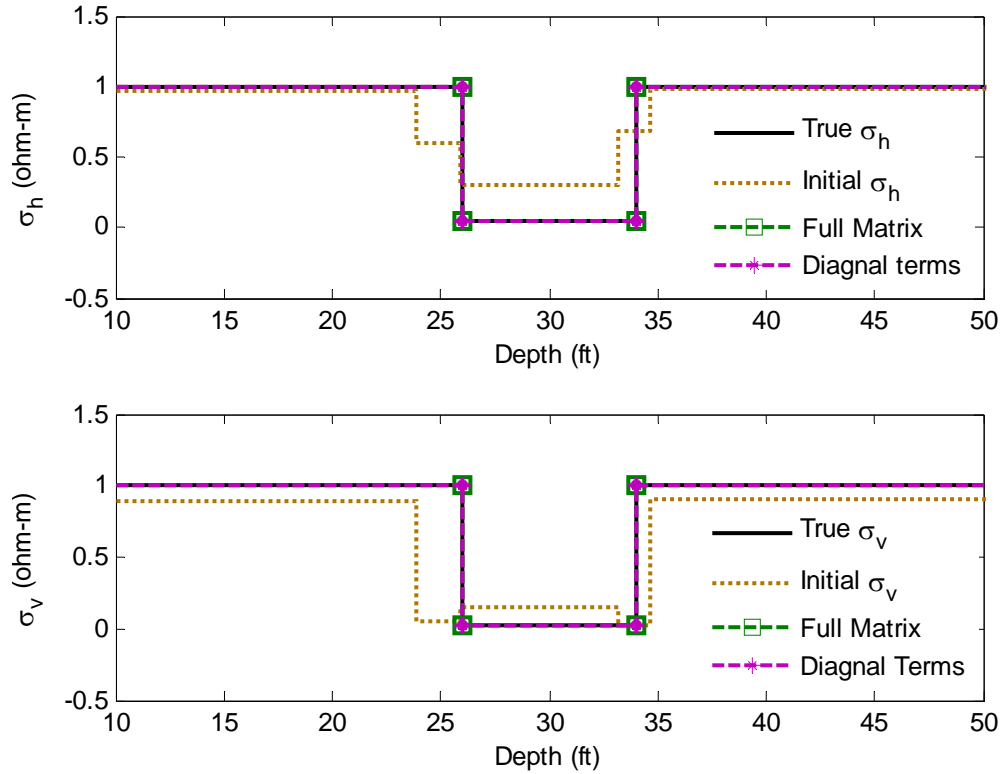


Fig 4. Inverted conductivity profile with the synthetic raw data for the model in Fig. 3.

The true dipping angle and rotation angle are 30° and 60° , respectively. The solid black line represents true anisotropic resistivity. The initial guess is shown by the gray dotted line. The green dashed line with square mark represents the inverted results using the full resistivity matrix. The purple dashed line with star mark represents the inverted result using the diagonal terms.

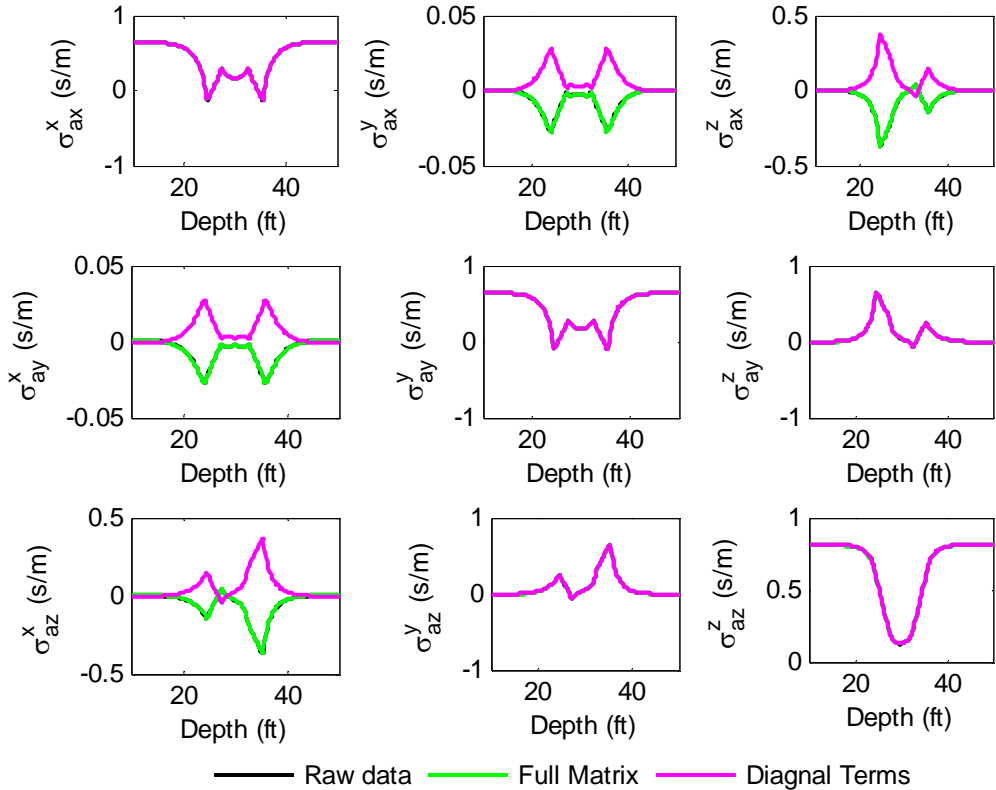


Fig 5. Comparison of the apparent conductivity simulated from the two inverted model and the raw data.

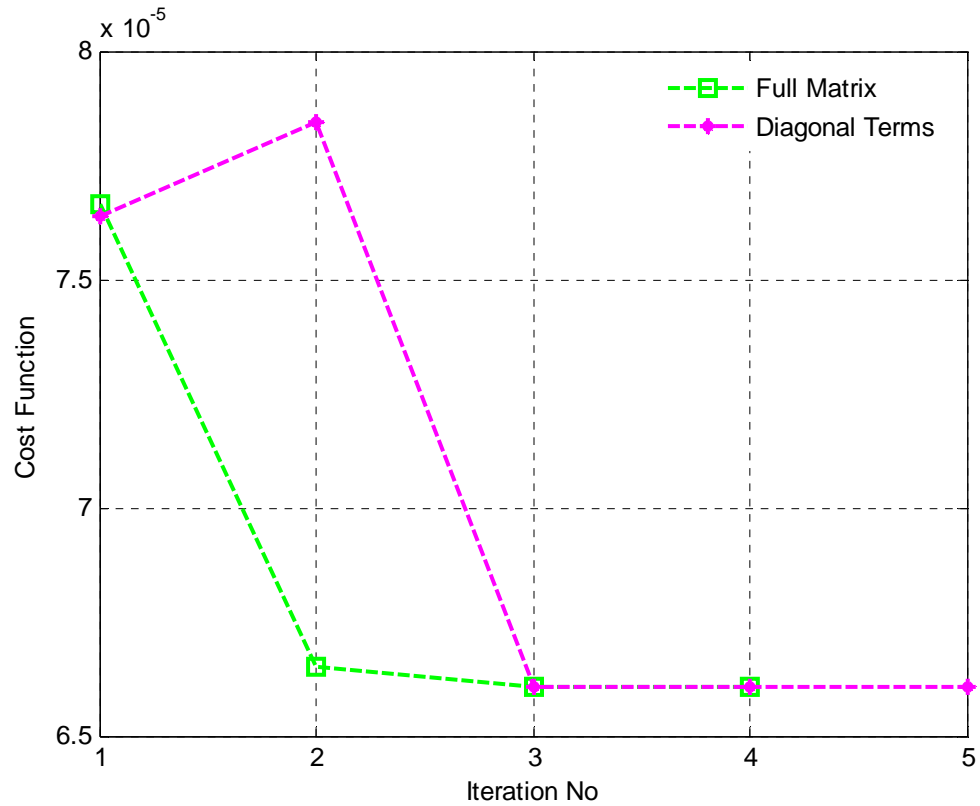


Fig 6. The cost function of the two inversion models versus the number of iterations.

Validation II— 5% coherent noise

Next, we add 5% coherent noise to the raw data and repeat the inversion procedure. The initial guess of the dipping and rotation angle are 30.53° and 27.54° , respectively while the inverted dipping and rotation angle are 30.16° and 60.04° , respectively. Fig. 7 compares the inverted conductivity with the true parameters. Very good agreement is observed. The maximum error of the inverted horizontal and vertical conductivity is about 3%. The entire inversion cost about 220 seconds to obtain a convergent result.

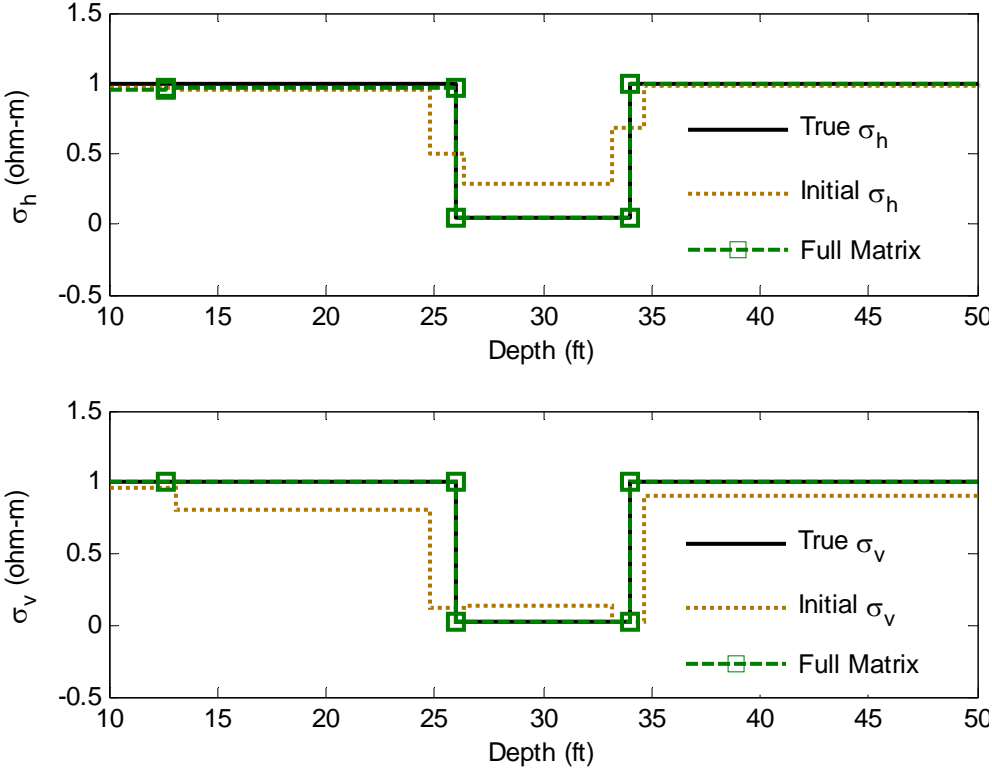


Fig 7. Inverted conductivity obtained from the synthetic data for the model in Fig. 3 with the input log contaminated by 5% coherent noise.

Validation III— 5% incoherent noise

Next, we add 5% incoherent noise to the input log data and repeat the inversion. The inverted dipping and rotation angle are 30.5° and 59.33° , respectively, with a relative error of 1.7 % and 1.2 % respectively. Fig.8 presents the inveted horizontal and vertical conductivities. The maximum relative error of the inverted horizontal and vertical conductivities is about 8%. From Fig.8, we can see that the presence of the incoherent noise cause a stronger negative impact on the Zero-D inversion than the coherent noise and more layers are generated in the initial guess. However, the inversion still yields satisfactory results despite the bad initial guess. It cost about 508 seconds to obtain the final inversion result.

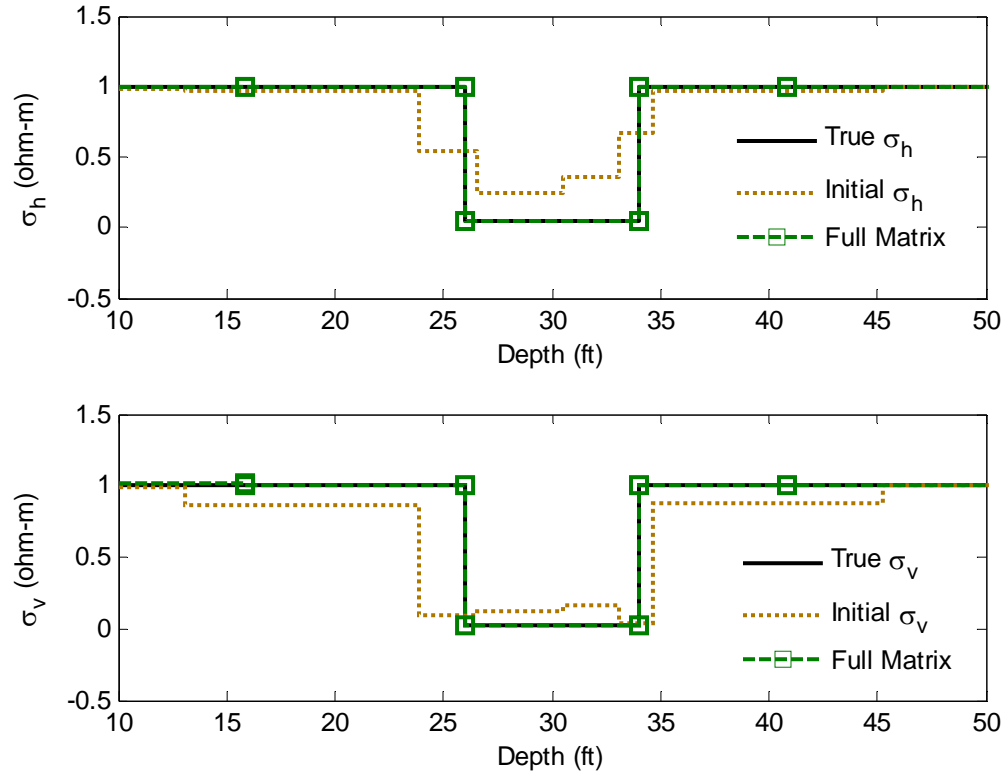


Fig 8. Inverted conductivity obtained from the synthetic data for the model in Fig. 3 with the input log contaminated by 5% incoherent noise.

Example 2

Next, we will further validate our inversion algorithm using the Oklahoma benchmark model [17]. The formation has 23 layers. The distance between the transmitter and the receiver is 20 inches and the operating frequency is 20 KHz. The dipping angle is 60° and the rotation angle is 0° .

Fig. 9 shows the real conductivity and the inverted conductivity obtained from the contaminated data with 5% coherent noise and 5% incoherent noise. Table 3 gives the initial guess of the dipping angle, rotation angle and the inverted dipping and rotation angle for each case. The initial guess is modified from the Zero-D inversion results when applying the raw data. Although redundant initial layers are given, our inversion code

successfully converged and provides reliable inversion results in all the three cases. In Fig.10 we show the convergence property of the three cases. It is observed that the cost function with the 5% coherent noise is a slightly higher than the other two cases due to the misfit between the eighth and ninth layer. The inversion with 5% incoherent noise consumes the most time. For this multilayer model, the inversion code took about 590, 491 and 650 minutes to obtain the final result under the three cases: uncontaminated raw data, 5% coherent noise and 5% incoherent noise. It is found that the third case cost the most time. Furthermore, we can see from Fig. 9 that the error becomes larger for high resistive layers (the resistivity is larger than 100 ohm-m). This is reasonable since the induction logging tool has a better sensitivity to the conductive layer than the resistive layer. When the formation resistivity is larger than 100 ohm-m, the resolution of the induction logging tool significantly decreased.

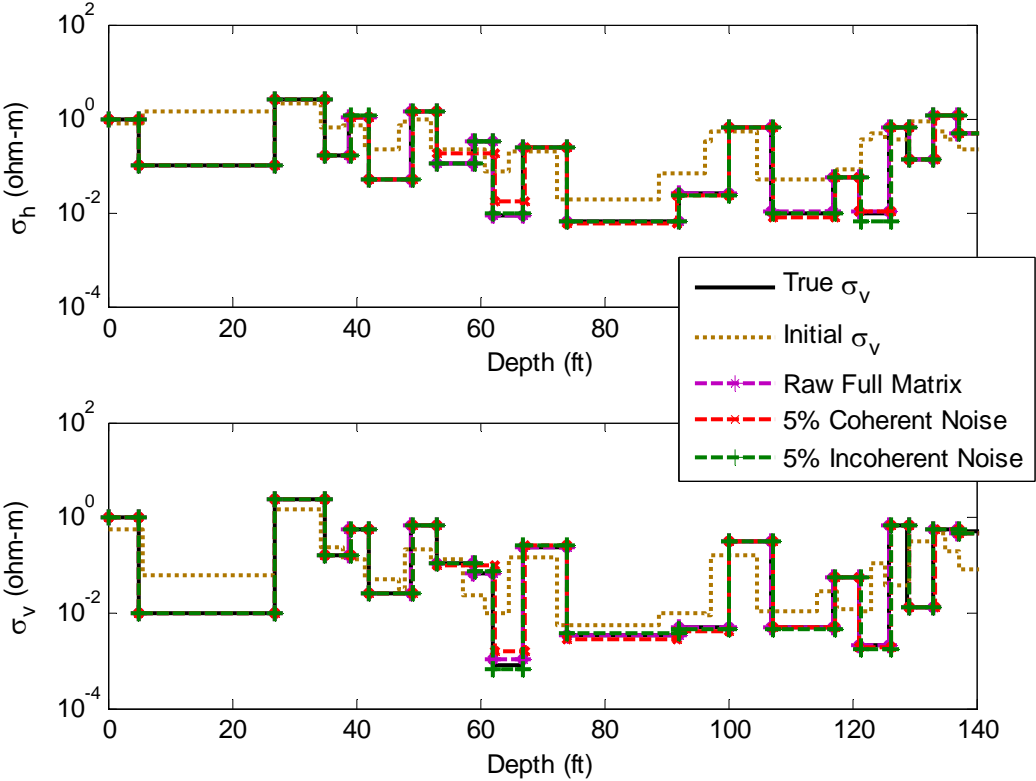


Fig 9. Inverted conductivity with the synthetic raw data for the Oklahoma benchmark model.

Table.3 Inverted dipping angle, rotation angle with different input data

	Initial Guess	Raw Full Matrix	Coherent Noise	Incoherent Noise
α ($^\circ$)	60.99	59.99	59.93	59.95
γ ($^\circ$)	0.005	0.005	0.005	0.005

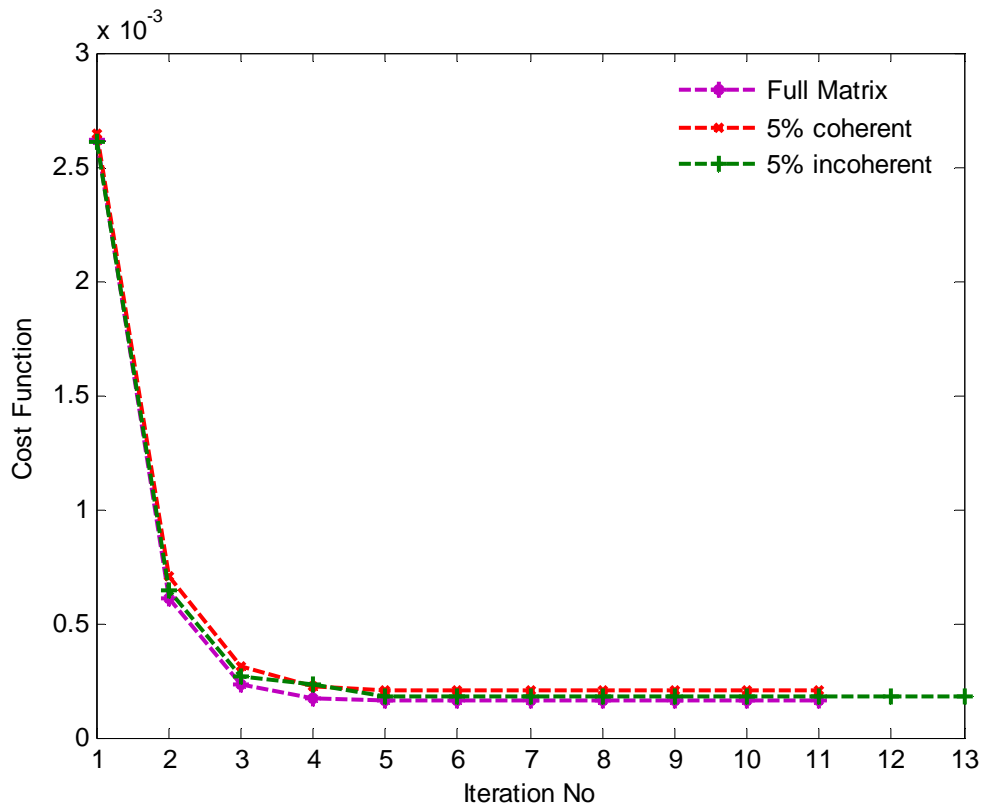


Fig 10. The cost functions versus the iteration number for the three inversion cases.

Example 3

As the final example, we apply the present inversion algorithm to an induction field log taken from Well No 36-6, East Newkirk, Oklahoma [18], as shown in Fig. 11. The induction tool is 6FF40. We use this example to investigate the capability of our 1-D

inversion model in the field exploration.

In Fig. 11, the solid line represents the field log from 6FF40. The dashed line represents the inverted log from Ref. [18]. The polynomial expansion is used to fit the field log and plot it in Fig. 12. Fig. 13 shows the inversion results from our 1-D inversion code. For this example, we only need to invert the horizontal conductivity since it is traditional induction logging. Both the dipping angle and rotation angle are 0° . In Fig. 14 we plot the calculated response from the inverted parameters and compare it with the field log. By comparing Fig. 11 and Fig. 14, we can see that our calculated log is much smoother compared with the inverted log from the published paper. In the beginning 20 ft, our calculated log is much closer to the raw field data.

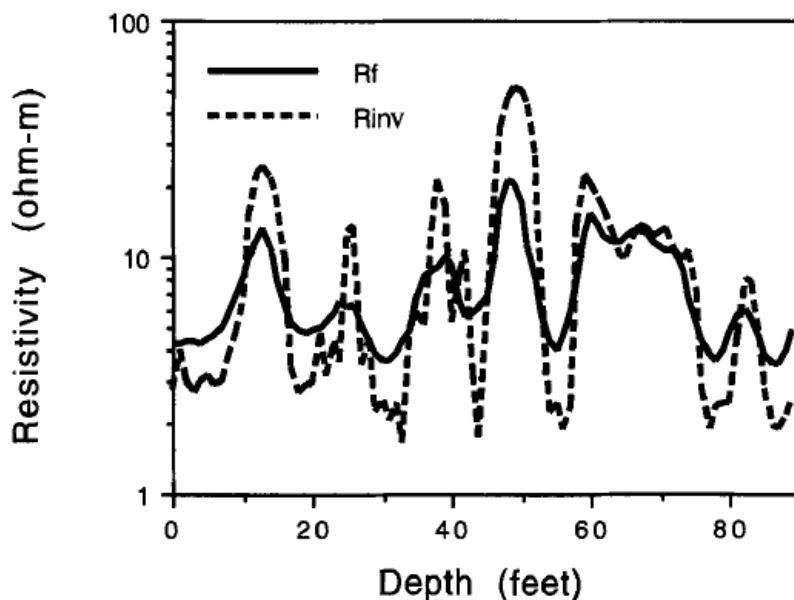


Fig 11. Field log measured by 6FF40 from Well No 36-6, East Newkirk, Oklahoma [19]. The solid line represents the field log and the dashed line represents the inversion values in Ref. [18].

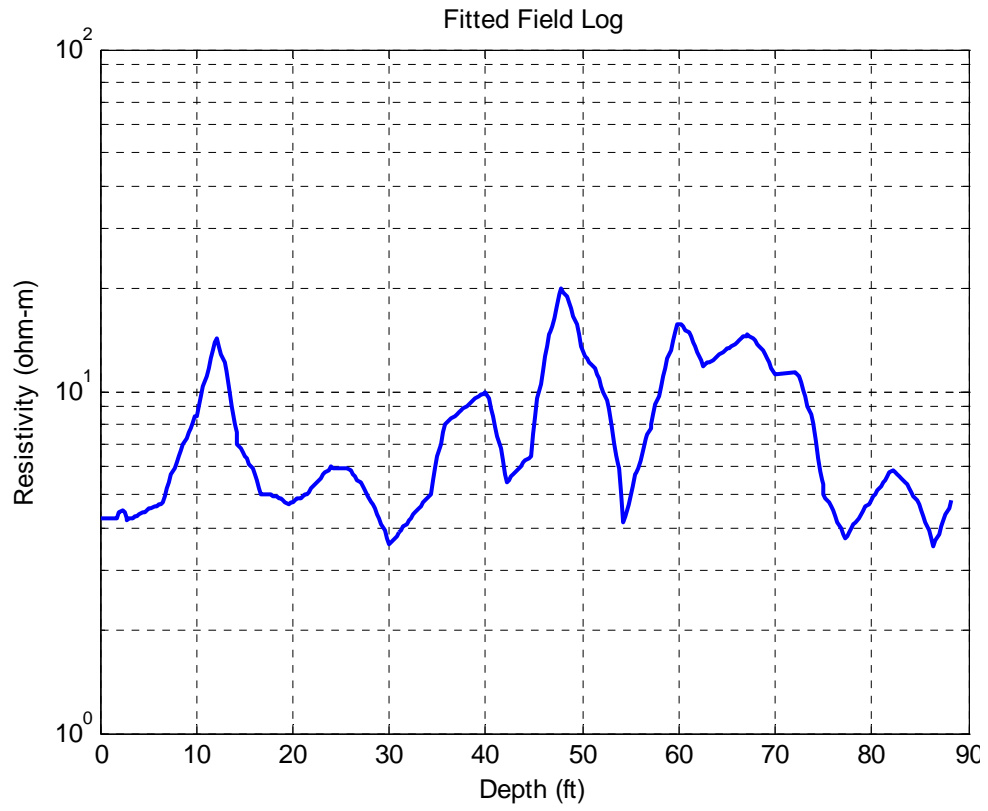


Fig 12. Fitted field log as shown in Fig. 11

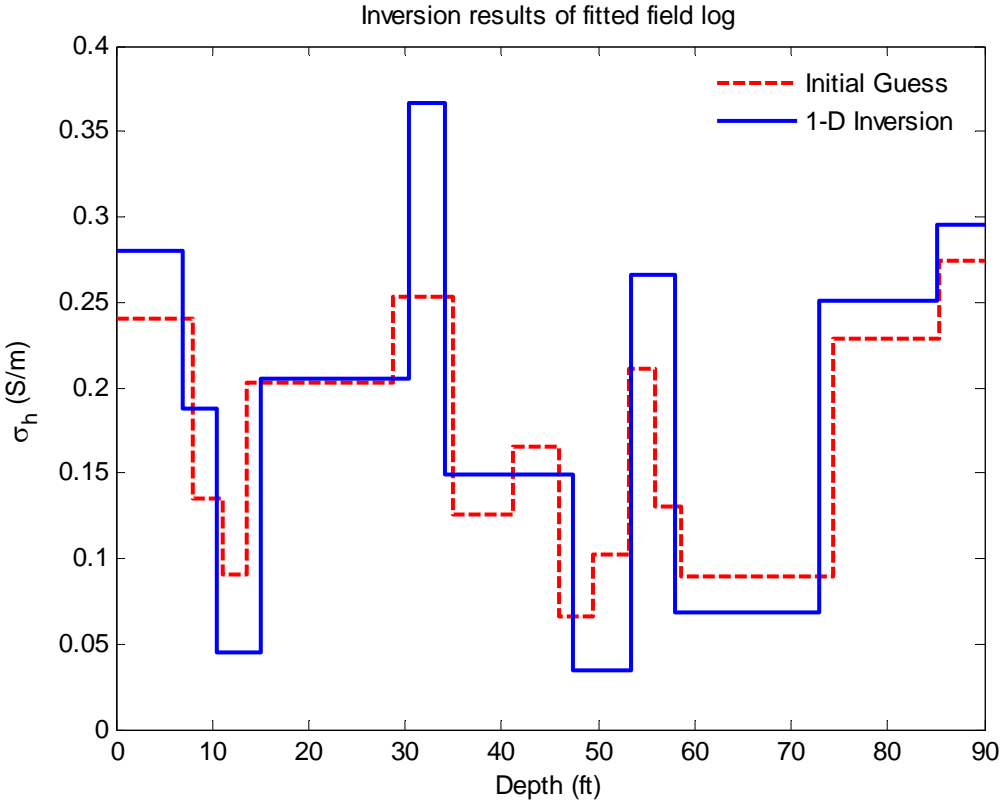


Fig 13. Inverted resistivity of the fitted field log in Fig. 12 by applying the 1-D inversion algorithm.

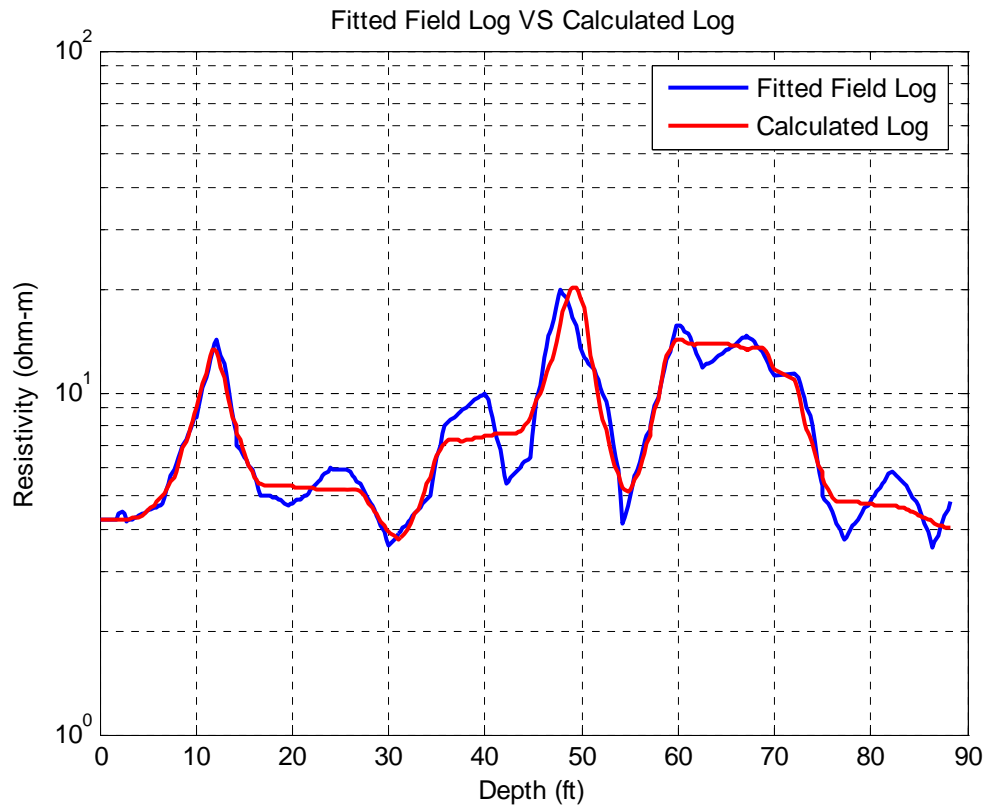


Fig 14. Comparison between the fitted field log from the Ref.[18] and the calculated log from the inverted formation. The blue line is the fitted field log and the red line is the calculated log from the 1-D inversion.

4. Summary

In this paper, we presented an inversion algorithm for triaxial induction logging in 1-D layered transverse isotropic formation. The Gauss-Newton algorithm is employed to modify Newton step from Gauss-Newton algorithm and thus reduces the cost function. In order to improve the effectiveness of the Gauss-Newton algorithm, Gill and Murray Cholesky factorization is used to calculate the Hessian matrix in the Quadratic model of the cost function. Zero-D inversion is used to generate the initial guess. In order to obtain

good initial guess, both the variance-based method and the horn effect of the cross components are used to determine the initial boundary. Then golden section search is applied to merge redundant initial boundaries during the inversion. The resultant inversion algorithm was validated by synthetic data from our forward modeling and other different forward modeling. Satisfactory inversion results can be obtained in various cases despite of the noise. We also demonstrate the capability of our code in the application of the real field log inversion.

References

- [1] C. J. Weiss and G. A. Newman, “Electromagnetic induction in a fully 3-D anisotropic earth”, *Geophysics*, vol. 67, issue. 4, pp.1104–1114, July 2002.
- [2] A. Abubakar, T. M. Habashy, V. Druskin, L. Knizhnerman, and S. Davydycheva, “A 3D parametric inversion algorithm for tri-axial induction data”, *Geophysics*, Vol. 71, No. 1, pp. G1–G9, January 2006.
- [3] A. B. Cheryauka and M. S. Zhdanov, “Fast modeling of a tensor induction logging response in a horizontal well in inhomogeneous anisotropic formations”, *SPWLA 42nd Annual Logging Symposium*, June 2001.
- [4] L. Yu, B. Kriegshauser, O. Fanini, and J. Xiao, “A fast inversion method for multicomponent induction log data”, 71st Annual International Meeting, *SEG*, Expanded Abstracts, pp. 361–364, 2001
- [5] X. Lu, and D. Alumbaugh, “One-dimensional inversion of three component induction logging in anisotropic media”, 71st Annual International Meeting, *SEG*, Expanded Abstracts, pp. 376–380, 2001.
- [6] Z. Zhang, L. Yu, B. Kriegshauser, and L. Tabarovsky, “Determination of relative angles and anisotropic resistivity using multicomponent induction logging data”, *Geophysics*, vol. 69, 898–908, July 2004.
- [7] H. Wang, T. Barber, R. Rosthal, J. Tabanou, B. Anderson, and T. M. Habashy, “Fast and rigorous inversion of triaxial induction logging data to determine formation resistivity anisotropy, bed boundary position, relative dip and azimuth angles”, 73rd Annual International Meeting, *SEG*, Expanded Abstracts, pp. 514–517, 2003.
- [8] A. Abubakar, P. M. van den Berg, and S.Y. Semenov, “Two- and three-dimensional algorithms for microwave imaging and inverse scattering,” *Journal of Electromagnetic Waves and Applications*, vol.17, pp. 209-231, 2003.

- [9] Davydycheva, V. Druskin, and T. M. Habashy, “An efficient finite-difference scheme for electromagnetic logging in 3D anisotropic inhomogeneous media,” *Geophysics*, vol. 68, pp. 1525–1536, September 2003.
- [10] T. M. abashy, and A. Abubakar, “A general framework for constraint minimization for the inversion of electromagnetic measurements,” *Progress in Electromagnetic Research*, vol. 46, pp. 265-312, 2004.
- [11] L. L. Zhong, J. Ling, A. Bhardwaj, S. C. Liang and R. C. Liu, “Computation of Triaxial Induction Logging Tools in Layered Anisotropic Dipping Formations,” *IEEE Trans. Geosci. Remote Sens.*, vol.46, no.4, pp. 1148–1163, March 2008.
- [12] J. E. Dennis, Jr. and R. B. Schnabel, “Numerical Methods for Unconstrained Optimization and Nonlinear Equations”, in Prentice Hall series in computational mathematics, 1983, pp.1-378.
- [13] P. E. Gill and W. Murray, “Newton-type methods for unconstrained and linearly constrained optimization,” *Mathematical Programming*, no. 28, pp.311-350, July 1974.
- [14] P. Wu, G. L. Wang, and T. Barber, “Efficient Hierarchical Processing and Interpretation of Triaxial Induction Data in Formations With Changing Dip,” *SPE Annual Technical Conference and Exhibition*, September 2010
- [15] M. Zhdanov, D. Kennedy, and E. Peksen, “Foundations of tensor induction well-logging”, *Petrophysics*, vol. 42, pp. 588-610, 2001.
- [16] B. I. Anderson, T. D. Barber, and T. M. Habashy, “The interpretation and inversion of fully triaxial induction data; a sensitivity study”, *SPWLA 43rd Annual Logging Symposium*, 2002.
- [17] R. Rosthal, T. Barber, S. Bonner, “Field test results of an experimental fully-triaxial induction tool”, *SPWLA 44th Annual Logging Symposium*, 2003.

- [18] B. I. Anderson, T. D. Barber, and T. M. Habashy, "The interpretation and inversion of fully triaxial induction data; a sensitivity study", *SPWLA 43rd Annual Logging Symposium*, 2002.
- [19] R. Freedman, and G. N. Ninerbo, "Maximum entropy inversion of induction-log data", *SPE formation evaluation*, June 1991.
- [20] N. Yuan, X. Chun Nie and R. Liu, "Improvement of 1-D simulation codes for induction, MWD and triaxial tools in Multi-layered dipping beds", *Well Logging Laboratory Technical Report*, pp.32-71, October 2010.
- [21] M. J. Wilt, D. L. Alumbaugh, H. F. Morrison, A. Becker, K. H. Lee, and M. Deszcz-Pan, "Crosswell electromagnetic tomography: System design considerations and field results", *Geophysics*, vol. 60, no. 871-885, May 1995.
- [22] Wang, and L. C. Shen, "IND2D users' guide", *Well Logging Laboratory Technical Report*, pp.32-71, 1996.
- [23] Y. Zhang, L. C. Shen, and C. Liu, "Inversion of induction logs based on maximum flatness, maximum oil, and minimum oil algorithms", *Geophysics*, vol. 59, no.9, pp. 1320-1326, September 1994.

CHAPTER 2

Parallelization of Forward Modeling Codes using OpenMP

Abstract

Efficiency of a forward modeling code is very important for both efficient evaluation of tool responses and log data interpretation in real time/post processing. With the advancement of various high performance computing techniques such as Message Passing Interface (MPI), Open Multi-Processing (OpenMP). OpenMP and computer hardware technology such as graphics processing units (GPU), it is possible to significantly improve the efficiency of the forward modeling by using these techniques. In this paper, we apply OpenMP to parallelize several previously developed codes: 1. The simulation codes for wireline induction and LWD triaxial tools in one-dimensional (1-D) multilayered anisotropic formation 2. The three-dimensional (3-D) simulation code for triaxial induction logging tools in arbitrarily anisotropic formations. The parallel process is explained in detail and numerical examples are presented to demonstrate the capability of the parallel codes. Comparison of the original code and the parallel code shows that the latter is much faster without loss of accuracy. Then the codes are used to do some investigations about directional electromagnetic (EM) propagation measurements.

1. Introduction

Efficiency of a computing code is always an important issue for users. In well logging area, on one hand, an efficient forward modeling code can simulate the tool responses fast and save CPU time for users. On the other hand, since the inversion process requires a repeated computation of the forward modeling, efficient forward modeling is crucial to faithful interpretation of log data acquired. Nowadays, the development of high performance computing techniques provides us various choices to improve the speed of the forward modeling without loss of accuracy. A graphics processing unit or GPU is a specialized circuit designed to rapidly manipulate and alter memory in such a way so as to accelerate the building of images in a frame buffer intended for output to a display.

Modern GPUs are very efficient at manipulating computer graphics, and their highly parallel structure makes them more effective than general-purpose CPUs for algorithms where processing of large blocks of data is done in parallel. The most popular CPU-based parallel techniques are Message Passing Interface (MPI) and Open Multi-Processing (OpenMP). MPI was first implemented in 1992 [1] and remains the dominant method used in high-performance computing today [2-4]. MPI is language-independent and can be run on either symmetric multiprocessor (*SMP*), distributed shared memory (*DSM*) processor or clusters, and supercomputers. However, MPI is relatively difficult to implement in programming. On the contrary, the latest developed OpenMP is easy to implement and therefore becomes an appropriate choice for less complicated algorithms. OpenMP is an application programming interface that supports multi-platform shared memory multiprocessing programming in Fortran, C, and C++ [5-8]. In this paper, we apply OpenMP to parallelize the following forward modeling codes: 1. the forward modeling code for wireline induction and LWD triaxial tools in 1-D layered anisotropic formation; 2. the simulation code for induction triaxial logging tools in three-dimensional (3-D) arbitrarily anisotropic formation. The principals of the forward modeling are briefly explained and the parallel implementation of the codes is described in details. In the numerical result section, we compare the total CPU time as well as the simulation results of several examples between the original code and the parallelized code. After parallelization, the computation speed is significantly on a multi-core computer and the speed can be further improved as the number of the processor cores increases. The codes are also used to do some interesting investigations and discussions will be presented in the numerical result section.

2. Theory

2.1 Parallelization of the 1-D Simulation Codes for Wireline Induction and LWD Triaxial Tools in Anisotropic Formations

In this section, we will explain how to use OpenMP to parallel the simulation code for wireline or LWD triaxial tools in 1-D layered anisotropic formation. This section is arranged as follows. First, for the completeness of the paper, we briefly present the theory on which the forward modeling of wireline and LWD triaxial logging is based. Then, we will explain the parallel implementation of the codes using OpenMP for the 1-D Fortran codes.

A. Forward Modeling of Wireline/LWD Triaxial Logging

Triaxial tool is an emerging logging tool to detect formation anisotropy and delineate low resistivity reservoirs. A triaxial tool usually comprises one coaxial transmitter-receiver pair and two coplanar transmitter-receiver pairs [9-15]. The transmitter/receiver coils are perpendicular to each other. The formation anisotropy responds to different components in tool transmitter–receiver combinations, thus providing additional information for better formation evaluation. Our 1-D simulation for the response of triaxial tools in anisotropic formations is based on an analytical method which solves the Maxwell’s equations in the presence of magnetic dipole excitation analytically (both the transmitter and receivers are modeled as magnetic dipoles since they are infinitely small) [16-18]. The generalized upward and downward reflection coefficients are obtained from the equivalent transmission line theory [19].

Consider a triaxial tool which includes three orthogonal transmitters and three orthogonal receivers oriented at x, y and z direction, respectively, as shown in Fig.1. The coils are assumed to be sufficiently small and can be replaced by point magnetic dipoles in the modeling. Thus, the magnetic source excitation of the triaxial tool can be expressed as $\mathbf{M} = (M_x, M_y, M_z)\delta(\mathbf{r})$. If the transmitter/receiver is oriented at arbitrary directions, the magnetic dipole will be projected to the x, y, z direction first and follow the same analysis procedure.

For each component of the transmitter moments M_x, M_y and M_z , there are in general three components of the induced field at each point in the medium. Thus there are

nine field components at each receiver location. These field components can be expressed by a matrix representation of a dyadic $\hat{\mathbf{H}}$ as:

$$\hat{\mathbf{H}} = \begin{bmatrix} H_{xx} & H_{xy} & H_{xz} \\ H_{yx} & H_{yy} & H_{yz} \\ H_{zx} & H_{zy} & H_{zz} \end{bmatrix} \quad (2)$$

where the first subscript corresponds to the transmitter index and the second subscript corresponds to the receiver index, i.e. H_{ij} denotes the magnetic field received by the j -directed receiver coil excited by the i -directed transmitter coil. Next, we will derive the expressions for the nine magnetic field components in 1-D multiple layered transverse isotropic formation. A sketch showing a general geometry of a multi-component induction logging tool in a layered anisotropic formation is given in Fig.2.

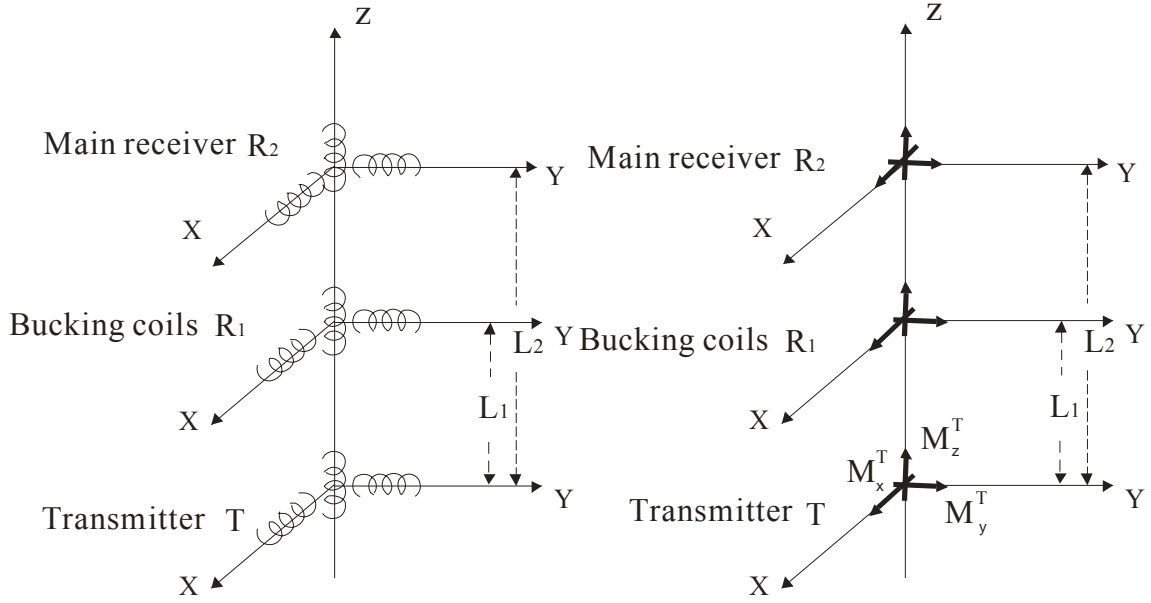


Fig.1. Basic structure of a triaxial tool and the equivalent dipole model

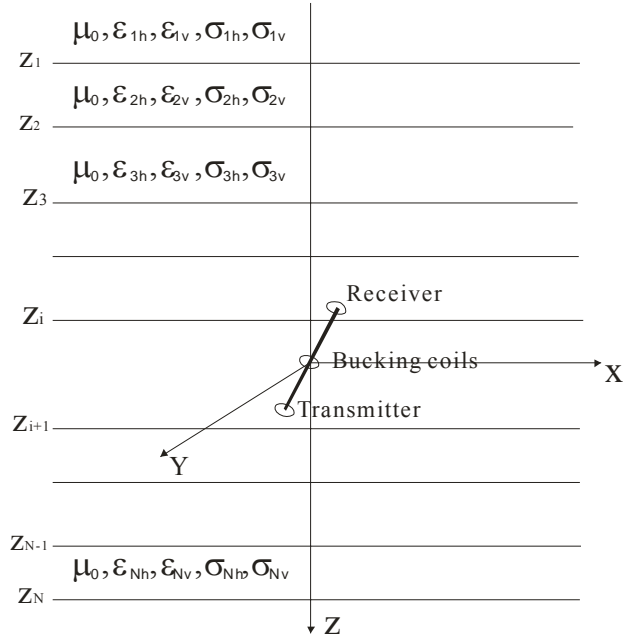


Fig. 2 A triaxial tool in a 1-D layered anisotropic formation

The electromagnetic fields in a homogeneous transverse isotropic medium satisfy the following Maxwell's equation:

$$\nabla \times \mathbf{H}(\mathbf{r}) = (\hat{\sigma} - i\omega\hat{\epsilon})\mathbf{E}(\mathbf{r}) = \hat{\sigma}'\mathbf{E}(\mathbf{r}) \quad (3a)$$

$$\nabla \times \mathbf{E}(\mathbf{r}) = i\omega\mu\mathbf{H}(\mathbf{r}) + i\omega\mu\mathbf{M}_s(\mathbf{r}). \quad (3b)$$

A harmonic time dependence $e^{-i\omega t}$ is used and suppressed throughout the paper. The complex conductivity tensor $\hat{\sigma}'$ is

$$\hat{\sigma}' = \begin{bmatrix} \sigma'_h & 0 & 0 \\ 0 & \sigma'_h & 0 \\ 0 & 0 & \sigma'_v \end{bmatrix} \quad (4)$$

where $\sigma'_h = \sigma_h - i\omega\epsilon_h$ and $\sigma'_v = \sigma_v - i\omega\epsilon_v$.

First, we will solve the Maxwell's equation (3a) and (3b) in homogeneous transverse isotropic medium. Following the procedure in [20], we introduce the Hertz vector potential π and scalar potential Φ to represent the electric and magnetic field:

$$\mathbf{E}(\mathbf{r}) = i\omega\mu\sigma'_h\hat{\sigma}^{-1} \cdot \nabla \times \pi \quad (5)$$

and

$$\mathbf{H}(\mathbf{r}) = i\omega\mu\sigma'_h\pi + \nabla\left(\frac{\nabla \cdot (\hat{\sigma}' \cdot \pi)}{\sigma'_v}\right) \quad (6)$$

For a x -directed magnetic dipole $\mathbf{M} = (M_x, 0, 0)^T$, the Hertz vector potential has both x and z components, i.e.

$$\pi = \pi_x \hat{x} + \pi_z \hat{z} \quad (7)$$

where

$$\pi_x = \frac{M_x}{4\pi\lambda} \frac{e^{ik_v s}}{s}, \quad (8)$$

$$\pi_z = \frac{M_x x}{4\pi\rho^2} \left(\lambda z \frac{e^{ik_v s}}{s} - z \frac{e^{ik_h r}}{r} \right), \quad (9)$$

where $\lambda^2 = \sigma'_h / \sigma'_v$ is the anisotropy ratio. $k_h^2 = i\omega\mu\sigma'_h$ is the complex wave number in the horizontal direction and $k_v^2 = i\omega\mu\sigma'_v$ is the complex wave number in the vertical direction. The distance ρ , r and s are given by $\rho = \sqrt{x^2 + y^2}$, $r = \sqrt{x^2 + y^2 + z^2}$, and $s = \sqrt{x^2 + y^2 + \lambda^2 z^2}$, respectively.

For a y -directed magnetic dipole $\mathbf{M} = (0, M_y, 0)^T$, the Hertz vector potential has both y and z components and for a z -directed magnetic dipole $\mathbf{M} = (0, 0, M_z)^T$, the Hertz vector potential has only z component.

Substituting the expressions of the Hertz vector potential into Eq. (6), we can obtain all the nine components of the magnetic field generated by a magnetic dipole

$\mathbf{M} = (M_x, M_y, M_z)\delta(\mathbf{r})$ in a homogeneous TI medium,

$$H_{xx} = \frac{e^{ik_v s}}{4\pi} \left[\frac{k_h^2}{\lambda s} + \frac{ik_h s - k_h k_v x^2}{s\rho^2} - \frac{2ik_h x^2}{\rho^4} \right] - \frac{e^{ik_h r}}{4\pi} \left[\frac{ik_h r - k_h^2 x^2}{r\rho^2} - \frac{2ik_h x^2}{\rho^4} - \frac{ik_h}{r^2} + \frac{(k_h^2 x^2 + 1)}{r^3} + \frac{3ik_h x^2}{r^4} - \frac{3x^2}{r^5} \right] \quad (10)$$

$$H_{yx} = H_{xy} = xy \frac{e^{ik_v s}}{4\pi\rho^2} \left[-\frac{k_h k_v}{s} - \frac{2ik_h}{\rho^2} \right] - \frac{e^{ik_h r} xy}{4\pi} \left[-\frac{k_h^2}{r\rho^2} - \frac{2ik_h}{\rho^4} + \frac{k_h^2}{r^3} + \frac{3ik_h}{r^4} - \frac{3}{r^5} \right], \quad (11)$$

$$H_{zx} = H_{xz} = -xz \frac{e^{ik_h r}}{4\pi r^3} \left[k_h^2 + \frac{3ik_h}{r} - \frac{3}{r^2} \right], \quad (12)$$

$$H_{yy} = \frac{e^{ik_v s}}{4\pi} \left[\frac{k_h^2}{\lambda s} + \frac{ik_h s - k_h k_v y^2}{s\rho^2} - \frac{2ik_h y^2}{\rho^4} \right] - \frac{e^{ik_h r}}{4\pi} \left[\frac{ik_h r - k_h^2 y^2}{r\rho^2} - \frac{2ik_h y^2}{\rho^4} - \frac{ik_h}{r^2} + \frac{(k_h^2 y^2 + 1)}{r^3} + \frac{3ik_h y^2}{r^4} - \frac{3y^2}{r^5} \right], \quad (13)$$

$$H_{zy} = H_{yz} = -yz \frac{e^{ik_h r}}{4\pi r^3} \left[k_h^2 + \frac{3ik_h}{r} - \frac{3}{r^2} \right], \quad (14)$$

$$H_{zz} = \frac{e^{ik_h r}}{4\pi r} \left[k_h^2 + \frac{ik_h}{r} - \frac{(k_h^2 z^2 + 1)}{r^2} - \frac{3ik_h z^2}{r^3} + \frac{3z^2}{r^4} \right] \quad (15)$$

By solving the Maxwell's equation (3) in multi-layered TI medium, we can obtain the magnetic field response of multi-component induction tools in the formation. For a z -directed magnetic dipole $\mathbf{M} = (0, 0, M_z)^T$, the Hertz vector potential and the magnetic field in the i th layer are given by

$$\pi_{zi} = \frac{M_z}{4\pi} \int_0^\infty \left(\frac{\beta_i}{\xi_{hi}} e^{-\xi_{hi}|z-z_0|} + F_i e^{-\xi_{hi}z} + G_i e^{\xi_{hi}z} \right) \alpha J_0(\alpha\rho) d\alpha \quad (16)$$

$$H_{xzi} = \frac{M_z}{4\pi} \cos\phi \int_0^\infty \xi_{hi} \left(\frac{\beta_i}{\xi_{hi}} \frac{|z-z_0|}{z-z_0} e^{-\xi_{hi}|z-z_0|} + F_i e^{-\xi_{hi}z} - G_i e^{\xi_{hi}z} \right) \alpha^2 J_1(\alpha\rho) d\alpha \quad (17)$$

$$H_{yzi} = \frac{M_z}{4\pi} \sin\phi \int_0^\infty \xi_{hi} \left(\frac{\beta_i}{\xi_{hi}} \frac{|z-z_0|}{z-z_0} e^{-\xi_{hi}|z-z_0|} + F_i e^{-\xi_{hi}z} - G_i e^{\xi_{hi}z} \right) \alpha^2 J_1(\alpha\rho) d\alpha \quad (18)$$

$$H_{zzi} = \frac{M_z}{4\pi} \int_0^\infty \left(\frac{\beta_i}{\xi_{hi}} e^{-\xi_{hi}|z-z_0|} + F_i e^{-\xi_{hi}z} + G_i e^{\xi_{hi}z} \right) \alpha^3 J_0(\alpha\rho) d\alpha \quad (19)$$

where $J_n(x)$ is the nth order Bessel function, and

$$\xi_{hi} = (\alpha^2 - k_{hi}^2)^{1/2},$$

$$\beta_i = \begin{cases} 1, & \text{if } M_z \text{ is in the } i\text{th layer} \\ 0, & \text{if } M_z \text{ is not in the } i\text{th layer} \end{cases}$$

The term with $e^{-\xi_{hi}z}$ represents the wave traveling in the +z direction and the term with $e^{+\xi_{hi}z}$ represents the wave traveling in the -z direction. The \pm sign is chosen to assure the fields decay as $|z|$ increases.

The generalized upward and downward reflection coefficients F_i and G_i can be derived by enforcing the boundary conditions at the horizontal boundary $z = z_i$ based on the equivalent transmission line theory [16-18]. The detailed derivation and expression are omitted here.

For a x -directed magnetic dipole $\mathbf{M} = (M_x, 0, 0)^T$, the Hertz vector potential and the magnetic field in the i th layer are given by

$$\pi_{xi} = \frac{M_x}{4\pi\lambda_i} \int_0^\infty \left(\frac{\beta_i}{\xi_{vi}} e^{-\xi_{vi}\lambda_i|z-z_0|} + P_i e^{-\xi_{vi}\lambda_i z} + Q_i e^{\xi_{vi}\lambda_i z} \right) \alpha J_0(\alpha\rho) d\alpha \quad (20)$$

$$\pi_{zi} = \frac{M_x}{4\pi} \cos\phi \int_0^\infty \left(S_i e^{-\xi_{hi}z} + T_i e^{\xi_{hi}z} - \xi_{vi} P_i e^{-\xi_{vi}\lambda_i z} + \xi_{vi} Q_i e^{\xi_{vi}\lambda_i z} \right) J_1(\alpha\rho) d\alpha$$

$$+ \frac{M_x}{4\pi} \cos \phi \int_0^\infty \beta_i \left(e^{-\xi_{hi}|z-z_0|} - e^{-\xi_{vi}\lambda_i|z-z_0|} \right) \frac{|z-z_0|}{z-z_0} J_1(\alpha\rho) d\alpha, \quad (21)$$

After tedious derivation, we can obtain the expression for the magnetic field components:

$$\begin{aligned} H_{xxi} = & \frac{M_x}{4\pi} \int_0^\infty \left(\frac{\beta_i}{\lambda_i \xi_{vi}} k_{hi}^2 \sin^2 \phi e^{-\xi_{vi}\lambda_i|z-z_0|} - \beta_i \cos^2 \phi \xi_{hi} e^{-\xi_{hi}|z-z_0|} + \frac{P_i}{\lambda_i} k_{hi}^2 \sin^2 \phi e^{-\xi_{vi}\lambda_i z} \right. \\ & + \frac{Q_i}{\lambda_i} k_{hi}^2 \sin^2 \phi e^{\xi_{vi}\lambda_i z} - S_i \cos^2 \phi \xi_{hi} e^{-\xi_{hi} z} + T_i \cos^2 \phi \xi_{hi} e^{\xi_{hi} z} \left. \right) \alpha J_0(\alpha\rho) d\alpha \\ & + \frac{M_x}{4\pi\rho} \cos 2\phi \int_0^\infty \left(\lambda_i \frac{\beta_i}{\xi_{vi}} k_{vi}^2 e^{-\xi_{vi}\lambda_i|z-z_0|} + \beta_i \xi_{hi} e^{-\xi_{hi}|z-z_0|} + P_i \lambda_i k_{vi}^2 e^{-\xi_{vi}\lambda_i z} + Q_i \lambda_i k_{vi}^2 e^{\xi_{vi}\lambda_i z} \right. \\ & \left. + S_i \xi_{hi} e^{-\xi_{hi} z} - T_i \xi_{hi} e^{\xi_{hi} z} \right) J_1(\alpha\rho) d\alpha \end{aligned} \quad (22)$$

$$\begin{aligned} H_{yxi} = & \frac{M_x}{4\pi} \sin \phi \cos \phi \int_0^\infty \left(-\frac{\beta_i}{\lambda_i \xi_{vi}} k_{hi}^2 e^{-\xi_{vi}\lambda_i|z-z_0|} - \beta_i \xi_{hi} e^{-\xi_{hi}|z-z_0|} - \frac{P_i}{\lambda_i} k_{hi}^2 e^{-\xi_{vi}\lambda_i z} \right. \\ & \left. - \frac{Q_i}{\lambda_i} k_{hi}^2 e^{\xi_{vi}\lambda_i z} - S_i \xi_{hi} e^{-\xi_{hi} z} + T_i \xi_{hi} e^{\xi_{hi} z} \right) \alpha J_0(\alpha\rho) d\alpha \\ & + \frac{M_x}{4\pi\rho} \sin 2\phi \int_0^\infty \left(\lambda_i \frac{\beta_i}{\xi_{vi}} k_{vi}^2 e^{-\xi_{vi}\lambda_i|z-z_0|} + \beta_i \xi_{hi} e^{-\xi_{hi}|z-z_0|} + P_i \lambda_i k_{vi}^2 e^{-\xi_{vi}\lambda_i z} \right. \\ & \left. + Q_i \lambda_i k_{vi}^2 e^{\xi_{vi}\lambda_i z} + S_i \xi_{hi} e^{-\xi_{hi} z} - T_i \xi_{hi} e^{\xi_{hi} z} \right) J_1(\alpha\rho) d\alpha \end{aligned} \quad (23)$$

$$H_{zxi} = \frac{M_x}{4\pi} \cos \phi \int_0^\infty \left(\beta_i \frac{|z-z_0|}{z-z_0} e^{-\xi_{hi}|z-z_0|} + S_i e^{-\xi_{hi} z} + T_i e^{\xi_{hi} z} \right) \alpha^2 J_1(\alpha\rho) d\alpha \quad (24)$$

where

$$\xi_{vi} = \left(\alpha^2 - k_{vi}^2 \right)^{1/2}$$

The generalized upward and downward coefficients P_i, Q_i, S_i and T_i can be obtained by matching the boundary conditions at the interface of the i th and $(i+1)$ th layer [16-18].

For a y -directed magnetic dipole $\mathbf{M} = (0, M_y, 0)^T$, the Hertz vector potential and the magnetic field in the i th layer are given by

$$\pi_{yi} = \frac{M_y}{4\pi\lambda_i} \int_0^\infty \left(\frac{\beta_i}{\xi_{vi}} e^{-\xi_{vi}\lambda_i|z-z_0|} + P_i e^{-\xi_{vi}\lambda_i z} + Q_i e^{\xi_{vi}\lambda_i z} \right) \alpha J_0(\alpha\rho) d\alpha \quad (25)$$

$$\begin{aligned} \pi_{zi} &= \frac{M_y}{4\pi} \sin\phi \int_0^\infty \left(S_i e^{-\xi_{hi}z} + T_i e^{\xi_{hi}z} - \xi_{vi} P_i e^{-\xi_{vi}\lambda_i z} + \xi_{vi} Q_i e^{\xi_{vi}\lambda_i z} \right) J_1(\alpha\rho) d\alpha \\ &+ \frac{M_y}{4\pi} \sin\phi \int_0^\infty \beta_i \left(e^{-\xi_{hi}|z-z_0|} - e^{-\xi_{vi}\lambda_i|z-z_0|} \right) \frac{|z-z_0|}{z-z_0} J_1(\alpha\rho) d\alpha \end{aligned} \quad (26)$$

$$\begin{aligned} H_{xyi} &= \frac{M_y}{4\pi} \sin\phi \cos\phi \int_0^\infty \left(-\frac{\beta_i}{\lambda_i \xi_{vi}} k_{hi}^2 e^{-\xi_{vi}\lambda_i|z-z_0|} - \beta_i \xi_{hi} e^{-\xi_{hi}|z-z_0|} - \frac{P_i}{\lambda_i} k_{hi}^2 e^{-\xi_{vi}\lambda_i z} \right. \\ &\quad \left. - \frac{Q_i}{\lambda_i} k_{hi}^2 e^{\xi_{vi}\lambda_i z} - S_i \xi_{hi} e^{-\xi_{hi}z} + T_i \xi_{hi} e^{\xi_{hi}z} \right) \alpha J_0(\alpha\rho) d\alpha \\ &+ \frac{M_y}{4\pi\rho} \sin 2\phi \int_0^\infty \left(\lambda_i \frac{\beta_i}{\xi_{vi}} k_{vi}^2 e^{-\xi_{vi}\lambda_i|z-z_0|} + \beta_i \xi_{hi} e^{-\xi_{hi}|z-z_0|} + \frac{P_i}{\lambda_i} k_{hi}^2 e^{-\xi_{vi}\lambda_i z} \right. \\ &\quad \left. + \frac{Q_i}{\lambda_i} k_{hi}^2 e^{\xi_{vi}\lambda_i z} + S_i \xi_{hi} e^{-\xi_{hi}z} - T_i \xi_{hi} e^{\xi_{hi}z} \right) J_1(\alpha\rho) d\alpha \end{aligned} \quad (27)$$

$$\begin{aligned} H_{yyi} &= \frac{M_y}{4\pi} \int_0^\infty \left(-\frac{\beta_i}{\lambda_i \xi_{vi}} k_{hi}^2 \cos^2\phi e^{-\xi_{vi}\lambda_i|z-z_0|} - \beta_i \sin^2\phi \xi_{hi} e^{-\xi_{hi}|z-z_0|} + \frac{P_i}{\lambda_i} k_{hi}^2 \cos^2\phi e^{-\xi_{vi}\lambda_i z} \right. \\ &\quad \left. + \frac{Q_i}{\lambda_i} k_{hi}^2 \cos^2\phi e^{\xi_{vi}\lambda_i z} - S_i \sin^2\phi \xi_{hi} e^{-\xi_{hi}z} + T_i \sin^2\phi \xi_{hi} e^{\xi_{hi}z} \right) \alpha J_0(\alpha\rho) d\alpha \\ &+ \frac{M_y}{4\pi\rho} \cos 2\phi \int_0^\infty \left(-\lambda_i \frac{\beta_i}{\xi_{vi}} k_{vi}^2 e^{-\xi_{vi}\lambda_i|z-z_0|} - \beta_i \xi_{hi} e^{-\xi_{hi}|z-z_0|} - P_i \lambda_i k_{vi}^2 e^{-\xi_{vi}\lambda_i z} \right. \\ &\quad \left. - Q_i \lambda_i k_{vi}^2 e^{\xi_{vi}\lambda_i z} - S_i \xi_{hi} e^{-\xi_{hi}z} + T_i \xi_{hi} e^{\xi_{hi}z} \right) J_1(\alpha\rho) d\alpha \end{aligned} \quad (28)$$

$$H_{zyi} = \frac{M_y}{4\pi} \sin\phi \int_0^\infty \left(\beta_i \frac{|z-z_0|}{z-z_0} e^{-\xi_{hi}|z-z_0|} + S_i e^{-\xi_{hi}z} + T_i e^{\xi_{hi}z} \right) \alpha^2 J_1(\alpha\rho) d\alpha \quad (29)$$

Again, the generalized upward and downward reflection coefficients P_i , Q_i , S_i and T_i can be obtained by matching the boundary conditions at the interface of the i th and $(i+1)$ th layer [16-18].

In the present work, both the errors in the equations and the code for the Hertz potential and magnetic fields in [16,17] are corrected.

For convenience of explanation of the parallelization procedure, we plot the flow chart of the forward modeling code in Fig.3. From the flow chart, we can see that the dominant part of the computation including the calculation of the generalized upward and downward reflection coefficients and the Hankel transforms of the highly oscillating integrals of the Bessel functions is repeated for every logging point. This code is programmed in serial and only one core is used even the code is run on a multi-core computer. To fully explore the resources of the multi-core computer, we parallel the forward modeling code using OpenMP.

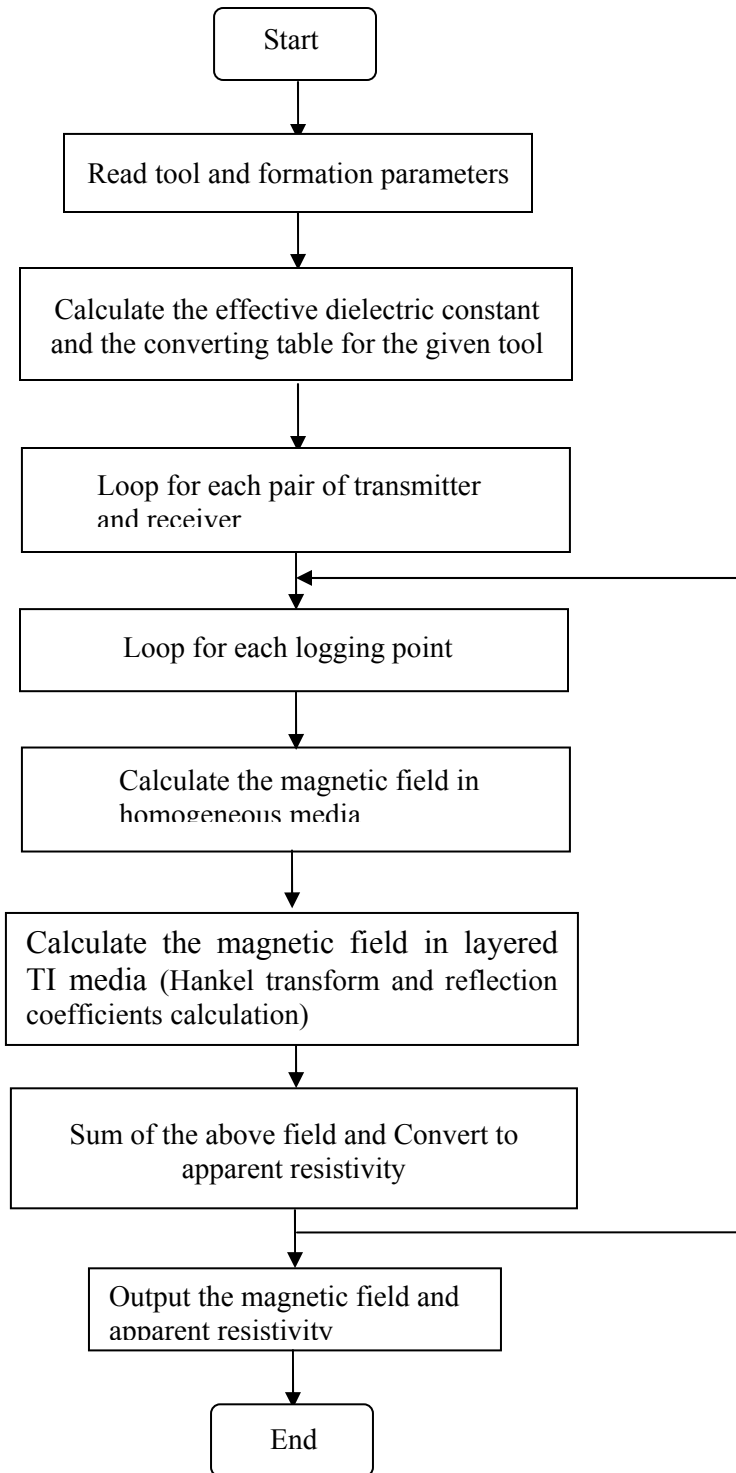


Fig. 3 Flow chart of the forward modeling code for simulation of triaxial tool responses

In the forward modeling code for LWD triaxial tools, we use the effective dielectric constant in the tool response simulation and apparent resistivity/conductivity conversion. We use the effective dielectric constant model shown in Table 1 for different service companies.

Table 1 Dielectric Constant Model

Company	Dielectric constant model
APS Technology	$\epsilon_r = 210 \times R_t^{-0.42}$ (for 2MHz) $\epsilon_r = 480 \times R_t^{-0.49} + 8$ (for 400KHz)
Baker Hughes INTEQ	$\epsilon_r = 6.4 + 4.5255\sqrt{1 + \sqrt{1 + (2275/R_t)^2}}$ (for 2MHz) $\epsilon_r = 6.4 + 4.5255\sqrt{1 + \sqrt{1 + (11375/R_t)^2}}$ (for 400KHz)
GE Energy	$\epsilon_r = 108.5 \times R_t^{-0.35} + 5$
Halliburton Sperry-Sun	$\epsilon_r = 10$
Pathfinder	$\epsilon_r = 108.5 \times R_t^{-0.35} + 5$ (AWR) $\epsilon_r = 10$ (CWR)
Schlumberger Anadrill	$\epsilon_r = 108.5 \times R_t^{-0.35} + 5$ (for 2MHz) $\epsilon_r = 279.7 \times R_t^{-0.46} + 5$ (for 400KHz)
Weatherford	$\epsilon_r = 210 \times R_t^{-0.42}$ (for 2MHz) $\epsilon_r = 480 \times R_t^{-0.49} + 8$ (for 400KHz)

B. Parallelization of the 1-D Forward Modeling Codes

We choose OpenMP to improve the performance of the code, and at the same time, keeping the clarity of the original serial code. Thus, OpenMP emerge as reliable alternative as it is just a set of compiler directives with library routines for parallel application that greatly simplifies writing multi-threaded programs. We choose Intel Fortran as the compiler since it supports the OpenMP interface. The main loop shown in Fig.3 repeated for every logging point dominants the entire computation time. Since the calculation for each logging point is completely independent with each other, we can

thread the whole repeated calculation as a master thread and run the calculations for different logging points through several slave threads. The number of threads is determined by the number of computer cores. Consequently, more than one logging point is computed simultaneously but just consuming a single point's time. We apply PARALLEL DO to realize the parallel implementation and the programming structure of the parallel code is shown in Fig. 4. The basic directive of PARALLEL DO is semantically equivalent to:

```

!$OMP PARALLEL DO
DO I = 1, Nlog
.....
END DO
$OMP END PARALLEL DO
    
```

Then we implement PARALLEL DO to realize parallelization, as shown in Fig. 5.

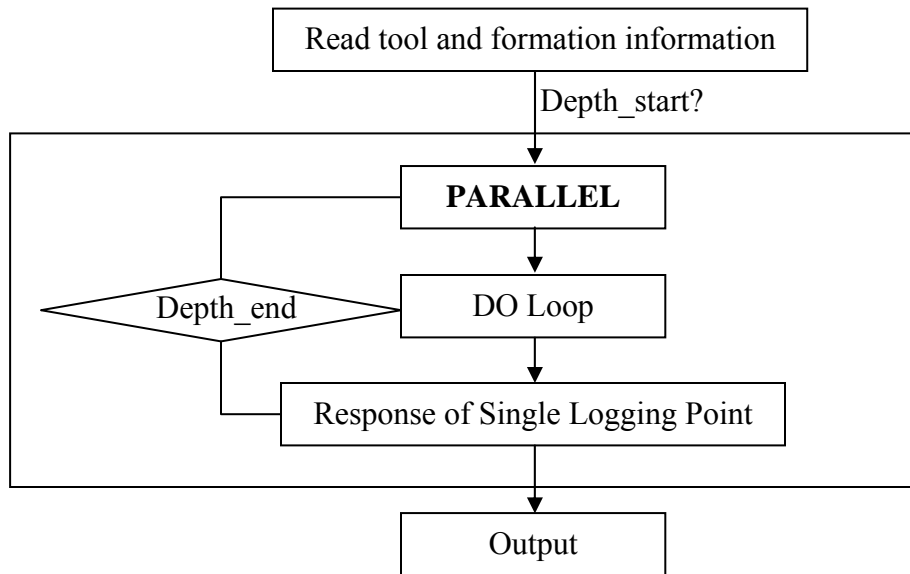


Fig. 4 Programming structure of parallel 1-D simulation codes for wireline/LWD triaxial tools

In the programming, we should pay attention to the common block/variables in the code. Since OpenMP is based on a shared-memory structure, all the threads are allowed

to access the common block or variables. However, some common blocks are not supposed to be shared among different threads. The command `THREADPRIVATE` allows us to specify named common blocks and variables as private to other threads but global within their own thread. Once we declare a common block or variable as `THREADPRIVATE`, each thread in the team maintains a separate copy of that common block or variable. Data written to a `THREADPRIVATE` common block or variable remain private to that thread and is not available to other threads in the team. Use the clause `COPYIN` after the directive `PARALLEL DO` to specify that upon entry into a parallel region, data of a named common block or named variable in the master thread are copied to the common block or variable of each thread. Fig. 5 shows the comparison of the structure of the serial and the parallel codes. Assume the code need to calculate 1000 logging point on a 4-core computer. In the serial code, the computer handles one logging point at one time with only one processor active. On the contrary, in the parallel code, the computer divides all the 1000 points into 4 groups (we assume the division is even without loss of generality). As a result, 4 threads synchronously run the calculation and the total computation time is significantly reduced.

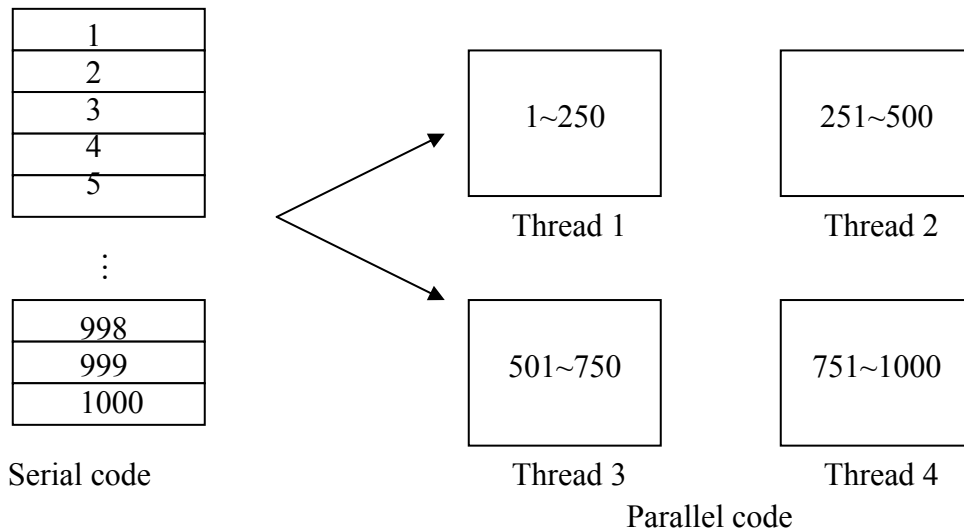


Fig. 5 Comparison of the structure of the serial code and the parallel code

2.2 Parallelization of the 3-D Simulation Code for Triaxial Tools in Arbitrarily Anisotropic Formations

A. Forward Modeling of Triaxial Tools in 3-D Arbitrarily Anisotropic Formations

In this part, we will use the finite difference method (FDM) to simulate the response of a triaxial tool in 3-D arbitrarily anisotropic formation.

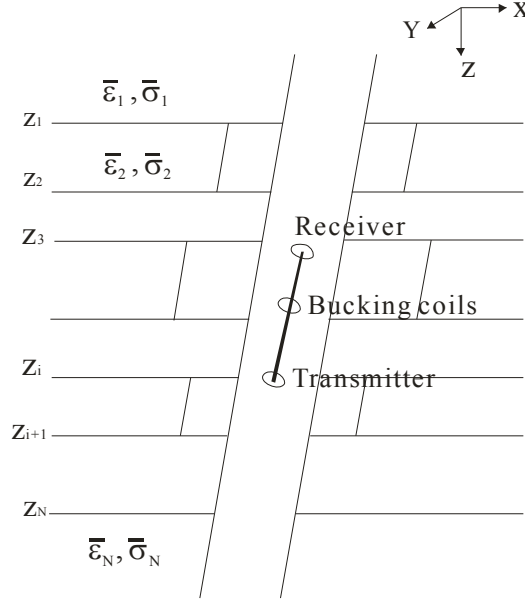


Fig. 6 A triaxial tool in a 3-D arbitrarily anisotropic formation

Consider a triaxial tool in a 3-D formation as shown in Fig.6. The governing equations for EM induction in the 3-D geometry are Faraday's law and Ampere's law

$$\nabla \times \mathbf{E} = -i\omega\mathbf{B} \quad (30a)$$

$$\nabla \times \mathbf{H} = \mathbf{J}_i + \mathbf{J}_s + i\omega\mathbf{D} \quad (30b)$$

where \mathbf{J}_s is the source current density and \mathbf{J}_i is the induced current density. In the above equations, a time-harmonic dependence of $e^{i\omega t}$ is assumed and suppressed. The induced current density \mathbf{J}_i is related to the electric field by

$$\mathbf{J}_i = \bar{\sigma}\mathbf{E} \quad (31)$$

The total electric field \mathbf{E} can be expressed as the sum of a primary field \mathbf{E}_0 from \mathbf{J}_s embedded in a background reference medium and a scattered field \mathbf{E}' arising from the conductivity and permittivity variations which deviate from the background medium. In geophysical applications, we usually prefer a scattered-field formulation instead of a total-field one since the former computations are more robust and accurate, particularly when the measurements are made very close to the source. A total-field solution usually requires very fine meshes, resulting in large demands of computational resources. In addition, it is impossible to obtain accurate in-phase responses from the total-field solution since the direct-coupled field is dominant in the total field.

Setting $\mathbf{E} = \mathbf{E}'$ in (30) and combining (30)-(31) yield a single, second order partial-differential equation (PDE) in terms of the scattered electric field:

$$\nabla \times \nabla \times \mathbf{E}' + i\omega\mu_0(\bar{\sigma} + i\omega\epsilon)\mathbf{E}' = -j\omega\mu_0\mathbf{J}_0 \quad (32)$$

The term \mathbf{J}_0 is the effective source current density for the scattered fields,

$$\mathbf{J}_0 = [(\bar{\sigma}(\mathbf{r}) - \sigma_0\mathbf{I}) + j\omega(\epsilon(\mathbf{r}) - \epsilon_0)\mathbf{I}]\mathbf{E}_0 \quad (33)$$

where \mathbf{I} is the 3×3 identity matrix. It is noted that both the conductivity and permittivity are position-dependant and can be fully anisotropic, *i.e.*:

$$\bar{\sigma}(\mathbf{r}) = \begin{bmatrix} \sigma_{xx} & \sigma_{xy} & \sigma_{xz} \\ \sigma_{yx} & \sigma_{yy} & \sigma_{yz} \\ \sigma_{zx} & \sigma_{zy} & \sigma_{zz} \end{bmatrix}, \bar{\epsilon}(\mathbf{r}) = \begin{bmatrix} \epsilon_{xx} & \epsilon_{xy} & \epsilon_{xz} \\ \epsilon_{yx} & \epsilon_{yy} & \epsilon_{yz} \\ \epsilon_{zx} & \epsilon_{zy} & \epsilon_{zz} \end{bmatrix} \quad (34)$$

Next, we use the finite-difference method based on the staggered Yee grid [21] to solve (32). The solution domain is discretized into Cartesian cells and the scattered electric field components E_x , E_y and E_z are defined on the edges of the cells. The magnetic-field component H_x is staggered in y and z , H_y in x and z , and H_z in x and y , as shown in Fig. 7.

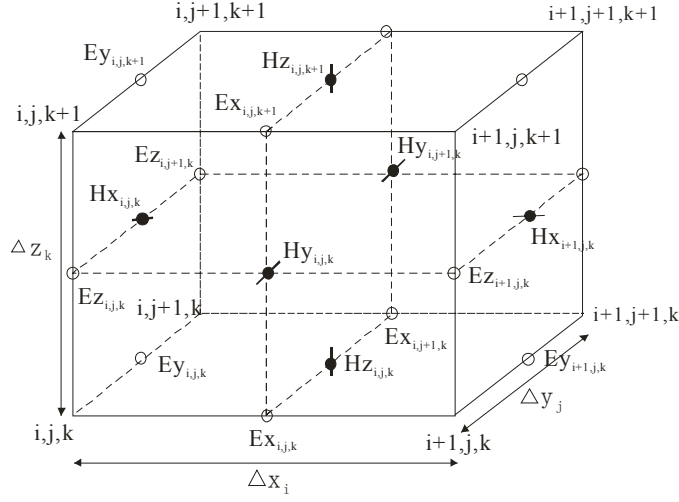


Fig. 7 The staggered grid used for the finite-difference method

Combing (32) and (33) and expanding the curl operations yield the following coupled expressions for the scattered electric field:

$$\begin{aligned} & \frac{\partial}{\partial y} \left(\frac{\partial \mathbf{E}_y^s(\mathbf{r})}{\partial x} - \frac{\partial \mathbf{E}_x^s(\mathbf{r})}{\partial y} \right) - \frac{\partial}{\partial z} \left(\frac{\partial \mathbf{E}_x^s(\mathbf{r})}{\partial z} - \frac{\partial \mathbf{E}_z^s(\mathbf{r})}{\partial x} \right) \\ & + j\omega\mu_0 (\sigma_{xx}(\mathbf{r})\mathbf{E}_x^s(\mathbf{r}) + \sigma_{xy}(\mathbf{r})\mathbf{E}_y^s(\mathbf{r}) + \sigma_{xz}(\mathbf{r})\mathbf{E}_z^s(\mathbf{r})) \\ & = -j\omega\mu_0 (\boldsymbol{\sigma}(\mathbf{r}) - \sigma_0(\mathbf{r}))\mathbf{E}_x^b(\mathbf{r}) \end{aligned} \quad (35a)$$

$$\begin{aligned} & \frac{\partial}{\partial z} \left(\frac{\partial \mathbf{E}_z^s(\mathbf{r})}{\partial y} - \frac{\partial \mathbf{E}_y^s(\mathbf{r})}{\partial z} \right) - \frac{\partial}{\partial x} \left(\frac{\partial \mathbf{E}_y^s(\mathbf{r})}{\partial x} - \frac{\partial \mathbf{E}_x^s(\mathbf{r})}{\partial y} \right) \\ & + j\omega\mu_0 (\sigma_{yx}(\mathbf{r})\mathbf{E}_x^s(\mathbf{r}) + \sigma_{yy}(\mathbf{r})\mathbf{E}_y^s(\mathbf{r}) + \sigma_{yz}(\mathbf{r})\mathbf{E}_z^s(\mathbf{r})) \\ & = -j\omega\mu_0 (\boldsymbol{\sigma}(\mathbf{r}) - \sigma_0(\mathbf{r}))\mathbf{E}_y^b(\mathbf{r}) \end{aligned} \quad (35b)$$

$$\begin{aligned} & \frac{\partial}{\partial x} \left(\frac{\partial \mathbf{E}_x^s(\mathbf{r})}{\partial z} - \frac{\partial \mathbf{E}_z^s(\mathbf{r})}{\partial x} \right) - \frac{\partial}{\partial y} \left(\frac{\partial \mathbf{E}_z^s(\mathbf{r})}{\partial y} - \frac{\partial \mathbf{E}_y^s(\mathbf{r})}{\partial z} \right) \\ & + j\omega\mu_0 (\sigma_{zx}(\mathbf{r})\mathbf{E}_x^s(\mathbf{r}) + \sigma_{zy}(\mathbf{r})\mathbf{E}_y^s(\mathbf{r}) + \sigma_{zz}(\mathbf{r})\mathbf{E}_z^s(\mathbf{r})) \\ & = -j\omega\mu_0 (\boldsymbol{\sigma}(\mathbf{r}) - \sigma_0(\mathbf{r}))\mathbf{E}_z^b(\mathbf{r}) \end{aligned} \quad (35c)$$

In this paper, a 13-point centered finite-difference stencil [22] is used to approximate the curl-curl operator in (32). The above differential equation is converted to a linear system equation as follows,

$$\mathbf{KE} = \mathbf{S} \quad (36)$$

where the matrix \mathbf{K} is the system matrix of dimension $3N_x N_y N_z \times 3N_x N_y N_z$ for a model with $3N_x N_y N_z$ cells. \mathbf{E} is a vector of length $3N_x N_y N_z$ containing the secondary electric field values E_x^s, E_y^s, E_z^s for all nodes. \mathbf{S} (length $3N_x N_y N_z$) is the secondary-source vector given by the right-hand side of (35). The system matrix \mathbf{K} is a sparse matrix with up to 13 nonzero entries per line. The entries depend on the grid spacing and the frequency-dependent properties of the media.

In the derivation of the linear equations, a conductivity averaging scheme is used to obtain the conductivity at the center of the cell edge (where the electric field is defined). Following the scheme in [22], the conductivity at the center of the edge is expressed as a weighted sum of the conductivities of the four adjoining cells. The Dirichlet condition is applied to the scattered electric field components on the outmost boundary of the finite-difference mesh. The detailed expression of the matrices can be found in the Appendix. It should be noted that the system equation is non-symmetric originally. By multiplying (A-1) by $\Delta x_{i+1/2} \Delta y_j \Delta z_k$, (A-2) by $\Delta x_i \Delta y_{j+1/2} \Delta z_k$, and (A-3) by $\Delta x_i \Delta y_j \Delta z_{k+1/2}$, we can obtain the symmetric form of the system equation, where $\Delta x_i, \Delta y_j, \Delta z_k$ are the length of grid cells i, j , and k ; $\Delta x_{i+1/2}, \Delta y_{j+1/2}$ and $\Delta z_{k+1/2}$ are the distances between the centers of cells $i+1$ and $i, j+1$ and j , and $k+1$ and k , respectively.

The linear system in (36) is solved efficiently using a generalized minimal residual (GMRES) algorithm [23] and the incomplete LU preconditioner (ILU) [24] is used to improve the convergence of the matrix equation. Once the electric field is obtained from equation (36), the magnetic field can be calculated from Faraday's law.

Since the formation we considered is inhomogeneous and anisotropic, a fine mesh is necessary to model the complicated structures and interfaces between different media. However, a fine mesh yields large computer resource. A feasible way to alleviate this difficulty is to use reasonably coarse mesh to model the geometry and use the averaged conductivity for each cell to model the electrical property of the media. This is a good compromise between accuracy and computational complexity. So in most cases, the grid

used in the finite-difference method is independent on the electrical property of the formation and different media can be included in a single rectangular cell by using the averaged conductivity. In this paper, a technique similar to the one described in [22] is used to calculate the average conductivity tensor. After a series of derivation, we can write out the average conductivity entry $\langle \sigma_{xx} \rangle$ as,

$$\langle \sigma_{xx} \rangle = \langle J_x \rangle / (V_0 / \Delta x) = \frac{\sum_{j=1}^{N_y} \sum_{k=1}^{N_z} \left(\frac{N_x}{\sum_{i'=1}^{N_x} (1/\sigma_{xx}^{(i',j,k)})} \right)}{N_y N_z} \quad (37)$$

Equation (37) implies that the averaged conductivity $\langle \sigma_{xx} \rangle$ is obtained by first combining in series the N_x subcells with the same superscript i in a line and then combining in parallel the $N_x \times N_y$ lines of subcells.

The average conductivity $\langle \sigma_{yx} \rangle$ can be derived as,

$$\langle \sigma_{yx} \rangle = \langle J_y \rangle / (V_0 / \Delta x) = \frac{\sum_{i=1}^{N_x} \sum_{j=1}^{N_y} \sum_{k=1}^{N_z} \sigma_{yx}^{(i,j,k)} \left(\frac{1}{\sum_{i'=1}^{N_x} (\sigma_{xx}^{(i,j,k)} / \sigma_{xx}^{(i',j,k)})} \right)}{N_y N_z} \quad (38)$$

The other average conductivity entries $\langle \sigma_{yy} \rangle$, $\langle \sigma_{zz} \rangle$, $\langle \sigma_{xz} \rangle$ and $\langle \sigma_{yz} \rangle$ can be derived out following a similar derivation procedure and written in a similar form. To preserve the symmetric character of the average conductivity tensor, we set the average conductivity entries $\langle \sigma_{\alpha\beta} \rangle$ to be the average of the calculated $\langle \sigma_{\alpha\beta} \rangle$ and $\langle \sigma_{\beta\alpha} \rangle$, that is

$$\langle \sigma_{\alpha\beta} \rangle = \langle \sigma_{\beta\alpha} \rangle = \frac{1}{2} (\langle \sigma_{\alpha\beta} \rangle + \langle \sigma_{\beta\alpha} \rangle) \quad \alpha = x, y, z \quad \beta = x, y, z \quad \alpha \neq \beta \quad (39)$$

The details of the derivation are omitted and can be referred to Ref. [25].

Based on the above theory, we developed a forward modeling code to simulate the responses of triaxial induction tools in 3-D arbitrarily anisotropic formation. Fig. 8 shows the flow chart of the code. It is known that in the FDM, the mesh should be denser in the vicinity of the tool in order to obtain good accuracy, and coarser in the region far away from the tool to keep the overall grid size in a reasonable level. As can be seen in the flow chart, there two options: 1) the mesh can be adjusted for different observation point;

2) a fixed mesh is used for all observation points. If the mesh is adjusted according to the observation points, the computation of the average conductivity tensor, the filling of the matrix equation and the computation of the preconditioner must be repeated once the mesh is changed. In this paper, we use a fixed mesh for all the observation points so that the above time consuming computation is performed only once. This will yield some scarification in the accuracy, particularly for points at the formation boundary. Fortunately, via the use of the averaged conductivity technique mentioned previously, the problem is greatly alleviated. Again, besides the calculation of the ILU preconditioner, the most time consuming of the 3-D code is the repeated calculation for large number of logging points. We use the OpenMP to parallel this part of the code. If users prefer an adjustable mesh for different logging point, both the coefficient matrix and the preconditioner matrix must be calculated repeatedly. Then this part also needs to be implemented in parallel, as shown in Fig.8.

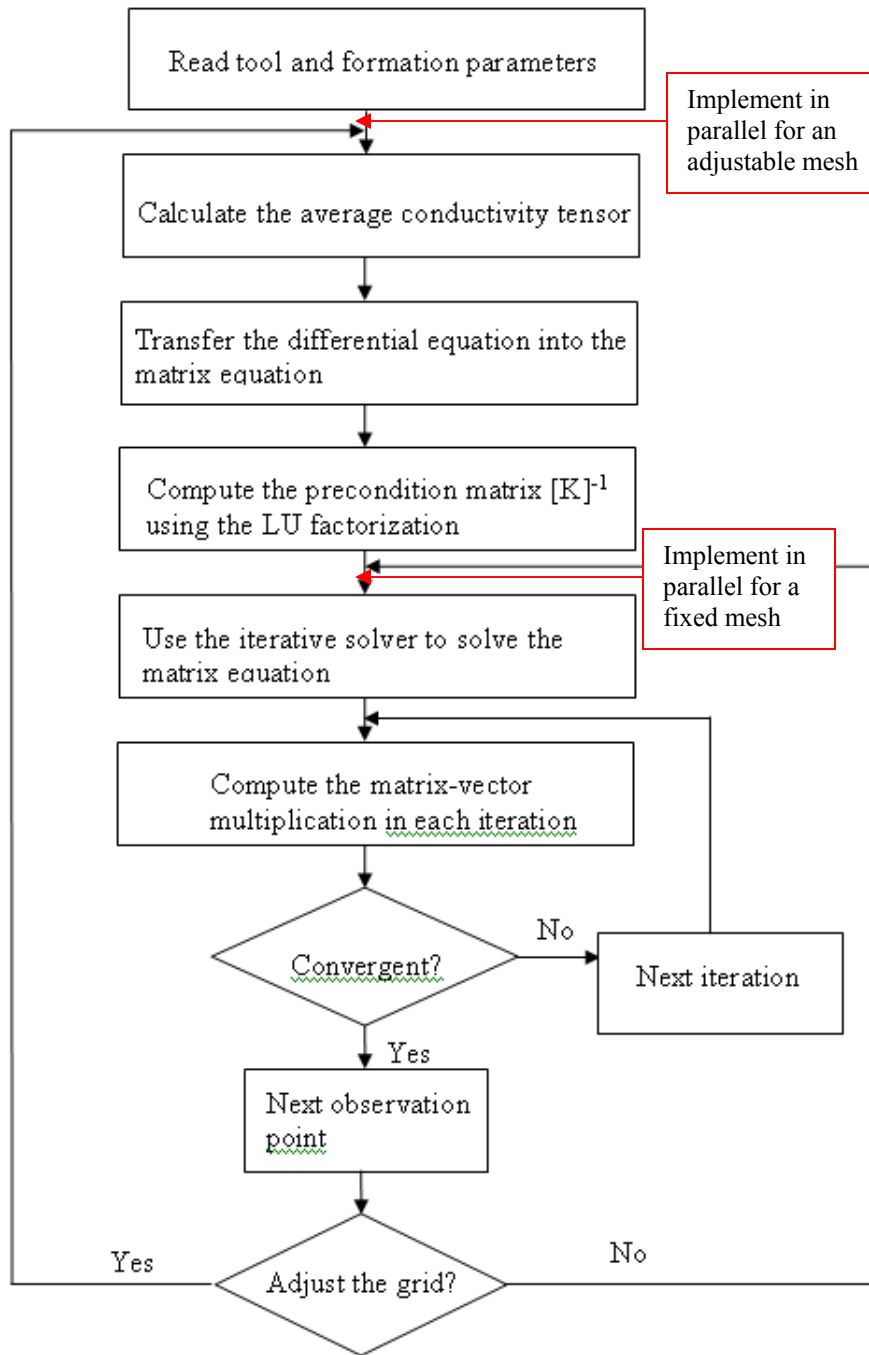


Fig.8 The flow chart of the 3-D FDM forward modeling code

2. Numerical Results

In this section, we will present examples to demonstrate the performance of the parallelized 1-D and 3-D forward modeling code respectively.

A). 1-D Forward Modeling Code

First, we compare the performance of the original serial 1-D forward modeling code and the parallel code.

The first example is a 7-layer anisotropic model as shown in Fig.9. The parameters are given in the figure. The dipping angle (the angle between the tool axis and the normal to the layer boundaries) is 30° and the spacing between the transmitter and receiver is 1.8m.

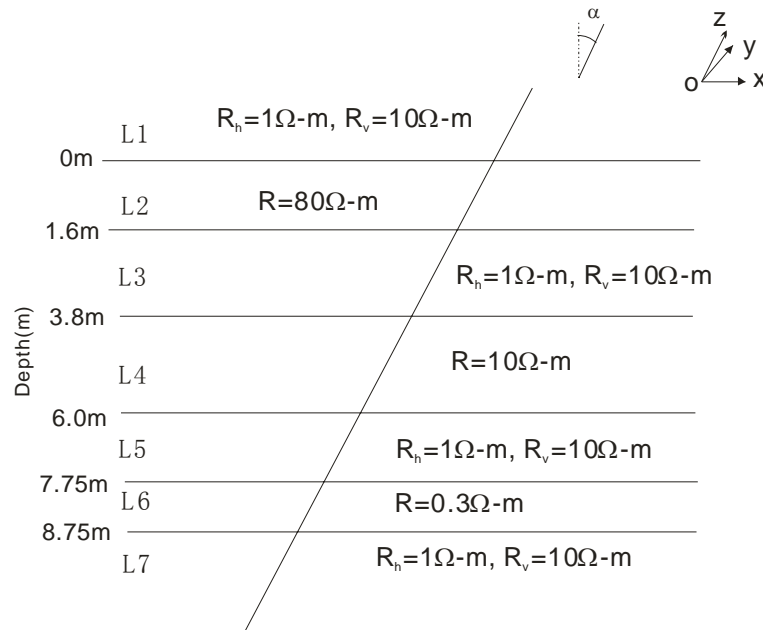
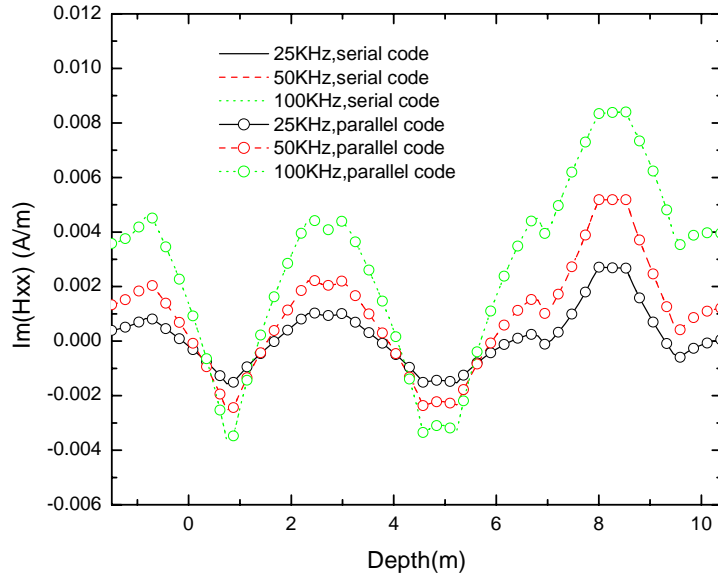


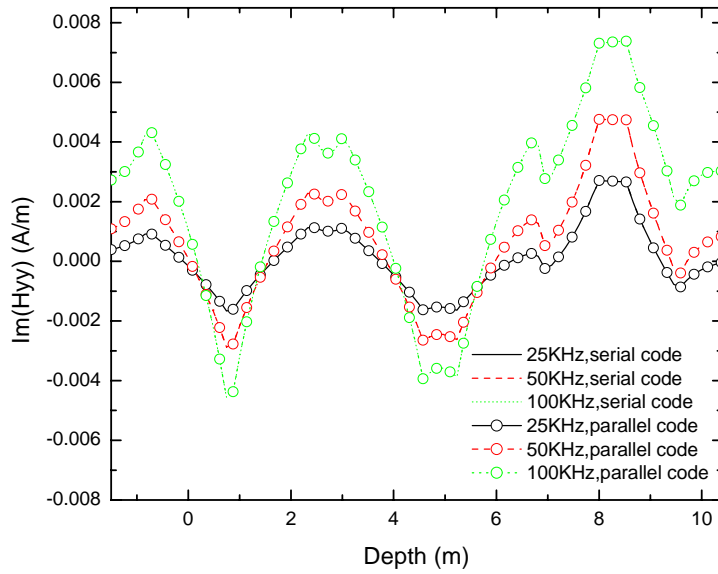
Fig. 9 A Seven-layer anisotropic model

Fig. 10 shows the magnetic field responses at 25KHz, 50KHz and 100KHz obtained from the serial code and the parallel code. We can see that the results from the two codes coincide perfectly with each other, implying that the parallelization does not introduce any error. Fig. 11 shows the computation time of the two codes as a function of the number of logging points. It can be seen that as the number of logging points increases, the total CPU time of both codes increase. But the increase of the parallel code is much slower than that of the serial code. For the same number of logging point, the parallel

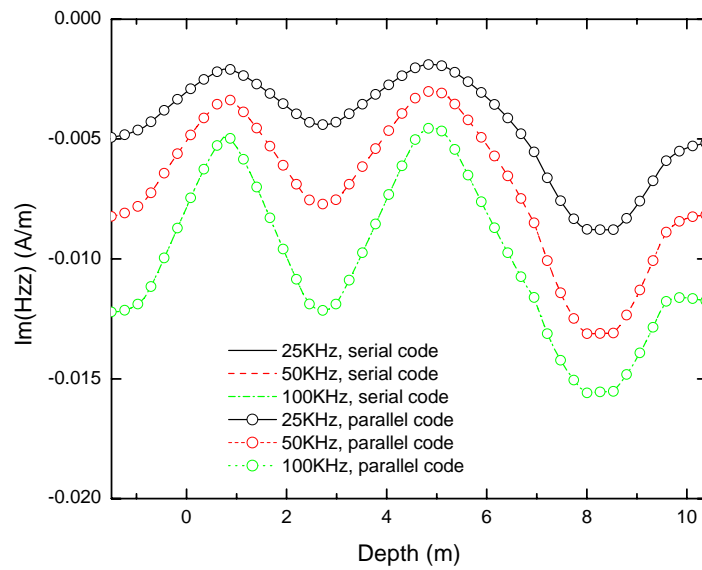
code cost only 1/3 time that of the serial code when the code is run on a 4-core 2.33GHz PC.



(a) H_{xx}



(b) H_{yy}



(b) H_{zz}

Fig.10 The magnetic field response of the 7-layer model obtained from the serial code and the parallel code

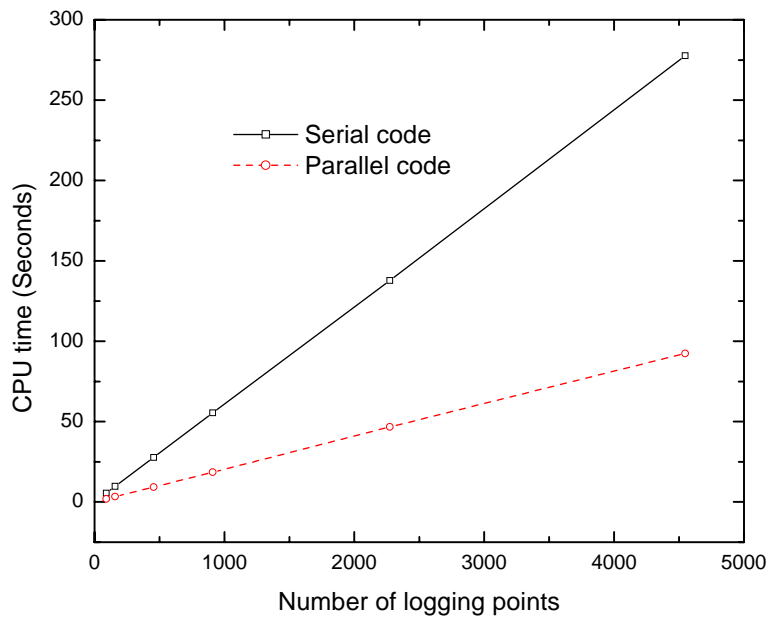


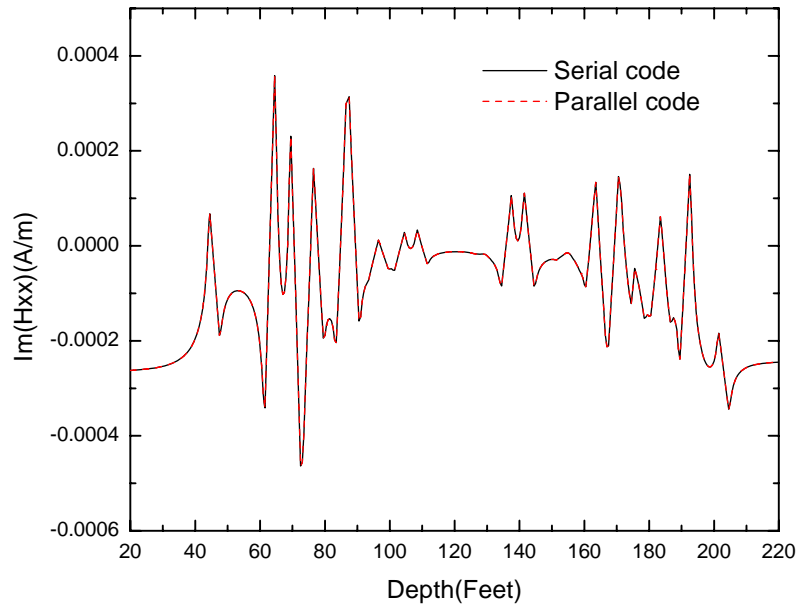
Fig. 11 The CPU time cost by the serial code and the parallel code as a function of the number of logging points

Next, we consider the 28-layer benchmark Oklahoma model as shown in Fig. 12. The boundary and horizontal resistivity of each layer is shown in the figure. The anisotropy contrast is 2.0 namely $R_v/R_h=2.0$. A two-coil triaxial tool spaced by 40 inches is used in the example and the working frequency is 20 KHz. Fig. 13 shows the calculated magnetic field response from the original serial code and the parallel code. Again, perfect agreement is observed between the two results. In Fig. 14, we compare the computation time of the serial code and the parallel code for different number of logging points. In this figure, 4 threads are used. We can see that the parallel code is about 3.8 times faster than the serial code. Comparison of the above two examples, we can conclude that when the layer number of the formation increases, the comparison is in favor of the parallel code.

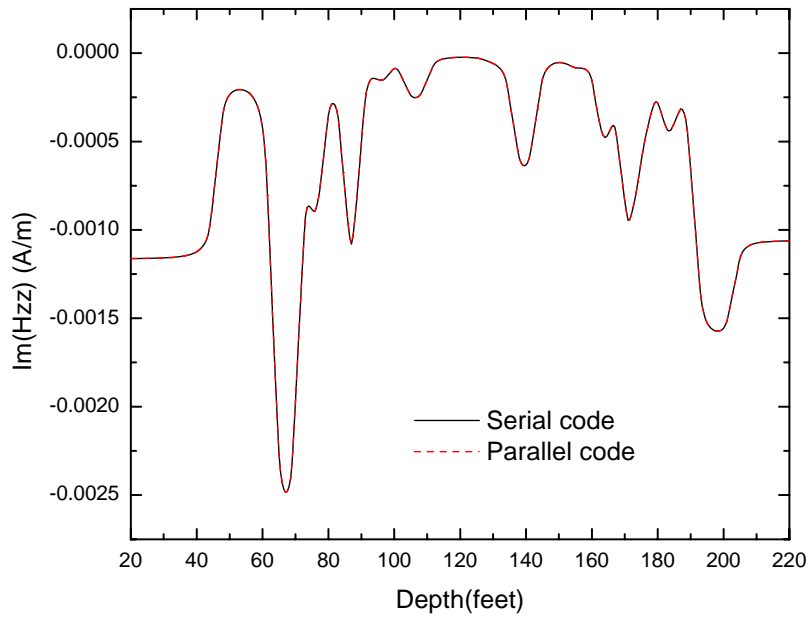
Finally, we change the number of threads to investigate the performance of the parallel code. In Fig.15, we compare the CPU time when different number of threads are used. It can be seen that for a given number of logging points, the more threads are used, the less time is consumed by the code. Therefore, we can expect that the speed of the forward modeling to be further improved as multi-core computers are used.

46'	$R_h = 10 \text{ ohm-m}$
	$R_h = 100 \text{ ohm-m}$
63'	$R_h = 4 \text{ ohm-m}$
71'	$R_h = 30 \text{ ohm-m}$
75'	$R_h = 9 \text{ ohm-m}$
78'	$R_h = 200 \text{ ohm-m}$
85'	$R_h = 7 \text{ ohm-m}$
89'	$R_h = 909 \text{ ohm-m}$
95'	$R_h = 60 \text{ ohm-m}$
98'	$R_h = 1250 \text{ ohm-m}$
103'	$R_h = 40 \text{ ohm-m}$
110'	$R_h = 1416 \text{ ohm-m}$
128'	$R_h = 400 \text{ ohm-m}$
136'	$R_h = 15 \text{ ohm-m}$
143'	$R_h = 1000 \text{ ohm-m}$
153'	$R_h = 179 \text{ ohm-m}$
157'	$R_h = 1000 \text{ ohm-m}$
162'	$R_h = 15 \text{ ohm-m}$
165'	$R_h = 75 \text{ ohm-m}$
169'	$R_h = 9 \text{ ohm-m}$
173'	$R_h = 20 \text{ ohm-m}$
177'	$R_h = 100 \text{ ohm-m}$
182'	$R_h = 18 \text{ ohm-m}$
185'	$R_h = 200 \text{ ohm-m}$
187'	$R_h = 75 \text{ ohm-m}$
189'	$R_h = 149 \text{ ohm-m}$
191'	$R_h = 7 \text{ ohm-m}$
203'	$R_h = 11 \text{ ohm-m}$

Fig. 12 A 28-layer Oklahoma model



(a) H_{xx}



(b) H_{zz}

Fig.13 The magnetic field response of the 28-layer Oklahoma model

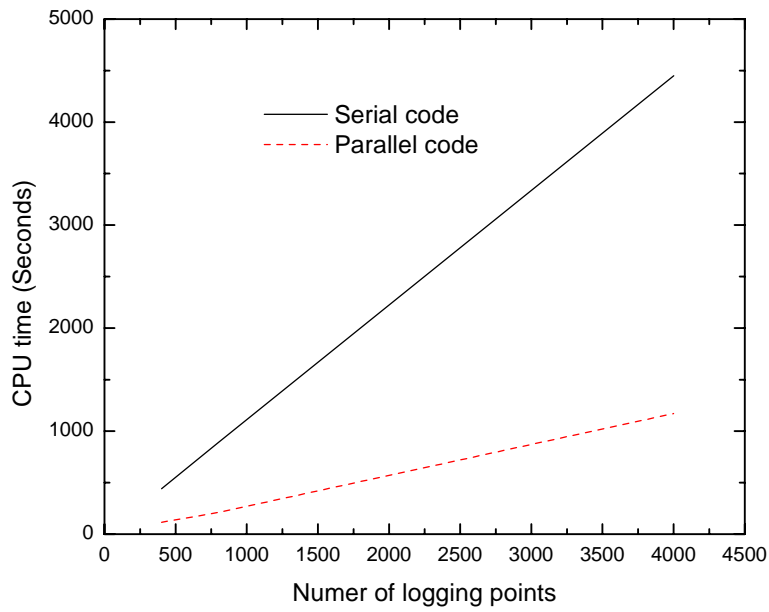


Fig. 14 The total computation time of the serial code and the parallel code for the 28-layer Oklahoma model

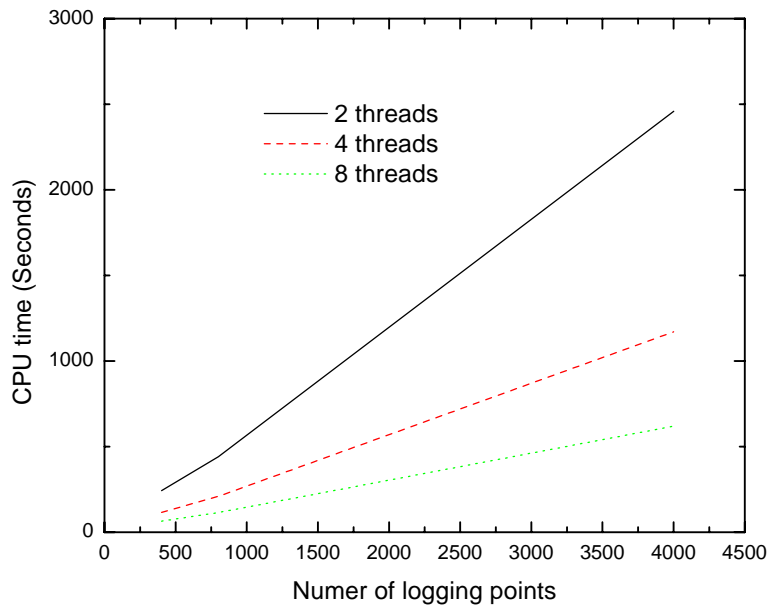


Fig. 15 Comparison of the time cost for different number of threads

After investigating the performance of the parallel code, we use it to study the directional propagation measurements. Geosteering is the technique to actively guide the horizontal wells based on real-time formation evaluation data. A key industry need is having the ability to geosteer wells with respect to reservoir boundaries, even when the wellbore does not intersect the boundary. New directional LWD tools incorporates tilted and transverse antennas in the drilling collar, thus are able to detect and resolve anisotropy in wells and indicate whether a nearby boundary is approaching from above or below [26]. As a basis of the directional LWD tool study, in this paper, we use the developed code to study the sensitivity and detection range of a single directional transmitter-receiver pair.

Consider a single transmitter-receiver pair directional tool moves across a 20-ft thick, 20 Ohm-m bed in a horizontal well (i.e. the relative dip is 90°). As shown in Fig .16, the transmitter is oriented along the axis of the tool while the receiver is tilted 45° with respect to the tool axis. The transmitter and receiver are spaced 96 in. The upper and lower layer has a resistivity of 2 and 5 ohm-m, respectively. Fig. 17 shows the amplitude attenuation and phase shift of the response (the ratio of the received signal when the receiver is pointed 45° and -45° degree) as a function of the true vertical depth at 100KHz and 400KHz. We can observe the following fact from Fig.17. First, the peak values of both the amplitude ratio and phase shift appear at the boundaries, determining the boundaries of different media. Second, the peak values increase as the frequency increases. Furthermore, when the tool approaches a more conductive layer from below, the directional phase shift and attenuation are positive. On the contrary, when the tool approaches a more conductive layer from above, the directional phase shift and attenuation are negative. This is a very important application in geosteering. The polarity can be used while drilling as a simple indicator to determine whether the directional driller should steer up or down.

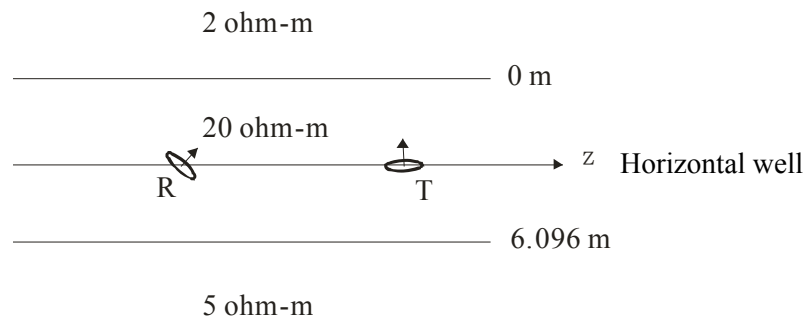
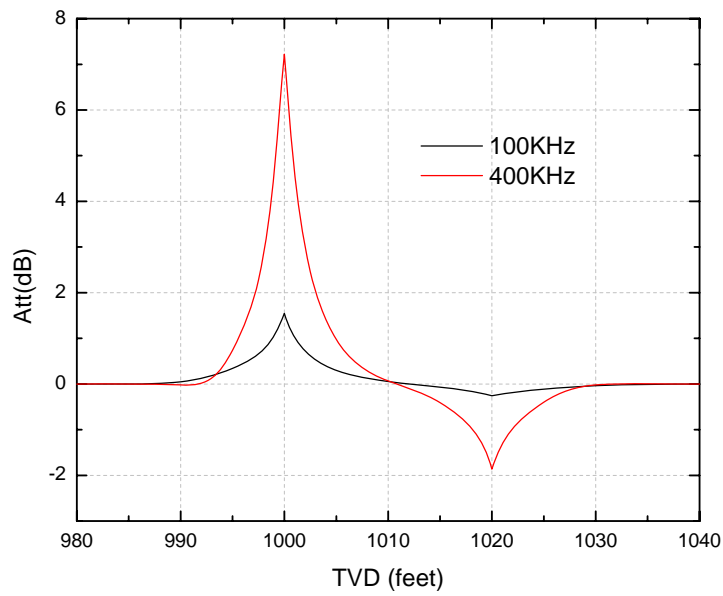
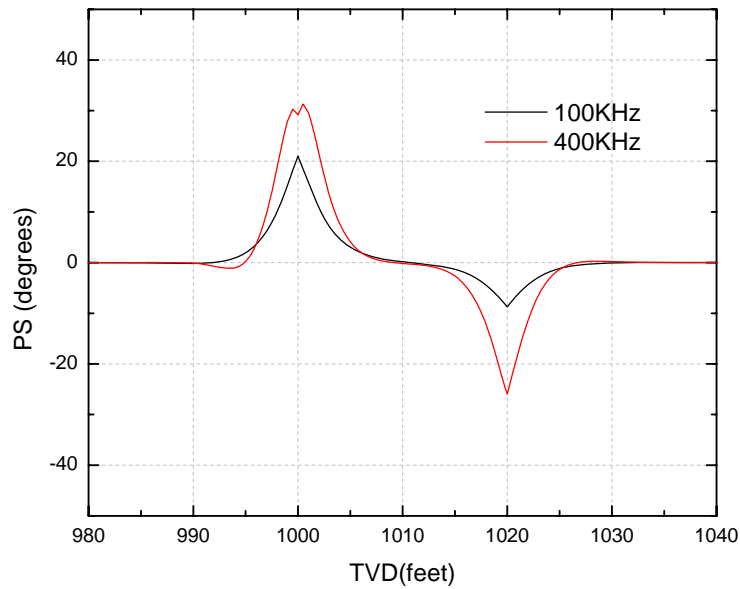


Fig. 16 A tilted transmitter-receiver pair in a 20 Ohm-m bed sandwiched between 2 and 5 Ohm-m shoulders



(a) Attenuation



(b) Phase-shift

Fig. 17 Response of a 96-in directional propagation measurement

Next, we study the depth of investigation (DOI) of the tool as a function of the TR spacing. Fig. 18-20 shows the attenuation of the magnetic field at 20KHz, 100KHz and 400KHz, respectively, as a function of the distance to boundary (DTB) for TR spacing varying from 1ft to 10ft. From these figures, we observed that the attenuation signal increases as the TR spacing increases and decreases as the distance to boundary increases.

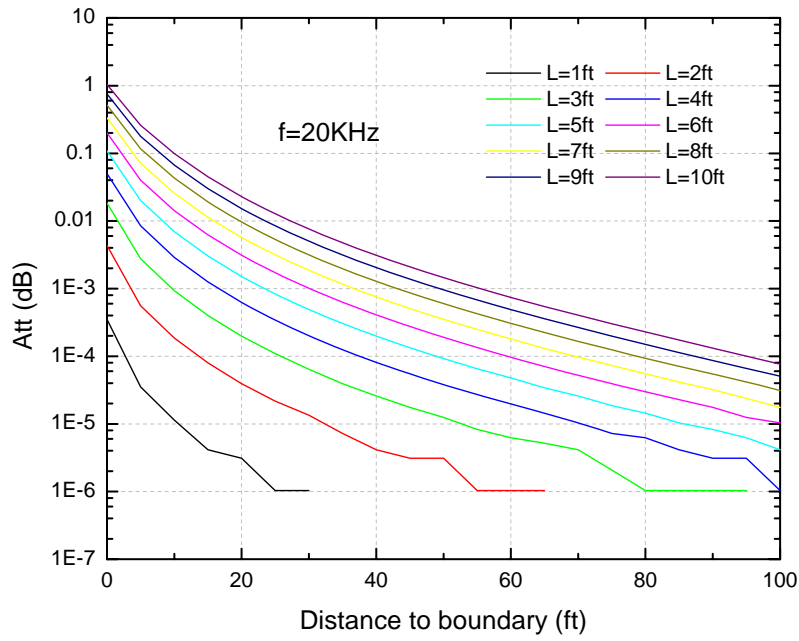


Fig. 18 Amplitude attenuation versus distance to boundary at 20KHz

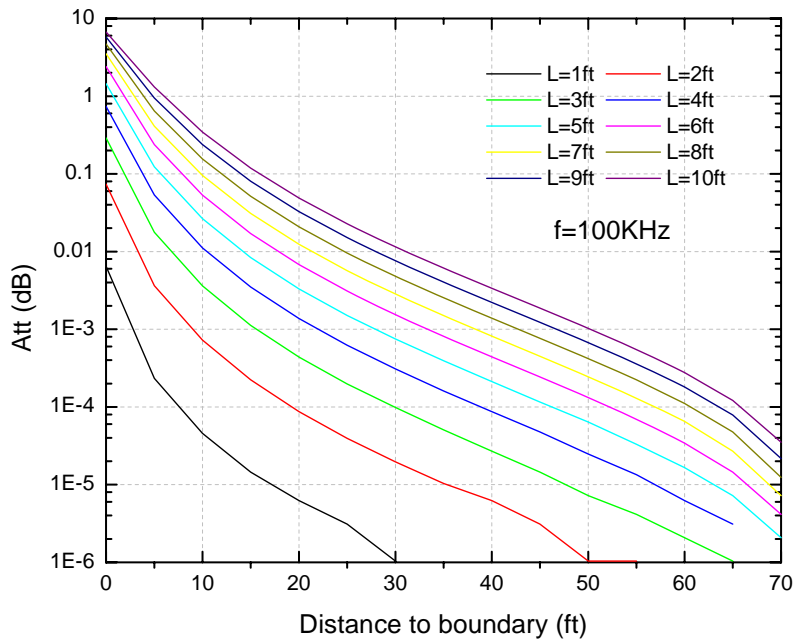


Fig. 19 Amplitude attenuation versus distance to boundary at 100KHz

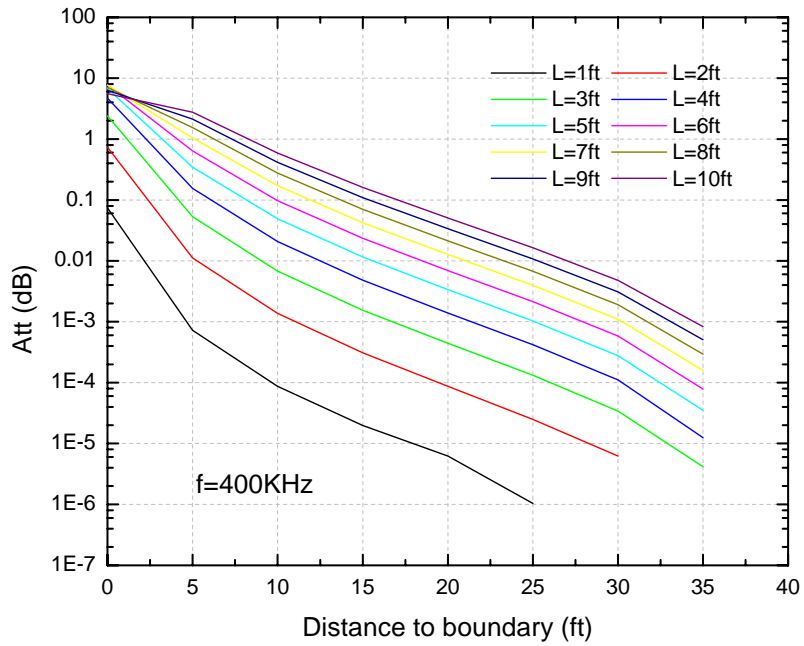


Fig. 20 Amplitude attenuation versus distance to boundary at 400 KHz

From the above figures, we can plot the depth of investigation (DOI) as a function of TR spacing at the three frequencies, as shown in Fig. 21-23. In these figures, the solid line is corresponding to a detection threshold of 0.001dB and the dashed line corresponding to 0.01dB. We can see that as the TR spacing increases, the depth of investigation increases.

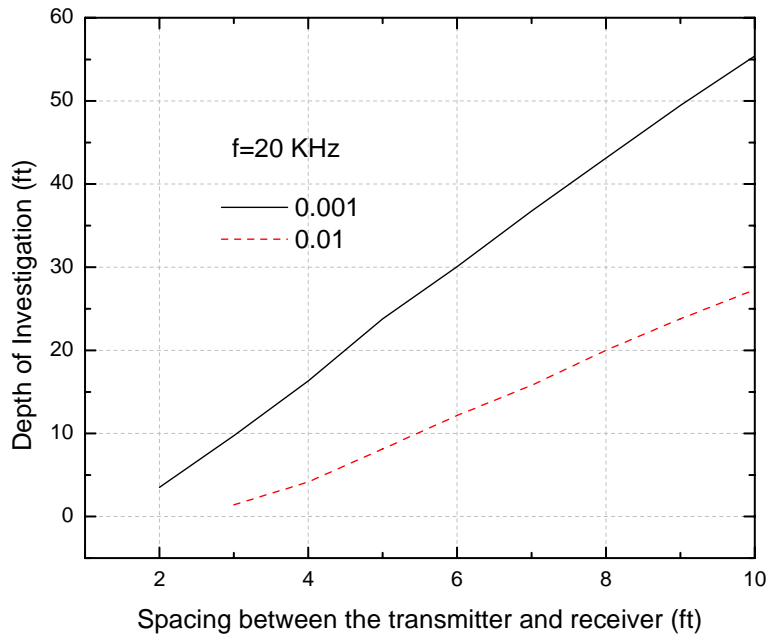


Fig. 21 Depth of investigation (DOI) versus TR spacing at 20KHz

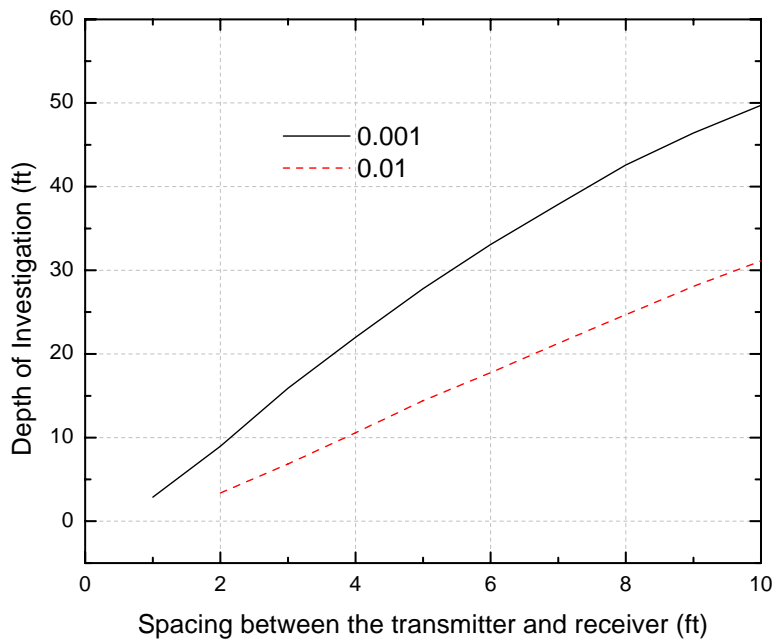


Fig. 22 Depth of investigation (DOI) versus TR spacing at 100KHz

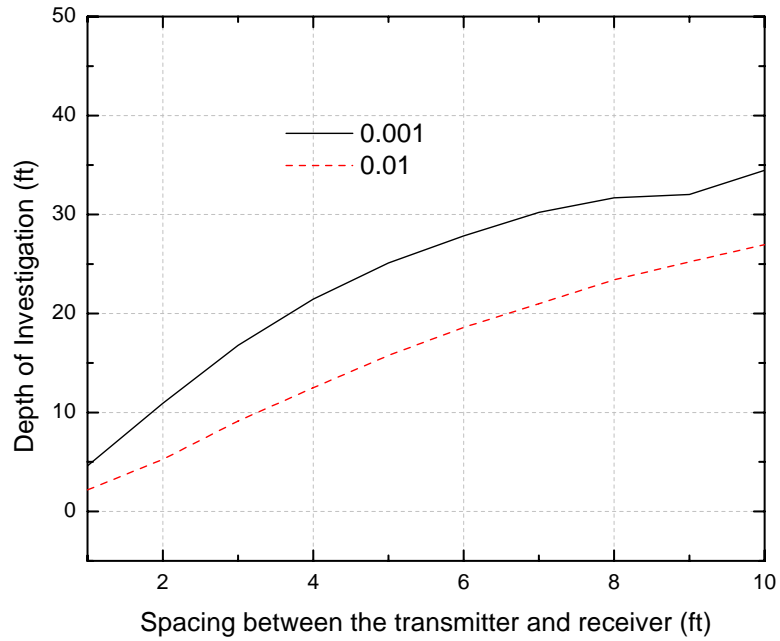


Fig. 23 Depth of investigation (DOI) versus TR spacing at 400KHz

Next, we study the sensitivity of the amplitude of the magnetic field. Fig. 24 shows the amplitude of the magnetic field versus the DTB for different TR spacing at 20KHz. Fig. 25 and Fig. 26 are the corresponding figures for 100 KHz and 400KHz, respectively. Fig. 27 shows the depth of investigation as a function of the TR spacing for different frequencies when the detection threshold is 60dB. It can be seen that the DOI does not increase monotonically with the TR spacing. For 20 KHz, the maximum DOI is reached when the transmitter and receiver is spaced around 3-4 ft. For 100 KHz and 400 KHz, when the TR spacing is about 6 ft, the tool obtains maximum investigation depth.

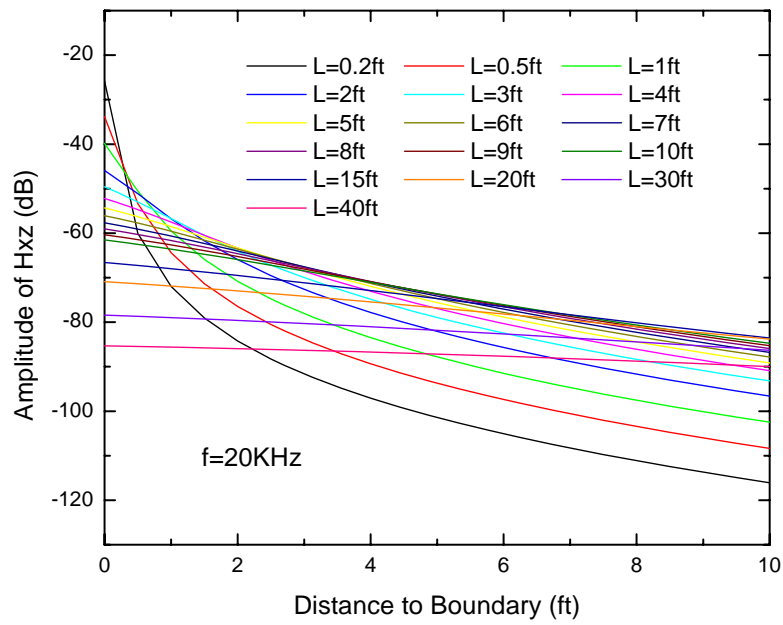


Fig. 24 Amplitude of magnetic field versus DTB at 20 KHz

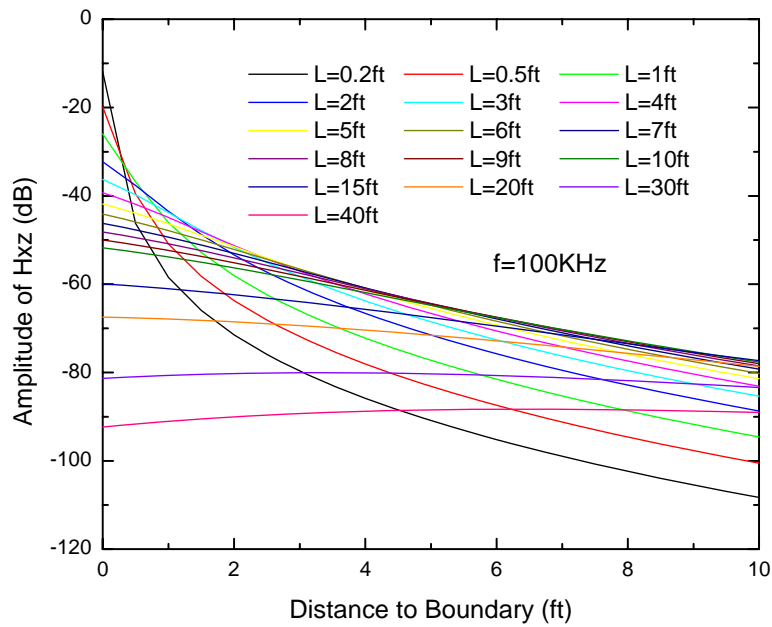


Fig. 25 Amplitude of magnetic field versus DTB at 100 KHz

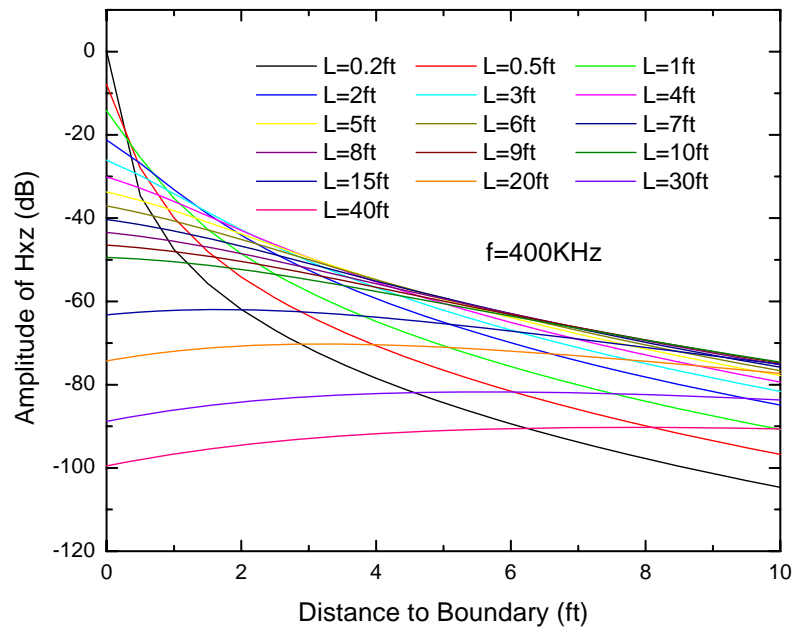


Fig. 26 Amplitude of magnetic field versus DTB at 400 KHz

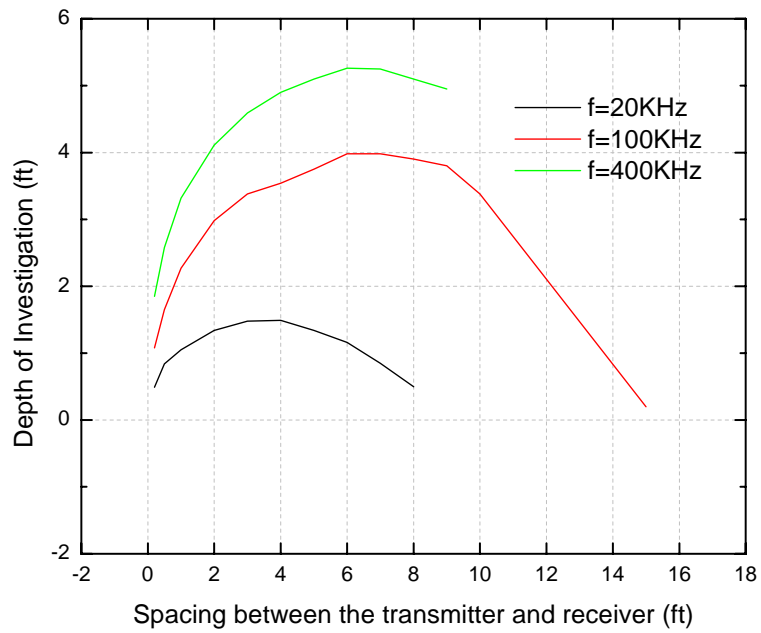


Fig. 27 Depth of Investigation at 60dB

B. The 3-D FEM Code

In this part, we will show some numerical examples for the 3-D FDM code. We consider a 7-layer anisotropic formation as shown in Fig. 28. It consists of a sequence of reservoir layers—ranging from conductive brine bearing to resistive hydrocarbon bearing — shouldered by conductive shale layers. This model was adapted from an actual borehole-logging situation, a dipping well located in Gulf of Mexico deep water and penetrating Tertiary unconsolidated turbidite sediments. It includes a wide range of variations of conductivity/resistivity contrasts. Layer 1, 3, 5 and 7 are anisotropic and has a horizontal resistivity of 1 ohm-m and a vertical resistivity of 10 ohm-m. There are invasions in Layer 2, 4 and 6. Diameters of the borehole and invasion are 21.59cm and 30.48cm, respectively. The mud resistivity in the borehole is 0.4 ohm-m. Other parameters are given in the figure. We use a tool consisting of three collocated orthogonal transmitter coils and three collocated orthogonal receiver coils to measure the magnetic field profile of the model. The transmitter and receiver coils are oriented at the x-, y- and z-direction. The dipping angle (the angle between the tool axis and the normal to the layer boundaries) is 30° . The spacing between the transmitter and receiver is 1.8m.

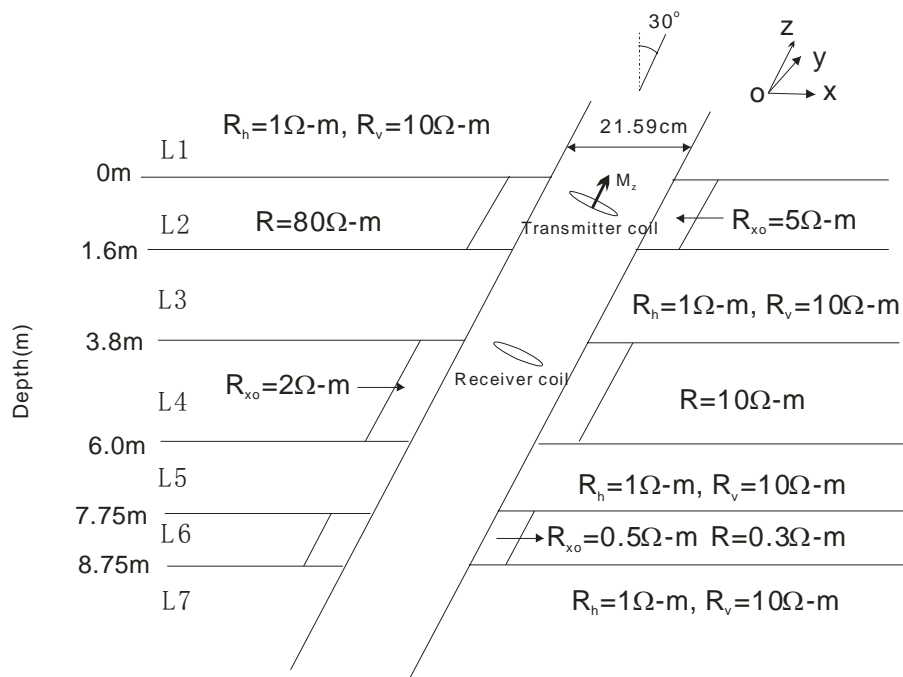


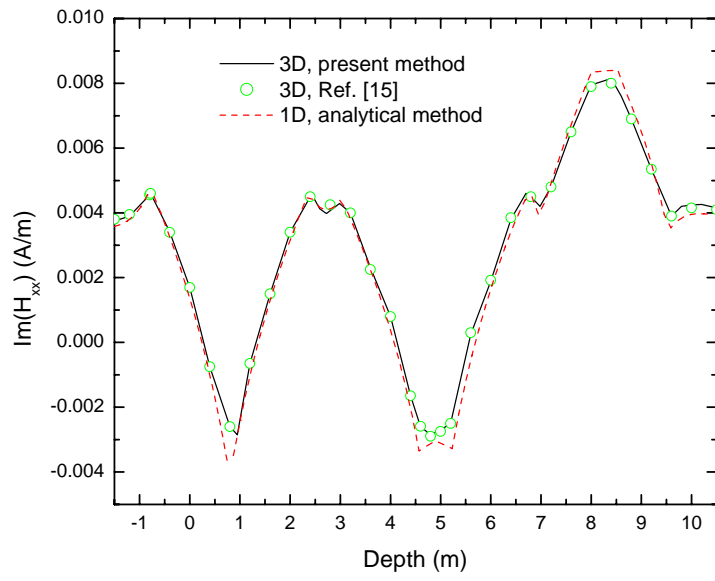
Fig. 28 Geometry of a 3-D 7-layer anisotropic model

A mesh consisting 28x28x92 cells in the x-, y- and z- directions is used to model the solution domain. For 79 observation points, Table 2 compares the CPU time cost by the serial code and the parallel code on a 4-core computer. It can be seen that the speed of the parallel code increase significantly as the number of core increases.

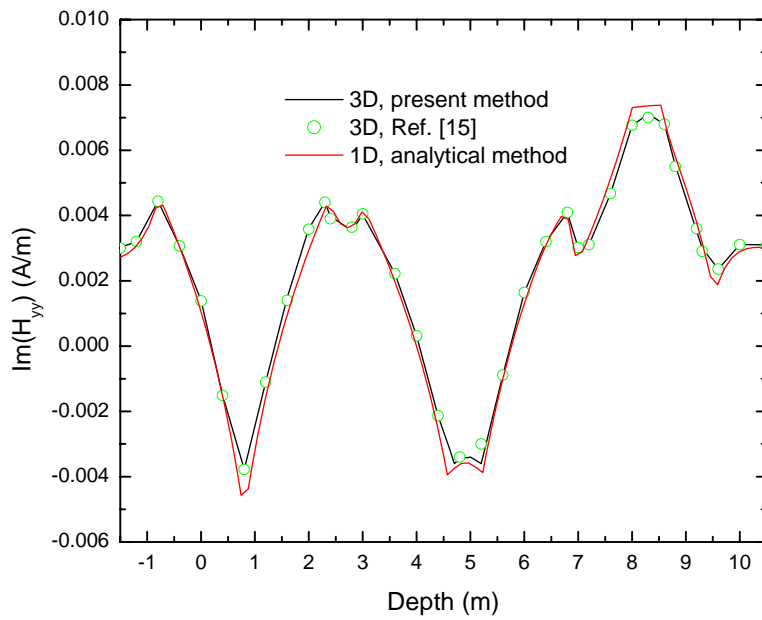
Table 2. Comparison of the CPU time cost by the serial code and parallel code

Number of cores	1	2	4	8
CPU time cost by The serial code (mins)	192	192	192	192
CPU time cost by The parallel code (mins)	198	132	87	56
Speedup (%)	-3.1%	30.8%	54.5%	60.7%

Fig. 29 shows the calculated imaginary part of the H_{xx} , H_{yy} and H_{zz} responses at 100KHz using the parallel code. The results from [27] are also presented in the figure for comparison. Good agreements are observed, validating the present parallel 3-D FDM code. In these figures, we also present the 1-D result calculated by the 1-D analytical method with the borehole and invasion neglected. It can be seen that the in the layers where there are no invasions, the 1-D and 3-D results are very close to each other since the borehole effect is not obvious in this case. However, in Layers 2, 4 and 6 where invasions exist, the 1-D and 3-D results have discrepancy, implying that 3-D simulation is necessary to get accurate results and more information of surrounding media.



(a) H_{xx}



(b) H_{yy}

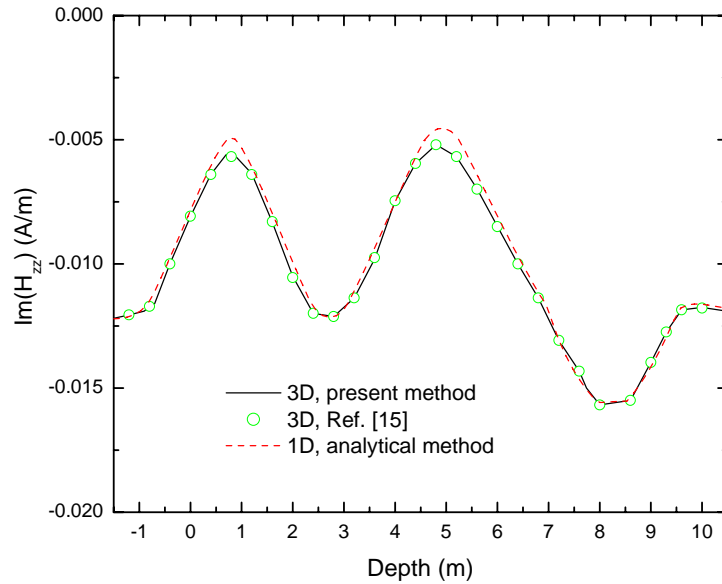

 (c) H_{zz}

Fig. 29 Comparison of the imaginary part of the magnetic field response of a 2-coil triaxial tool at 100KHz

To investigate the application of the average conductivity technique, we consider an example with/without using this technique. Consider a 1-D layered structure as shown in Fig.30. Layer 1, 3 and 5 are isotropic media with resistivity of 50 ohm-m, 0.5 ohm-m and 1.0 ohm-m, respectively. Layer 2 is anisotropic medium and has a vertical resistivity of 11 ohm-m and a horizontal resistivity of 1.9 ohm-m. Layer four has a vertical resistivity of 2.0 ohm-m and a horizontal resistivity of 1.0 ohm-m. The depth of each layer is shown in the figure. In the first model, we assume the principal axes of the resistivity tensor of the media coincide with the x - y - z coordinate system and the transmitter and receiver coils are tilted 60° , as shown in Fig. 30(a). In the second model, we tilt the principal axes of the media and aligning the source in the z -direction while the multi-layered formation is tilted in the x' - y' - z' reference frame, as shown in Fig. 30(b). The two models are expected to give the same results although the implementation of the codes are different, thus providing an internal consistency check for the developed code.

In the first model, there is no need to simulate the averaged conductivity tensor since the meshes coincide with the boundaries of the layers. But the axial component of the magnetic field is a combination of the field generated by an x -directed source and a z -directed source. In the second model, the meshes do not coincide with the formation boundaries any more, so we need to calculate the averaged conductivity tensor for all the cells. It should be noted that the conductivity tensors for each cell in the original principle coordinate system x - y - z should be transformed to the new coordinate system x' - y' - z' before they are used to get the averaged conductivity tensors. The transformation can be performed by multiplying the original conductivity tensor with a rotation matrix \mathbf{R} ,

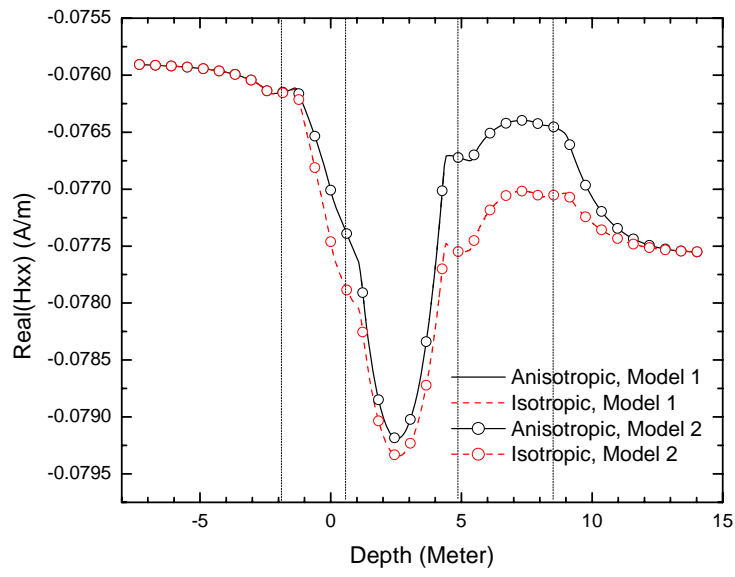
$$\bar{\sigma}' = \mathbf{R}^T \text{diag}(\sigma_{xx}, \sigma_{yy}, \sigma_{zz}) \mathbf{R} \quad (40)$$

The rotation matrix \mathbf{R} can be expressed by

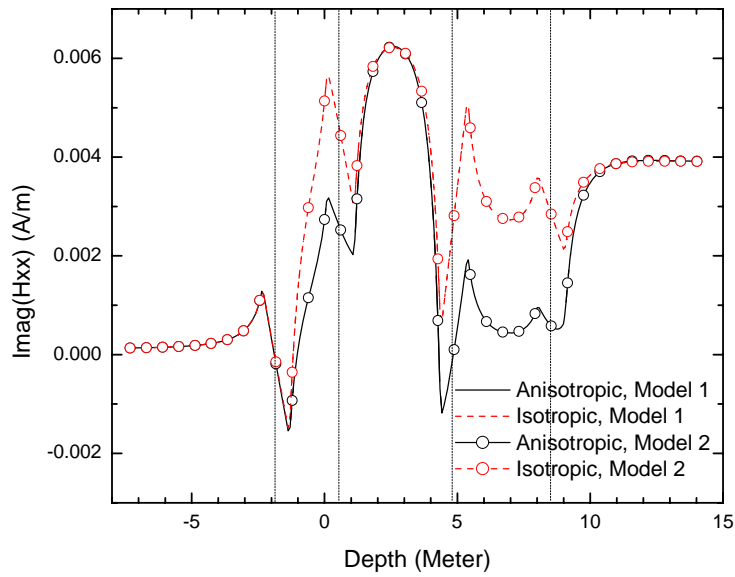
$$\mathbf{R} = \begin{bmatrix} \cos\theta\cos\phi & -\sin\phi & \sin\theta\cos\phi \\ \cos\theta\sin\phi & \cos\phi & \sin\theta\sin\phi \\ -\sin\theta & 0 & \cos\theta \end{bmatrix} \quad (41)$$

where θ and ϕ are the two Euler angles corresponding to the dip and strike angles of the laminations. After rotation, the conductivity tensor will be a full tensor in the coordinate system x' - y' - z' in stead of a diagonal tensor in the original coordinate system x - y - z . Fig. 31 shows the calculated magnetic field H_{xx} (both the transmitter coil and receiver coils are in the x direction) and H_{zz} (both the transmitter and receiver coils are in the y direction) at different vertical depth for a pair of transmitter and receiver spaced by 1.016m and working at 20KHz. Perfect agreement is observed between the results from the two different models, verifying the implementation of finite-difference method and the averaged conductivity tensor calculation.

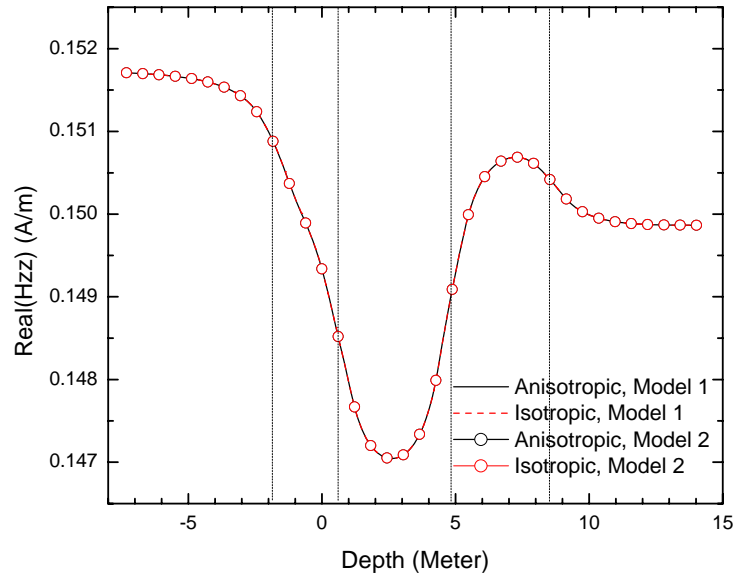
In Fig. 31, besides the results for the anisotropic case, we also present the H_{xx} and H_{zz} for the isotropic case, namely, Layer 2 and Layer 4 are also isotropic with resistivity being 1.0ohm-m and 1.9 ohm-m, respectively. From Fig. 31(c) and (d), we can see that the z -directed coupling H_{zz} are the same in the isotropic and anisotropic cases, implying that H_{zz} has no sensitivity to the vertical resistivity. On the contrary, Fig. 31 (a) and (b) shows that the x -directed coupling H_{xx} can detect the anisotropy property of the media.



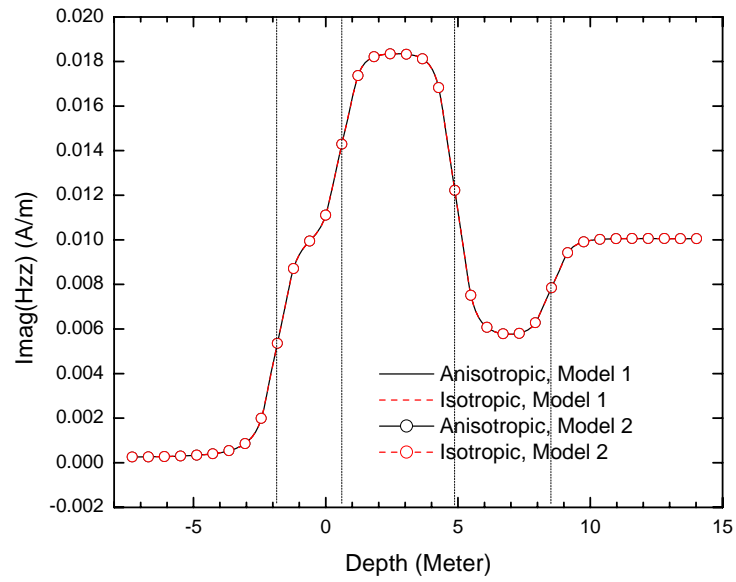
(a) Real (H_{xx})



(b) Imag (H_{xx})



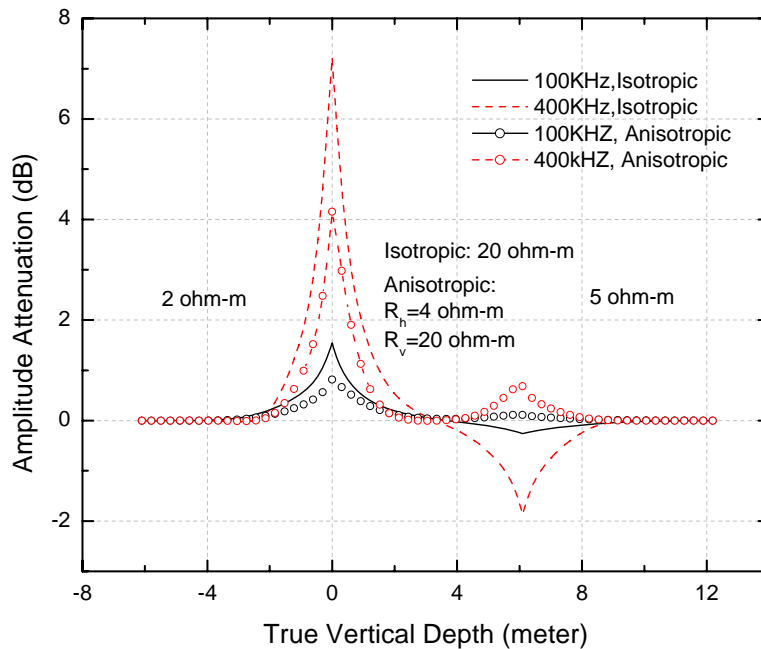
(c) Real (H_{zz})



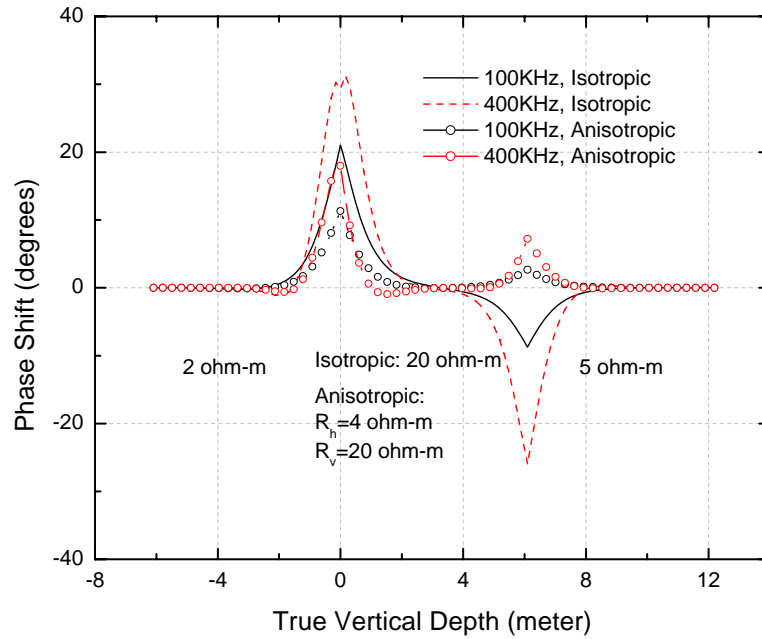
(d) Imag (H_{zz})

Fig. 31 The calculated magnetic field from the two models

The 3-D FDM code can also be used to study the response of arbitrarily oriented transmitter-receiver pairs which are usually used in geosteering. We consider the example shown in Fig.16 again. In Fig.32, we also present the results of an anisotropic case for comparison, in which the center layer has a horizontal resistivity of 4 ohm-m and a vertical resistivity of 20 ohm-m. From the figure, we can see that the existing of the anisotropy in the center layer changes the polarity of the phase shift and attenuation, as shown by the dotted curves between 4-8 m.



(a) Amplitude Attenuation



(b) Phase shift

Fig. 32 The response of a tilted transmitter-receiver pair in a 3-layer isotropic/anisotropic media

4. Conclusions

In this report, we use OpenMP to parallel the 1-D analytical forward modeling code and 3-D FDM code for the simulation of wireline induction/LWD triaxial tools in anisotropic formation. The implementation of the parallelization was described. Numerical examples were presented to demonstrate the efficiency of the parallel code. Then the codes were used to investigate some interesting problems. The parallelization of the forward modeling codes significantly increases the efficiency of the original codes and renders future real-time inversion possible.

References

- [1] W. Gropp and E. Lusk, [A Test Implementation of the MPI Data Message-Passing Standard](#), *Technical Report ANL-92/47*, December 1992.
- [2] W. Gropp, E. Lusk, N. Doss and A. Skjellum, “A high-Performance, portable implementation of the *MPI* Message-Passing Interface standard,” *Parallel Computing*, vol. 22, pp. 789–828, 1996.
- [3] G. Krawezik, F. Cappello, “Performance comparison of *MPI* and *OpenMP* on shared memory multiprocessors,” *Concurrency and Computation: Practice & Experience*, vol.18, issue. 1, pp.29-61, 2003.
- [4] I. Dorta, C. Leon, C. Rodriguez, “A comparison between *MPI* and *OpenMP* branch-and-bound skeletons,” *Proceedings of the International Parallel and Distributed Processing Symposium*, 2003.
- [5] R. Chandra, R. Menon, L. Dagum, D. Kohr, D. Maydan, J. McDonald, *Parallel Programming in OpenMP*, Morgan Kaufmann, San Francisco, 2000.
- [6] B. Chapman, G. Jost, R. van der Pas, D.J. Kuck, *Using OpenMP: Portable Shared Memory Parallel Programming*, The MIT Press, Massachusetts, 2007.
- [7] M. Hermanns, “Parallel Programming in Fortran 95 using OpenMP,” <http://www.openmp.org/presentations/miguel/F95-OpenMPv1-v2.pdf>, 2002.
- [8] C. Bischof, M. Bucker, P. Gibbon, G. Joubert, T. Lippert, *Parallelizing a Real-Time Steering Simulation for Computer Games with OpenMP*, IOS Press, Netherlands, 2008.
- [9] B. Kriegshäuser, O. Fanini, S. Forgang, G. Itskovich, M. Rabinovich, L. Tabarovsy, L. Yu, M. Epov, P. Gupta, and J. V. D. Horst, “A new multicomponent induction logging tool to resolve anisotropic formations,” *Trans. SPWLA 41st Annual Logging Symp.*, Paper D Dallas, TX, 2000.
- [10] M. Zhdanov, D. Kennedy, and E. Peksen, “Foundations of tensor induction well-logging,” *Petrophysics*, vol. 42, no. 6, pp. 588–610, Nov./Dec. 2001.

- [11] B. Anderson, T. Barber, and T. M. Habashy, "The interpretation and inversion of fully triaxial induction data: a sensitivity study," *36th Annual Logging Symposium Transactions, Society of Professional Well Log Analyst*, Paper O, 2002.
- [12] R. Rosthal, T. Barber, S. Bonner, K. C. Chen, S. Davydycheva, G. Hazen, D. Homan, C. Kibbe, G. Minerbo, R. Schlein, L. Villegas, H. Wang, and F. Zhou, "Field test result of an experimentally fully-triaxial induction tool," *Trans. SPWLA 44th Annual Logging Symposium*, Paper QQ, Galveston, TX, 2003.
- [13] M. Rabinovich, L. Tabarovsky, B. Corley, J. van der Horst, and M. Epov, "Processing multi-component induction data for formation dips and anisotropy," *Petrophysics*, vol.47, no.6, pp.506–526, 2006.
- [14] M. Rabinovich, M. Gonfalini, T. Rocque, B. Corley, D. Georgi, L. Tabarovsky, and M. Epov, "Multi-component induction logging: 10 years after," *48th Annual Logging Symposium, Society of Professional Well Log Analysts*, 2007.
- [15] Z.Y. Zhang, L.M. Yu, B. Kriegshauser, and R. Chunduru, "Simultaneous determination of relative angles and anisotropic resistivity using multicomponent induction logging data," *SPWLA 42th Annual Logging Symposium*, Paper Q, June 17-20, 2001.
- [16] L. L. Zhong, "", Ph D Dissertation, University of Houston, 2004
- [17] L. L. Zhong, J. Li, L.C. Shen, and R. C. Liu, "Computation of triaxial induction logging tools in layered anisotropic dipping formations," *IEEE Trans. on Geoscience and Remote Sensing*, vol.46, no.4, pp.1148-1163, 2008.
- [18] N. Yuan, X.C. Nie and R. Liu, "Responses of Triaxial Induction Tools in 1-D Multi-Layered Transverse Isotropic Formations," Well Logging Lab Technical Report, Chapter 2, 2009, University of Houston
- [19] M. Huang and L. C. Shen, "Computation of induction logs in multiplelayer dipping formation," *IEEE Trans. Geosci. Remote Sens.*, vol. 27, no. 3, pp. 259–267, May 1989.
- [20] J. H. Moran and S. Gianzero, "Effects of formation anisotropy on resistivity logging measurement," *Geophysics*, vol. 44, pp.1266-1286, 1979.

- [21] K. S. Yee, "Numerical solution of initial boundary value problems involving Maxwell's equations in isotropic media," *IEEE Trans. Antennas Propagat.*, vol. 14, no. 3, p.302-307, Jan. 1984.
- [22] T. Wang and S. Fang, "3-D electromagnetic anisotropic modeling using finite difference," *Geophysics*, vol.66, no.5, p. 1386-1398, Sept-Oct 2001.
- [23] Y. Saad and Schultz M. H., "GMRES: A generalized minimal residual algorithm for solving nonsymmetric linear systems," *SIAM Journal of Sci. STAT. Comput.*, vol.7, no.3, p.856-869, 1986.
- [24] Y. Saad, "ILUT: A dual threshold incomplete LU factorization," *Numer. Linear Algebra Appl.*, vol. 1, no. 4, p. 387-402, 1994.
- [25] X. C. Nie, N. Yuan and R. Liu, "Finite-Difference Modeling of Triaxial Induction Tools in 3D Anisotropic Media," *Well Logging Lab Technical Report*, Chapter 1, 2010, University of Houston.
- [26] Q. M. Li, D. Omeragic, L. Chou, L.B. Yang, K. Duong, J. Smits, J. Yang, T. Lau, C. B. Liu, R. Dworak, V. Dreuillault, and H. Ye, "New Directional electromagnetic tool for proactive geosteering and accurate formation evaluation while drilling," *SPWLA 46th Annual Logging Symposium*, June 26-29, 2005.
- [27] J. S. Hou, R. K. Mallan and C. Torres-Verdin, "Finite-difference simulation of borehole EM measurements in 3D anisotropic media using coupled scalar-vector potentials," *Geophysics*, vol.71, no.5, p. G225-G233, Sept-Oct 2006.

CHAPTER 3

Simulation of Mandrel Effect on Logging-While-Drilling Propagation Tools

Abstract

We investigate the impact of the presence of collar in Logging-while-drilling (LWD) propagation resistivity tools by simulating the tool response in various types of media such as homogeneous isotropic formation, isotropic layered media and anisotropic layered dipping beds. Both the transmitters and the receivers can be oriented parallel to the tool body or perpendicular to it, thus both the z-directed and x-directed coils are studied. The study will be focused on the effect caused by the conductive metallic drilling collar (from now on referred to as mandrel) of LWD tool which is different from wireline induction tools. For all the examples, two models will be studied: one treats antenna as point-magnetic dipole without the presence of mandrel, the other models the antenna as finite-size coils around a metallic mandrel. Simulations of both dipole model and finite size loop coil with mandrel in one-dimensional (1-D) and two dimensional formations are performed by the Wellog Inversion Package developed at the Well Logging Laboratory. All the three dimensional (3-D) simulations are carried out using COMSOL RF module. Results indicate that the presence of mandrel produces a significant ($\sim 0.5\text{db}$) downward shift in attenuation but has very little effect on phase-difference. By using proper conversion charts, the R_a and R_p readings in isotropic layered dipping beds only show differences between dipole model and model with mandrel near the bed boundary. However, for the R_a and R_p readings in anisotropic layered dipping beds, differences would show up even at the depths far away from the bed boundary.

1. Introduction

LWD propagation resistivity tool uses high conductive steel as mandrel due to the high stress drilling environment. This is quite different from some wireline resistivity tools whose mandrel is non-magnetic and non-conductive. Early studies suggest that the

presence of mandrel can be ignored when simulating the tool response because very little electromagnetic field and eddy current penetrate inside the mandrel at the MHz high operating frequency of LWD tools [1]. Hence point-magnetic dipole model is used to simulate the tool response of the LWD resistivity tool, similar to what is done for wireline induction tools. Study of the impact of mandrel profile on LWD tool resistivity transform in homogeneous formation [2] indicated the attenuation is more influenced by that presence of metallic mandrel than the phase-shift measurement. Recent work characterized the effects of the metallic mandrel on tilted coils in homogeneous medium [3]. Another study in isotropic layered formation pointed out that the effect of the mandrel is large near the bed boundary but it would not affect the result of inversion [4]. It would be very interesting to perform a comprehensive study of the mandrel effect in layered formation for conventional and directional LWD propagation resistivity tools.

In this project, point-magnetic dipole model and the model with mandrel and finite size antennas will be analyzed to study the effects caused by the presence of a metallic mandrel. This study will be carried out in both homogeneous isotropic medium and layered anisotropic media, including one-dimensional (1-D), two-dimensional (2-D) and three-dimensional (3-D) calculations. The antennas can be conventional axial coils and also new directional coils. The primary goal of this project is to ascertain how significant the mandrel effect is in different cases, and then decide whether and how the effect can be corrected in interpretation.

The simulation of point-magnetic dipole models can be easily accomplished by running existing WLL layered 1-D code for homogeneous isotropic formation and layered anisotropic dipping beds. The model with mandrel can be simulated in radial 1-D calculation for homogeneous or radial-layered formation. For the model with mandrel, we use 2-D calculation to simulation tool responses in horizontal-layered formation. All the calculations mentioned above are carried out with the WLL Wellog Inversion software. If the model with mandrel is in layered-dipping beds, the problem becomes three-dimensional in nature. The commercial software COMSOL RF module is used to carry out all the 3-D calculations in this project.

2. Theory and Models

2.1 Principle of LWD propagation resistivity tool

The principle of LWD propagation resistivity tool has been described in many literatures. A good introduction can be found in Ref. [1-2]. Figure 1 is a basic configuration of a LWD resistivity tool. It consists of one transmitter and two receivers. Since LWD resistivity tools usually operate at frequencies in the range of 100 kHz to 2MHz, typically 2 MHz, 500 kHz and 400 kHz, the skin effect at these frequencies in rock formations is sufficiently high for us to detect the phase shift and attenuation directly. Also because of the high frequency, the effect of dielectric constant no longer can be ignored. We measure the signals at the two receivers, and then convert the phase shift and amplitude ratio of these two signals to phase-shift resistivity (R_p) and attenuation resistivity (R_a), respectively, using a chart built from homogeneous formations and some simple dielectric relations between dielectric constant and the formation resistivity

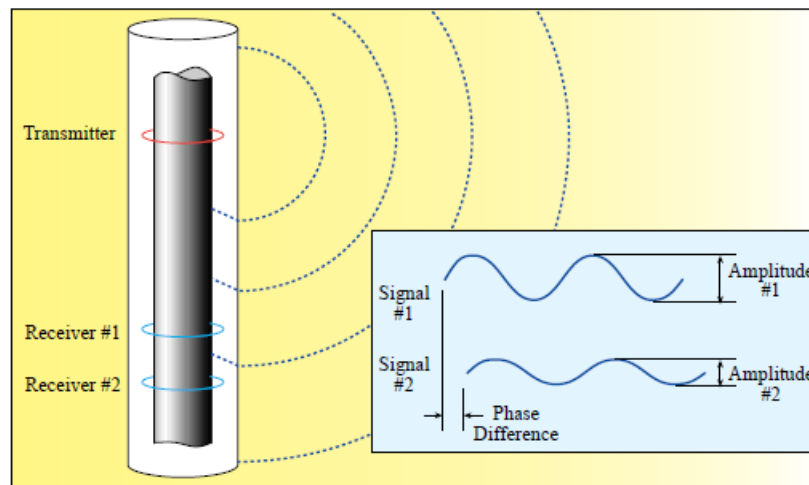


Figure 1 Wave Propagation Resistivity Operating Principle (from TRACS International, Ltd [5])

In the simulations, we start from Maxwell's equations to derive voltage responses on each receiver and further obtain the phase-shift and amplitude ratio by taking the ratio of complex voltages on the two receivers. Utilizing a pre-built converting chart, we can convert tool response (phase-shift and amplitude ratio) in multi-layered formation into

apparent phase-shift and attenuation conductivity. The main steps of our approach are shown in Figure 2. The corresponding relationship between tool response (phase-shift and amplitude ratio) in the homogeneous medium and the conductivity of the homogeneous medium is referred to as "Conversion Chart" or "resistivity transform".

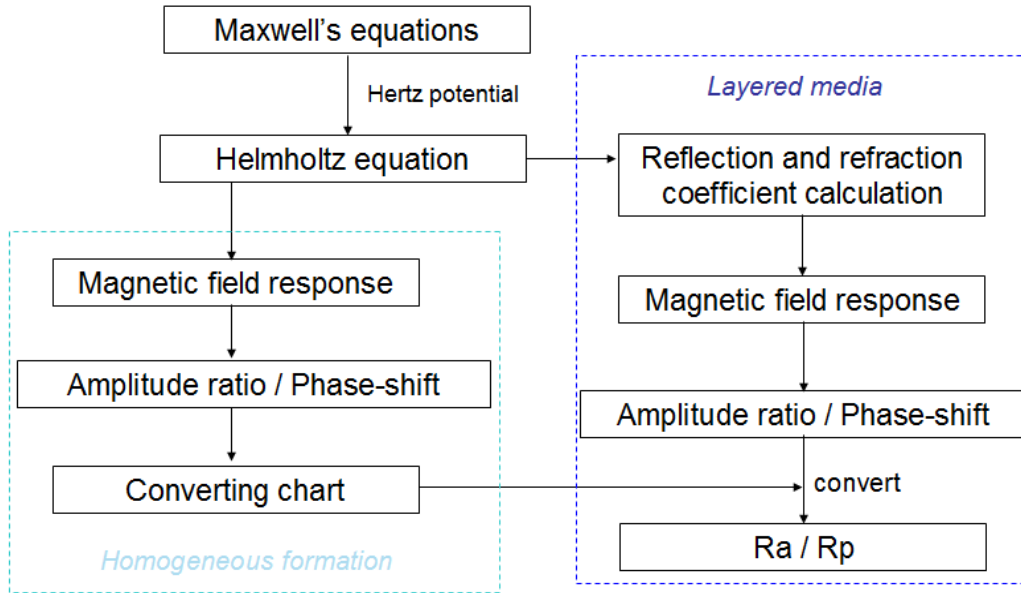


Figure 2 Steps of the simulation of LWD propagation resistivity tool response

For LWD propagation resistivity tools, dielectric properties of the surrounding formation play an important role in the response, especially when the conductivity of formation is relatively low. So we can not ignore the dielectric effect in LWD propagation resistivity tool simulation. Moreover, in order to derive a resistivity curve from phase-shift and attenuation separately for LWD propagation tool, the dielectric constant of formation is assumed to depend on the formation conductivity in a specific way. This is known as dielectric assumptions. Different assumptions are used by different service providers. The specific relationship between conductivity and dielectric constant can be found in Ref. [6]. Figure 3 shows the Schlumberger arcVision resistivity tool configuration. For Schlumberger 2 MHz propagation resistivity measurement, dielectric constant is assumed to be related to the conductivity by the following formula:

$$\varepsilon_r = 108.5 * \sigma^{0.35} + 5.$$

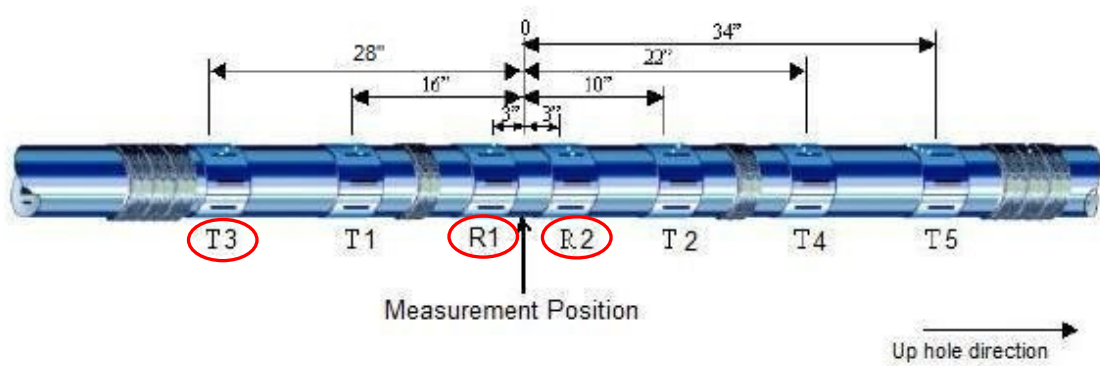


Figure 3 ARC475 from Schlumberger [6]

2.2 1-D Point-Magnetic-Dipole Model

The geometrical configuration of 1D horizontal-layered formation is depicted in Figure 4. In this model, we do not consider the presence of mandrel, and the transmitter is treated as an infinitesimally small magnetic dipole, i.e., point magnetic dipole. In this model, two orthogonal coils are set to be transmitters, one with magnetic moment pointed in vertical z-direction and the other in horizontal x-direction. To simulate tool response in this model, we need to calculate the magnetic fields produced by a z-directed magnetic dipole and an x-directed magnetic dipole.

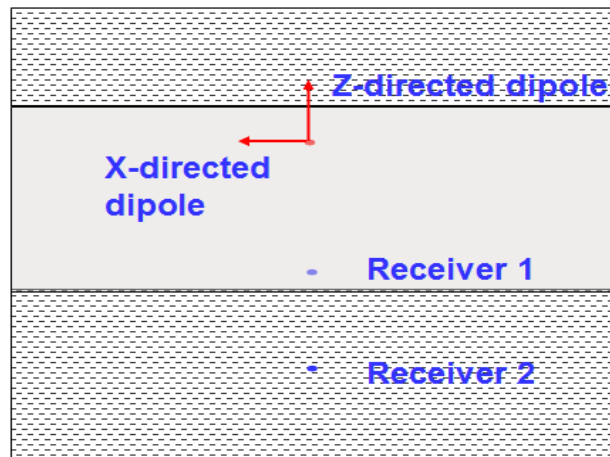


Figure 4 Profile of the 1-D point-magnetic dipole model

Note the receivers are also treated as point-magnetic-dipole and can be either z- or x-directed.

Assuming the harmonic time dependence to be $e^{-j\omega t}$, Maxwell's equations for the electric and magnetic fields are

$$\nabla \times \underline{\mathbf{H}} = -j\omega \underline{\mathbf{D}} + \underline{\mathbf{J}}, \quad (1a)$$

$$\nabla \times \underline{\mathbf{E}} = j\omega \underline{\mathbf{B}}. \quad (1b)$$

Assume no anisotropy in magnetic properties, then we can get

$$\underline{\mathbf{B}} = \mu \underline{\mathbf{H}} + \mu \underline{\mathbf{M}}_s, \quad (2a)$$

$$\underline{\mathbf{J}} = \hat{\sigma} \underline{\mathbf{E}} + \underline{\mathbf{J}}_s, \quad (2b)$$

and

$$\underline{\mathbf{D}} = \hat{\epsilon} \underline{\mathbf{E}}, \quad (2c)$$

where $\underline{\mathbf{M}}_s$ represents the dipole-source distribution and $\underline{\mathbf{J}}_s$ is the source distribution of current.

Placing equations (2) into equations (1), we can get

$$\nabla \times \underline{\mathbf{H}} = (\hat{\sigma} - j\omega \hat{\epsilon}) \underline{\mathbf{E}} + \underline{\mathbf{J}}_s, \quad (3a)$$

$$\nabla \times \underline{\mathbf{E}} = j\omega \mu \underline{\mathbf{H}} + j\omega \mu \underline{\mathbf{M}}_s. \quad (3b)$$

Define a complex conductivity tensor $\hat{\sigma}'$ as follows

$$\hat{\sigma}' = \begin{bmatrix} \sigma'_h & 0 & 0 \\ 0 & \sigma'_h & 0 \\ 0 & 0 & \sigma'_v \end{bmatrix} = \begin{bmatrix} \sigma_h - j\omega \epsilon_h & 0 & 0 \\ 0 & \sigma_h - j\omega \epsilon_h & 0 \\ 0 & 0 & \sigma_v - j\omega \epsilon_v \end{bmatrix}, \quad (4)$$

then equation (3a) will become

$$\nabla \times \underline{\mathbf{H}} = \hat{\sigma}' \underline{\mathbf{E}} + \underline{\mathbf{J}}_s. \quad (5)$$

For LWD propagation tools, we set $\underline{J}_s = 0$. From equation (5), we can get

$$\nabla \bullet \hat{\sigma}' \underline{E} = 0. \quad (6)$$

This allows to introduce the hertz vector $\underline{\Pi}$ and a scalar potential Φ [6], such that

$$\hat{\sigma}' \underline{E} = j\omega\mu\sigma_h \nabla \times \underline{\Pi}, \quad (7)$$

$$\underline{H} = j\omega\mu\sigma_h \underline{\Pi} + \nabla\Phi. \quad (8)$$

Adopting a gauge condition

$$\nabla \bullet (\hat{\sigma}' \bullet \underline{\Pi}) = \sigma'_v \Phi, \quad (9)$$

we will have

$$\underline{E} = j\omega\mu\sigma_h \hat{\sigma}'^{-1} \bullet \nabla \times \underline{\Pi}, \quad (10)$$

$$\underline{H} = j\omega\mu\sigma_h \underline{\Pi} + \nabla \left(\frac{\nabla \bullet (\hat{\sigma}' \bullet \underline{\Pi})}{\sigma'_v} \right). \quad (11)$$

Substituting equation (10), (11) into equation (3b), we obtain

$$\nabla_\lambda^2 \Pi_x + k_v^2 \Pi_x = -\frac{1}{\lambda^2} M_x \quad (12)$$

$$\nabla_\lambda^2 \Pi_y + k_v^2 \Pi_y = -\frac{1}{\lambda^2} M_y \quad (13)$$

$$\nabla_\lambda^2 \Pi_z + k_h^2 \Pi_z = -M_z + (1 - \lambda^2) \frac{\partial}{\partial z} \left(\frac{\partial \Pi_x}{\partial x} + \frac{\partial \Pi_y}{\partial y} \right) \quad (14)$$

where $\nabla_\lambda^2 = \left(\frac{\partial^2}{\partial x^2} + \frac{\partial^2}{\partial y^2} + \frac{1}{\lambda^2} \frac{\partial^2}{\partial z^2} \right)$, $k_h^2 = i\omega\mu\sigma'_h$, $k_v^2 = i\omega\mu\sigma'_v$ and $\lambda = \sigma'_h / \sigma'_v$.

2.2.1. Magnetic Field Response of Dipoles in Homogeneous Medium

For a z-directed magnetic dipole with moment $\underline{M}_s = (0, 0, M_z)^T$, the hertz vector is given by [5]

$$\underline{\Pi} = \Pi_z \hat{z} = \frac{M_z}{4\pi} \frac{e^{jk_h r}}{r}, \quad (15)$$

where $r = \sqrt{x^2 + y^2 + z^2}$.

For an x-directed magnetic dipole $\underline{\mathbf{M}}_s = (M_x, 0, 0)^T$, the hertz vector is given by

$$\underline{\mathbf{\Pi}} = \Pi_x \hat{x} + \Pi_z \hat{z}, \quad (16)$$

where

$$\Pi_x = \frac{M_x}{4\pi\lambda} \frac{e^{jk_v s}}{s}, \quad (17)$$

$$\Pi_z = \frac{M_x x}{4\pi\rho^2} \left(\lambda z \frac{e^{jk_v s}}{s} - \frac{e^{jk_h r}}{r} \right), \quad (18)$$

$$s = \sqrt{x^2 + y^2 + \lambda^2 z^2}, \quad (19)$$

and

$$\rho = \sqrt{x^2 + y^2}. \quad (20)$$

Placing equation (15)-(20) into (11), we can get the magnetic field response of the magnetic dipole with moment in x-directed and z-directed $\underline{\mathbf{M}}_s = (M_x, M_y, M_z)\delta(\underline{\mathbf{r}})$ in a homogeneous transverse isotropic medium as follows

$$H_{xx} = \frac{e^{jk_v s}}{4\pi} \left[\frac{k_h^2}{\lambda s} + \frac{jk_h s - k_h k_v x^2}{s\rho^2} - \frac{2jk_h x^2}{\rho^4} \right] - \frac{e^{jk_h r}}{4\pi} \left[\frac{jk_h r - k_h^2 x^2}{r\rho^2} - \frac{2jk_h x^2}{\rho^4} - \frac{jk_h}{r^2} + \frac{(k_h^2 x^2 + 1)}{r^3} + \frac{3jk_h x^2}{r^4} - \frac{3x^2}{r^5} \right], \quad (21)$$

$$H_{xz} = H_{zx} = -xz \frac{e^{jk_h r}}{4\pi r^3} \left[k_h^2 + \frac{3jk_h}{r} - \frac{3}{r^2} \right], \quad (22)$$

and

$$H_{zz} = \frac{e^{jk_h r}}{4\pi r} \left[k_h^2 + \frac{jk_h}{r} - \frac{(k_h^2 z^2 + 1)}{r^2} - \frac{3jk_h z^2}{r^3} + \frac{3z^2}{r^4} \right]. \quad (23)$$

Here H_{ij} represents i-directed component of the magnetic field due to j-directed dipole moment of the source $\underline{\mathbf{M}}_s$.

To generate conversion charts, we need first to calculate tool response in isotropic medium. Then equation (21)-(23) can be simplified to

$$H_{xx} = \frac{e^{jkr}}{4\pi} \left[\frac{k^2}{r} + \frac{jk}{r^2} - \frac{k^2 x^2 + 1}{r^3} - \frac{3jkx^2}{r^4} + \frac{3x^2}{r^5} \right], \quad (24)$$

$$H_{zx} = H_{xz} = \frac{-xz e^{jkr}}{4\pi r^3} \left[k^2 + \frac{3jk}{r} - \frac{3}{r^2} \right], \quad (25)$$

and

$$H_{zz} = \frac{e^{jkr}}{4\pi r} \left[k^2 + \frac{jk}{r} - \frac{k^2 z^2 + 1}{r^2} - \frac{3jkz^2}{r^3} + \frac{3z^2}{r^4} \right]. \quad (26)$$

These equations can be used to calculate the coupling between point-dipole transmitters and receivers in homogeneous isotropic media which is then used as conversion chart.

2.2.2. Magnetic Field Response of Dipoles in Multi-layered Media

1) z-directed magnetic dipole

For the z-directed magnetic dipole, Hertz vector is given by,

$$\underline{\Pi} = \Pi_z \hat{z}. \quad (27)$$

In the i -th layer ($z_{i-1} < z < z_i$) of the formation, the hertz vector is [6-7]

$$\Pi_{zi} = \frac{M_z}{4\pi} \int_0^\infty \left(\frac{\beta_i}{\xi_{hi}} e^{-\xi_{hi}|z-z_0|} + F_i e^{-\xi_{hi}z} + G_i e^{\xi_{hi}z} \right) \alpha J_0(\alpha r) d\alpha, \quad (28)$$

where z_i is the lower boundary of the i -th layer,

$J_n(x)$ is the n -th order Bessel function,

$$\xi_{hi} = (\alpha^2 - k_{hi}^2)^{1/2} \quad (29)$$

$$k_{hi} = (i\omega\mu\sigma'_{hi})^{1/2} \quad (30)$$

and

$$\beta_i = \begin{cases} 0, & \text{if } M_z \text{ is not in the } i\text{-th layer} \\ 1, & \text{if } M_z \text{ is in the } i\text{-th layer} \end{cases}. \quad (31)$$

Substituting equation (28) into (11), we can get the magnetic field as follows

$$H_{zzi} = \frac{M_z}{4\pi} \int_0^\infty \left(\frac{\beta_i}{\xi_{hi}} e^{-\xi_{hi}|z-z_0|} + F_i e^{-\xi_{hi}z} + G_i e^{\xi_{hi}z} \right) \alpha^3 J_0(\alpha\rho) d\alpha, \quad (32)$$

$$H_{xzi} = \frac{M_z}{4\pi} \int_0^\infty \xi_{hi} \left(\frac{\beta_i}{\xi_{hi}} \frac{|z-z_0|}{z-z_0} e^{-\xi_{hi}|z-z_0|} + F_i e^{-\xi_{hi}z} - G_i e^{\xi_{hi}z} \right) \alpha^2 \cos\phi J_1(\alpha\rho) d\alpha, \quad (33)$$

$$H_{yzi} = \frac{M_z}{4\pi} \int_0^\infty \xi_{hi} \left(\frac{\beta_i}{\xi_{hi}} \frac{|z-z_0|}{z-z_0} e^{-\xi_{hi}|z-z_0|} + F_i e^{-\xi_{hi}z} - G_i e^{\xi_{hi}z} \right) \alpha^2 \sin\phi J_1(\alpha\rho) d\alpha. \quad (34)$$

To obtain reflection and transmission coefficients F_i and G_i , we need to enforce boundary conditions. From the continuity of electromagnetic fields at horizontal boundary $z = z_i$, the boundary conditions of hertz vector are

$$\frac{\partial \Pi_{zi}}{\partial z} = \frac{\partial \Pi_{z(i+1)}}{\partial z}, \quad (35)$$

$$\mu_i \Pi_{zi} = \mu_{i+1} \Pi_{z(i+1)}. \quad (36)$$

The numerical scheme developed to solve F_i and G_i can be found in Ref. [8].

2) x-directed magnetic dipole

For the x-directed magnetic dipole, hertz vector is given by

$$\underline{\Pi} = \Pi_x \hat{x} + \Pi_z \hat{z}. \quad (37)$$

In the i -th layer ($z_{i-1} < z < z_i$) of the formation, the hertz vector is

$$\Pi_{xi} = \frac{M_x}{4\pi\lambda_i} \int_0^\infty \left(\frac{\beta_i}{\xi_{vi}} e^{-\xi_{vi}|z-z_0|} + P_i e^{-\xi_{vi}\lambda_i z} + Q_i e^{\xi_{vi}\lambda_i z} \right) \alpha J_0(\alpha\rho) d\alpha, \quad (38)$$

and

$$\begin{aligned} \Pi_{zi} = & \frac{M_x}{4\pi} \int_0^\infty \left(S_i e^{-\xi_{hi}\lambda_i z} + T_i e^{\xi_{hi}\lambda_i z} - \xi_{vi} P_i e^{-\xi_{vi}\lambda_i z} + \xi_{vi} Q_i e^{\xi_{vi}\lambda_i z} \right) \cos\phi J_1(\alpha\rho) d\alpha + \\ & \frac{M_x}{4\pi} \int_0^\infty \beta_i \left(e^{-\xi_{hi}|z-z_0|} - e^{-\xi_{vi}\lambda_i|z-z_0|} \right) \cos\phi \frac{|z-z_0|}{z-z_0} J_1(\alpha\rho) d\alpha. \end{aligned} \quad (39)$$

Substituting equations (38)-(39) into (11), we can get the magnetic field as follows

$$H_{xxi} = \frac{M_x}{4\pi} \int_0^\infty \left(\begin{array}{l} \frac{\beta_i \sin^2 \phi}{\lambda_i \xi_{vi}} k_{hi}^2 e^{-\xi_{vi} \lambda_i |z-z_0|} - \beta_i \cos^2 \phi \xi_{hi} e^{-\xi_{hi} |z-z_0|} \\ + \frac{P_i}{\lambda_i} \sin^2 \phi k_{hi}^2 e^{-\xi_{vi} \lambda_i z} + \frac{Q_i}{\lambda_i} \sin^2 \phi k_{hi}^2 e^{\xi_{vi} \lambda_i z} \\ - S_i \cos^2 \phi \xi_{hi} e^{-\xi_{hi} z} + T_i \cos^2 \phi \xi_{hi} e^{\xi_{hi} z} \end{array} \right) \alpha J_0(\alpha \rho) d\alpha$$

$$+ \frac{M_x}{4\pi \rho} \cos 2\phi \int_0^\infty \left(\begin{array}{l} \lambda_i \frac{\beta_i}{\xi_{vi}} k_{vi}^2 e^{-\xi_{vi} \lambda_i |z-z_0|} + \beta_i \xi_{hi} e^{-\xi_{hi} |z-z_0|} \\ + P_i \lambda_i k_{vi}^2 e^{-\xi_{vi} \lambda_i z} + Q_i \lambda_i k_{vi}^2 e^{\xi_{vi} \lambda_i z} \\ + S_i \xi_{hi} e^{-\xi_{hi} z} - T_i \xi_{hi} e^{\xi_{hi} z} \end{array} \right) J_1(\alpha \rho) d\alpha, \quad (40)$$

$$H_{yyi} = \frac{M_x}{4\pi} \sin \phi \cos \phi \int_0^\infty \left(\begin{array}{l} -\frac{\beta_i}{\lambda_i \xi_{vi}} k_{hi}^2 e^{-\xi_{vi} \lambda_i |z-z_0|} - \beta_i \xi_{hi} e^{-\xi_{hi} |z-z_0|} \\ -\frac{P_i}{\lambda_i} k_{hi}^2 e^{-\xi_{vi} \lambda_i z} - \frac{Q_i}{\lambda_i} k_{hi}^2 e^{\xi_{vi} \lambda_i z} \\ -S_i \xi_{hi} e^{-\xi_{hi} z} + T_i \xi_{hi} e^{\xi_{hi} z} \end{array} \right) \alpha J_0(\alpha \rho) d\alpha$$

$$+ \frac{M_x}{4\pi \rho} \sin 2\phi \int_0^\infty \left(\begin{array}{l} \lambda_i \frac{\beta_i}{\xi_{vi}} k_{vi}^2 e^{-\xi_{vi} \lambda_i |z-z_0|} + \beta_i \xi_{hi} e^{-\xi_{hi} |z-z_0|} \\ + P_i \lambda_i k_{vi}^2 e^{-\xi_{vi} \lambda_i z} + Q_i \lambda_i k_{vi}^2 e^{\xi_{vi} \lambda_i z} \\ + S_i \xi_{hi} e^{-\xi_{hi} z} - T_i \xi_{hi} e^{\xi_{hi} z} \end{array} \right) J_1(\alpha \rho) d\alpha, \quad (41)$$

$$H_{zxi} = \frac{M_x}{4\pi} \cos \phi \int_0^\infty \left(\beta_i \frac{|z-z_0|}{z-z_0} e^{-\xi_{hi} |z-z_0|} + S_i e^{-\xi_{hi} z} + T_i e^{\xi_{hi} z} \right) \alpha^2 J_1(\alpha \rho) d\alpha, \quad (42)$$

where

$$\lambda_i = \frac{k_{hi}}{k_{vi}}, \quad (43)$$

$$\xi_{vi} = (\alpha^2 - k_{vi}^2)^{1/2}, \quad (44)$$

$$k_{vi} = (i\omega\mu\sigma'_{vi})^{1/2}, \quad (45)$$

$$\beta_i = \begin{cases} 0, & \text{if } M_x \text{ is not in the } i\text{-th layer} \\ 1, & \text{if } M_x \text{ is in the } i\text{-th layer} \end{cases}. \quad (46)$$

The coefficients P_i , Q_i , S_i and T_i can be calculated by matching the boundary conditions. From the continuity of electromagnetic fields at horizontal boundary $z = z_i$, the boundary conditions of hertz vector are

$$\mu_i \frac{\partial \Pi_{xi}}{\partial z} = \mu_{i+1} \frac{\partial \Pi_{x(i+1)}}{\partial z} \quad (47)$$

$$\mu_i \Pi_{zi} = \mu_{i+1} \Pi_{z(i+1)} \quad (48)$$

$$\lambda_i^2 \frac{\partial^2 \Pi_{xi}}{\partial x^2} + \frac{\partial^2 \Pi_{zi}}{\partial x \partial z} = \lambda_{i+1}^2 \frac{\partial^2 \Pi_{x(i+1)}}{\partial x^2} + \frac{\partial^2 \Pi_{z(i+1)}}{\partial x \partial z} \quad (49)$$

$$k_{hi}^2 \Pi_{xi} = k_{h(i+1)}^2 \Pi_{x(i+1)} \quad (50)$$

The numerical scheme developed to solve P_i , Q_i , S_i and T_i can be found in Ref. [15].

We derived all the tool response in previous two parts with tool axes lining up with the coordinates of formation beddings. However, in reality the tool axis can be arbitrary direction with respect to the coordinate of formation. A rotation matrix is implemented to do the transformation [16]. Explicitly, we first convert dipole moments given in tool coordinates into formation coordinates by using rotation matrix R. That is

$$\underline{\mathbf{M}} = R \underline{\mathbf{M}}', \quad (51)$$

Then we do an inverse transformation when we get the magnetic field $\underline{\mathbf{H}}$ in the formation coordinates. So the final response in tool coordinates will be

$$\underline{\mathbf{H}}' = R^{-1} \underline{\mathbf{H}}. \quad (52)$$

2.3 1-D Model of Finite-size Antennas with Mandrel

The geometrical configuration of the model with finite size antenna outside a mandrel is shown in Figure 5. The radii of the transmitter and receivers are b. The outer boundary

of the m -th region is denoted r_m ; and ϵ_m , σ_m and μ_m represent respectively the dielectric constant, the conductivity and the magnetic permeability.

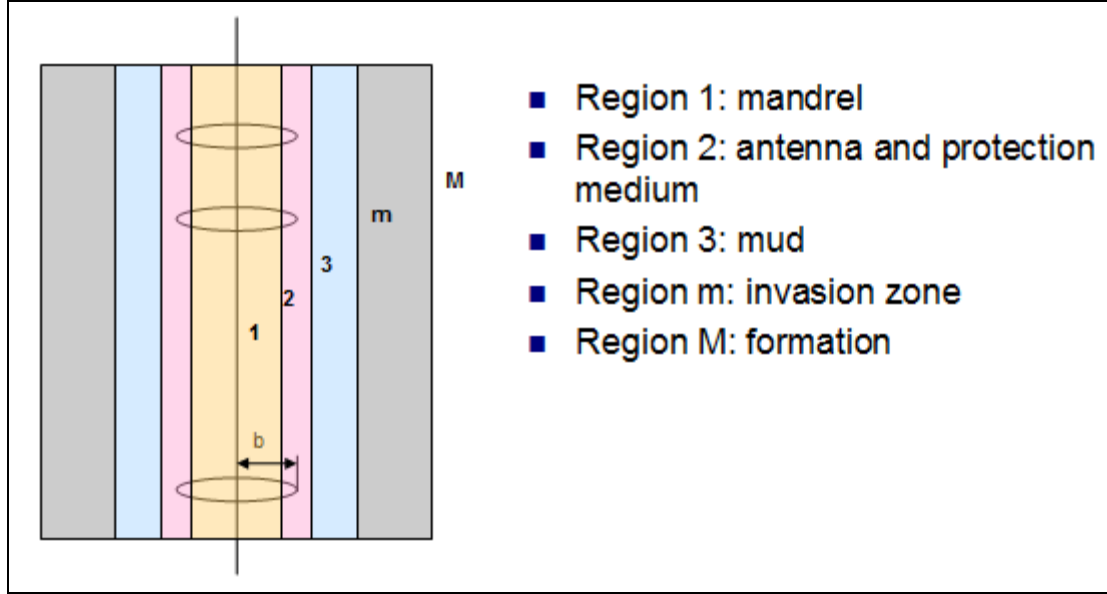


Figure 5 Profile of 1-D radial-layered media

Assuming azimuthally symmetry, the electric field E_ϕ in region 2 can be expressed as following [11]:

$$E_{\phi 2} = E_s - \frac{\omega\mu_2 I b}{2} \int_0^\infty dk \cos(kz) [W_1 + W_2] \quad (53)$$

where

$$W_1 = \frac{1}{D} [q_1 p_{22} e^{-j\lambda_2(2b-2r_1)} - q_2 p_{12} e^{-j\lambda_2(2r_2-2r_1)}] h_1^{(2)}(\lambda_2 b) \quad (54)$$

$$W_2 = \frac{1}{D} [q_2 p_{11} e^{-j\lambda_2(-2b+2r_2)} - q_1 p_{21} e^{-j\lambda_2(2r_2-2r_1)}] h_1^{(1)}(\lambda_2 b) \quad (55)$$

$$D = p_{22} p_{11} - p_{12} p_{21} e^{-j\lambda_2(2r_2-2r_1)} \quad (56)$$

$$p_{11} = \frac{\lambda_2}{\mu_2} h_0^{(2)}(\lambda_2 r_1) - \frac{\lambda_1}{\mu_1} g_1 h_1^{(2)}(\lambda_2 r_1) \quad (57)$$

$$p_{12} = \frac{\lambda_2}{\mu_2} h_0^{(1)}(\lambda_2 r_1) - \frac{\lambda_1}{\mu_1} g_1 h_1^{(1)}(\lambda_2 r_1) \quad (58)$$

$$p_{21} = \frac{\lambda_2}{\mu_2} h_0^{(2)}(\lambda_2 r_2) - \frac{\lambda_3}{\mu_3} G_3 h_1^{(2)}(\lambda_2 r_2) \quad (59)$$

$$p_{22} = \frac{\lambda_2}{\mu_2} h_0^{(1)}(\lambda_2 r_2) - \frac{\lambda_3}{\mu_3} G_3 h_1^{(1)}(\lambda_2 r_2) \quad (60)$$

$$q_1 = -\left[\frac{\lambda_2}{\mu_2} j_0(\lambda_2 r_1) - \frac{\lambda_1}{\mu_1} g_1 j_1(\lambda_2 r_1) \right] h_1^2(\lambda_2 b) \quad (61)$$

$$q_2 = -p_{21} j_1(\lambda_2 b) \quad (62)$$

$$g_1 = \frac{j_0(\lambda_1 r_1)}{j_1(\lambda_1 r_1)}, \quad (63)$$

and E_s is the electric field due to the source in a homogeneous medium characterized by the medium 2 parameters. It can be expressed as follow:

$$E_s = \frac{-j\omega\mu_2 I b}{4\pi} \int_{-\pi}^{\pi} d\phi \cos\phi \frac{e^{-jk_2 R}}{R}, \quad (64)$$

where

$$R = (z^2 + 2b^2 - 2b^2 \cos\phi)^{\frac{1}{2}} \quad (65)$$

$$G_3 = \frac{h_0^{(2)}(\lambda_3 r_2)}{h_1^{(2)}(\lambda_3 r_2)}. \quad (66)$$

The voltage induced at the receiving coil is equal to $2\pi b E_{\phi 2}$.

When we build converting chart in this 1D cylindrical layered medium, we set the conductivity to be infinity in region 1 (collar) which is characterized by perfect conductor parameters. For normal steel collar/mandrel, this is an excellent approximation at MHz frequency. The conductivities of other regions are all set to be the same as formation.

2.4 2-D and 3-D Model

Z-directed coils in horizontal layers. Figure 6 shows a model which can have layers both in vertical direction and in radial direction. The tool is positioned at the center of the borehole and the transmitter and receiver coils are all z-directed. Due to axis-symmetry, this is a 2-D model. In this thesis, this 2-D model will be studied both with MWD2D99 code inside Wellog Inversion Package and with RF Module of a commercial multiphysics modeling package called COMSOL (from now on referred to as COMSOL).

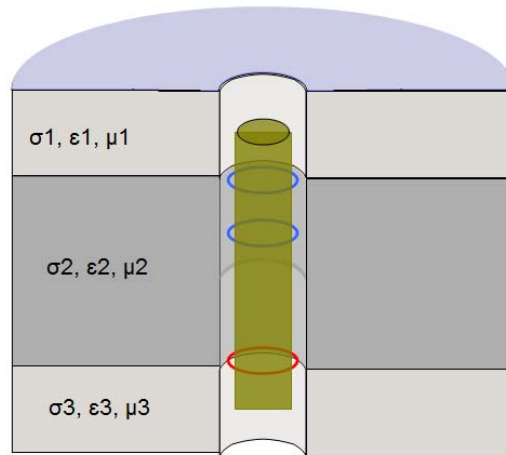


Figure 6 Schematic of 2-D model

Figure 7 shows the 2-D axis-symmetric model setup in COMSOL. A large rectangular domain is selected so the boundary is far away from the tool which is put in the center of the domain. The metallic mandrel is shown as a narrow black box in the middle and the locations of the transmitter and receivers are indicated as well. Finite size transmitter and receiver loop antenna are represented by a point in the r-z plan due to axis-symmetry. A line source ($I = 1A$) was assigned to “T” point serving as transmitter. Complex voltages were calculated on the two receivers to obtain amplitude ratio and phase difference. At $r=0$ axis, axis-symmetry condition was added. Radial depth of the surrounding formation was set to be slightly more than 5 times the skin-depth which ensures the signal decays sufficiently small at the boundary. Scattering boundary condition was set to the outer

boundary. Alternatively the impedance boundary condition can be applied at the edge of the overall domain to reduce the size to simulation domain [12].

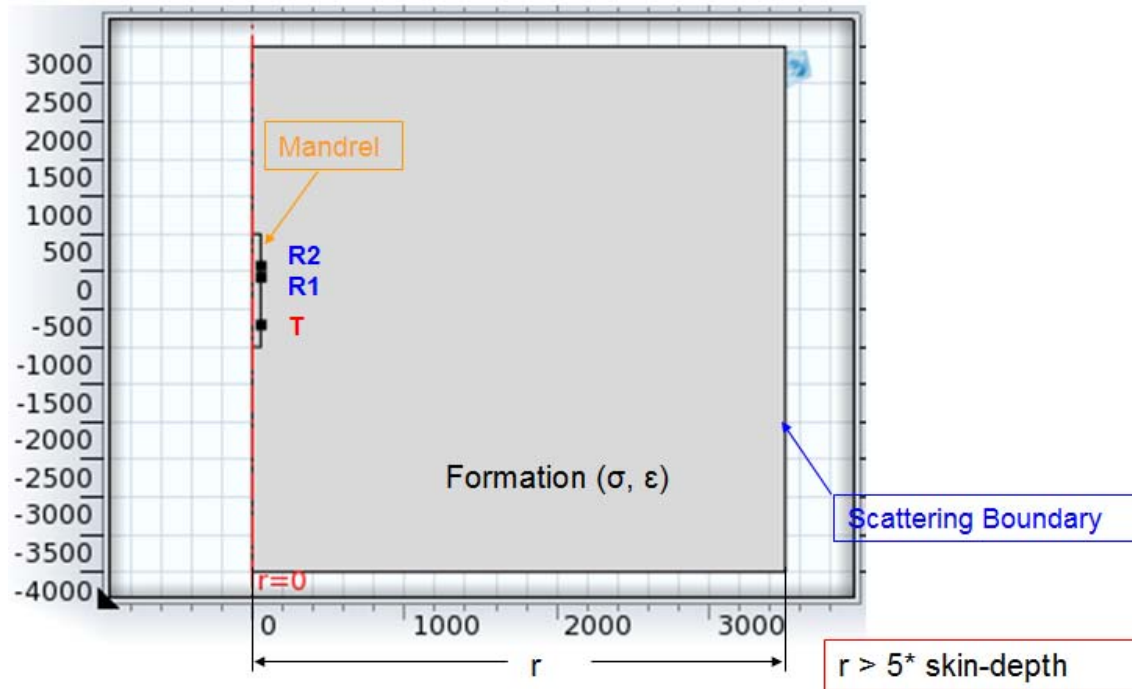


Figure 7 Geometry of 2-D axis-symmetric model in COMSOL.

Finite size z-directed coils with mandrel in dipping beds. For cases like finite size antennas with mandrel in dipping layered beds, they are not axis-symmetrical any more. They are genuinely 3-D models as shown in Figure 8. In this report, calculations on these 3-D models will be conducted in COMSOL. Figure 9 shows an example of model geometry of the z-directed coil with mandrel in homogeneous medium. Again the outer box represents the surrounding formation. The cylinder represents metallic mandrel. Three circles represent transmitter and receiver coils. An edge current is used to excite the transmitter. For ease of simulation, the transmitter and receiver are modeled as finite size loop with an infinitesimal thin wire. In actual tools, multiple windings are typically

used. But we believe that this simplification will not affect the simulation results and is not a serious deficiency.

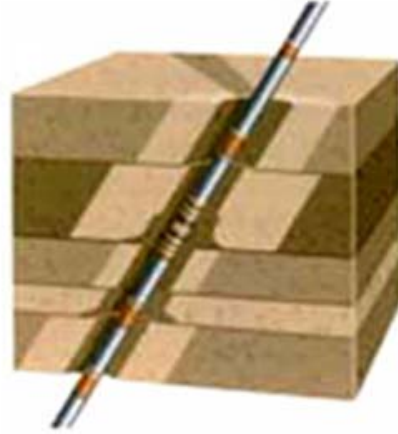


Figure 8 Schematic of 3-D model

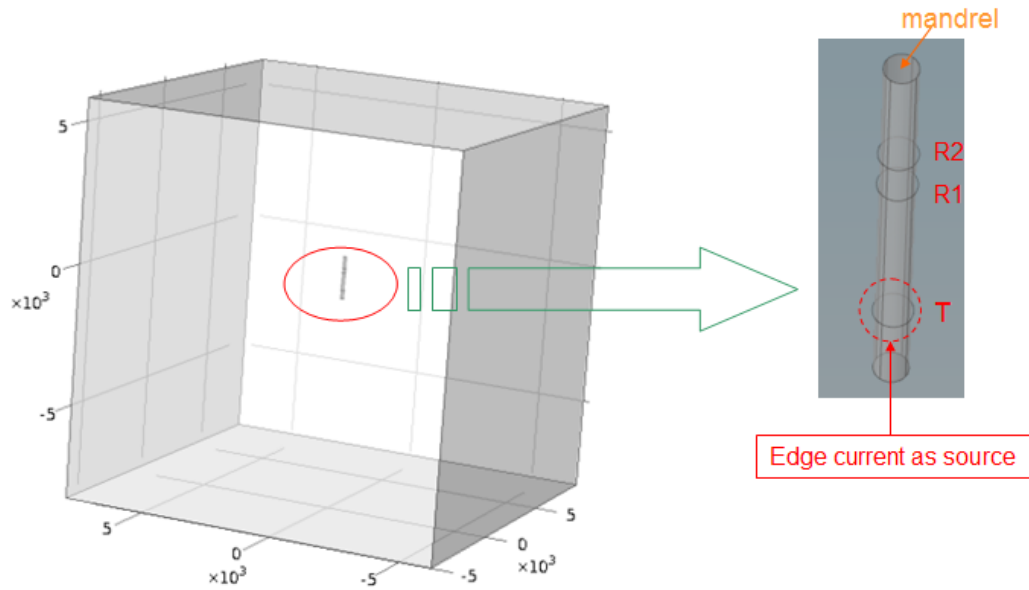


Figure 9 Z-directed coil model in COMSOL

X-directed Antenna. For x-directed antennas, we can not use 2-D axis-symmetric model any more even in vertical wells. All x-directed antennas with mandrel are modeled in 3-D with COMSOL. X-directed coils are modeled as saddle coil as shown in Figure 10. A saddle coil has two straight wires and two semi-circular loops. The two straight wires

are parallel to the tool axis. The semi-circular loops with a radius of 3.5” are concentric to the collar.

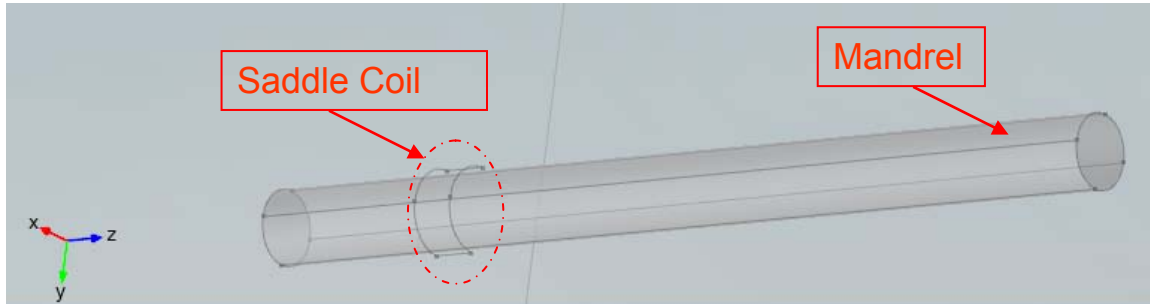


Figure 10 Saddle coil as x-directed dipole

Typically a pair of saddle coils is connected to form the actual saddle coil which will generate a more symmetric field and in turn reduce the potential excitation of unwanted mode in borehole.

In constructing the models, we need to be aware that the size of the geometry could be very large in less conductive formation. Therefore, finer meshes should be adopted to ensure the convergences in less conductive formation.

3. Results and Analysis

The main goal of the project is to compare responses between point-dipole model and finite-loop-with-mandrel model to determine when a point-dipole model no longer is sufficient to interpret LWD propagation resistivity tool. This section will show all the 1-D, 2-D and 3-D calculations for z-directed and x-directed coils of both point-dipole model and model with mandrel in various types of media such as laminated isotropic beddings and anisotropic dipping beds.

3.1 Results of Z-directed coils

1) In homogeneous isotropic medium

Figure 11 shows one example of electric field distribution from a z-directed loop dipole of LWD propagation resistivity tool operating at 2MHz in homogeneous isotropic

medium (0.1 S/m conductivity), produced by an axis-symmetrical 2-D model using COMSOL. The mesh is chosen sufficiently fine so the field is smooth. This is evident from the figure and the observation that even though the simulation space is rectangular, the dipole field is well represented even close to the boundary. This is also an ideal case where the skin depth is such that the field has been attenuated many orders of magnitude at the boundary.

We have simulated LWD tool with TR spacing 28-in. and RR spacing of 6-in. in homogeneous isotropic formation with the conductivity varying from 0.005 to 5 S/m. The characteristic plots (referred to as Conversion Chart) of attenuation and phase-shift versus formation resistivity are shown in Figure 12 and Figure 13, respectively. The absolute differences between different charts are shown in Figure 14. Note the Schlumberger dielectric assumption is used in all simulations. From the charts, we can see that the results from the analytical code and those from COMSOL 2-D and 3-D models agree very well. It is gratify to see such excellent agreement between COMSOL results and results form analytical code. We also notice that the presence of mandrel produces a significant ($\sim 0.5\text{db}$) downward shift in attenuation but has very little effect on phase-difference. This is consistent with the conclusion from an earlier study [2]. This difference in attenuation would not necessarily make the dipole-model unusable for interpretation. It only means we cannot use the same conversion chart between different models. In other words, each model has to use its own conversion chart. The more important question is whether the apparent resistivity would behave differently once the appropriate conversion chart is used. In the following sections, we will use the conversion charts shown in Figure 12-13 to convert amplitude ratio and phase difference in layered media to attenuation resistivity (R_a) and phase-shift resistivity (R_p), respectively.

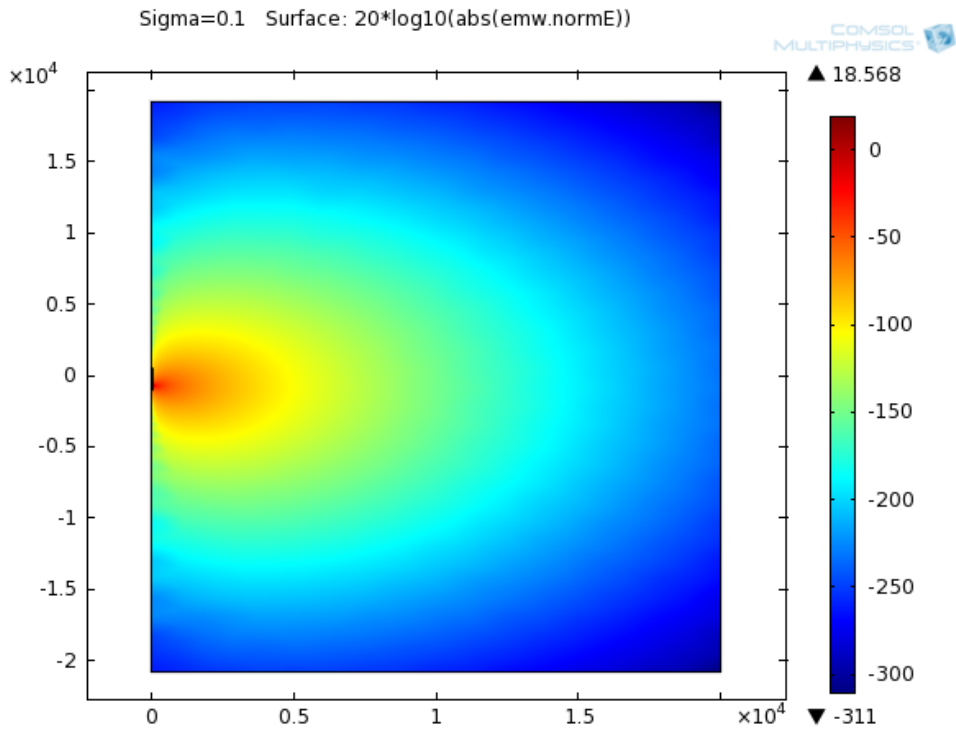


Figure 11 E field distributions in homogeneous medium. The r and z units are in millimeters.

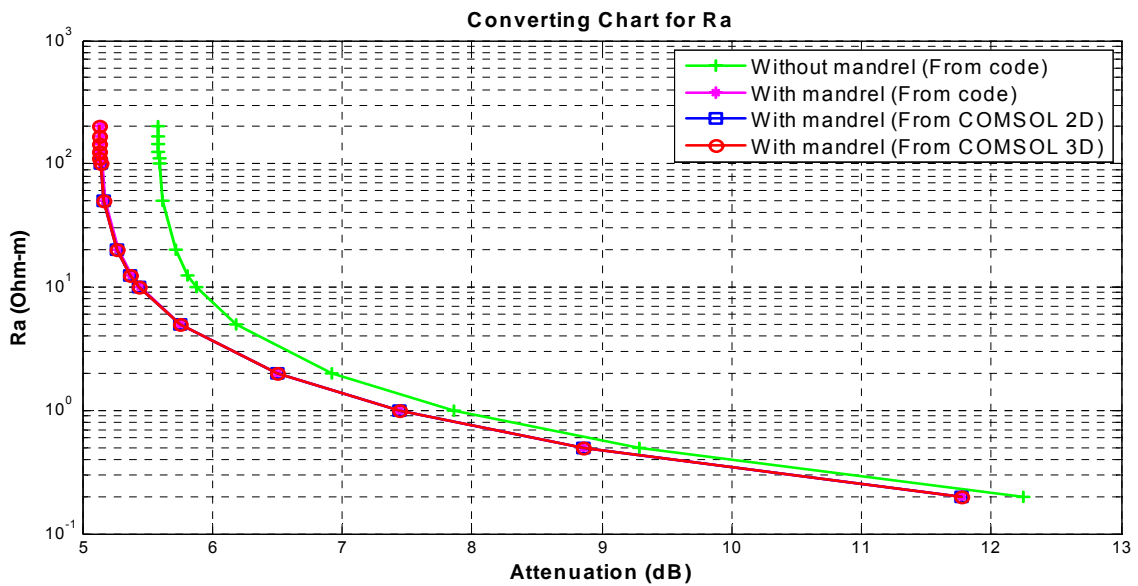


Figure 12 Conversion chart for Ra

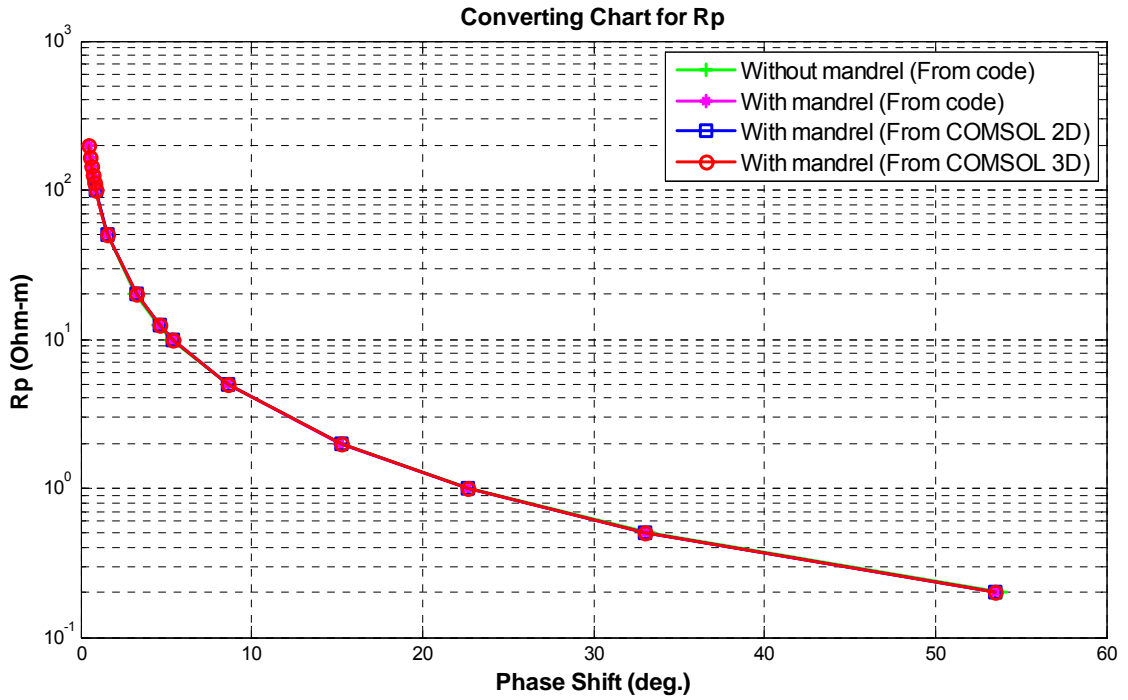


Figure 13 Conversion chart for Rp

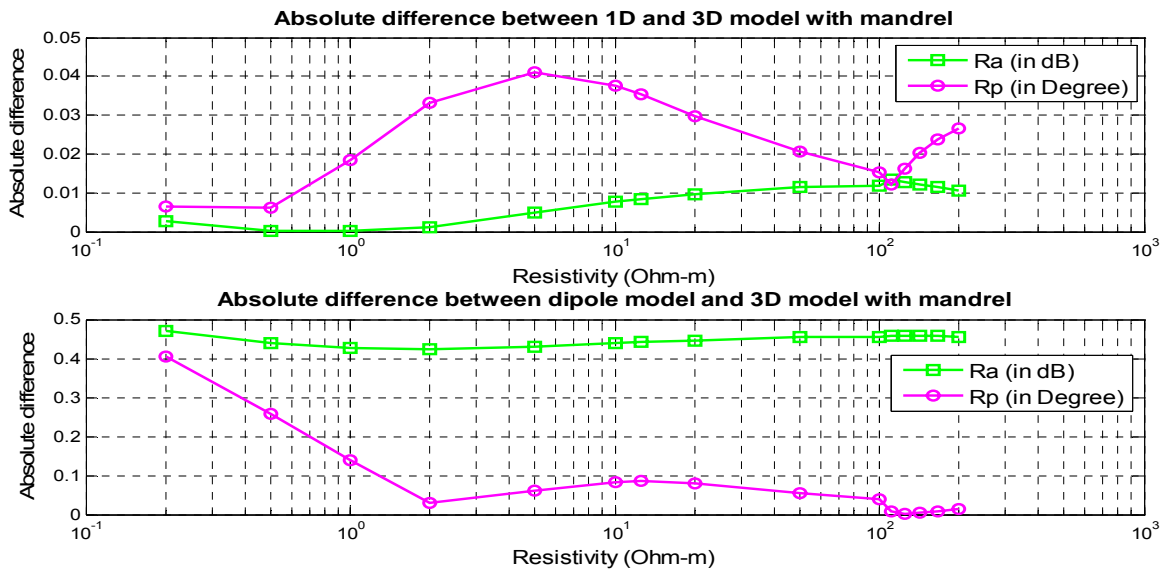


Figure 14 Absolute differences between charts

2) In isotropic layered dipping beds

Dipole model response in isotropic layered dipping beds can be obtained from 1D simulation code from the WLL Inversion Package. The study of the response of the tool with finite size antenna with mandrel requires 3D codes and COMSOL modeling package is used. Figure 15 indicates the profile of the formation. The tool responses are shown in Figure 16 and Figure 17 for dip = 60 deg. The depths shown in figures are measured depth (MD). The bed boundary is at zero MD. We can see that mandrel effect only affects Ra and Rp readings near the bed boundary.

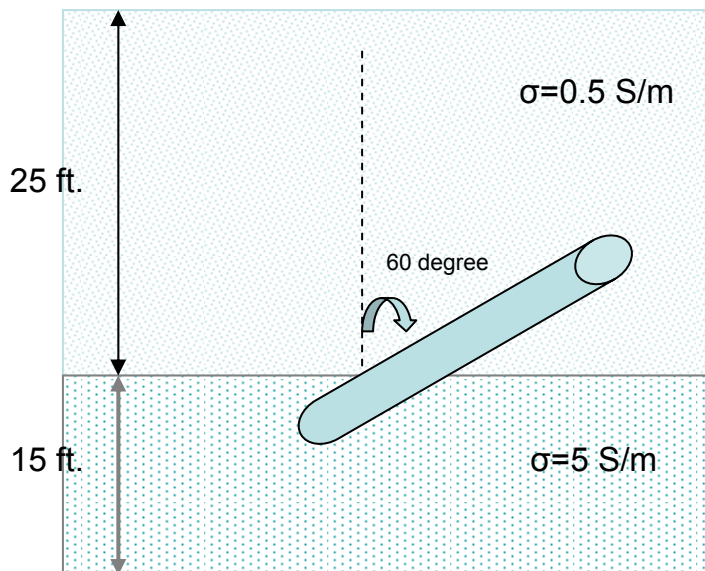


Figure 15 Profile of a 2-layer isotropic media

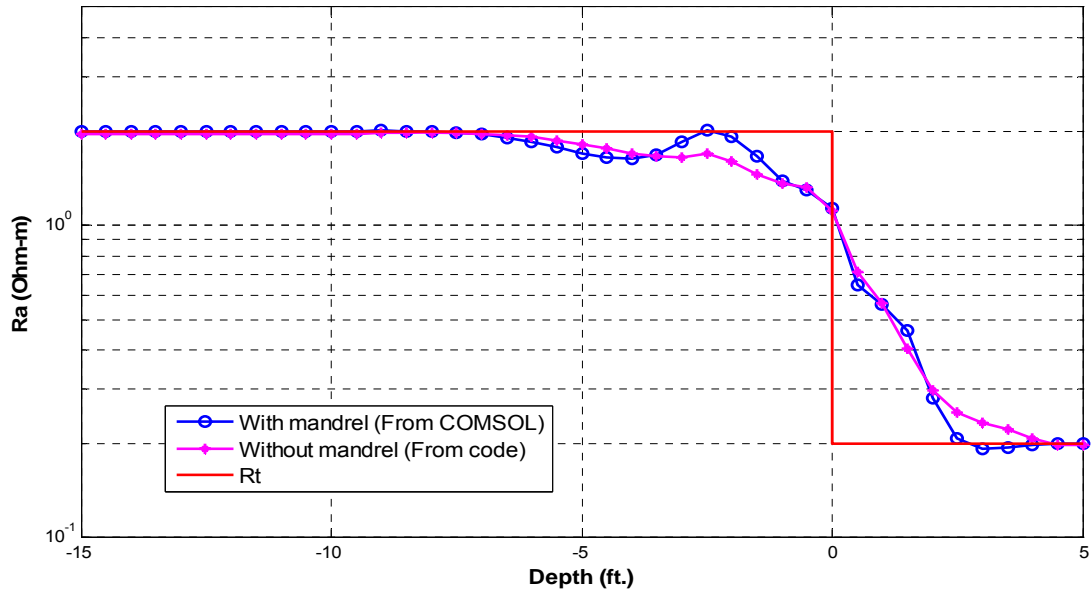


Figure 16 Ra from dipole model and mandrel model

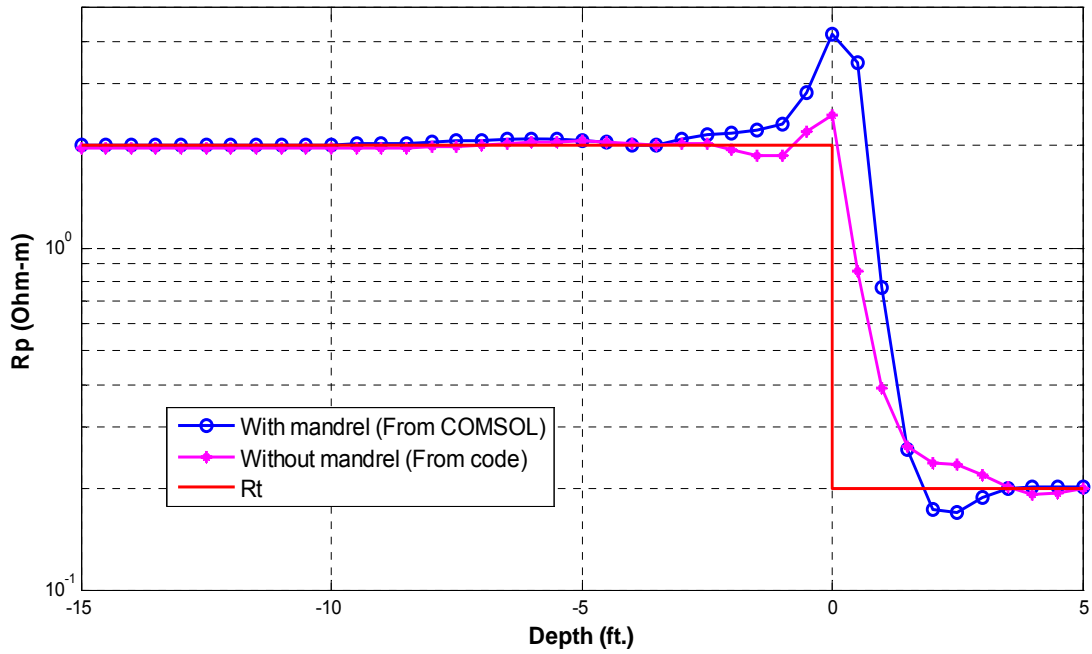


Figure 17 Rp from dipole model and mandrel model

3) In anisotropic layered dipping beds

In dipping beds, the effect of anisotropy can be detected by z-directed coils. Early study [13] showed that LWD resistivity measurements from z-directed coils have higher sensitivity to anisotropy at higher dipping angles. This project studied anisotropic cases with dipping angle at 60 degrees and 80 degrees.

Figure 18 is the profile of the first example of the anisotropy cases. The dipping angle is 60 degree. For both layers, the conductivity of horizontal direction is 1 S/m. The anisotropy ratio R_v / R_h for the upper layer and lower layer is chosen to be 10 and 2, respectively, so that we can analyze the mandrel effect in R_a and R_p readings contributed by anisotropy. The R_a and R_p logs are shown in Figure 19 and 20, respectively.

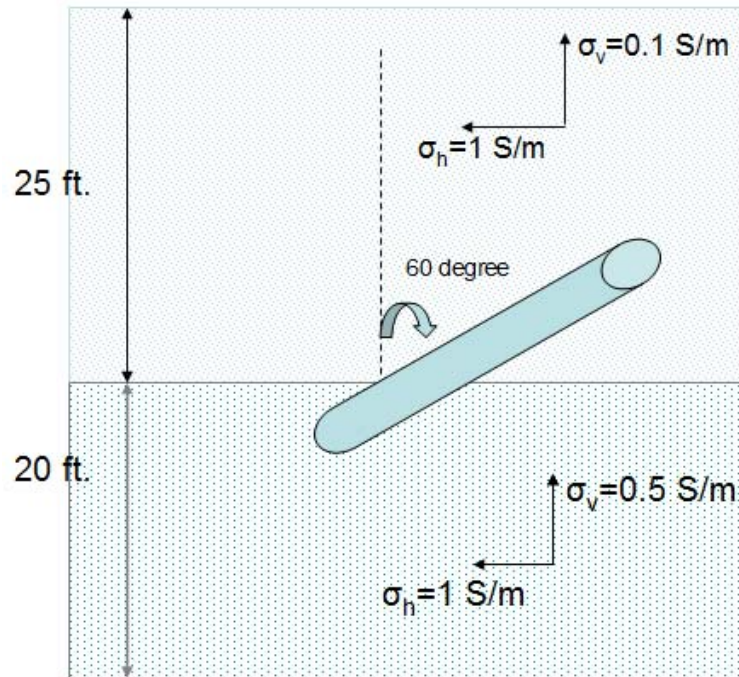


Figure 18 Profile of a 2-layer anisotropic formation

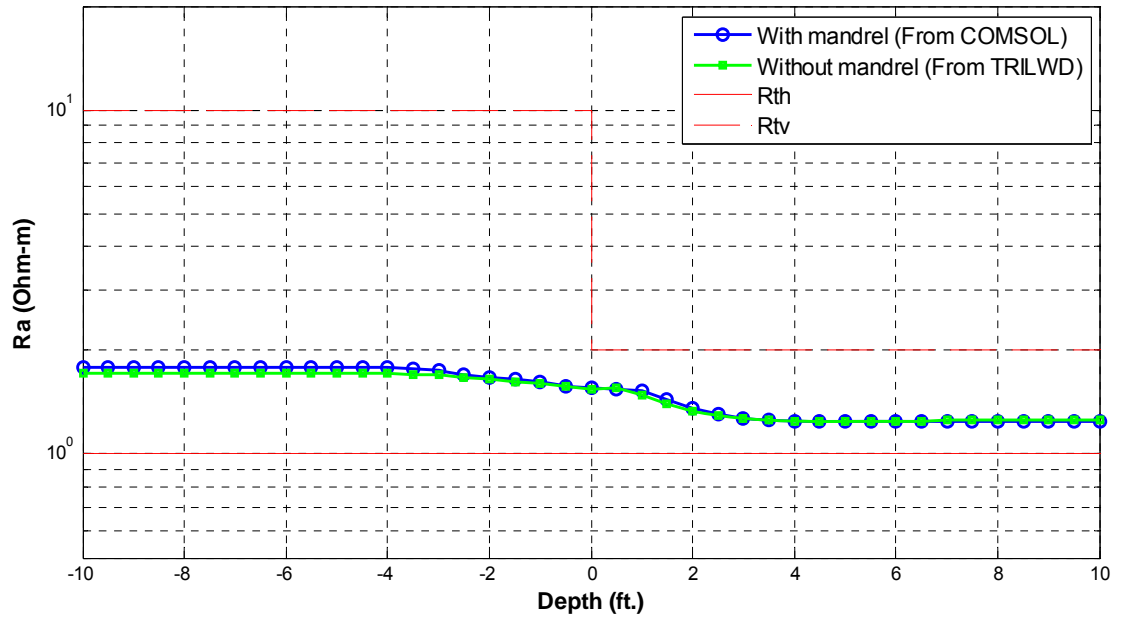


Figure 19 R_a of the dipole model and the mandrel model

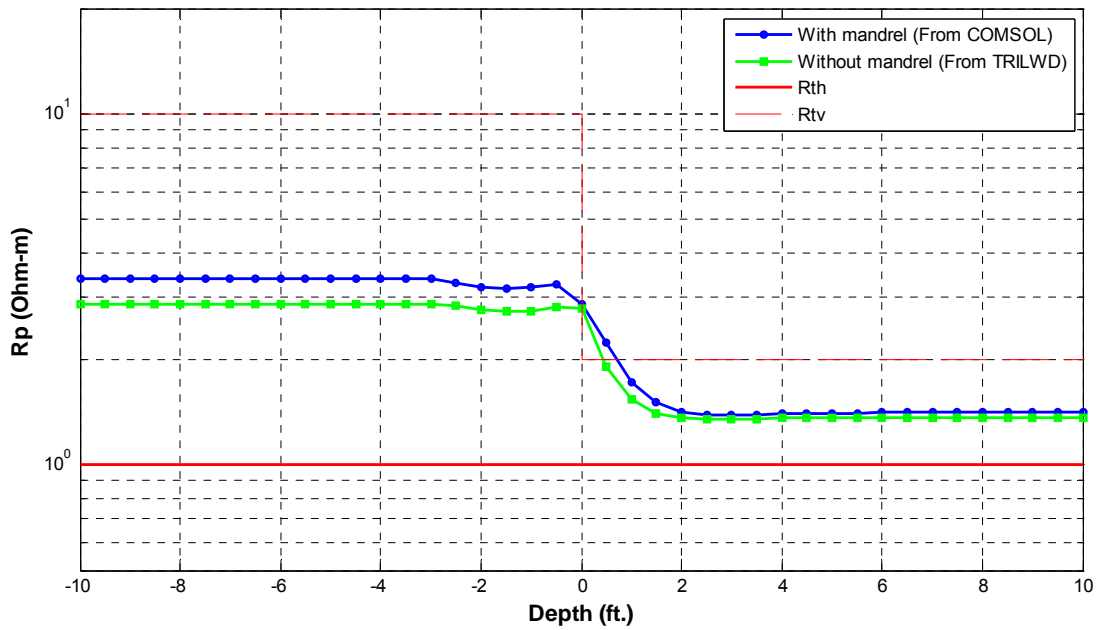
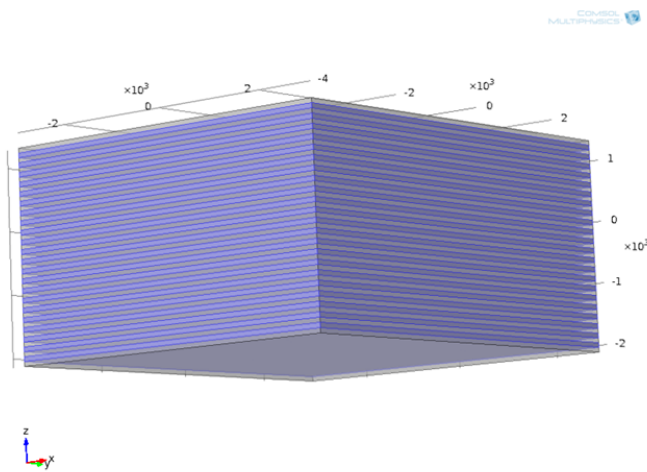


Figure 20 R_p of the dipole model and the mandrel model

We can observe that Ra and Rp readings differ between dipole model and model with mandrel even in the bed far away from the boundary, especially in the formation with higher anisotropy ratio. To verify the anisotropy implementation in COMSOL, we built a laminated formation which is equivalent to the upper layer in this example. The model of the laminated formation is shown in Figure 21. We investigated the tool response at six logging points. The results are rendered in Figure 22 and Figure 23. We can see that the results from the equivalent lamination model confirmed our simulation in anisotropic model.



Shale- sand: 50%-50%

R_sand: 19.4932 Ohm-m

R_shale: 0.5132 Ohm-m

Bed thickness: 3 inches

Equivalent:

Rh=1 ohm-m

Rv=10 ohm-m

Figure 21 Equivalent lamination model

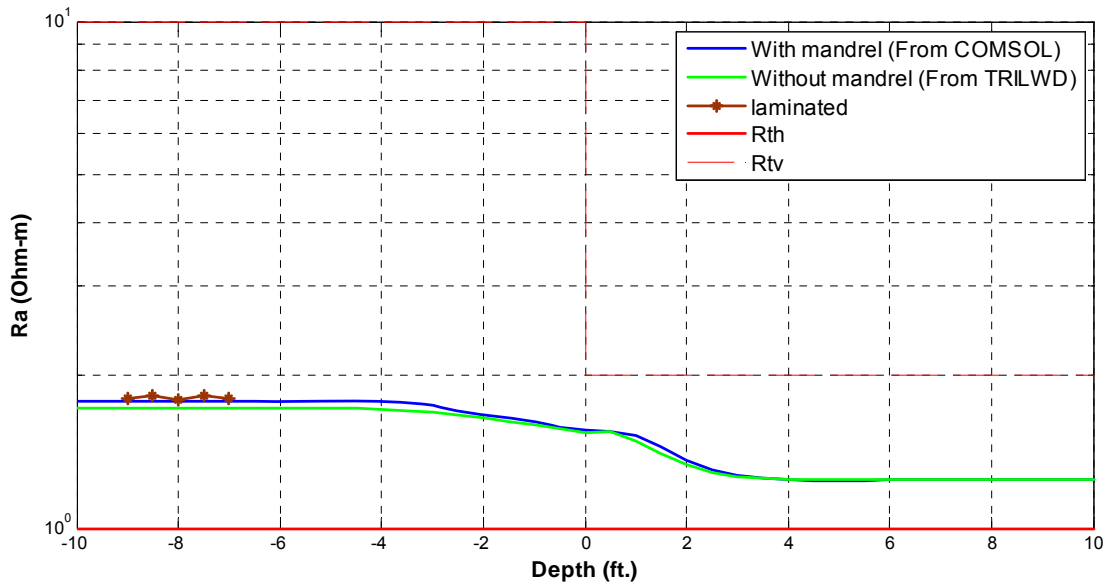


Figure 22 Ra result of laminated formation

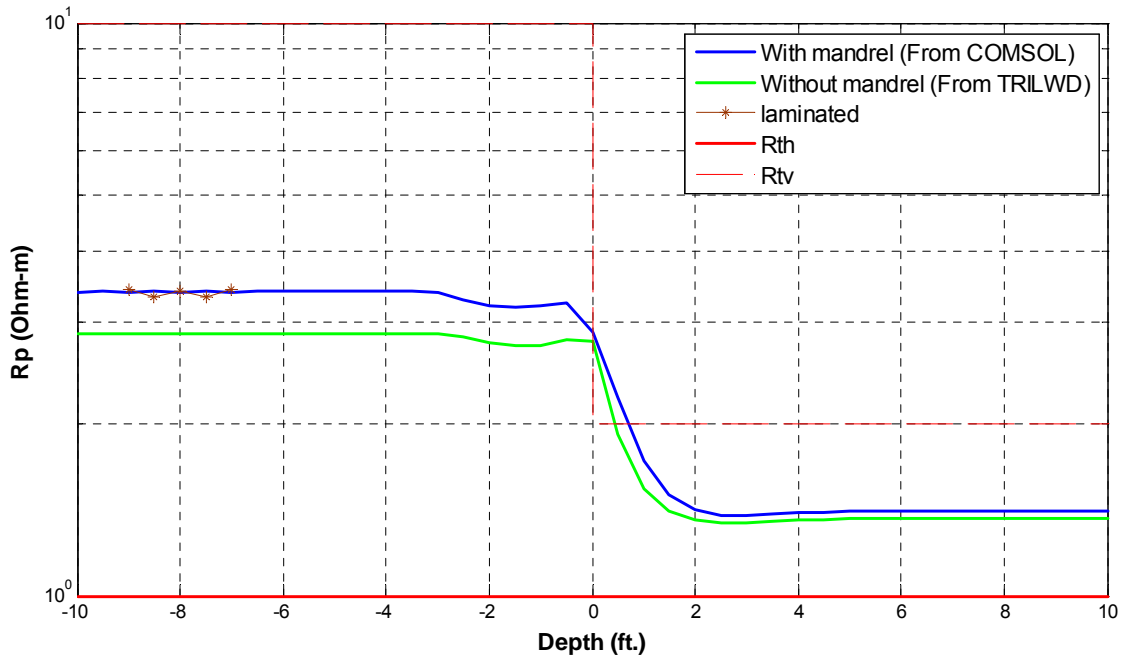


Figure 23 Rp result of laminated formation

Another example of anisotropy case with different anisotropy ratio is shown below. Figure 24 indicates the profile of the 2-layer anisotropic formation. The dipping angle is

60 degree. The anisotropy ratio R_v / R_h is 10 for both layers. The bulk is more conductive compared to the previous case. The Ra and Rp logs are shown in Figure 25 and 26, respectively. Difference in Ra and Rp readings caused by the presence of mandrel can also be observed in this example.

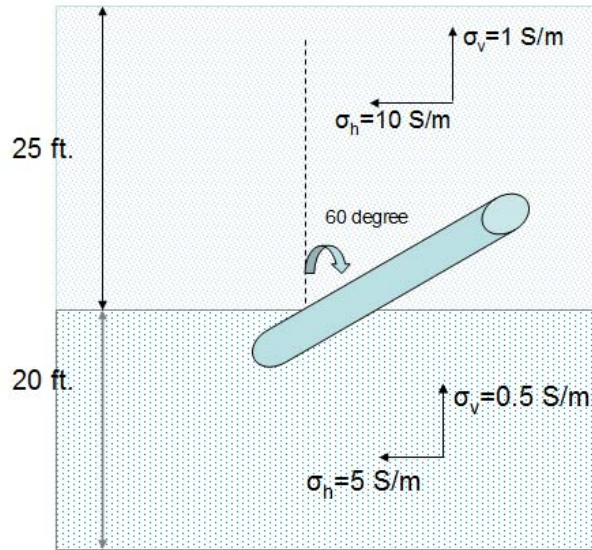


Figure 24 Profile of a 2-layer anisotropic formation

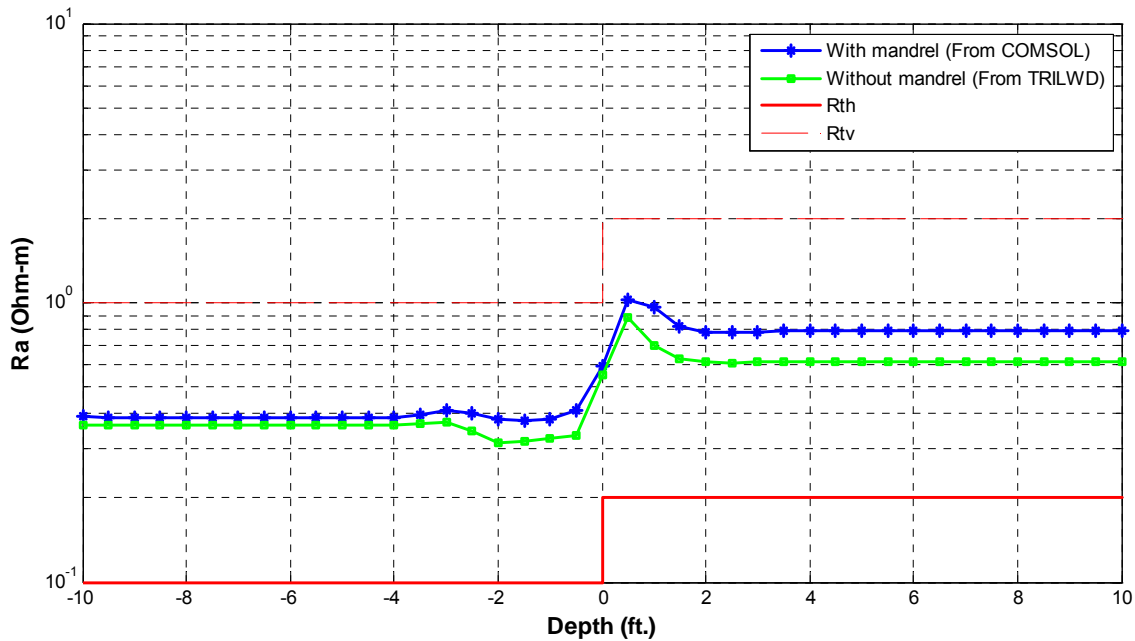


Figure 25 Ra of the dipole model and the mandrel model

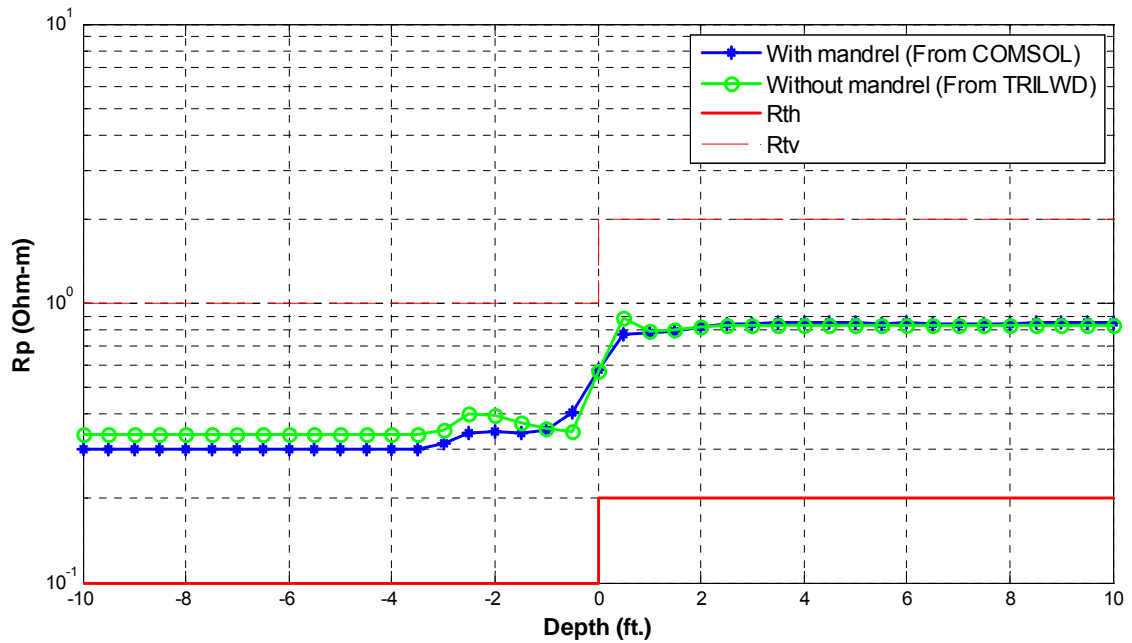


Figure 26 Rp of the dipole model and the mandrel model

The following case is a two-layer formation with 80 degree dip. Figure 27 shows the profile. The upper layer is isotropic with conductivity of 0.05 S/m. The lower layer is anisotropic formation. The anisotropy ratio R_v / R_h is 2. The Ra and Rp logs are shown in Figure 28 and 29, respectively. Due to the high dipping angle, horn effect shows at the boundary. The difference between the response of the dipole model and that of a model with mandrel is also large in this region. As a result, the dipole approximation in interpretation process could have error in evaluation the depth of the boundary. We can also observe that the presence of mandrel does not seem to generate visible effect in anisotropic layer. The reason is the anisotropy ratio is low in this example.

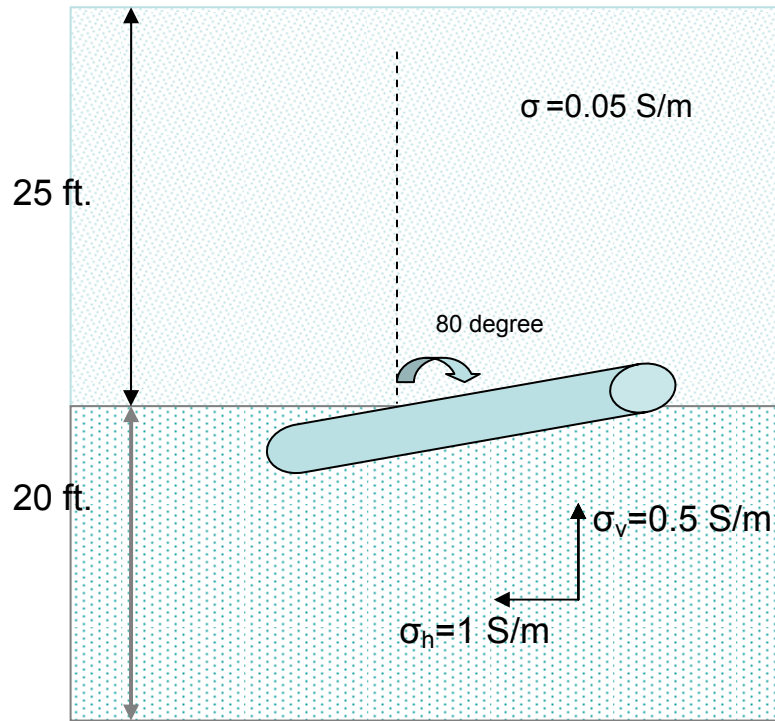


Figure 27 Profile of a 2-layer anisotropic formation

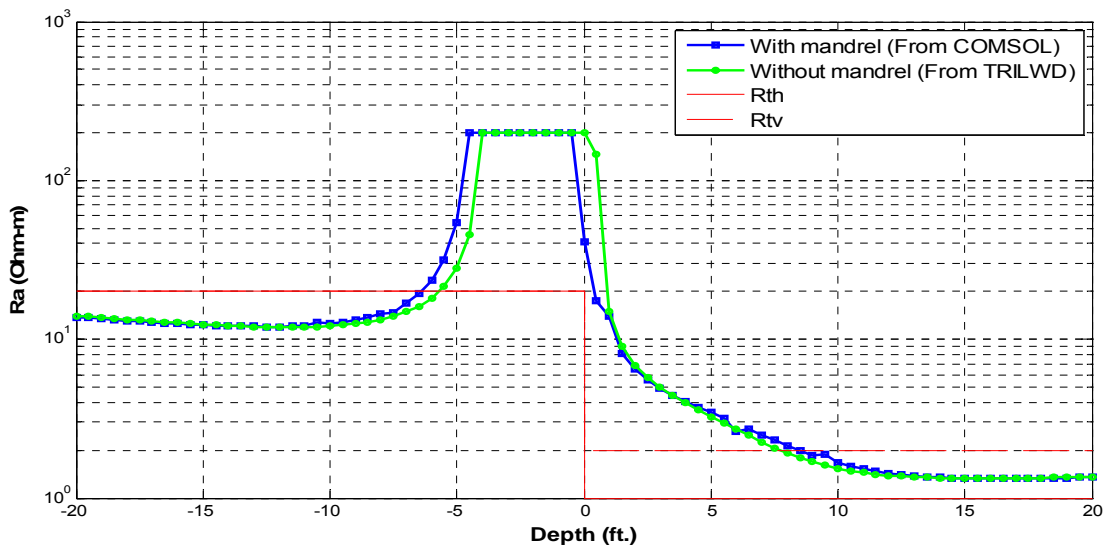


Figure 28 R_a of the dipole model and the mandrel model

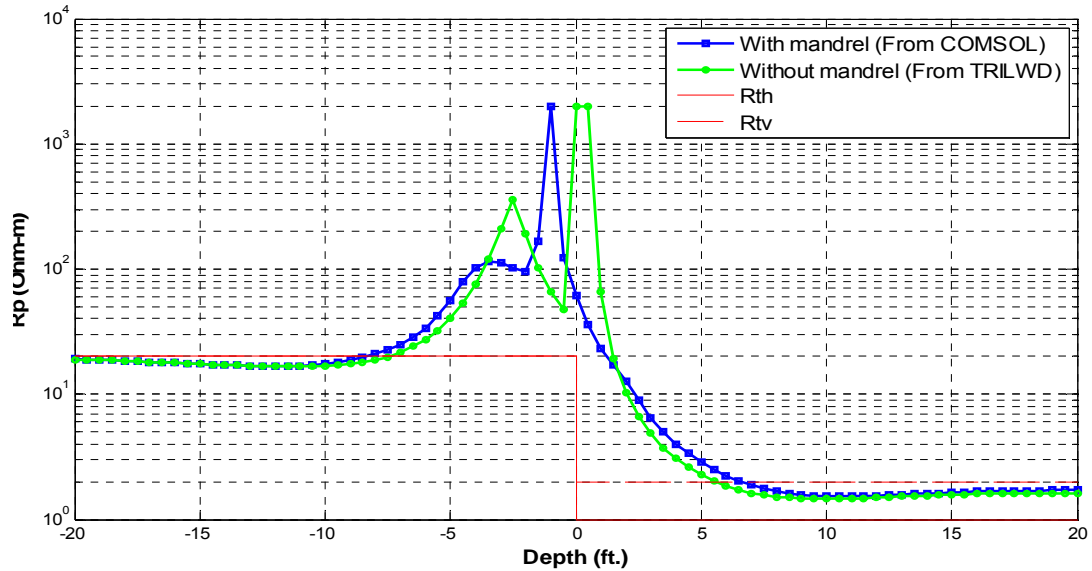


Figure 29 Rp of the dipole model and the mandrel model

From previous examples, we know that the effect caused by the presence of mandrel is larger when the anisotropy ratio is higher. Table 2 shows 7 cases of tool response in anisotropic homogeneous formation with anisotropy ratio at 10 and 20. We can see that the difference from Ra and Rp can be up to 0.6 Ohm-m and 1.8 Ohm-m, respectively.

		code		COMSOL		code		COMSOL		difference	
sigmaH	sigmaV	amp	phase	amp	phase	Ra	Rp	Ra	Rp	Ra	Rp
10	1	10.1433	40.8315	9.3996	42.0751	0.3633	0.3397	0.3906	0.3005	0.0273	-0.0392
0.1	0.01	5.7552	3.2465	5.3101	3.2321	16.0547	19.2323	16.1215	20.3528	0.0668	1.1205
0.05	0.005	5.6543	1.9383	5.2051	1.9433	32.1930	37.0320	31.5838	38.8524	-0.6092	1.8204
10	0.5	9.6882	39.1157	9.0049	40.0960	0.4256	0.3664	0.4641	0.3292	0.0385	-0.0372
0.1	0.005	5.7486	3.0349	5.3073	2.9762	16.5915	21.0751	16.1290	22.6501	-0.4625	1.5750
1	0.1	7.0641	12.1322	6.6233	11.0362	1.7232	2.8659	1.7849	3.4044	0.0617	0.5385
1	0.05	6.9738	10.8163	6.5133	9.4530	1.8642	3.4080	1.9681	4.3247	0.1039	0.9167

Table 2 Tool response in anisotropic homogeneous formation

3.2 Results of x-directed coils

1) In homogeneous isotropic medium

Figure 30-31 are two examples of E field distributions of x-directed coil in homogeneous medium in xy-plane and yz-plane, respectively. Phase-difference and

attenuations from a x-directed transmitter and a pair of x-directed receivers are also calculated. Conversion chart for x-directed coil w are shown for Ra and Rp in Figure 32 and Figure 33, respectively. From the charts we can see that mandrel also affects more in Ra response than Rp for x-directed coils, similar to the z-directed coils.

Also notice that now the conversion chart becomes double valued, i.e., one attenuation may correspond to two different resistivities. This will make the direct conversion to resistivity not possible. This is not an issue because the industry does not yet have an x-directed propagation resistivity tool like the way we describe. We suggest that, for resistivity below 50 Ohm-m, two branches in the attenuation transform can be distinguished by referencing the values of the phase-shift resistivity.

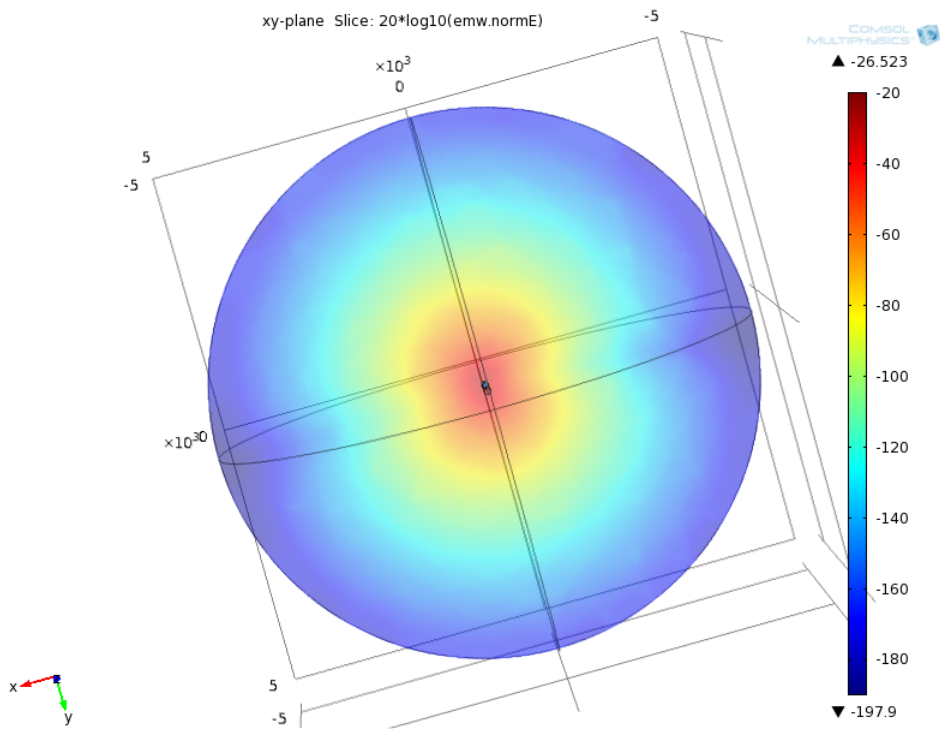


Figure 30 Slice view of E field distribution of x-directed coil in xy-plane

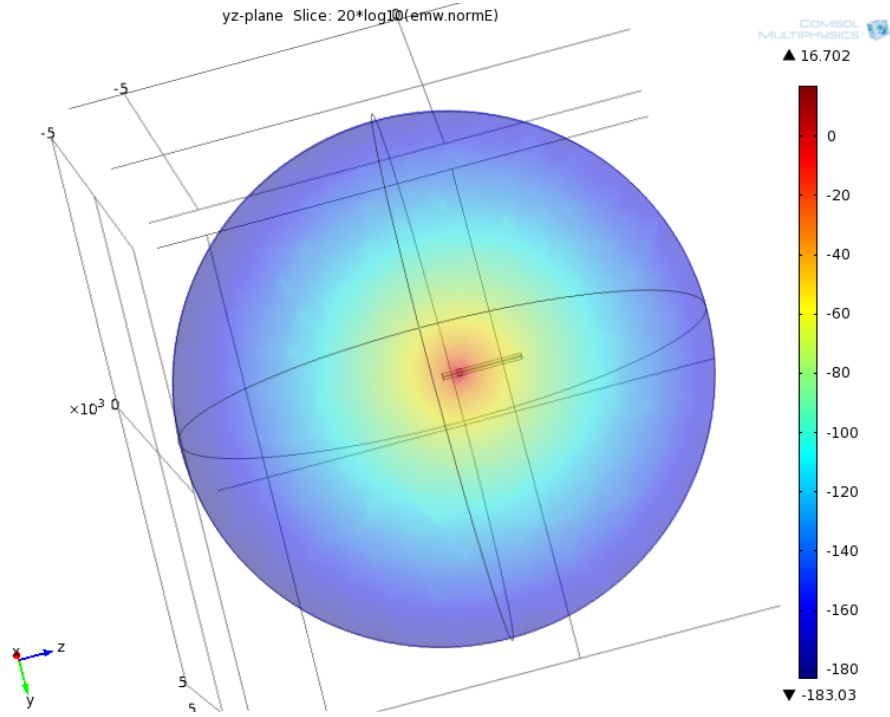


Figure 31 Slice view of E field distribution of x-directed coil in yz-plane

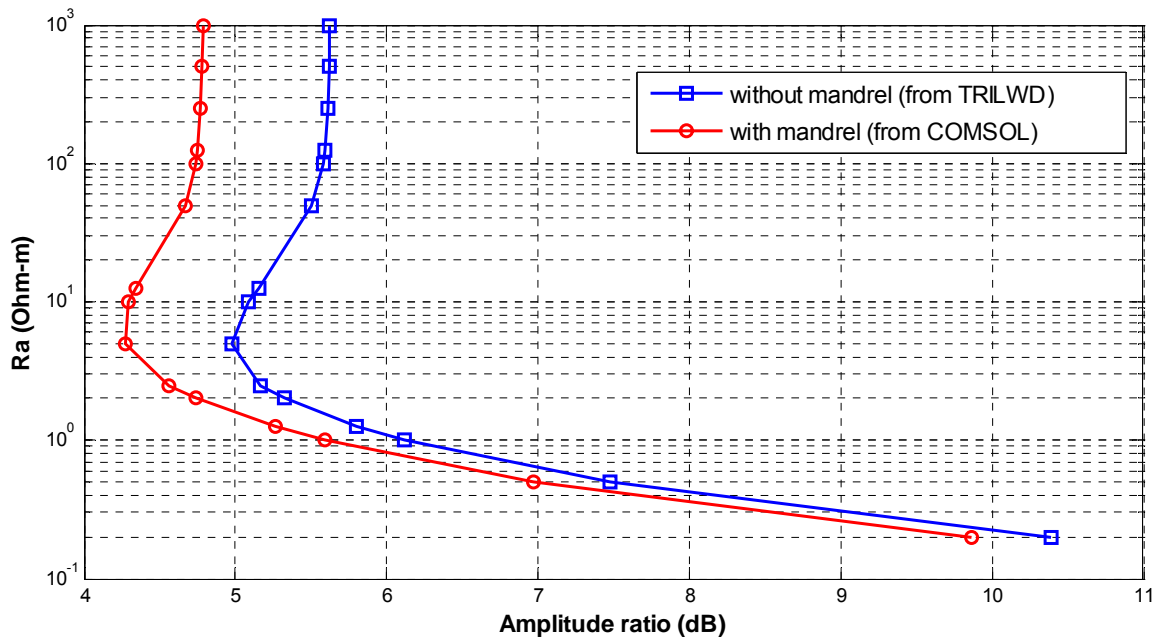


Figure 32 X-directed coils – Converting chart for Ra

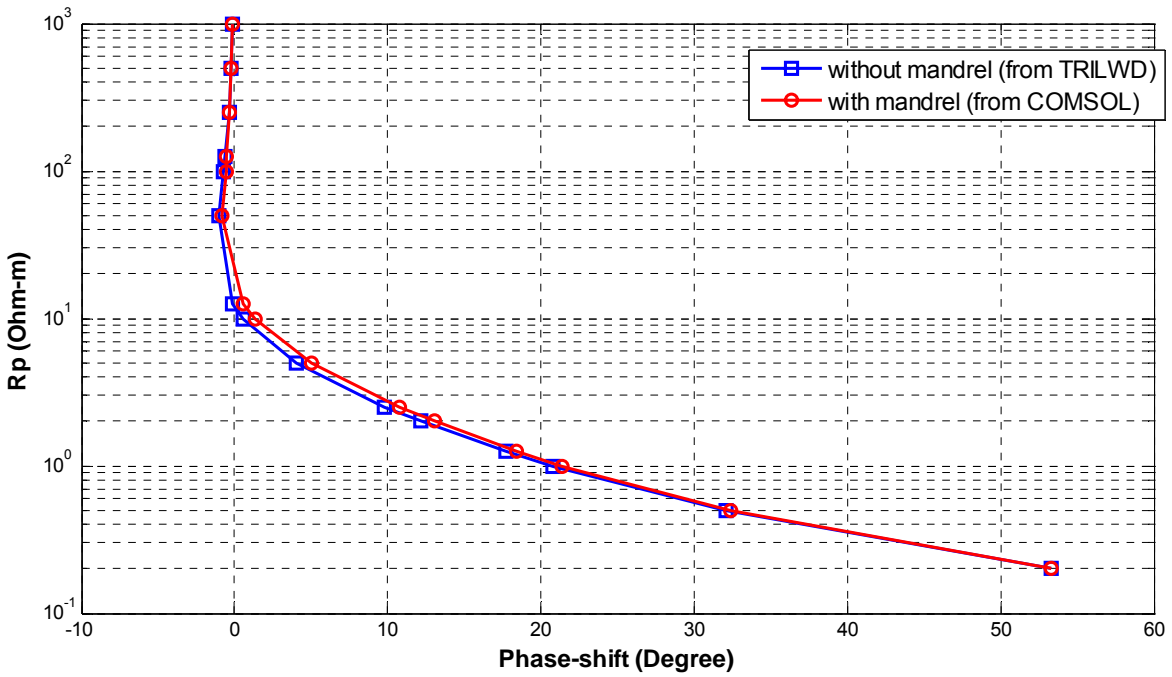


Figure 33 X-directed coils – Converting chart for Rp

2) In isotropic beds

Figure 34 indicates the profile of the formation. The tool responses are shown in Figure 35 and Figure 36 for attenuation and phase-difference, respectively. We can see that mandrel effect is only detectable at boundary for Rp. For Ra, mandrel effect is also large at bed boundary. Moreover, mandrel effect is more detectable in more resistive formation.

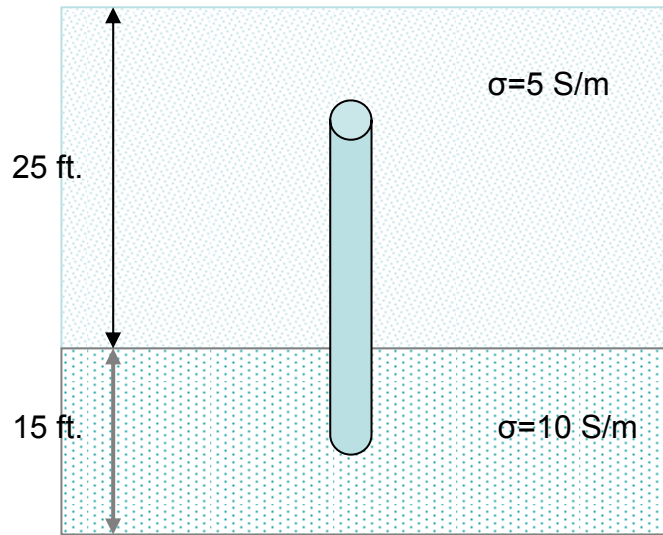


Figure 34 Profile of a 2-layer isotropic media

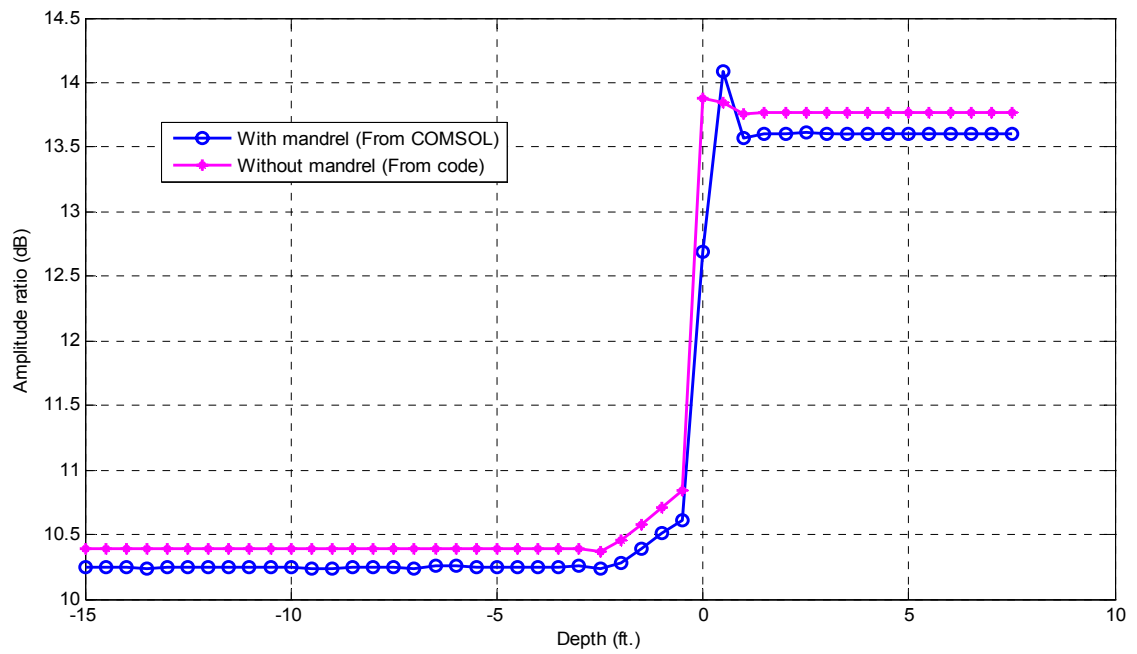


Figure35 Comparison of amplitude ratio in isotropic formation

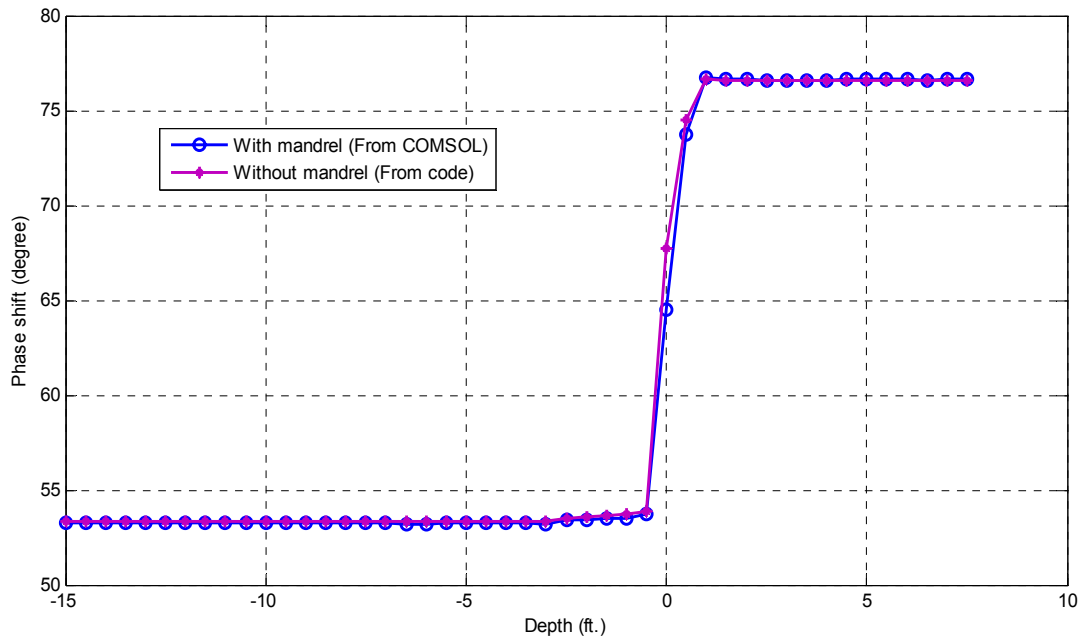


Figure 36 Comparison of phase-shift in isotropic formation

3) In anisotropic beds

We investigate the response of the x-directed coils only in vertical well because we need to analyze the effect only contributed by anisotropy. We define phase-shift and attenuation for the x-directed coils exactly the same way as for the z-directed coils. The profile of formation is rendered in Figure 37. The attenuation and phase-shift are shown in Figure 38 and Figure 39, respectively. We can see that the difference caused by mandrel in anisotropic formation is much the same as that in isotropic formation. We can also observe that the x-directed coil system detects very little effect of anisotropy. The converted logs, shown in Figure 40-41, read much the same as the resistivity of horizontal direction.

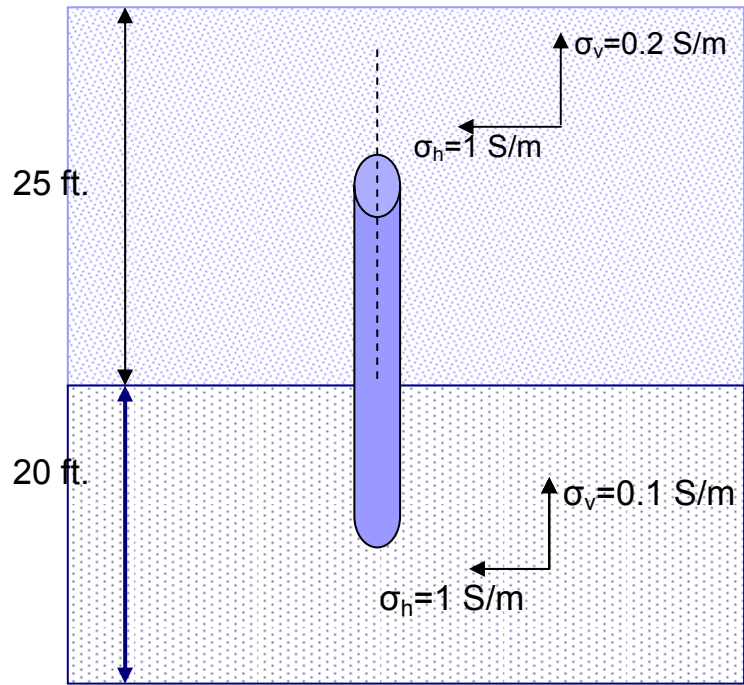


Figure 37 Profile of formation

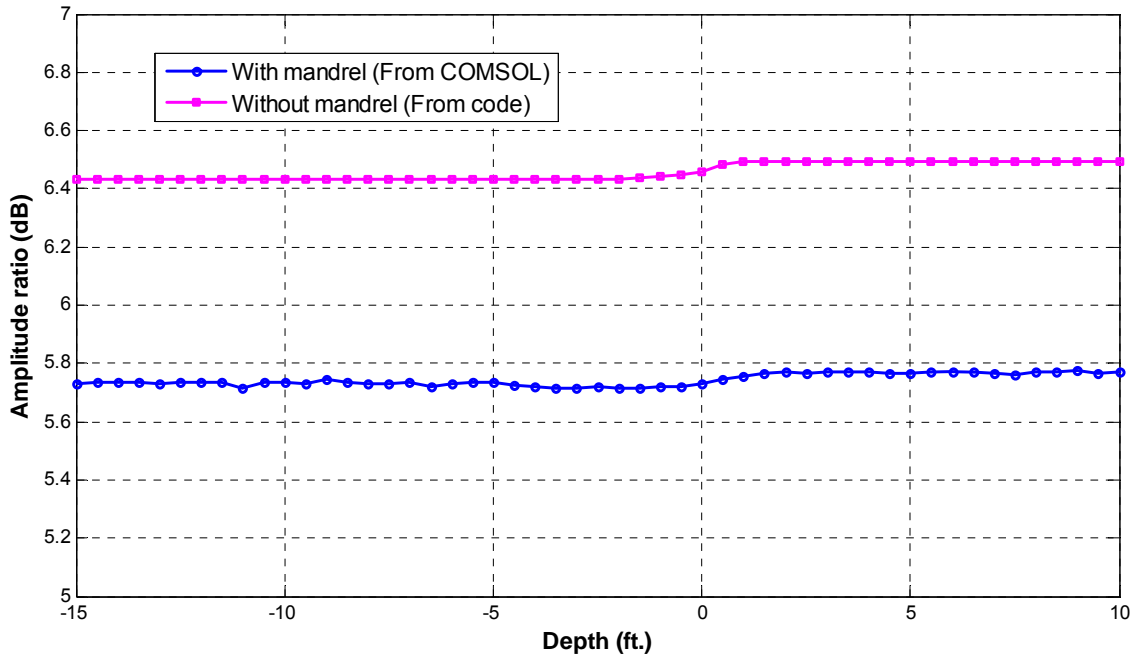


Figure 18 Comparison of amplitude ratio in anisotropic formation

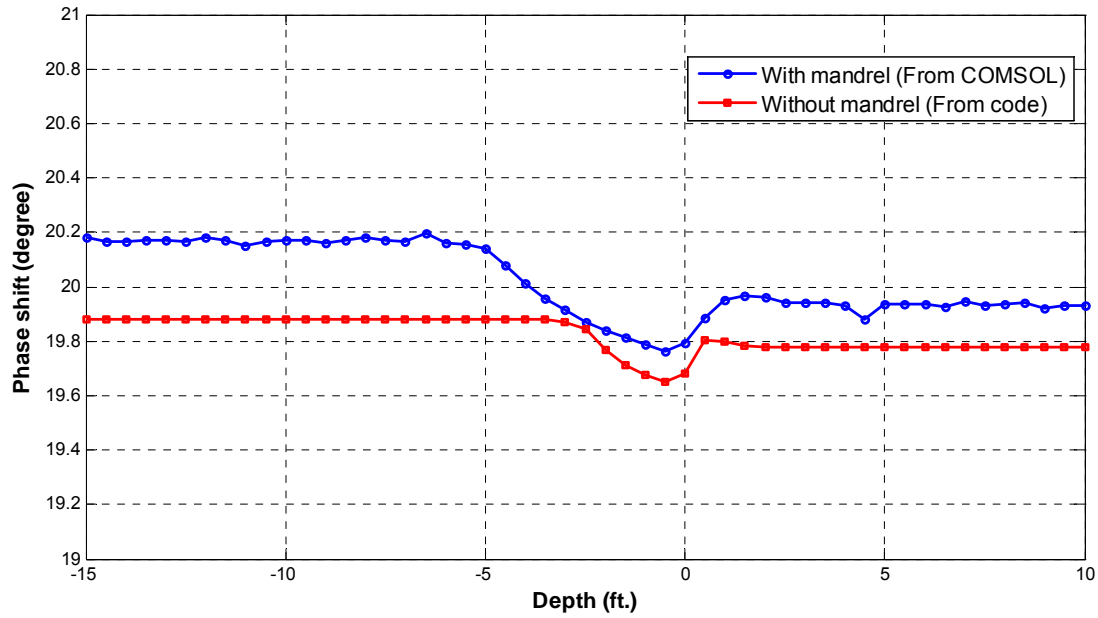


Figure 39 Comparison of phase-shift in anisotropic formation

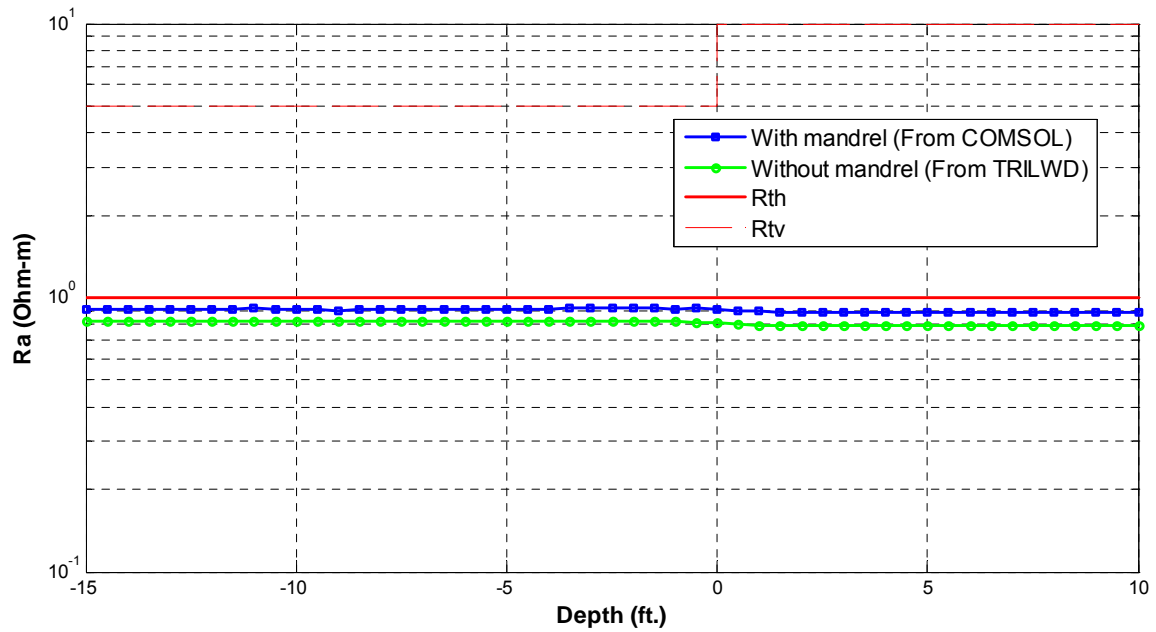


Figure 40 Ra logs of dipole model and model with mandrel

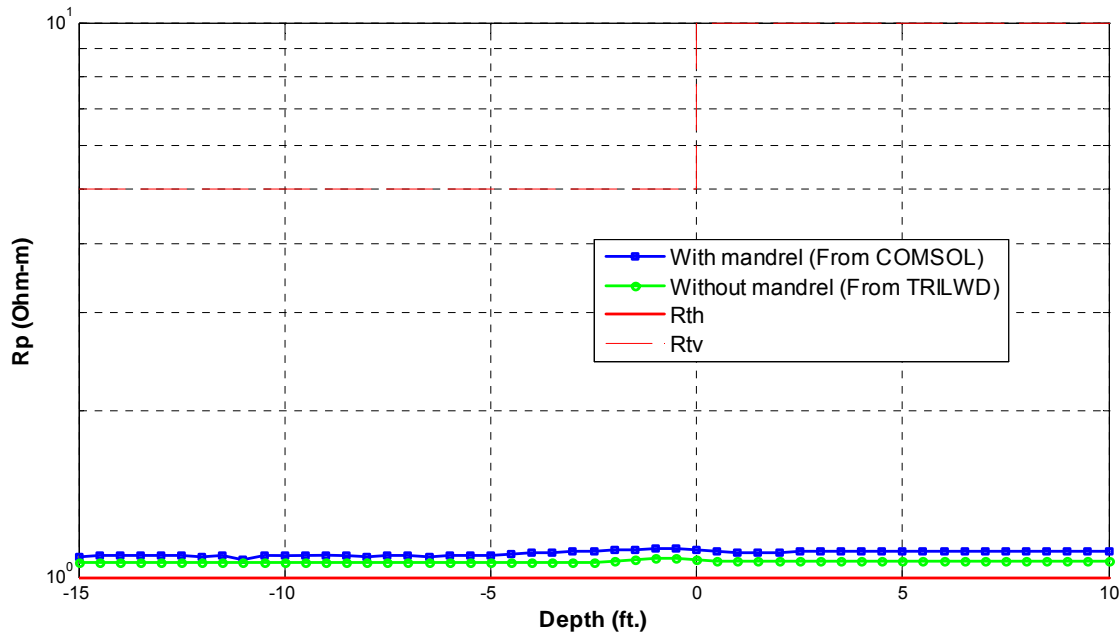


Figure 41 Rp logs of dipole model and model with mandrel

4. Summary and conclusions

To get a full picture of the mandrel effect in LWD resistivity tools, dipole model and model of finite size loop with mandrel have been used to simulate the tool response in various types of formation. Two types of measurement are included in this thesis: one with magnetic moment of coils pointed in the normal direction (z direction) of the beds, the other with magnetic moment of coils pointed in the horizontal direction (x -direction) of the beds.

Z-directed coils. In homogeneous media, results indicate that attenuation of dipole model and mandrel model has about 0.5 dB shift, but the difference in phase shift is not significant. In isotropic layered formation, R_a and R_p readings are only affected by the presence of mandrel near the boundary. In anisotropic layered dipping beds, R_a and R_p can be affected not only near the boundary but also the region far away from boundary. The difference in R_a and R_p caused by mandrel is larger in the anisotropic formation with higher anisotropy ratio.

X-directed coils. In homogeneous medium, we can see that mandrel also affects more in R_a response than R_p for x-directed coils, similar to the z-directed coils. The conversion chart for R_a and R_p become double valued. This will present difficulty when conversion from phase-shift and attenuation to resistivity is needed. In isotropic layered formation, the mandrel effect is obvious near the boundary. In anisotropic formation, the presence of the mandrel can cause difference in R_a and R_p readings, but the effect is smaller than what is seen with the z-directed coils.

Since in practice z-directed coil and x-directed coil are often combined to detect boundary or anisotropy, we will present more results of combined coil system in the future. With the confidence we gained on the COMSOL modeling of LWD propagation tools, study of 3D effects will be further explored in the future.

Acknowledgement

The authors want to thank Dr. Minerbo of Schlumberger for his guidance on COMSOL. We also appreciate KMSTechnologies for the donation of COMSOL software and the computer. We thank all the Well Logging Industrial Consortium members for their financial support.

References

- [1] Dan Coope, Liang C. Shen and Frank S. C. Huang, "The Theory of 2 MHz Resistivity Tool and Its Application to Measurement-While-Drilling," *The Log Analyst*, Vol. XXV, No. 3, May-June 1984, pp. 35-46.
- [2] Brain Clark, Martin G. Liiling, Jacques Jundt, Mike Ross, and David Best, "A Dual Depth Resistivity Measurement for FEWD," 29th Annual Logging Symposium, SPWLA, 1988.
- [3] Terry Hagiwara, Erik J. Banning, Richard M. Ostermeier and S. Mark Haugland, "Effects of Mandrel, Borehole, and Invasion for Tilt-Coil Antennas," SPE ATCE, Denver, CO, October 2003.
- [4] Jian Yang, Dzevat Omeragic, Chengbing Liu, Qiming Li, Jan Smits, and Mike Wilson, "Bed-Boundary Effect Removal to Aid Formation Resistivity Interpretation from LWD Propagation Measurements at All Dip Angles," 46th Annual Logging Symposium, SPWLA, 2005.
- [5] Self-learning Module, "Logging While Drilling (Geosteering Applications)," TRACS INTERNATIONAL.
- [6] John Zhou, "LWD/MWD Resistivity Tool Parameters," Maxwell Dynamics, 2010.
- [7] J. H. Moran and S. Gianzero, "Effects of formation anisotropy on resistivity-logging measurements," *Geophysics*, vol. 44, no.7, pp. 1266-1286, July 1979.
- [8] Ning Yuan, Zhijuan Zhang and Richard Liu, "Responses of Triaxial Induction Tools in 1-D Multi-Layered Transverse Isotropic Formations," Well Logging Laboratory Technical Report No. 30, University of Houston, Chapter 2, 2009.
- [9] L. L. Zhong, Simulation of Tri-axial Induction Tools in Dipping Anisotropic Beds, Ph.D. dissertation, University of Houston, pp. 23-42, 2004.
- [10] Zhijuan Zhang, 1D Modeling and Inversion of Triaxial Induction Logging Tool in Layered Anisotropic Medium, Ph.D. dissertation, University of Houston, pp. 14-15, 2011.

- [11] L. C. Shen, "Theory of Induction and MWD Tools in Cylindrically Layered Medium," Well Logging Laboratory Technical Report No.14, University of Houston, Chapter 4, 1993
- [12] Gerald Minerbo, Private Communication, August 2011
- [13] Keli Sun, Dzevat Omeragic, Chanh Cao Minh, John Rasmus, Jian Yang, Andrei Davydychev, Tarek Habashy, Roger Griffiths, Graham Reaper, and Qiming Li, "Evaluation of Resistivity Anisotropy and Formation Dip from Directional Electromagnetic Tools While Drilling," 51st Annual Logging Symposium, SPWLA, 2010

CHAPTER 4

Fast Finite-Difference Time-Domain Modeling for Marine-Subsurface Electromagnetic Problems using Artificially High Dielectric Constant

Abstract

Finite-difference time-domain (FDTD) method was proposed by Yee in 1966 and becomes one of the most popular numerical methods. It has been widely used in various areas especially in electromagnetic (EM) modeling. In some areas such as sea-bed logging, EM problems in marine-subsurface, ultra low frequency (ULF) is used and the FDTD method will require extremely large number of time steps to get convergent results. Thus, how to significantly reduce the large time-steps is essential for FDTD applications in ULF problems. In this paper, we use an artificially high dielectric constant technique in the FDTD simulation. The resultant method can obtain satisfying results with much less time-steps than the original method. Numerical Examples will be presented to demonstrate the capability of the present method.

1. Introduction

The finite-difference time-domain (FDTD) method was introduced by Yee in 1966 to solve partial difference equation. It has become one of the primary available computational electrodynamics modeling techniques and is widely used in various areas. Since it is a time-domain method, FDTD solutions can cover a wide frequency range with a single simulation run, and treat nonlinear material properties in a natural way.

Marine controlled-source has been under survey for many years, especially for geophysical investigations. One particular application, called seabed logging, was

introduced by Eidesmo et al. and Ellingsrud et al. [2, 4] for offshore hydrocarbon exploration. In this method, several receivers are set in different positions on the seabed. The electric dipole which is transmitting electromagnetic wave is towing by a ship across the seafloor and the receivers are recording electromagnetic waves in different positions during towing. This method is often used to collect information of the sea bed to detect hydrocarbon reservoirs. Hydrocarbon reservoirs are very resistive compared to the sediments (the resistivity of the water-filled marine sediments is 1-5 Ohm-m) around them.

In this paper, we are trying to use the FDTD method to deal with the EM problems in marine-subsurface. As we know, the computation speed of a numerical solution is very important for engineering and real-time problem solving..There are a lot of ways to increase the speed of the FDTD algorithm such as the perfect matched layers (PML), up scaling of artificially high electric permittivity. Both techniques have been implemented in the FDTD solution in this paper.

PML was introduced by Berenger [1]. It is a method that can model an infinite large solution domain by using the reflectionless boundaries in wave equations. That means when the wave is propagating towards and reaches the PML boundary, there is no reflection wave coming back to the solution domain. By introducing and implementing the PML boundary, the solution domain is truncated and thus yields much less unknowns in the FDTD simulation. Based on the Berenger' PML, many new boundaries such as the uniaxial PML, convolution PML etc. have been developed and proved to be more efficient to more general media such as conductive media, dispersive media etc..

Up scaling of artificially high electric permittivity is used when the frequency is extremely low like in sea bed logging. This method was introduced by Oristaglio and Hohmann (1984) in [5] for modeling the transient response in 2D conductive earth models. The main contribution is the introduction of an artificially high electric

permittivity. This method shows that in the case of extreme low frequency, we can increase the value of the electric permittivity without changing the solution much. One should note that the increase of the electric permittivity should not violate the stability conditions. It is an approximate method but it can really increase the computation speed and save much time. Both of the two methods mentioned above make the modeling of sea bed electromagnetic problems possible.

2. Theory

2.1 Maxwell's equations

First, the Maxwell's equations are as follows

$$(\varepsilon_{ij}\partial_t + \sigma_{ij})E_j = \delta_{ijk}\partial_j H_k - J_i \quad (1)$$

$$\mu\partial_t H_i = -\delta_{ijk}\partial_j E_k - M_i \quad (2)$$

δ_{ijk} is the Levi-Civita tenosr. ε_{ij} is the electric permittivity tensor, σ_{ij} is the conductivity tensor. The j components of the electric and magnetic fields are E_k and H_k . J_i and M_i are the i-components of the electric and magnetic sources. μ is the magnetic permeability which is assumed constant and equal to $4\pi \times 10^{-7}$ H/m.

The Fourier transforms of the Maxwell's equations from time to angular frequency yields:

$$(-i\omega\varepsilon_{ij} + \sigma_{ij})E_j = \delta_{ijk}\partial_j H_k - J_i \quad (3)$$

$$-i\omega\mu H_i = -\delta_{ijk}\partial_j E_k - M_i \quad (4)$$

As mentioned before, in sea-bed logging, the working frequency is usually as low as 0~10 Hz. In this situation, we notice that $|-i\omega\varepsilon_{ij}|$ is much smaller than $|\sigma_{ij}|$. To some extent, we can increase ε_{ij} so that the total simulation time will decrease. It should be

noted that the increased ε_{ij} must still follow the condition that $|\omega\varepsilon_{ij}| \ll |\sigma_{ij}|$.

2.2 Methodology of the 3D FDTD

The FDTD method starts from the Maxwell's time-domain Equations.

$$\nabla \times \bar{H} = \frac{\partial \bar{D}}{\partial t} + \bar{J} \quad (5)$$

$$\nabla \times \bar{E} = -\frac{\partial \bar{B}}{\partial t} - \bar{M} \quad (6)$$

where \bar{E} is the electric field, \bar{D} is the displacement vector, \bar{H} is the magnetic field strength vector, \bar{B} is the magnetic flux density vector, \bar{J} is the electric current density and \bar{M} is the magnetic current density.

For linear, isotropic, and non-dispersive materials, there are

$$\bar{D} = \varepsilon \bar{E} \quad (7)$$

$$\bar{B} = \mu \bar{H} \quad (8)$$

where ε , μ are the electric permittivity and magnetic permeability of the material.

In FDTD algorithm, the solution domain is discretized into a lot of small grids. The E and H field in every grid are calculated one by one. Fig. 1 shows the Yee grid used in this paper. The electric field components are defined at the centers of the edges of the Yee cells and oriented parallel to the respective edges while the magnetic field vector components are defined at the centers of the faces of the Yee cells and are oriented normal to the respective faces. This provides a simple picture of three-dimensional space being filled by an interlinked array of Faraday's law and Ampere's law contours. The material parameters of the Yee grid is shown in Fig.2.

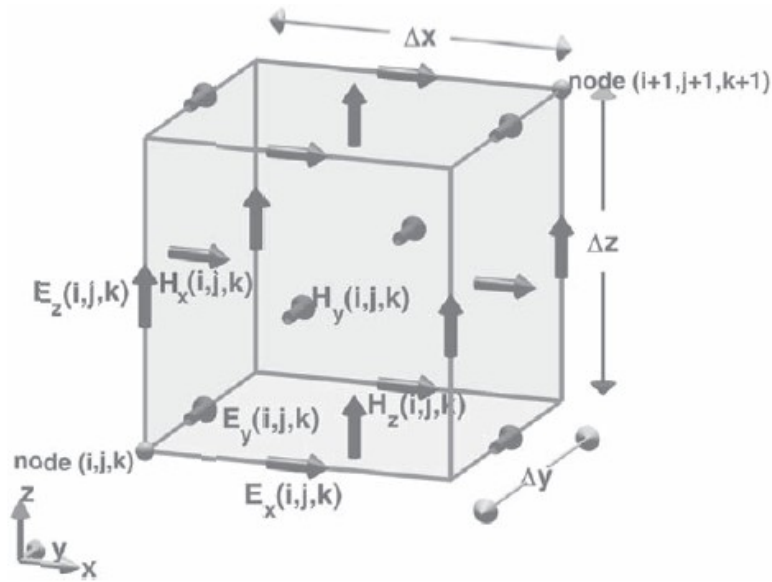


Fig. 1 The Yee grid for electrical filed

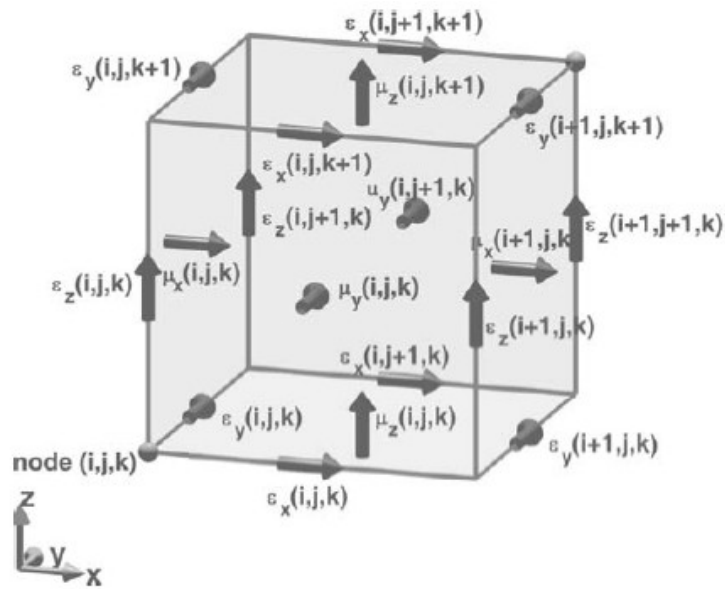


Fig. 2 The Yee grid for magnetic filed

After using the finite-difference skill, the Maxwell's equation can be written as

Updating E field:

$$\begin{aligned}
 E_x^{n+1}(i, j, k) &= C_{exe}(i, j, k) \times E_x^n(i, j, k) \\
 &+ C_{exbz}(i, j, k) \times (H_z^{n+1/2}(i, j, k) - H_z^{n+1/2}(i, j-1, k)) \\
 &+ C_{exby}(i, j, k) \times (H_y^{n+1/2}(i, j, k) - H_y^{n+1/2}(i, j, k-1)) \\
 &+ C_{exj}(i, j, k) \times J_{ix}^{n+1/2}(i, j, k)
 \end{aligned} \tag{9}$$

Where:

$$\begin{aligned}
 C_{exe}(i, j, k) &= \frac{2\varepsilon_x(i, j, k) - \Delta t \sigma_x^e(i, j, k)}{2\varepsilon_x(i, j, k) + \Delta t \sigma_x^e(i, j, k)} \\
 C_{exbz}(i, j, k) &= \frac{2\Delta t}{(2\varepsilon_x(i, j, k) + \Delta t \sigma_x^e(i, j, k)) \Delta y} \\
 C_{exby}(i, j, k) &= -\frac{2\Delta t}{(2\varepsilon_x(i, j, k) + \Delta t \sigma_x^e(i, j, k)) \Delta z} \\
 C_{exj}(i, j, k) &= -\frac{2\Delta t}{2\varepsilon_x(i, j, k) + \Delta t \sigma_x^e(i, j, k)}
 \end{aligned}$$

$$\begin{aligned}
 E_y^{n+1}(i, j, k) &= C_{eye}(i, j, k) \times E_y^n(i, j, k) \\
 &+ C_{eybx}(i, j, k) \times (H_x^{n+1/2}(i, j, k) - H_x^{n+1/2}(i, j, k-1)) \\
 &+ C_{eybz}(i, j, k) \times (H_z^{n+1/2}(i, j, k) - H_z^{n+1/2}(i-1, j, k)) \\
 &+ C_{eyj}(i, j, k) \times J_{iy}^{n+1/2}(i, j, k)
 \end{aligned} \tag{10}$$

Where:

$$\begin{aligned}
 C_{eye}(i, j, k) &= \frac{2\varepsilon_y(i, j, k) - \Delta t \sigma_y^e(i, j, k)}{2\varepsilon_y(i, j, k) + \Delta t \sigma_y^e(i, j, k)} \\
 C_{eybx}(i, j, k) &= \frac{2\Delta t}{(2\varepsilon_y(i, j, k) + \Delta t \sigma_y^e(i, j, k)) \Delta z} \\
 C_{eybz}(i, j, k) &= -\frac{2\Delta t}{(2\varepsilon_y(i, j, k) + \Delta t \sigma_y^e(i, j, k)) \Delta x} \\
 C_{eyj}(i, j, k) &= -\frac{2\Delta t}{2\varepsilon_y(i, j, k) + \Delta t \sigma_y^e(i, j, k)}
 \end{aligned}$$

$$\begin{aligned}
 E_z^{n+1}(i, j, k) &= C_{eze}(i, j, k) \times E_z^n(i, j, k) \\
 &+ C_{ezby}(i, j, k) \times (H_y^{n+1/2}(i, j, k) - H_y^{n+1/2}(i-1, j, k)) \\
 &+ C_{ezbx}(i, j, k) \times (H_x^{n+1/2}(i, j, k) - H_x^{n+1/2}(i, j-1, k)) \\
 &+ C_{ezj}(i, j, k) \times J_{iz}^{n+1/2}(i, j, k)
 \end{aligned} \tag{11}$$

Where:

$$\begin{aligned}
 C_{eze}(i, j, k) &= \frac{2\varepsilon_z(i, j, k) - \Delta t \sigma_z^e(i, j, k)}{2\varepsilon_z(i, j, k) + \Delta t \sigma_z^e(i, j, k)} \\
 C_{ezby}(i, j, k) &= \frac{2\Delta t}{(2\varepsilon_z(i, j, k) + \Delta t \sigma_z^e(i, j, k))\Delta x} \\
 C_{ezbx}(i, j, k) &= -\frac{2\Delta t}{(2\varepsilon_z(i, j, k) + \Delta t \sigma_z^e(i, j, k))\Delta y} \\
 C_{ezj}(i, j, k) &= -\frac{2\Delta t}{2\varepsilon_z(i, j, k) + \Delta t \sigma_z^e(i, j, k)}
 \end{aligned}$$

Updating H field:

$$\begin{aligned}
 H_x^{n+1}(i, j, k) &= C_{bxb}(i, j, k) \times H_x^{n-1/2}(i, j, k) \\
 &+ C_{bxey}(i, j, k) \times (E_y^n(i, j, k+1) - E_y^n(i, j, k)) \\
 &+ C_{bxez}(i, j, k) \times (E_z^n(i, j+1, k) - E_z^n(i, j, k)) \\
 &+ C_{bxm}(i, j, k) \times M_{ix}^n(i, j, k)
 \end{aligned} \tag{12}$$

Where

$$C_{bxb}(i, j, k) = \frac{2\mu_x(i, j, k) - \Delta t\sigma_x^m(i, j, k)}{2\mu_x(i, j, k) + \Delta t\sigma_x^m(i, j, k)}$$

$$C_{bxy}(i, j, k) = \frac{2\Delta t}{(2\mu_x(i, j, k) + \Delta t\sigma_x^m(i, j, k))\Delta z}$$

$$C_{bxz}(i, j, k) = -\frac{2\Delta t}{(2\mu_x(i, j, k) + \Delta t\sigma_x^m(i, j, k))\Delta y}$$

$$C_{bxm}(i, j, k) = -\frac{2\Delta t}{2\mu_x(i, j, k) + \Delta t\sigma_x^m(i, j, k)}$$

$$H_y^{n+1}(i, j, k) = C_{byb}(i, j, k) \times H_y^{n-1/2}(i, j, k)$$

$$+ C_{byez}(i, j, k) \times (E_z^n(i+1, j, k) - E_z^n(i, j, k))$$

$$+ C_{byex}(i, j, k) \times (E_x^n(i, j, k+1) - E_x^n(i, j, k))$$

$$+ C_{bym}(i, j, k) \times M_{iy}^n(i, j, k) \quad (13)$$

Where

$$C_{bxb}(i, j, k) = \frac{2\mu_y(i, j, k) - \Delta t\sigma_y^m(i, j, k)}{2\mu_y(i, j, k) + \Delta t\sigma_y^m(i, j, k)}$$

$$C_{byez}(i, j, k) = \frac{2\Delta t}{(2\mu_y(i, j, k) + \Delta t\sigma_y^m(i, j, k))\Delta x}$$

$$C_{byex}(i, j, k) = -\frac{2\Delta t}{(2\mu_y(i, j, k) + \Delta t\sigma_y^m(i, j, k))\Delta z}$$

$$C_{bym}(i, j, k) = -\frac{2\Delta t}{2\mu_y(i, j, k) + \Delta t\sigma_y^m(i, j, k)}$$

$$H_z^{n+1}(i, j, k) = C_{bzb}(i, j, k) \times H_z^{n-1/2}(i, j, k)$$

$$+ C_{bzex}(i, j, k) \times (E_x^n(i, j+1, k) - E_x^n(i, j, k))$$

$$+ C_{bzey}(i, j, k) \times (E_y^n(i+1, j, k) - E_y^n(i, j, k))$$

$$+ C_{bzm}(i, j, k) \times M_{iz}^n(i, j, k) \quad (14)$$

Where:

$$C_{bzb} (i, j, k) = \frac{2\mu_z(i, j, k) - \Delta t\sigma_z^m(i, j, k)}{2\mu_z(i, j, k) + \Delta t\sigma_z^m(i, j, k)}$$

$$C_{bzex} (i, j, k) = \frac{2\Delta t}{(2\mu_z(i, j, k) + \Delta t\sigma_z^m(i, j, k))\Delta x}$$

$$C_{bzey} (i, j, k) = -\frac{2\Delta t}{(2\mu_z(i, j, k) + \Delta t\sigma_z^m(i, j, k))\Delta y}$$

$$C_{bzm} (i, j, k) = -\frac{2\Delta t}{2\mu_z(i, j, k) + \Delta t\sigma_z^m(i, j, k)}$$

As a summary, we can use a flow chart in Fig.2 to illustrate the steps of the FDTD algorithm.

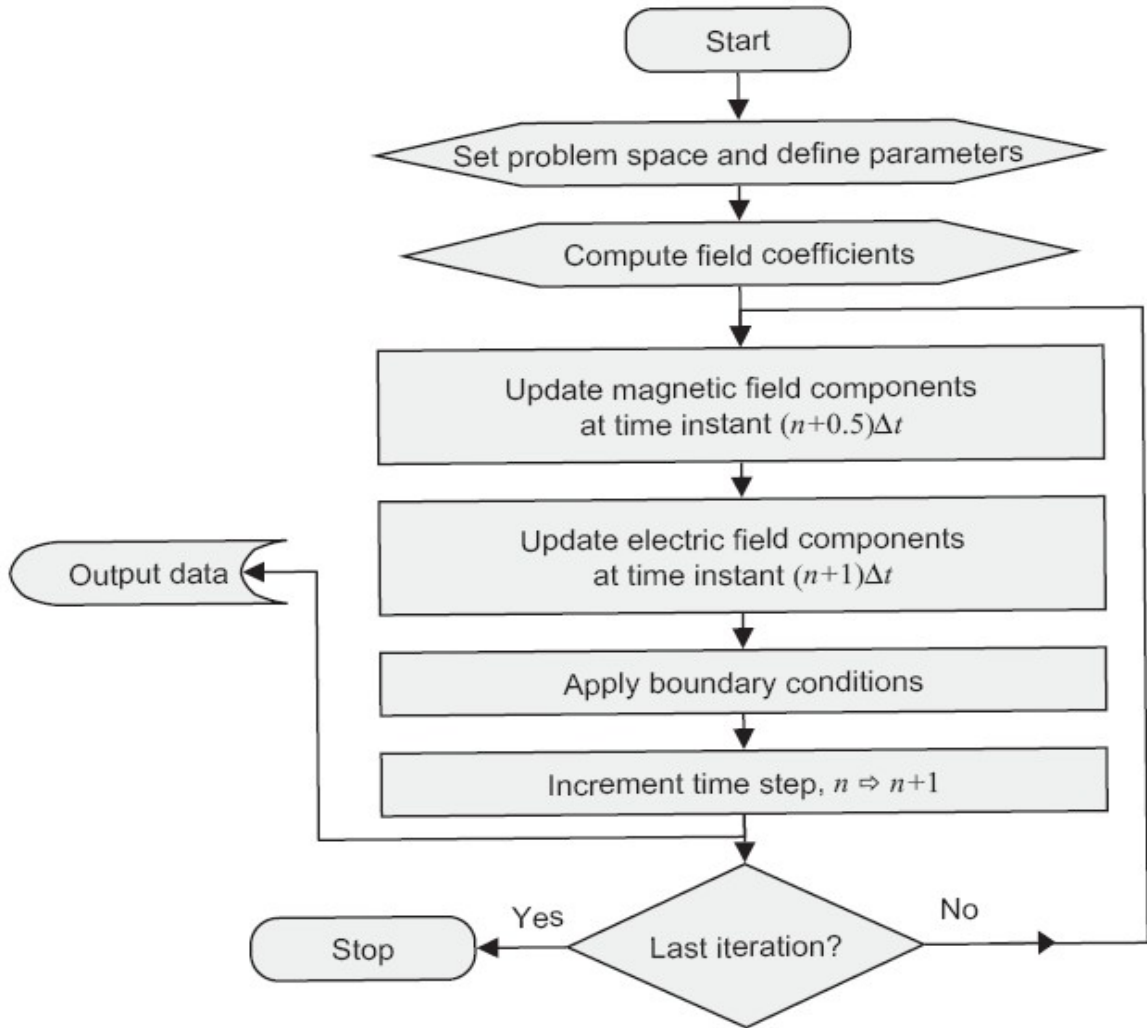


Fig.3 The flowchart of the FDTD algorithm

2.3 Material Approximations

When using the FDTD to solve the Maxwell's equation, if the solution domain is a homogenous medium, we just need to assign a value to ϵ_i , σ_i and μ_i , σ_i^m . However, in most cases, the media are inhomogeneous. Then, the average skill which take some approximation strategies need to be applied.

In this report, the problem space is divided into a lot of grids which has unique

dimensions in the x-,y-, and z- direction. By using the averaging skill, the material parameters ε_i , σ_i , μ_i , and σ_i^m can be calculated as follows

$$\begin{aligned}
 \varepsilon_i(i, j, k) &= \frac{\varepsilon(i, j, k) + \varepsilon(i, j-1, k) + \varepsilon(i-1, j-1, k) + \varepsilon(i-1, j-1, k)}{4} \\
 \sigma_i(i, j, k) &= \frac{\sigma(i, j, k) + \sigma(i, j-1, k) + \sigma(i-1, j-1, k) + \sigma(i-1, j-1, k)}{4} \\
 \mu_i(i, j, k) &= \frac{2 \times \mu(i, j, k) \times \mu(i, j, k-1)}{\mu(i, j, k) + \mu(i, j, k-1)} \\
 \sigma_i^m(i, j, k) &= \frac{2 \times \sigma^m(i, j, k) \times \sigma^m(i, j, k-1)}{\sigma^m(i, j, k) + \sigma^m(i, j, k-1)}
 \end{aligned} \tag{15}$$

where i can be x,y,z representing different direction.

2.4 Conditions for FDTD method

In the FDTD method, the internal time-stepping is restricted by the ratio of the grid spacing and the fastest propagation velocity, known as the Courant-Friedrichs-Lewy stability condition for hyperbolic equations:

$$\Delta t \leq \frac{1}{c \sqrt{\sum_{i=1,2,3} \frac{1}{(\Delta x_i)^2}}} \tag{16}$$

where Δt is the time-stepping, Δx_i is the spatial grid size in direction i, and $c = 1/\sqrt{\mu\varepsilon}$ is the speed of light in the medium. If we increase the electric permittivity ε_{ij} , the speed of light will reduce. Thus the internal time-stepping is increased, which will result in decrease in the total computational time-step.

For Δx_i , we usually choose $\Delta x_i < \text{wavelength}/10$ to get an accurate simulation results.

3. Numerical Results

In this section, we will present some numerical examples to demonstrate the performance of the present FDTD method.

Example 1:

In the first example, we consider a homogenous, isotropic and nonmagnetic medium as shown in Fig. 3. The highest frequency is 0.25 Hz and the conductivity of the medium is $\sigma^e = 0.5$ S/m. The 3D space is divided into $40 \times 40 \times 40$ grids and the grid size is 50 m. So it is modeling a space as large as $2000 \text{ m} \times 2000 \text{ m} \times 2000 \text{ m}$.

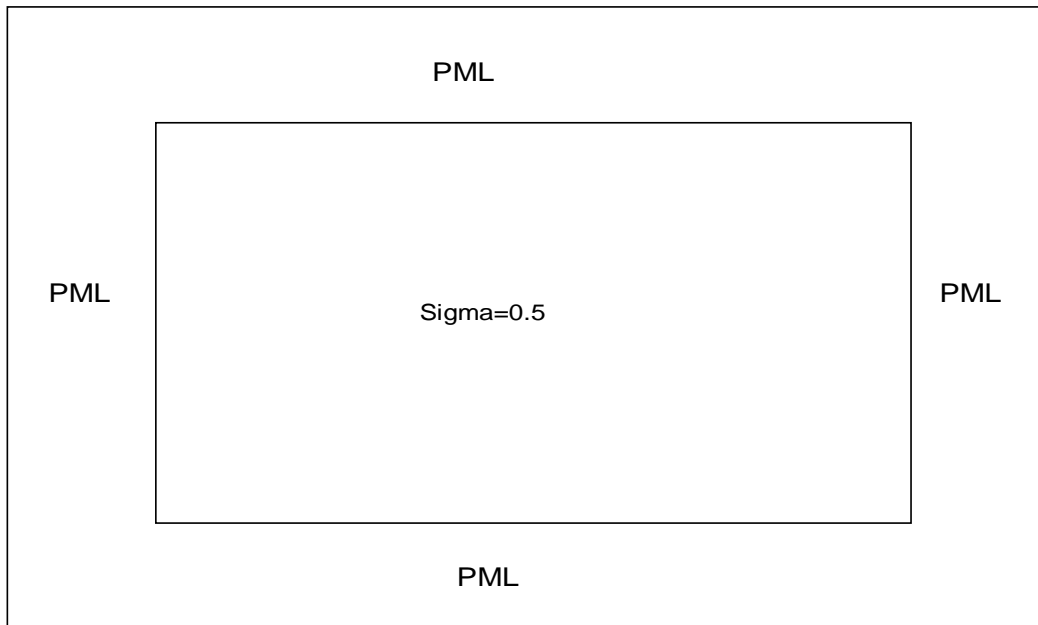


Fig. 4 A homogeneous 3-D space

The source here is a dipole source with a differential Gaussian waveform

$$E(t) = \frac{t - t_0}{\tau} e^{[-(\frac{t-t_0}{\tau})^2]}$$

We use two different boundary conditions: PEC and PML and different relative dielectric constant to compare the results. The thickness of the PML is 10 grids. Fig. 4 and 4 show

the results for different dielectric constant ($\epsilon_r = 9.6 \times 10^4$ and $\epsilon_r = 9.6 \times 10^6$) when the PEC boundary is used.

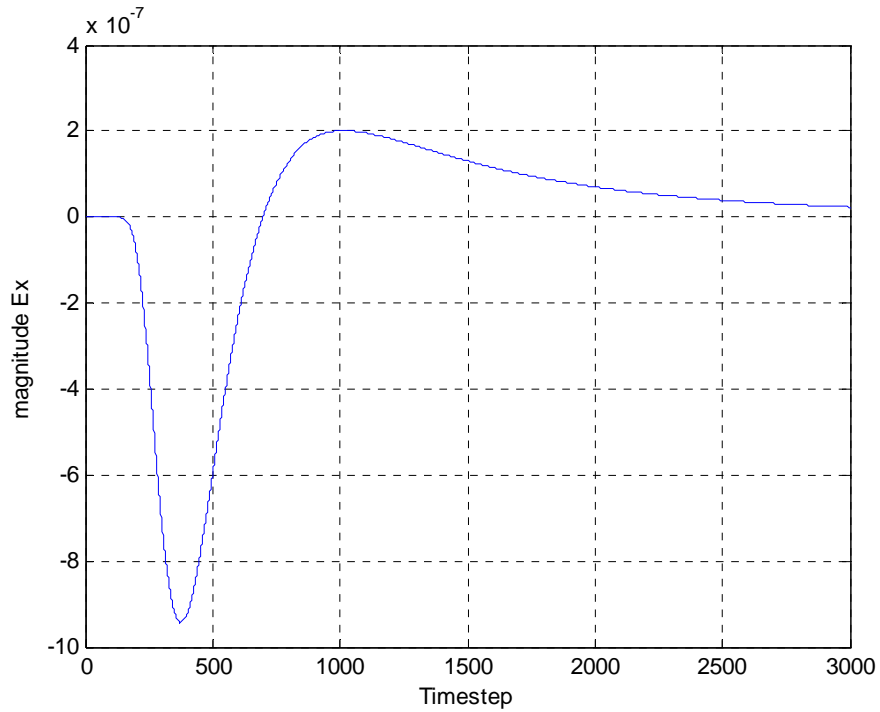


Fig.5 The magnitude of Ex for $\epsilon_r = 9.6 \times 10^4$

($dt = 2.685139170178605 \times 10^{-5}$, $\tau = 7.234573839333053 \times 10^{-4}$)

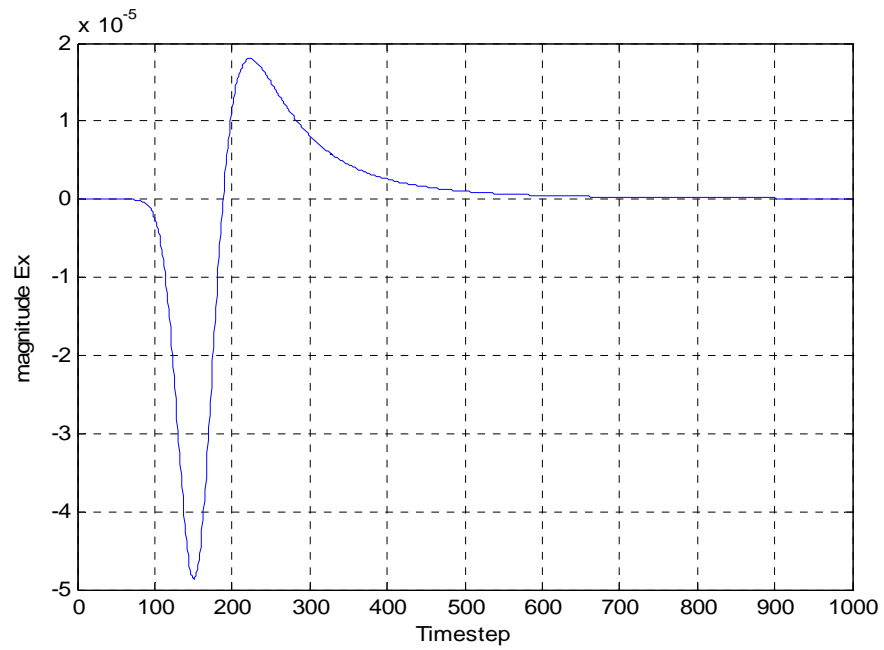


Fig. 6 The magnitude of Ex for $\epsilon_r = 9.6 \times 10^6$

($dt = 2.685139170178605 \times 10^{-4}$, $\tau = 0.00723457383933$)

Fig. 6 and 7 show the calculated magnitude of Ex when using the PML boundary. The transmitter position is at (22, 31, 31) and the receiver position is at (15, 31, 31).

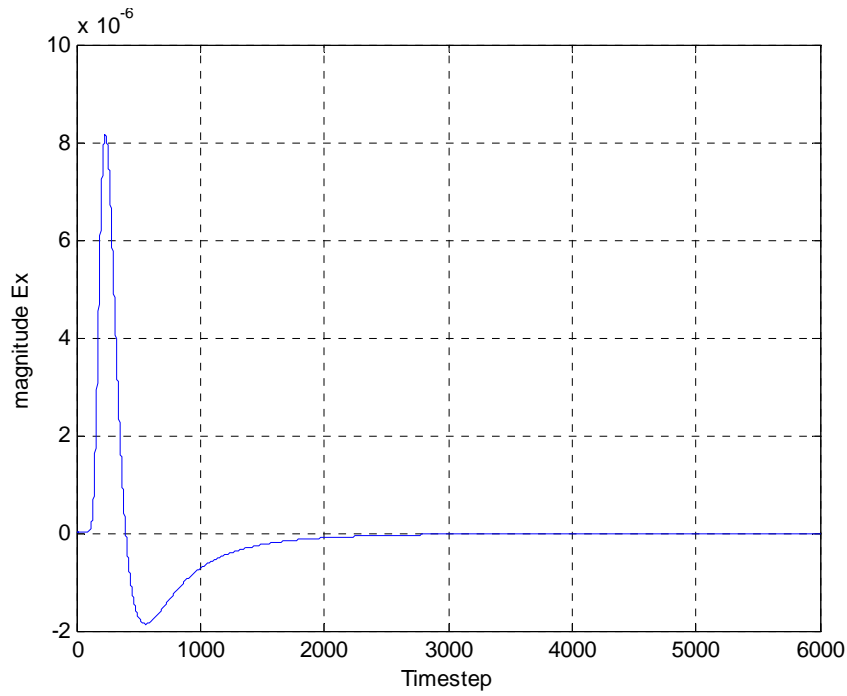


Fig. 7 The magnitude of Ex for $\epsilon_r = 9.6 \times 10^4$
($dt = 2.685139170178605 \times 10^{-5}$, $\tau = 7.234573839333053 \times 10^{-4}$)

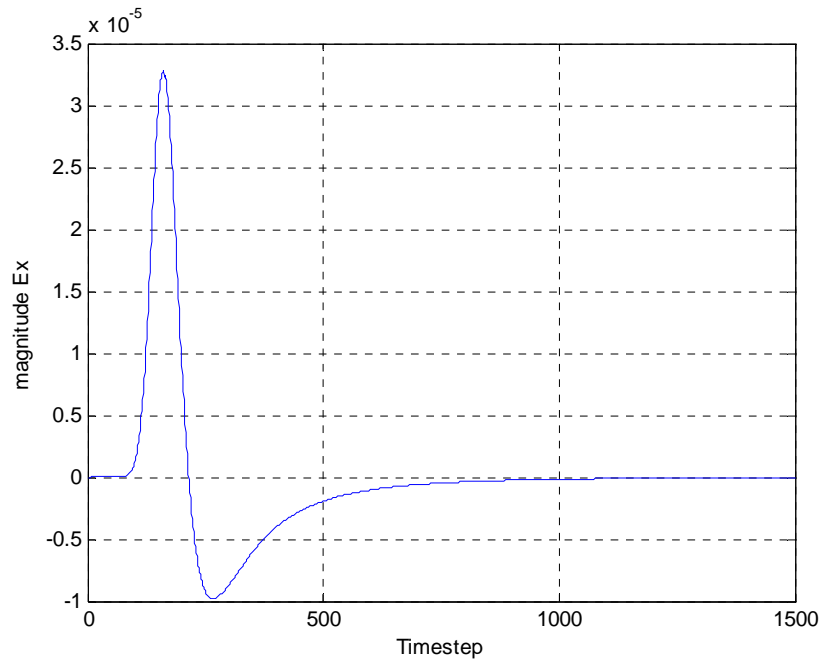


Fig.8 The magnitude of Ex for $\epsilon_r = 9.6 \times 10^5$
($dt = 8.491155612298863 \times 10^{-5}$, $\tau = 0.0022877731233$)

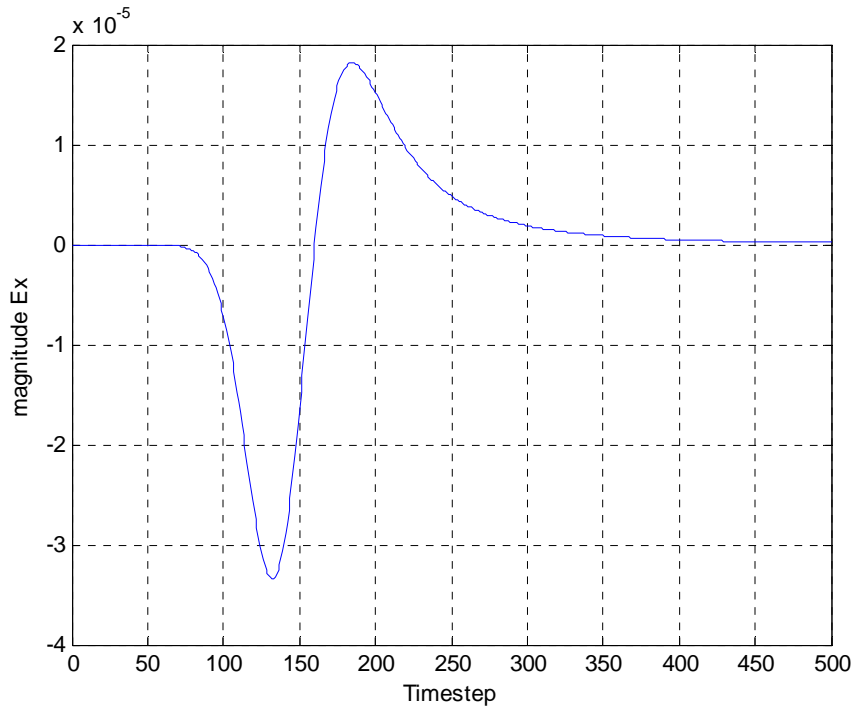


Fig.9 The magnitude of Ex for $\epsilon_r = 9.6 \times 10^8$
($dt = 0.00268513917018$, $\tau = 0.07234573839333$)

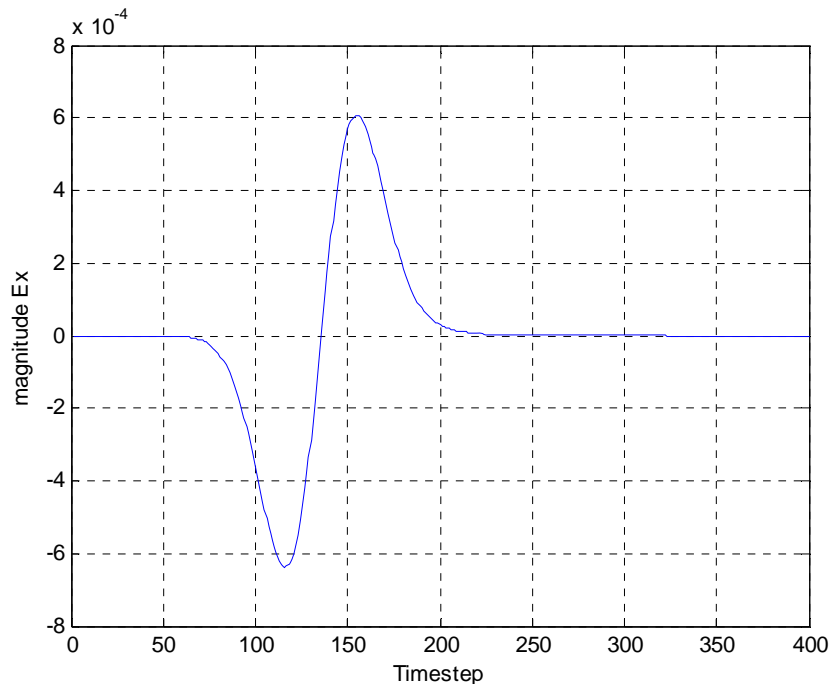


Fig.10 The magnitude of Ex for $\epsilon_r = 9.6 \times 10^8$
($dt = 0.00268513917018$, $\tau = 0.07234573839333$)

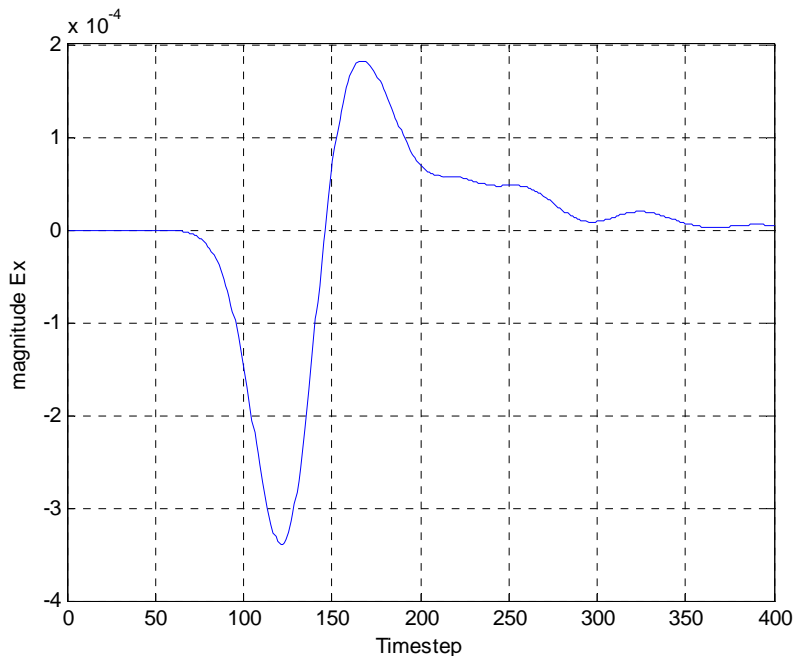


Fig.11 The magnitude of E_x for $\epsilon_r = 9.6 \times 10^{10}$
 ($dt = 0.02685139170179, \tau = 0.72345738393331$)

From the above plots, we can find that the curves changes with the value of dielectric constant. When dielectric constant is chosen to be 9.6×10^{10} , some unexpected ripples come out. So the dielectric constant can not be chosen too big since it will cause unexpected error from the curves.

Example 2

Next, we consider an inhomogeneous, isotropic and nonmagnetic space with the highest frequency being 0.25 Hz. The conductivity of each layer is 0.5, 0.02, 0.5 and 3.6 respectively, as shown in Fig.11. The 3D space is also divided into $40 \times 40 \times 40$ grids and the dimension for each grid is 25 meters. So it is modeling a space as large as $1000 \text{ m} \times 1000 \text{ m} \times 1000 \text{ m}$.

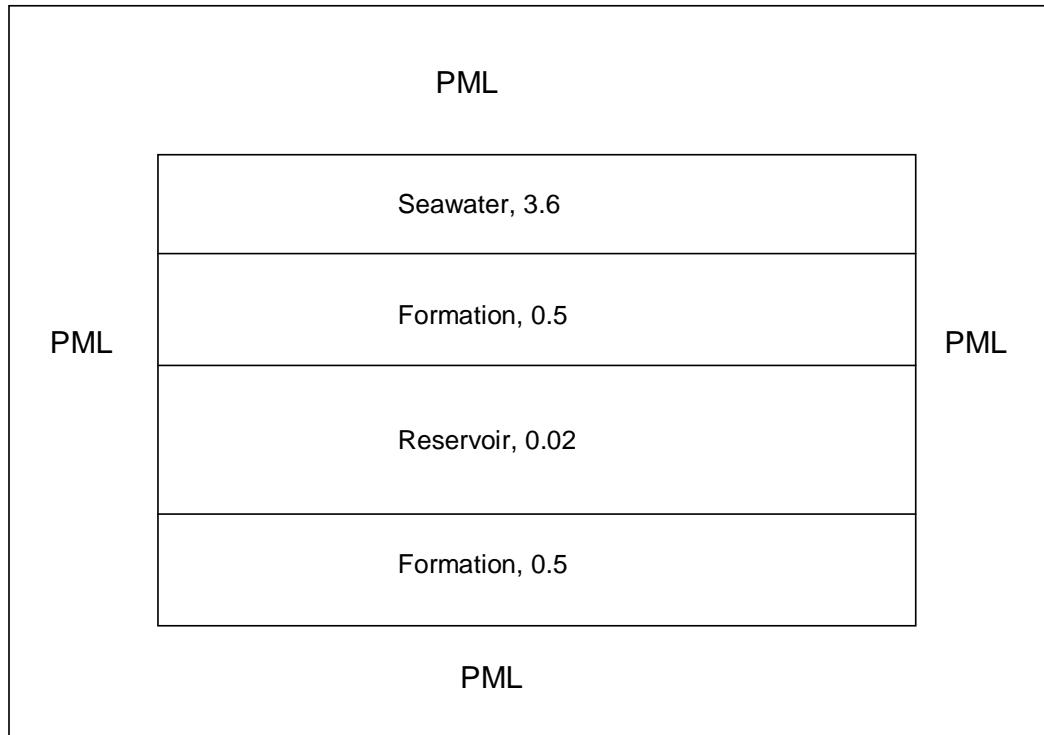


Fig 12 An inhomogeneous 3-D space

The source here is a dipole source Gaussian waveform. The distance between the source and the receiver is 500m. For this example, we only use the PML boundary. The thickness of the PML boundary is 10 grids. Different value of relative dielectric constant is used to compare results.

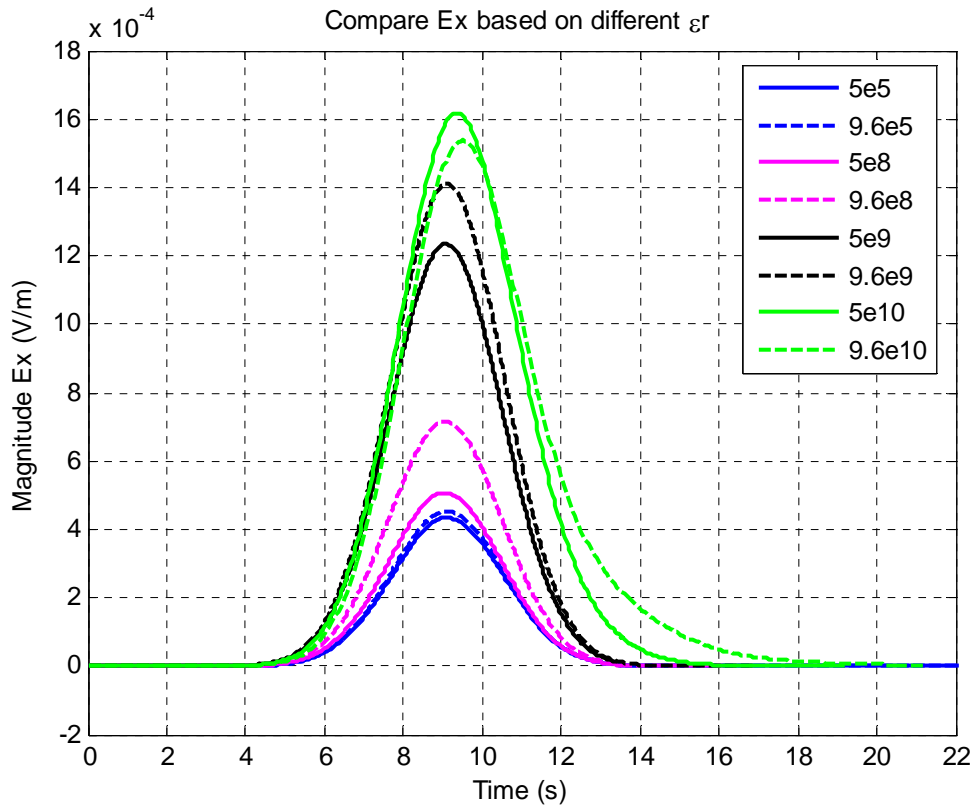


Fig 13 Ex with different dielectric constant

From the plots above, it can be seen that with the increase of the dielectric constant, the curves are changing from bottom to top. The bottom one is most accurate since the dielectric value is smallest but the computation speed is slowest.

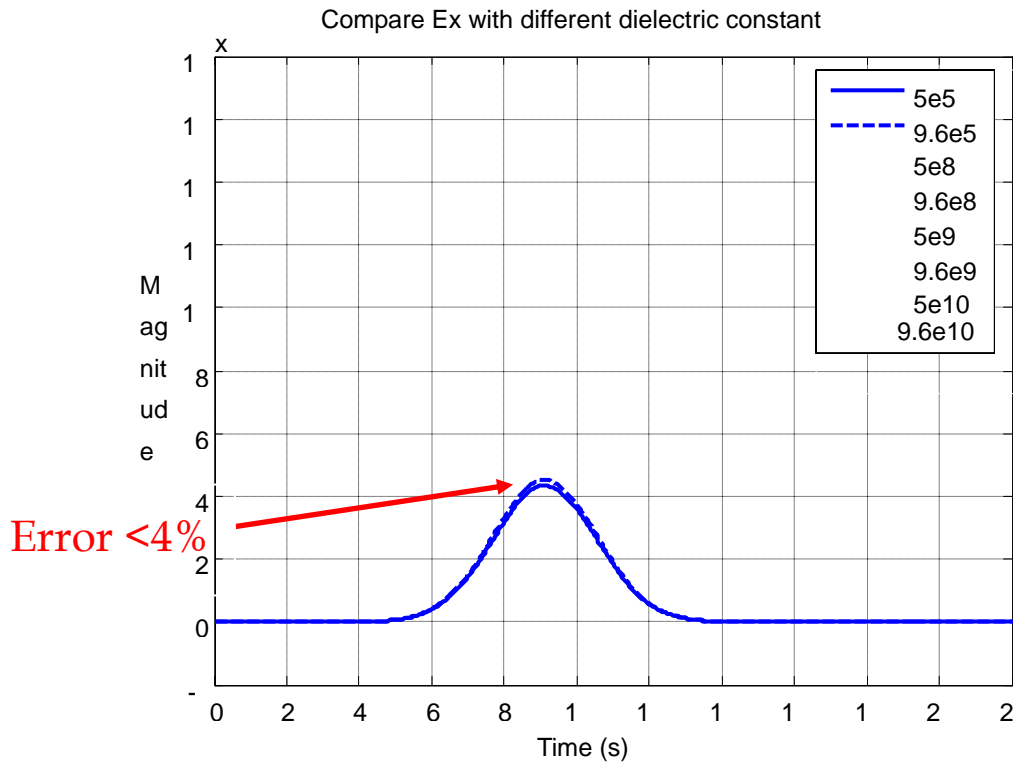


Fig 14 Error analysis

From this plot, I compare the bottom two curves. It can be seen that those two are almost overlap. The difference error which is calculated based on the peak value is less than 4 percent, which is very acceptable.

4. Conclusion

This report looks into the ultra low frequency problem and introduces an method (artificially high dielectric constant) to speed the computation. Speed of the EM waves is affected by dielectric constant, which will change the total number of time step. However, when the dielectric constant is increased artificially, it will reduce the accuracy of the results. Error analysis is also done in order to have a deep look into this kind of low frequency problem. So when the error is within an acceptable level, we can use this method to improve the computation speed.

References

- [1] J.P. Berenger, "A perfectly matched layer for the absorption of electromagnetic waves," *Journal of Computational Physics*, vol.62, 185–200,1994
- [2] T. Eidesmo, S. Ellingsrud, L.M MacGregor, S. Constable, M. C. Sinha, S. Johansen, F. N. Kong, and H. Westerdahl, "Sea bed logging SBL: a new method for remote and direct identification of hydro carbon filled layers in deepwater areas: First Break," 20, 144–152, 2002.
- [3] S. Ellingsrud, T. Eidesmo, S. Johansen, M. C. Sinha, L. M. MacGregor, and S. Constable, "Remote sensing of hydrocarbon layers by seabed logging SBL: Results from a cruise offshore Angola: The Leading Edge," vol.21, 971–982,2002.
- [4] A. M. Frank, "Fast finite-difference time-domain modeling for marine-subsurface electromagnetic problems," *Geophysics*, vol. 72, No.2 March April 2007; P.A19-A23,
- [5] M. L. Oristaglio and G. W. Hohmann, "Diffusion of electromagnetic fields into a two-dimensional earth: A finite difference approach," *Geophysics*, vol.49, 870–894, 1984
- [6] T. Wang and G. W. Hohmann, "A finite-difference, time-domain solution for three-dimensional electromagnetic modeling," *Geophysics*, 58,797–809, 1993.
- [7] The Finite Difference Time Domain Method for Electromagnetics: With MATLAB Simulations Atef Elsherbeni (Author), Veysel Demir (Author)
- [8] Computational Electrodynamics: The Finite-Difference Time-Domain Method, Third Edition Allen Taflove (Author), Susan C. Hagness (Author)

CHAPTER 5

New Addition and Modification to Well Logging Inversion Interface

Abstract

A new forward modeling CIND11 has been added to the Wellog Inversion Interface. It is for simulation of induction tools in radial-layered formation. A new dialog has been adopted in the interface for setting up radial-layered type formation. Moreover, a module has been added to do one-dimensional calculation of AIT focusing tool response. The forward model for LWD tool named LWD10 has been upgraded to take care of multi-channel LWD tool calculation. The dialog for LWD tool creation also upgraded for users to configure their own multi-channel LWD tools. The forward LWDANI11 has been added to calculate response of multi-channel LWD tool in anisotropic media. A simplified version of Wellog Inversion named Wellog Simulator 6.0 has been generated. Wellog Simulator has all the modules in Wellog Inversion for simulation but no modules for inversion. Many other new added features and fixed bugs will also be talked in this report.

1. New modeling codes added to the Interface

1.1 CIND11 code

CIND11 module is developed for calculating response of conventional induction tools in radial-layered media. From inner to outer, the layers can be treated as mandrel, borehole, invasion zones and formation. Number of regions should be no more than 99. The numerical integration accuracy is preset to be 0.01%. Due to the limitation of the code, the conductivity of the mandrel material should not be very high. Otherwise, user should switch to the corresponding module for LWD tool.

Figure 1 shows the new dialog for setting up radial-layered formation. It allows user to define at most 99 layers in one formation file. Users can add or remove any layer they want. Creating and editing function can be completed in this dialog. Note that the first layer is treated as mandrel, so the outer radius should not be larger than the radii of coils that defined in tool file. The default conductivity of mandrel has been set to $1e-6$ S/m. If user wants to change it, be sure it is not very high.

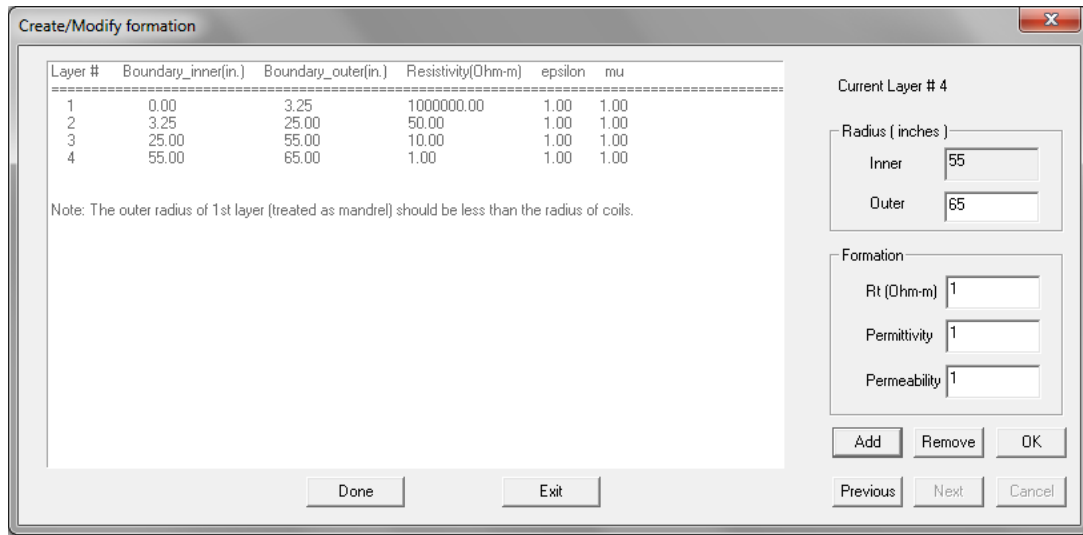


Figure 1 Dialog for cylindrical-layered formation design

The result of CIND11 is essentially zero dimensional calculation, so it is displayed in a list box as opposed to a log curve. An example result is shown in Figure 2. As we can see, all the tool information and formation parameters will also be listed.

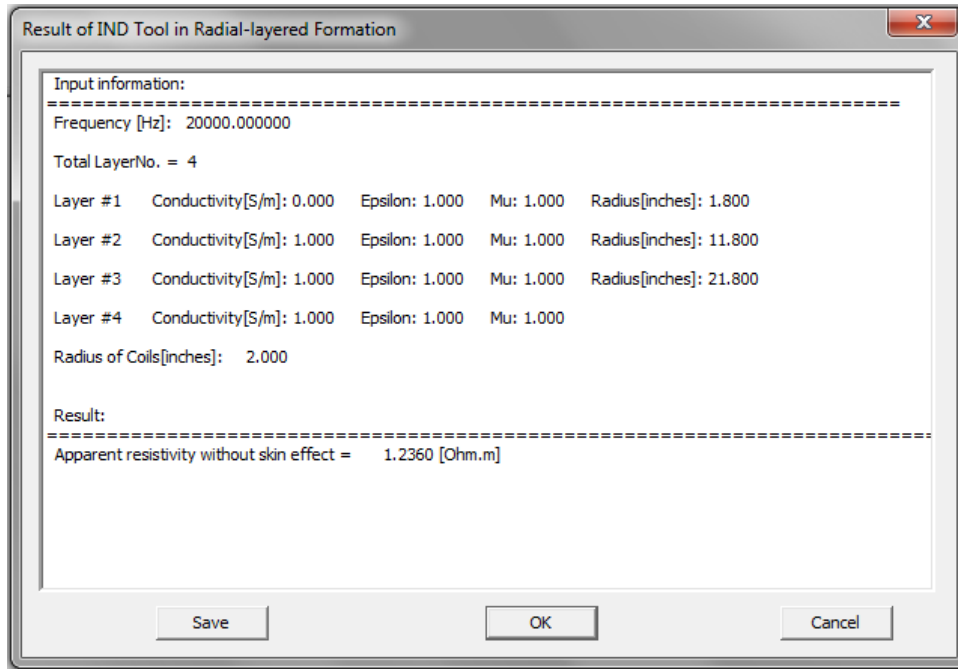


Figure 2 An example result of CIND11 module

1.2 AIT1D code

Previously, AIT tools can only be simulated in 2-D calculations because parameters of AIT tools are confidential and they are only wrapped in a 2-D module. Now we add a wrapper for induction 1-D calculation to provide AIT tools' parameters so that the module for conventional induction tools can also yield results for AIT tools. It is more convenient for users to compare 1-D and 2-D calculations for AIT tools. Figure 3 shows 1-D and 2-D results of a 4-foot set AIT tool in Oklahoma formation. The dipping angle is chosen to be zero.

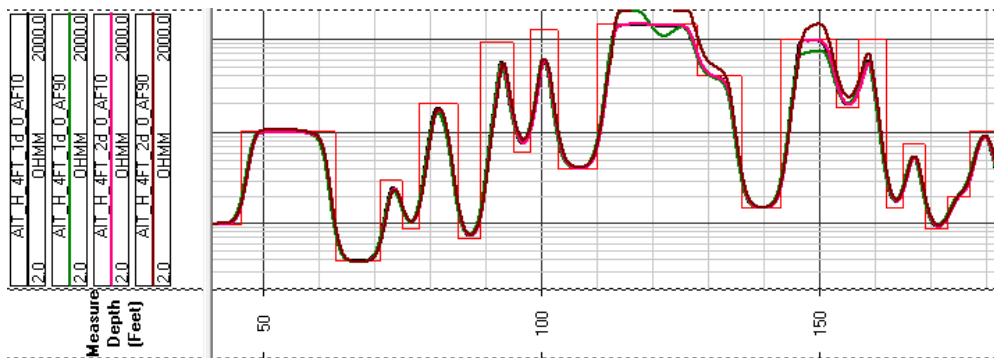


Figure 3 1-D and 2-D comparison of a 4-foot set AIT tool

To have this AIT1D code also allows us to calculate tool response in dipping beds which is not available in 2-D simulation. Figure 4 is the logs of a 2-foot set AIT tool response in Oklahoma formation with a 70 degrees dip. We can see that the results agree well with an early publication [2] which is rendered in Figure 5.

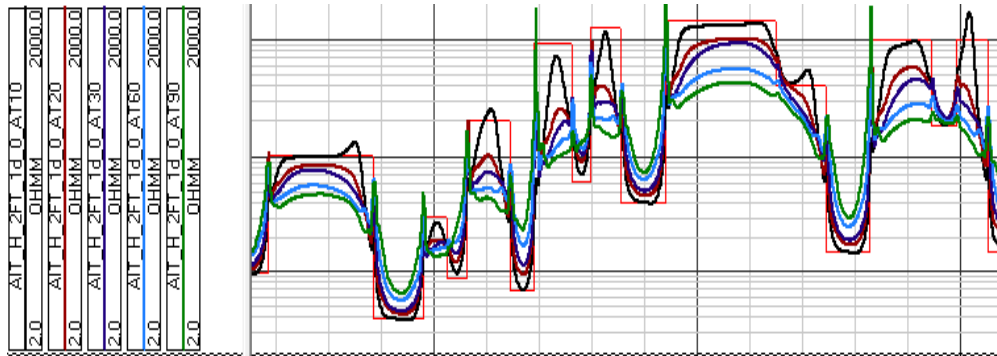


Figure 4 2-ft set AIT tool in Oklahoma formation with 70-degree dip (Wellog Inversion)

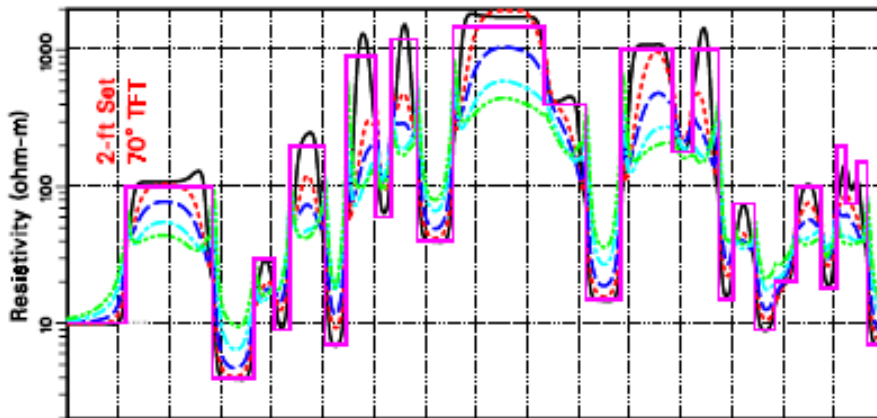


Figure 5 2-ft set AIT tool in Oklahoma formation with 70-degree dip (Barber, 2001)

1.3 Upgraded LWD10 code

Previously, LWD10 code can only calculate the response of a group of one transmitter and two receivers (referred to as a channel) of a LWD tool at one time. That means if a LWD tool has four channels, we need to define four different tool files, and as a results we need to calculate four times to get all the response for this tool. Now the upgraded LWD10 code can take care of multi-channel calculation

which means all the channels' parameters saved in one tool file and the code can yield all the channels' responses at the same time.

To gain a good comparison of every log in each category, two tracks have been adopted for LWD propagation tool, one for attenuation resistivity the other for phase-shift resistivity. Figure 6 is an example layout where the two tracks at right are for attenuation resistivity and phase-shift resistivity respectively.

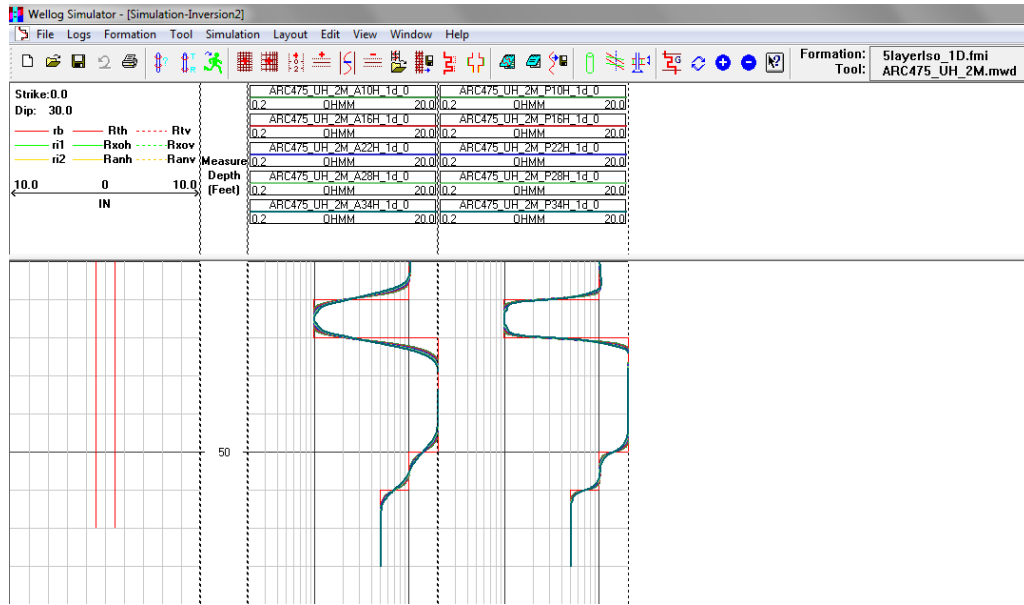


Figure 6 An example layout of LWD propagation tool in Wellog Inversion

So far more than 30 standard LWD tools have been built into Wellog Inversion. All the standard tools' parameters can be found in Ref. [1]. Other than these standard tools, users can define their own tools. Figure 74 and Figure 8 are the dialogs for setting up multi-channel LWD propagation tool. Note that we can define at most 5 channels in one tool file. The dielectric constant equation will decide by company name and operation frequency. Details can be found in table 1. If the company name chose to be "Default", the relative permittivity will be 1.

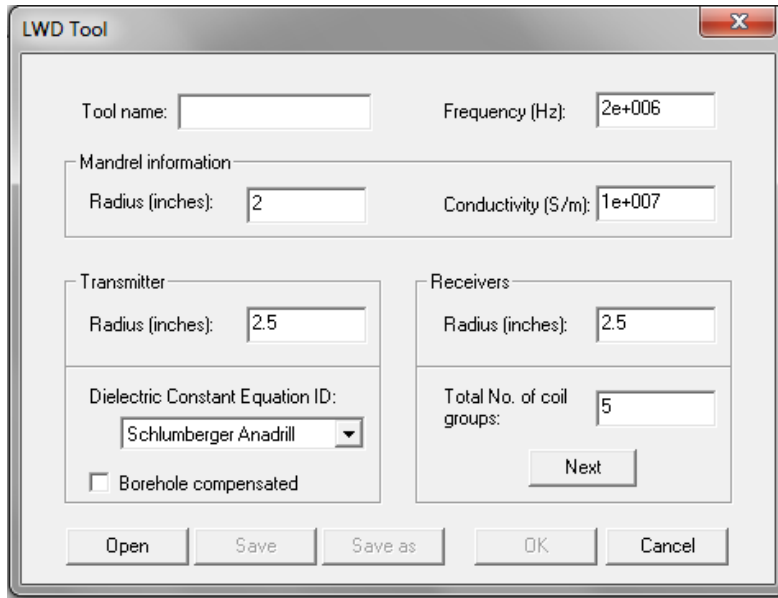


Figure 7 Dialog for LWD tool configuration

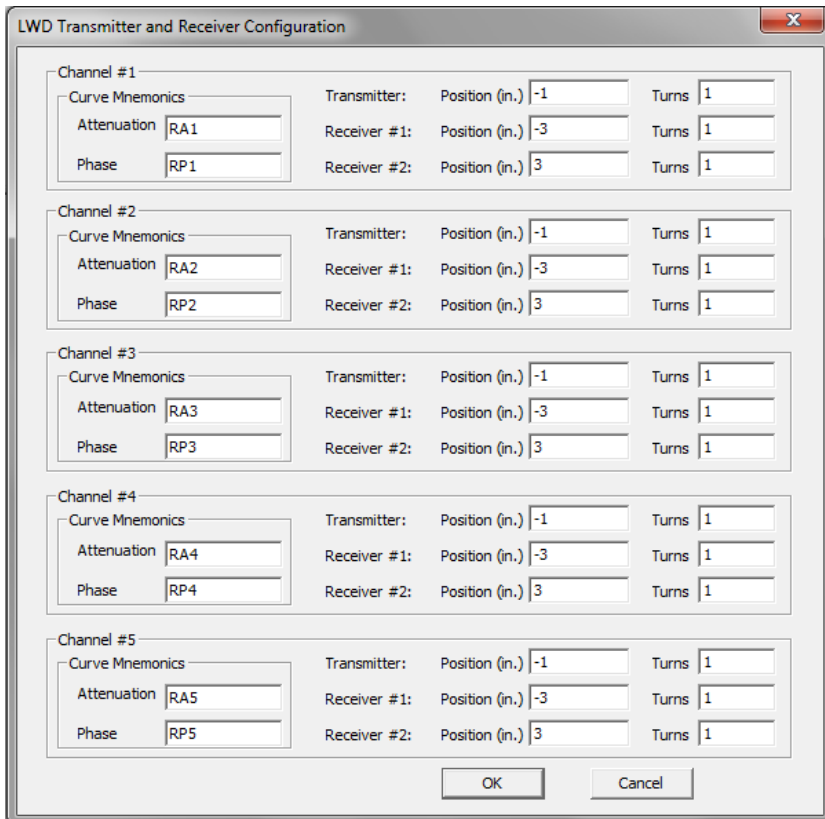


Figure 8 Dialog for LWD tool coils spacing setting

Company	Dielectric Constant Model	ID
APS Technology	$\epsilon = 210 \times R_t^{-0.42}$ (for 2MHz)	11
	$\epsilon = 480 \times R_t^{-0.49} + 8$ (for 400KHz)	12
Baker Hughes INTEQ	$\epsilon = 6.4 + 4.5255\sqrt{1 + \sqrt{1 + (2275/R_t)^2}}$ (for 2MHz)	21
	$\epsilon = 6.4 + 4.5255\sqrt{1 + \sqrt{1 + (11375/R_t)^2}}$ (for 400k)	22
GE Energy	$\epsilon = 108.5 \times R_t^{-0.35} + 5$	31
Halliburton Sperry-Sun	$\epsilon = 10$	41
Pathfinder	$\epsilon = 108.5 \times R_t^{-0.35} + 5$ (AWR)	51
	$\epsilon = 10$ (CWR)	52
Schlumberger Anadrill	$\epsilon = 108.5 \times R_t^{-0.35} + 5$ (for 2MHz)	61
	$\epsilon = 279.7 \times R_t^{-0.46} + 5$ (for 400KHz)	62
Weatherford	$\epsilon = 210 \times R_t^{-0.42}$ (for 2MHz)	71
	$\epsilon = 480 \times R_t^{-0.49} + 8$ (for 400KHz)	72

Table 1 Dielectric Constant Models (from Maxwell Dynamics, Inc [12])

1.4 LWDANI11 code

The forward modeling code LWDANI11 was developed to calculate the response of a LWD propagation tool in an anisotropic layered formation. The transducer axes of the sonde can be arbitrarily oriented with respect to the principal axes of the conductivity tensor of the anisotropic medium, i.e. the dipping angle α , azimuthal angle β , and tool orientation angle γ can be arbitrary. Attenuation resistivity (Ra) and phase-shift resistivity (Rp) are displayed in two tracks respectively.

The following is an example result of code LWDANI11. Figure 9 shows the formation and tool used in this example. The results are in Figure 10. The first logarithm track is for Ra, the other logarithm track is for Rp.

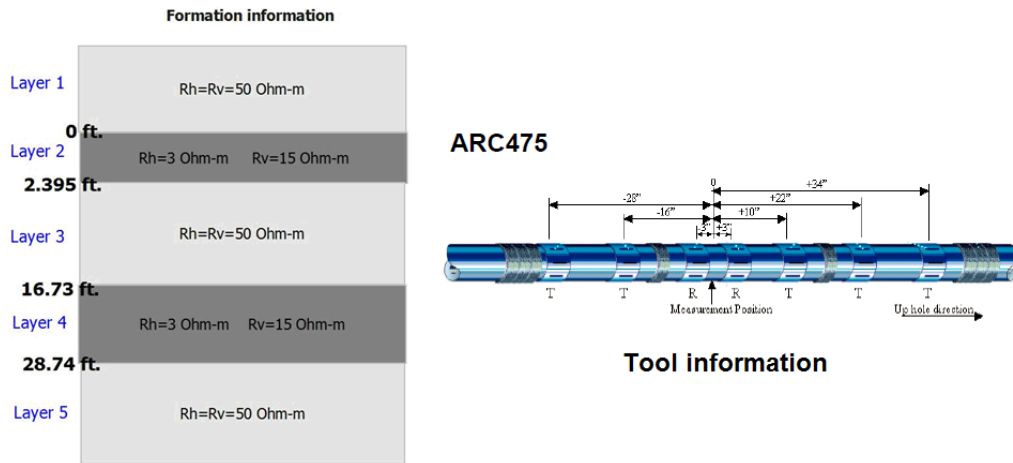


Figure 9 Formation and tool information of the example

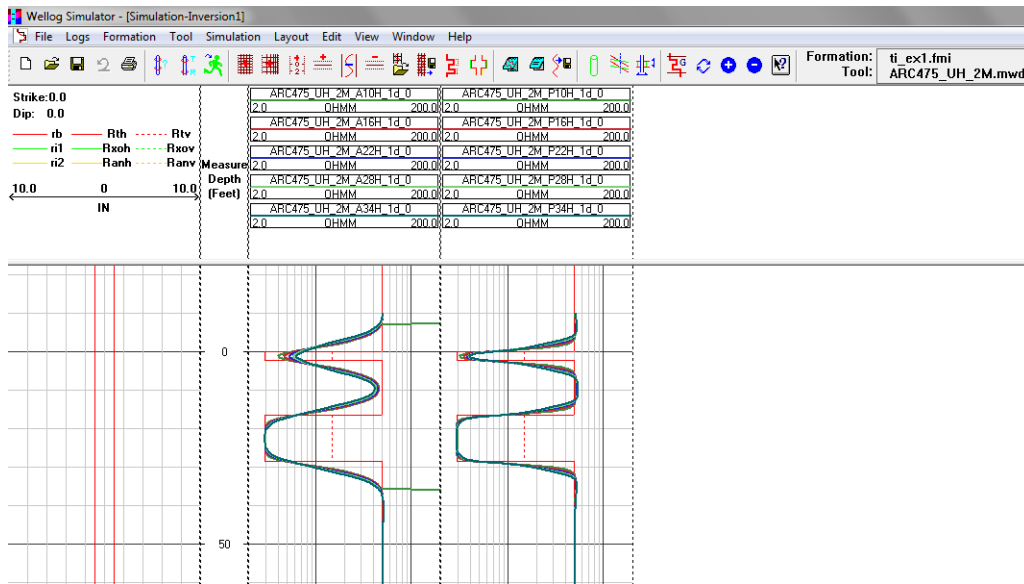


Figure 10 Example result of LWDANI11 code

2. Other improvements in the interface application

2.1 Different tracks for logs of different category

To gain a better view of layout and to make it easier for user to compare logs of different category, we will automatically load logs of different category to different tracks. For instance, we have two linear tracks for the results of TRITI09 code, one is for H-field logs and the other is for apparent resistivity logs. For the results of LWD tools, we have one logarithm track for logs of attenuation resistivity and the other for

logs of phase-shift resistivity.

2.2 Addition of select log dialog

Since there will be many curves in one track, it is not possible for users to view each curve clearly. Now a submenu has been added to enable users select any curve or several curves in a track to display at a time. Right clicking on the legend area of a track, a list box will pop out as shown in Figure 11. The list box lists all the names of logs belonged to this track. Click the names to select logs to be displayed. Figure 12 shows the layout of two selected logs, one in each track. The scale of each track will automatically adjust with scales of all the selected logs. We can see that the layout after selection is much clearer than the original one.

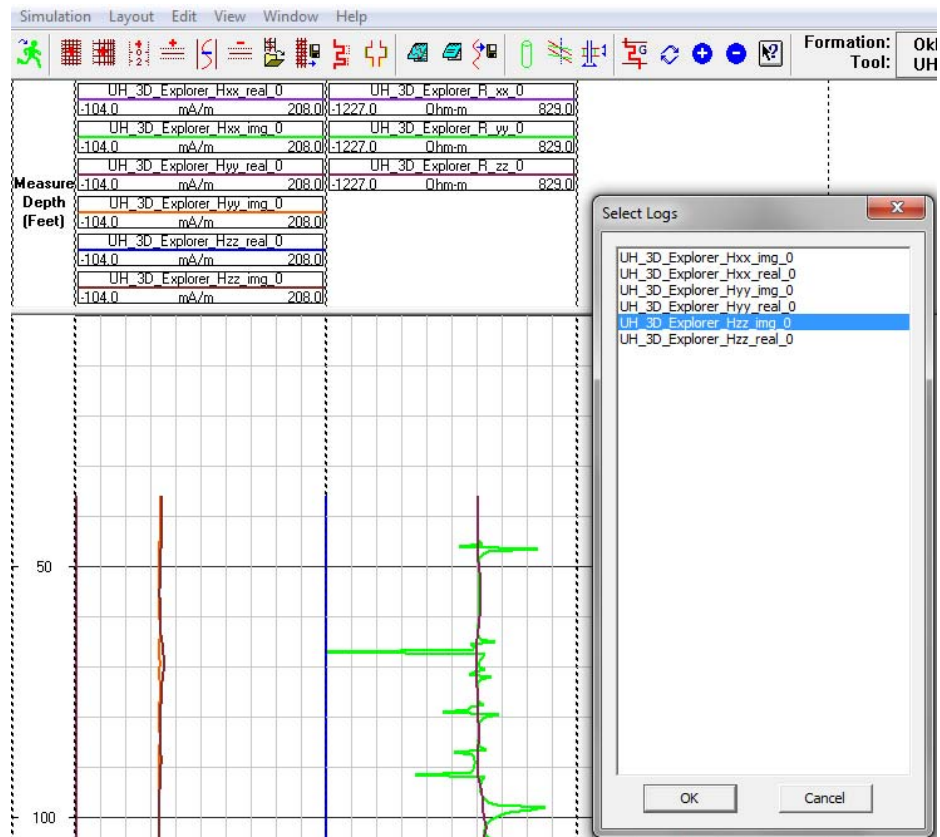


Figure 11 Dialog for select logs

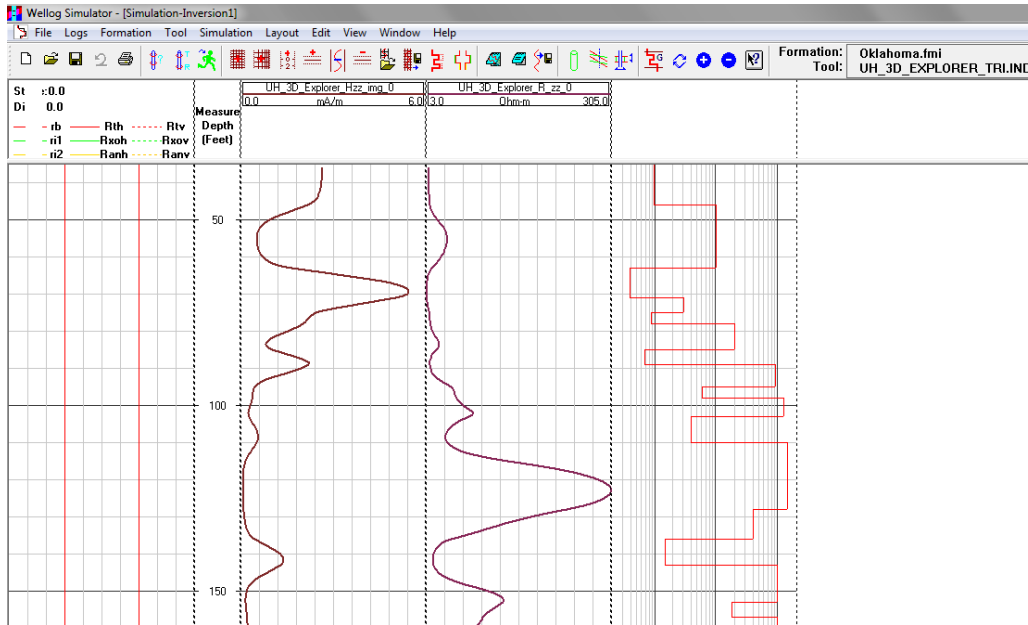


Figure 12 Layout with only selected logs

2.3 Displaying name of selected formation and tools

A region has been added on the toolbar to display names of selected formation and tools as shown in Figure 13. It is more convenient for users to check which formation and tool files they are using. If a new formation has just been created without saving, the displaying name would be “Untitled.fmi”.

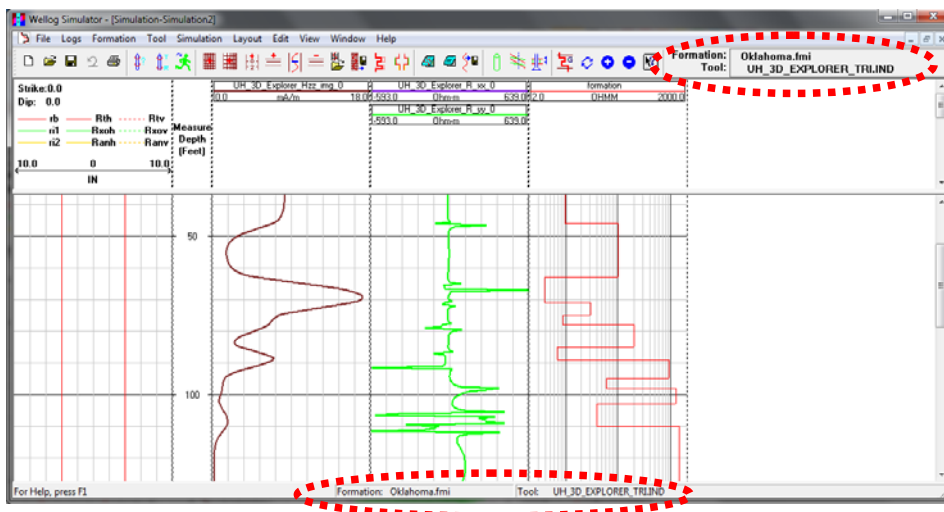


Figure 13 Region for displaying names of formation and tools

2.4 Addition of dialog for selected tools

Previously, all the tools' information is not able to check after they have been defined. Now a shortcut has been added to toolbar as shown in Figure 14 to let users check parameters of all the selected tools. Note that we would not list those tools whose parameters are confidential.

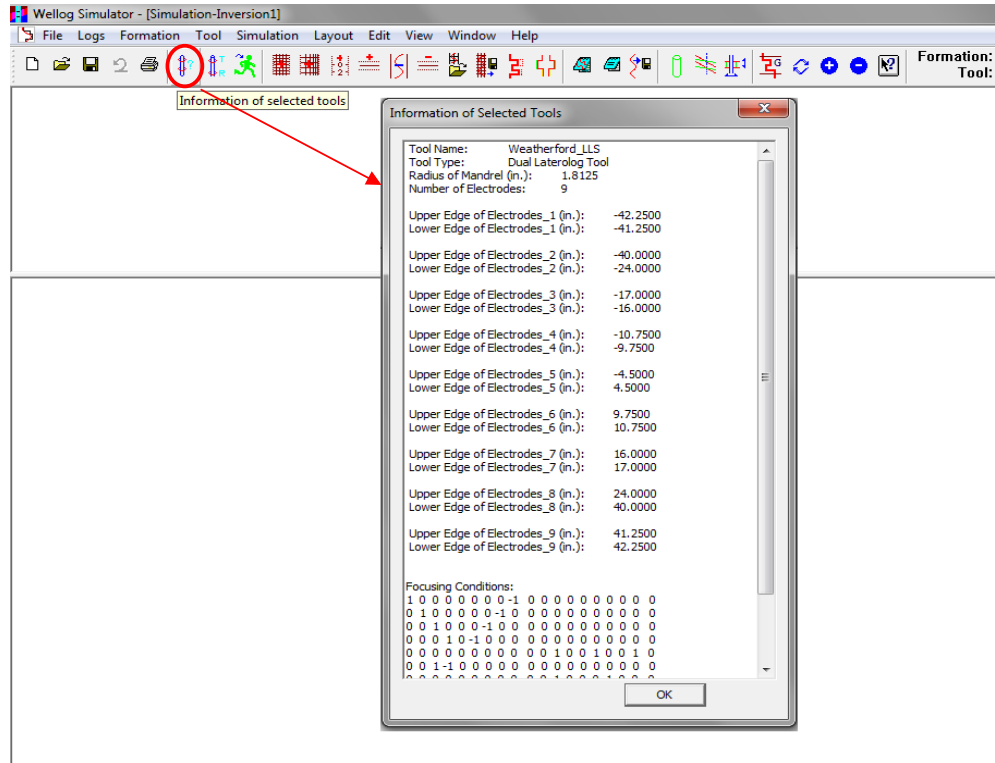


Figure 14 Shortcut button and list box for selected tools

2.5 Bucking coil configuration in tri-axial tool

The bucking coil is a coil placed between transmitter and receiver coils to reduce the direct coupling between transmitter and receiver coils. Figure 15 shows the dialog for setting up tri-axial induction tools. If there are two coils in receiver section, one as receiver the other as the bucking coil, the turns of the bucking coil will be calculated by code automatically. Explicitly,

$$Turn(bucking_coil) = -Turn(receiver) * \left(\frac{Dis\ tan\ ce(transmitter\ \&\ receiver)}{Dis\ tan\ ce(transmitter\ \&\ bucking_coil)} \right)^3$$

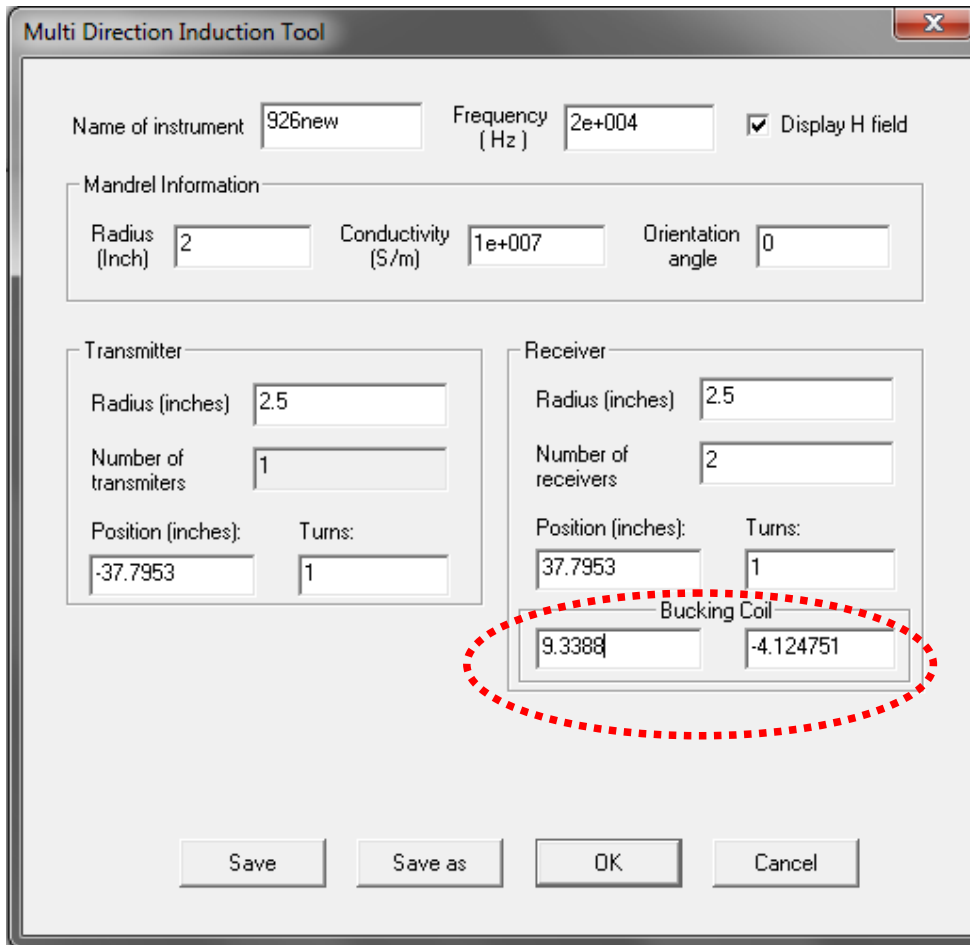


Figure 15 Dialog for tri-axial tool configuration

2.6 Updating help file and manual

All error codes in the help file have been corrected. New additions and modifications have been added to the help file and user manual.

2.7 Other fixed bugs in Wellog Inversion

1) Logging point restriction

In the old version, to avoid overflow in FORTRAN, Wellog Inversion had a limitation on logging stop position to be no larger than 10,000 feet. It is not reasonable since logging can be conducted at any depth. Now we have changed the restriction to the

maximum logging points to be 10,000.

2) Borehole compensated coil position

Previously, if the borehole compensated feature is checked, Wellog Inversion would take the opposite value of original transmitter's position as the compensated transmitter's position. It would be a problem if the middle point of the receiver pair is not at zero. Now new algorithm has been adopted to calculate the transmitter's position.

3) Dialog for run simulation crashes a lot

If any mal-operation happened, there would pop out an error message which would also disable the OK button. Even though the user made a right choice at last, the OK button is still disabled. Now this bug has been fixed.

4) Larger length for log name when saving a log

In the old version, the string length for log name was not large enough and as a result the log name was not complete when saving a log. Now we have made a larger string length for log names. Also, a limitation has been made to the length of tool name so that the log name would not exceed our expecting length.

5) Automatically calculate tool constant when saving laterolog tool file

Originally, when defining a laterolog tool, if user does not click "Calculate tool constant" before saving the tool, the tool constant would save as default value regardless of the tool's configuration. Now interface will calculate the tool constant automatically when saving the tool file.

3. Wellog Simulator 6.0

Wellog Simulator 6.0 is a simplified version of Wellog Inversion. It inherits all the forward modeling modules in Wellog Inversion and removes all the inversion modules. Wellog Simulator 6.0 intends to be a compact interface for 1D and 2D simulation for all the induction, LWD and laterolog tools. No 3D module is integrated to Wellog Simulator 6.0.

Wellog Simulator 6.0 requires users to select tool first. Formation selection or creation is allowed only after tool selection. This enables the interface to lead users to load proper formation for the tool they selected. For example, radial-layered formation is not allowed to create or load if the selected tool is not conventional induction tool. This makes sure that users do not waste their time.

Wellog Simulator 6.0 automatically checks all the allowed dimensions to calculate after formation and tool selection. If user wants to do other dimensional calculation, interface will give a reminder message and then automatically configure needed parameters for the chosen calculation. For instance, if a 1D formation is defined, but user wants to run 2D simulation, interface will remind user that it will automatically give borehole radius, mud conductivity and parameters of invasion and then do the 2D simulation.

References

- [1] John Zhou, “LWD/MWD Resistivity Tool Parameters,” Maxwell Dynamics, 2010.
- [2] Thomas D. Barber and Frank Shray, “Case Studies Using Advanced Interpretation Techniques for Induction Logs,” SPE, 2001

CHAPTER 6

Wireless Relay Network: Novel Data Transmission Approach for Measurement-While-Drilling Telemetry

Abstract

This project presents a novel downhole data transmission solution, Wireless Relay Network (WRN), to facilitate data telemetry in measurement-while-drilling (MWD) telemetry for oil and gas exploration. WRN includes the following key designs. First, we use small form factor transceivers (nodes) to construct bi-directional, multihop wireless links in the downhole environment. Second, we adopt an efficient hierarchical architecture consisting of Basic Relay Nodes (BRN) and Routing Initiation Nodes (RIN): BRN simply forwards packets to intended destinations, while RIN involves higher-level protocols such as routing and error detection. Finally, we propose a network protocol including routing and packet retransmission schemes to serve specific demands of WRN. Simulations with different settings are conducted to demonstrate the feasibility of WRN. Modeling the downhole MWD tools as a 1024 bps source, an overall throughput of 660 bps can be reached over a 10,000-meter transmission distance. As a high-speed transmission method, WRN can be a promising alternative to currently used data transmission techniques in the oil industry.

1. Introduction

High-speed data transmission has long been a preferable feature of advanced Measurement-While-Drilling (MWD) telemetry techniques in the oil and gas industry. Various downhole information is collected by sensors during drilling process, including directional parameters, drilling conditions, and formation characteristics. All the data are stored to be retrieved later to create a complete well log, while some are selected to be transmitted to the surface in real time. Operator can thus instantly make optimal decisions on drilling operation to maximize drilling efficiency and productivity, as well as to avoid

potential tool failures or subsurface accidents [1]. In some cases, it is also necessary to send commands downward to control the bottom hole assembly tools. Therefore, a two-way communication link is generally required.

The most widespread telemetry method used in current MWD systems is mud pulse telemetry (MPT), designed by J. J. Arps in 1964 [2]. Using a controllable valve in the drill collar, the pressure of drilling mud flow is modulated with a digital signal that can be recovered at the surface. During the past few decades, MPT has been improved by using advanced mud pulsers and data compression schemes [3]-[5], although the data rate is still as low as 1-30 bps [6], [7], limited by its intrinsic mechanical features. Moreover, it does not apply to certain circumstances such as underbalanced drilling, where the pressure of drilling mud cannot be easily changed due to the presence of compressible inert gas contents.

Another solution for data transmission from the bottom to the surface while drilling is Electromagnetic Telemetry (EMT), which uses electromagnetic propagation through the earth [8], [9]. By emanating a modulated signal from the borehole through the formations, data can be sent up to the surface at a rate of up to 100 bps. Although EMT is a good alternative to MPT in some cases, it is problematic in wells of great depth. Higher frequency signal suffers severe attenuation through the conductive formations [10]-[12], while low frequency signal is easily disturbed by seismic currents and other interference in the earth. Both factors consequently lead to an extremely low signal-to-noise-ratio at the receiver and therefore unreliable telemetry results.

To completely insulate the signal from environmental disturbance, a wired drill pipe system, Intellipipe, was presented by Grant Prideco in 2003 [13]. Intellipipe uses high-speed cables built in the drill pipe to accomplish a two-way communication link. According to the field trial reports, a bandwidth of 57,000 bps can be achieved [14]-[17]. However, the whole technology is based on the specially-designed equipment including adapted top drive and drillstring, which makes it expensive and non-adaptive. Another disadvantage lies in the potential mechanical weakness of the system. Any damage to a pipe joint can lead to a communication failure and increase downtime.

In this project we present a novel high-speed downhole data transmission solution, Wireless Relay Network (WRN), which utilizes small form factor radios to construct a multihop data link in the drill pipe. The radios (hereafter referred to as “nodes”) can be attached to the inner wall of the pipe or floated by the drilling mud, and act as transceivers to form a multihop network, realizing bi-directional data transmission. Using drilling liquid as the transmission medium, WRN is not subject to the limitations of EMT, while supporting a competitive data transmission rate from end to end.

The primary concept of WRN was originally proposed by Naseri and Liu in [18]. It shows the feasibility of using a few transceivers to build up a relay link in the drill pipe, but lacks a detailed system framework to make it deployable in practice. In this report, we provide a thorough discussion on the specifications and features of WRN, and accordingly develop a communication protocol to better serve its demands. A series of simulations are performed to verify the transmission capability of WRN. With appropriate hardware design, a data rate of over 660 bps can be expected along a 10,000-meter travel distance, which is able to facilitate most communication applications in downhole systems. Even for borehole assemblies with high-resolution imaging tools, real time data can be acquired and processed instantaneously at the surface.

2. Network Overview

The basic concept of WRN is illustrated in Figure 1. Wireless transceiver nodes are placed inside the drill pipe during periodical pipe augmentation, connecting downhole MWD tools and the computer station on the surface. Nodes can be attached to the inner pipe wall or not, leading to *static* or *mobile* WRN, respectively. For mobile WRN, floating nodes are carried by the drilling mud and flow back through the annulus for recycling purposes [18].

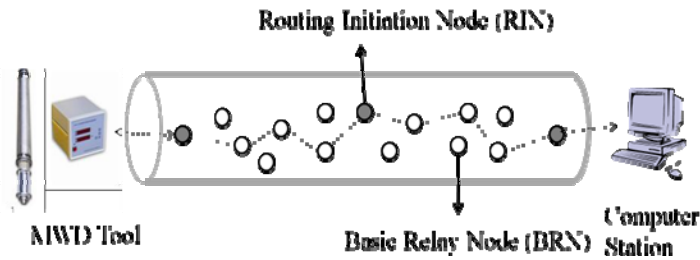


Figure 1 Basic concept of WRN

The hardware architecture of a WRN node is shown in Figure 2. Low-power RF transceiver is connected to microcontroller unit to accomplish necessary digital processing in the base band. The two parts are also integrated by System-on-Chips, e.g., CC2540, which can achieve a maximum data rate of 1Mbps at 2.4 GHz [19]. The prototype of WRN node is to utilize similar products.

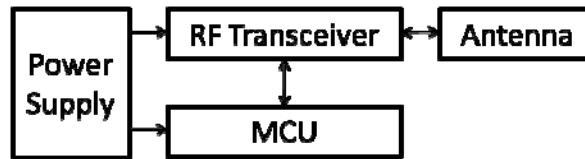


Figure 2 WRN node design

An effective power supply system is essential to WRN. For mobile WRN, the nodes should at least be powered while flowing from top to bottom, depending on the flow rate of the drilling liquid; for static WRN, the longevity problem of power supply is even more challenging, since it is inconvenient to retrieve nodes frequently. Potential power solutions, such as high-efficiency batteries, directional antennas, mud turbine generators and various power management schemes for communications, will be taken into consideration and keep open for discussion in the future stages of our research. However, instead of solving such general implementation issues, this paper will mainly focus on the network functionalities and pertinent transmission protocol optimization.

As an ad-hoc wireless network, WRN for MWD telemetry has some distinguished features that require special treatment to optimize the network performance:

High latency: WRN is a network with a single source node and a single destination node at each end of the pipe, and a large number of intermediate relay nodes. According to [18], a typical transmission range for a transceiver node in oil based mud is around 10 meters. This means for a 10,000-meter-long pipe, the minimum number of hops from end to end is 1000. Assume a 20 ms processing delay is added in at each hop, it will take over 20 s to deliver a single data packet. Given such conditions, some of the prevalent transmission schemes, like end-to-end packet acknowledgement, will simply become impractical and have to be modified.

Periodically increased network scale: WRN is a self-expanded network. New nodes are placed in with installation of every pipe section, thus the network size and span are increasing regularly and periodically. This feature can be leveraged to improve network performance. For example, since the network stays relatively static during the interval between every two pipe installation operations, route information can be updated less frequently to avoid unnecessary control overhead.

Reliability-oriented: Reliability is regarded as the top priority in WRN system. Since the source data are generated continuously while drilling, data loss can be critical. Therefore, error detection and/or correction and packet retransmission are necessary. Moreover, in case of node loss, a certain amount of node density should be guaranteed, so that the whole communication link would not be completely interrupted by a minor node failure. This in turn imposes a tradeoff between signal-to-interference ratio and redundancy on system design and protocol optimization.

In addition, WRN nodes are intended to be developed on relatively low-cost systems, which usually have limited memory and processing capability. As a result, the communication protocols of WRN should be light-weighted.

3. Network Hierarchy and Protocols

3.1 Network Hierarchy

Two types of nodes are defined in WRN: *Basic Relay Nodes (BRN)* and *Routing Initiation Nodes (RIN)*. RIN nodes are distributed equidistantly in the pipeline, while multiple BRN nodes are placed between every two RIN nodes, as shown in Figure 1 and Figure 3.

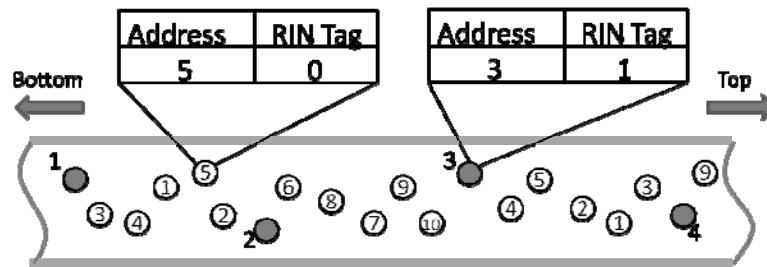


Figure 3 WRN addressing

BRN nodes function as the most fundamental relay stations, forwarding data packets until they reach the nearest RIN nodes. They do not generate or maintain any control information.

RIN nodes involve higher layer functions such as routing and reliability management. They act as bridges that connect two groups of BRN nodes from both sides. Local route information is collected and updated by RIN nodes. They also perform data error detection and request packet retransmissions to guarantee a reliable transmission.

The hierarchical architecture of WRN is designed to reduce control overhead and processing latency. Considering about the extremely slim network structure of WRN, it is unrealistic to acquire global information in a short time. With RIN nodes, the whole network is divided into multiple subnets, inside which local network statistics can be easily updated and handled. For example, instead of finding an end-to-end path, global route information is broken into segments and stored at RIN nodes. In other words, an RIN node only needs to know how to reach adjacent RIN nodes through a multihop BRN link. A similar structure is used in [20].

3.2 Routing

The addresses of RIN and BRN nodes are assigned separately. The two types of nodes are differentiated by the last bit in addresses (RIN tag): 1 for an RIN node and 0 for a BRN node.

RIN addresses are sequentially assigned from bottom to top. Since the relative depth information is implied by addresses of RIN nodes, the directions of packet transmission can be easily controlled. For example, for logging information that is supposed to be transferred from MWD tool to the surface, RIN nodes will select specific routes that can reach neighboring RIN nodes with larger RIN addresses instead of smaller ones.

BRN addresses are not strictly associated with location information but randomly assigned in a certain range. In fact, BRN addresses can be spatially reused without confusion. As shown in Figure 3, two groups of BRN addresses, 1-5 and 6-10, are used reciprocally in the pipe. There will be no identification problems because RIN nodes only collect local route information involving adjacent RINs, as mentioned above. Take the address assignment in Figure 3 for an example, if appeared in a routing table of RIN 2, a BRN 4 refers to the one located between RIN 2 and 1; but for RIN 3, BRN 4 is along the path to RIN 4.

Since the topology of WRN remains relatively static during most time, a proactive routing scheme is adopted, i.e., route discovery procedure is performed periodically instead of on demand. First, each RIN node broadcasts a route request (RREQ). All nearby BRN nodes forward this request until it reaches another RIN node, which immediately sends back a route reply (RREP) with available route information. This information is then kept in a routing table and updated if any route dynamics are detected. Since there could be multiple paths between RIN nodes, the whole communication link will not be completely broken due to any minor node loss.

The routing table consists of both upstream and downstream path information. When a data packet arrives, the RIN node checks the direction of its destination, and selects a route in the corresponding category. The used path is then set with an occupation flag for a certain time cycle before it can be selected again.

3.3 Packet Retransmission

We use cyclic redundancy check (CRC), a simple but effective code for error detection [21], because of its advantage to deal with burst errors which may happen frequently in WRN.

As shown in Figure 4, when a data packet arrives at an RIN node, CRC is re-calculated from the original data field and compared with the received value. If the check values match, the receiver RIN will send back an acknowledgment (ACK) to the previous RIN, and push the data packet to the buffer for transmission; otherwise it sends out a negative acknowledgment (NACK) to request a retransmission. The number of retransmissions cannot be higher than MAX_RETRANS, otherwise the data packet will be discarded. Every data packet should be stored at the RIN after being transmitted. Without ACK or NACK, a packet will be transmitted again along a different path.

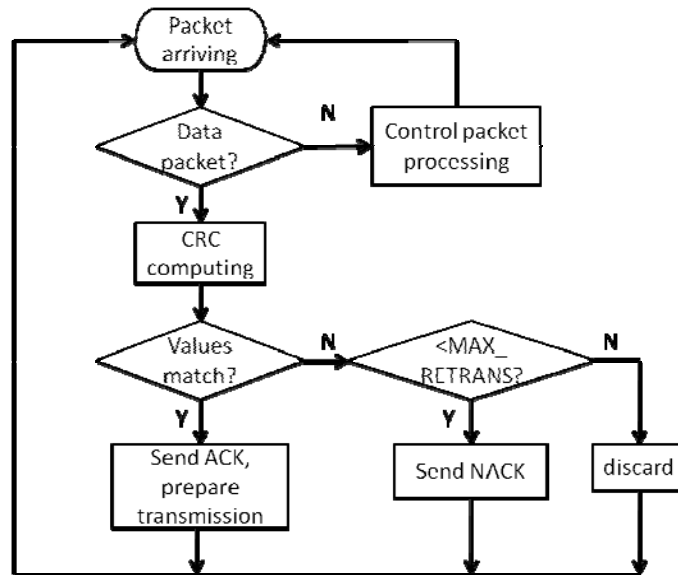


Figure 4 Error detection algorithm

4. Simulation

Simulations are performed to verify the feasibility of WRN. The main parameters are

listed in Table 1. Node locations are uniformly generated with an average density of 0.4 m^{-1} , i.e., the average distance between two nodes is 2.5 m, which allows a node with a 10-meter transmission range to reach 3 to 4 neighboring nodes in either direction for redundancy. RIN nodes are distributed with a constant percentage (5% or 10%) and equidistantly. Here we assume all the nodes are static, and no node loss happens.

Table 1 Simulation Parameters

Parameter	Value
data transmission rate	1 Mbps
transmission distance	1,000 m - 10,000 m
pipe diameter	10.47 cm (4.125 in)
node density	0.4 m^{-1}
RIN percentage	5%, 10%
data source rate	256, 512, 1024 bps
data packet size	16, 24, 32, 48 byte
transmission range	10 m
bit-error-rate (BER)	10^{-4}

First, throughputs under multiple scenarios are tested and listed in Table 2. A data source with three different rates is used to generate continuous binary stream, and data are split into 32-byte packets. The communication medium is modeled as a channel with a random bit-error-rate (BER) of 10^{-4} .

As the results show, the overall throughput dramatically decreases as the total transmission distance increases, due to more packet loss and higher end-to-end latency. However, the decreasing rate is much lower when there are more RIN nodes in the network. Take the case with 1024 bps source as an example, the throughput with 10% RINs is almost twice of that with 5% RINs over a 10,000-meter transmission distance. It can be inferred that although increasing RINs means longer computing and processing time, it prevents even more packets from being discarded by frequent check through transmission.

Table 2 End-to-End Throughput (bit per second)

RIN percentage	Transmission Distance (km)	source		
		256 bps	512 bps	1024 bps
5%	1	235.68	469.19	931.54
	2	208.88	426.52	827.93
	3	192.09	373.50	758.49
	4	173.96	341.13	678.63
	5	151.16	302.32	621.23
	6	137.83	278.39	549.73
	7	124.24	245.76	503.31
	8	111.78	220.06	443.32
	9	97.10	206.37	397.74
	10	88.06	179.84	368.43
10%	1	246.58	489.11	983.04
	2	233.01	469.32	939.69
	3	223.89	447.94	897.72
	4	214.14	433.14	847.44
	5	203.89	413.18	825.18
	6	195.62	396.12	789.23
	7	188.92	369.30	747.03
	8	179.80	350.32	716.36
	9	170.08	344.91	689.38
	10	165.55	329.30	659.25

It should be emphasized that although we used different source rates to simulate MWD tools on different complexity levels, the congestion conditions of the whole network was not taken into consideration. Buffers of the nodes are treated as ideal, which means no packet loss is caused by congestion. Therefore, although better throughput can be facilitated by a source with higher sampling rate, it raises higher demands on node design: buffer capacity, memory size, and so on. A compromise must be reached to balance all these factors well.

Next we observed the behavior of packet delivery rate and average delay against different packet lengths, as in Figure 5 and Figure 6. A 1024 bps source is used in this experiment. It can be reflected by the figures that longer packets are apparently more vulnerable to bit errors, and thus are more likely discarded over multihop links. Meanwhile,

the end-to-end latency is also higher for longer packets, because much processing time is consumed on CRC computing and retransmissions. Nevertheless, using shorter packets is usually accompanied with a large transmission overhead, which may limit the overall efficiency of the network.

It is also illustrated that introducing more RIN nodes in WRN indeed causes a higher delay, but the packet delivery rate is improved significantly. This confirms the conclusions we made earlier, and trading off time for reliability in WRN is worthwhile. We can also reach a higher delivery rate by adding up MAX_RETRANS, as long as the overall latency is acceptable by operators.

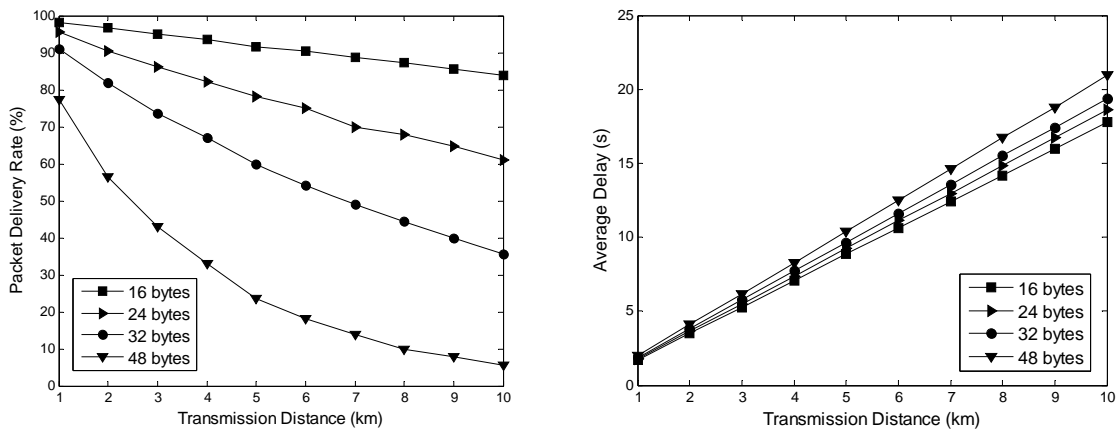


Figure 5 Packet delivery rate and average delay over transmission distance. 1024 bps source, 5% RIN.

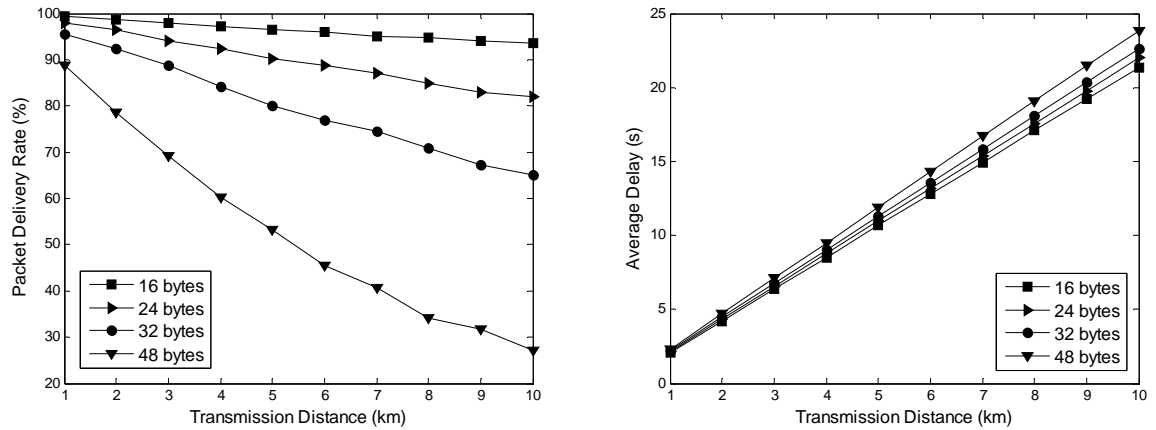


Figure 6 Packet delivery rate and average delay over transmission distance. 1024 bps source. 10% RIN.

5. Conclusion

A novel data transmission approach in MWD telemetry for oil drilling, Wireless Relay Network (WRN), is proposed in this paper. Compared to currently used methods, WRN excels in multiple aspects: First, it offers a competitive speed compared with MPT and EMT. With appropriate hardware designs, an end-to-end throughput of over 660 bps over a 10 km distance is reached. Second, the wireless connection allows the whole network to communicate continuously even during pipe installation or equipment maintenance, hence downhole conditions can be monitored at all times. Third, WRN is completely independent of parameters of conventional drill pipe. Since wireless nodes are easily installable, WRN can be directly applied to the current drill pipe with almost no modifications. Last, based on programmable microprocessors, WRN is open to further alternations on functionalities, or even customized by operators to satisfy particular requirements. Simulation results have shown the feasibility of WRN to establish a communication link in drill pipe. With further experiments and realizations in the future study, WRN will prove a promising and effective tool in the oil and gas exploration industry.

References

- [1] T. R. Bates, null, and D. R. Tanguy, "Downhole measurements while drilling," presented at the 11th World Petroleum Congress, London. UK, 1983.
- [2] J. J. Arps and J. L. Arps, "The subsurface telemetry problem – a practical solution," *SPE Journal of Petroleum Technology*, vol. 16, no. 5, pp. 487-493, May 1964.
- [3] S. P. Monroe, "Applying digital data encoding techniques to mud pulse telemetry," presented at the Petroleum Computer Conference, Denver, Colorado, Jun. 1990.
- [4] R. Hutin, R. W. Tennent, and S. V. Kashikar, "New mud pulse telemetry techniques for deepwater applications and improved real-time data capabilities," presented at the SPE/IADC Drilling Conference, Amsterdam, Netherlands, 2001.
- [5] C. Klotz, P. Bond, I. Wasserman, and S. Priegnitz, "A new mud pulse telemetry system for enhanced MWD/LWD applications," presented at the IADC/SPE Drilling Conference, Orlando, Florida, Mar. 2008.
- [6] W. R. Gardner, "High data rate MWD mud pulse telemetry," presented at the U.S. Department of Energy's Natural Gas Conference, Houston, Texas, Mar. 1997.
- [7] E. M. Tollefsen, A. Weber, A. B. Kramer, G. Sirkin, D. Hartman, and L. Grant, "Logging while drilling measurements: from correlation to evaluation," presented at the International Oil Conference and Exhibition in Mexico, Veracruz, Mexico, Jun. 2007.
- [8] N. Brown, "Electromagnetic MWD telemetry system sets depth record offshore," *Oil and Gas Journal*, vol. 100, pp. 46-47, Sept. 2002.
- [9] H. Wasada, T. Sakai, R. Taniguchi, and S. Hattori, "Advanced realtime drilling control by application of an EM-MWD system," presented at the 14th World Petroleum Congress, Stavanger, Norway, 1994.
- [10] P. DeGauque and R. Grudzinski, "Propagation of electromagnetic waves along a drillstring of finite conductivity," *SPE Drilling Engineering*, vol. 2, pp. 127-134, Jun. 1987.

- [11]P. K. Vong, D. Rodger, and A. Marshall, "Modeling an electromagnetic telemetry system for signal transmission in oil fields," *IEEE Transactions on Magnetics*, vol.41, no.5, pp. 2008-2011, 2005.
- [12]J. Schnitger and J. Macpherson, "Signal attenuation for electromagnetic telemetry systems," presented at the SPE/IADC Drilling Conference and Exhibition, Amsterdam, Netherlands, Mar. 2009.
- [13]M. J. Jellison and D. R. Hall, "Intelligent drill pipe creates the drilling network," presented at the SPE Asia Pacific Oil and Gas Conference and Exhibition, Jakarta, Indonesia, Apr. 2003.
- [14]M. E. Reeves, M. L. Payne, A. G. Ismayilov, and M. J. Jellison, "Intelligent drill string field trials demonstrate technology functionality," presented at the SPE/IADC Drilling Conference, Amsterdam, The Netherlands, Feb. 2005.
- [15]T. H. Ali, M. Sas, J. A. Hood, S. R. Lemke, A. Srinivasan, J. McKay, K. S. Fereday, C. Mondragon, S. C. Townsend, S. T. Edwards, M. Hernandez, and M. Reeves, "High speed telemetry drill pipe network optimizes drilling dynamics and wellbore placement," presented at the IADC/SPE Drilling Conference, Orlando, Florida, Mar. 2008.
- [16]S. Allen, C. McCartney, M. Hernandez, M. E. Reeves, A. Baksh, and D. MacFarlane, "Step-change improvements with wired-pipe telemetry," presented at the SPE/IADC Drilling Conference and Exhibition, Amsterdam, The Netherlands, Mar. 2009.
- [17]D. Veeningen, "Novel high speed telemetry system with measurements along the string mitigate drilling risk and improve drilling efficiency," presented at the Brasil Offshore Conference and Exhibition, Macae, Brazil, Jun. 2011.
- [18]H. Naseri and C. Liu, "Electromagnetic telemetry in measurement-while-drilling with small RF-transceivers," presented at the CPS/SEG Beijing 2009 Conference and Exposition, Beijing China, Apr. 2009.
- [19]*2.4-GHz Bluetooth Low Energy System-on-Chip*, Texas Instruments Inc., Dallas, TX, 2010.

- [20]I. Jawhar, N. Mohamed, M. M. Mohamed, and J. Aziz, "A routing protocol and addressing scheme for oil, gas, and water pipeline monitoring using wireless sensor networks," in *Wireless and Optical Communications Networks, 2008. WOCN '08. 5th IFIP International Conference on*, 2008, pp. 1-5.
- [21]M. A. Garcia, R. S. G. Villar, A. L. R. Cardoso, and J. C. T. B. Moraes, "A low-cost and high-reliability communication protocol for remote monitoring devices," *Instrumentation and Measurement, IEEE Transactions on*, vol. 53, pp. 612-618, 2004.

CHAPTER 7

Wireless MWD Telemetry System Using MEMS Radio

Abstract

The measurement-while-drilling (MWD) logging tool measures the geophysical properties of the formation that are critical in understanding the downhole environment. Current MWD telemetry techniques suffer from low data rate transmission. Improvement of MWD logging technology is required by oil and gas industry.

The purpose of this study is to design a high speed electromagnetic telemetry relay network that utilizes small RF wireless transceivers. These RF transceivers will be placed inside the drilling pipe. The MWD data collected at the bottom of the drilling pipe can be transmitted to the processor at the surface by using a large number of these RF transceivers. This method of transmission can achieve high data rate of up to a few kilo bits per second which significantly surpasses the conventional telemetry techniques. In this paper we use MEMS radio to build the wireless network. The MEMS radio has advantages of high sensitivity and low power consumption which are ideal for the system. It also has excellent receiver selectivity and blocking performance so that it will be reliable for the wireless network.

The transceivers built for this project were tested, the results show that the wireless telemetry system can achieve high speed data rate and low packet error rate. The results have proved the application of the transceiver in MWD telemetry.

1 Introduction

Nowadays, electrical logging is recognized as the only measurement to distinguish hydrocarbon from water. Lots of modern oil and gas wells are drilled directionally. Modern techniques now transmit continuous information from the bottom to the surface. This is known as measurement-while-drilling (MWD) or logging while drilling (LWD).

There are different methods of data transmission in MWD logs. Among these, Mud Pulse Telemetry (MDT) is the most common method used by MWD tools. Pulses generated downhole travel through drilling pipe within the drilling fluid towards the surface where they are received from pressure sensors. The received signals are processed by computers on surface and useful information will be reconstructed from them. Many factors restrict the speed of data transmission. Better methods of data transmission are still being developing by oilfield service companies. Electromagnetic telemetry (EMT) is an alternative to MPT. It has been studied for years. Many EMT tools have been designed by different companies on the market now. However, these tools still have limitations under specific applications, and have not yet gained universal acceptance by the oilfield service industry.

This report focuses on a novel electromagnetic telemetry wireless network which utilizes a large number of small size microwave transceivers to transmit data. By transmitting information to one another, these transceivers create a wireless network inside the drilling pipe from the bottom of the borehole tool to the surface. The schematic of the EMT wireless network is shown in Fig. 1.

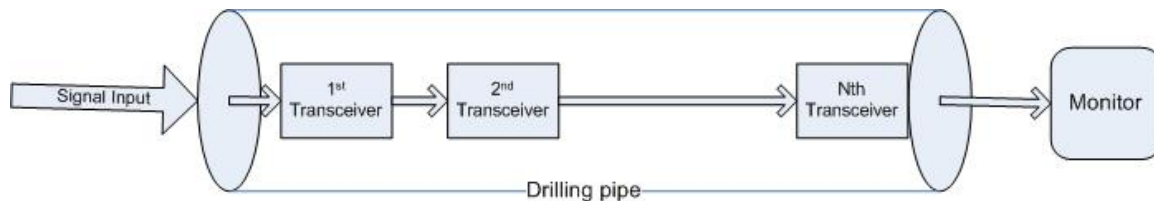


Fig. 1 Schematic of the EMT wireless network.

The downhole tool is one end of this wireless network while the surface receiver is the other end. The data transmission can be full duplex or half duplex depending on the requirements. So not only can we transmit data from downhole tool to surface, but also it creates a communication link from surface to downhole tool. Thus the drilling tool at the bottom of the pipe can be more precisely controlled. This electromagnetic telemetry wireless network leads the drilling procedure to be more efficient due to real-time data transmission.

The Texas Instrument CC2510 and CC2511 low-power system-on-chip 2.4 GHz RF transceiver used in this project can achieve data rates of up to 500 Kbps, which is much higher than conventional telemetry technique. The entire system includes the antenna and the circuit parts. A loop antenna is used for this system. The printed circuit board (PCB) is placed inside the loop antenna. The RF wireless transceiver and other external components are soldered on the PCB.

2 Antenna System Design

The downhole environment is so complicated which makes the radiation efficiency of the transceiver very challenging. The antenna system is critical in this project because efficient radiation of the RF transceiver largely depends on the antenna. The important factors, that need to be considered when we designing the antenna, include features of the drilling pipe, cutoff frequency of the pipe and resonant frequency of the RF transceiver.

A borehole model has the following parameters.

1. Drilling pipe diameter = 4 inches
2. Borehole diameter = 8 inches

The electromagnetic signal attenuates when propagating along the drilling pipe. The drilling fluid inside the pipe largely causes the attenuation of the EM signal. The complex permittivity of the mud is given by

$$\hat{\mathcal{E}} = \mathcal{E}_d - j \frac{\sigma}{\omega}, \quad (1)$$

where

$$\mathcal{E}_d = \mathcal{E}_0 \mathcal{E}_r, \quad (2)$$

and \mathcal{E}_r , σ , \mathcal{E}_0 are mud relative permittivity, mud conductivity and permittivity of the free space, respectively. The complex epsilon of the mud is used in calculating its attenuation constant or α_d . The relationship between wave number (k), critical wave number (k_c) and the propagation constant (k_z) is given by

$$k_c = \sqrt{k^2 - k_z^2}, \quad (3)$$

where

$$k_z = \beta - j\alpha. \quad (4)$$

The real part (β) is the phase constant and imaginary part (α) is the attenuation constant, respectively. Combining the last two equations we have

$$(\beta - j\alpha)^2 = k^2 - k_c^2, \quad (5)$$

or

$$\beta^2 - \alpha^2 - 2j\alpha\beta = \omega^2 \mu \epsilon_c - \omega_c^2 \mu \epsilon_0, \quad (6)$$

and finally

$$\beta^2 - \alpha^2 - 2j\alpha\beta = (2\pi f)^2 \mu (\epsilon_0 \epsilon_r - j \frac{\sigma}{\omega}) - (2\pi f_c)^2 \mu \epsilon_0. \quad (7)$$

In this equation, f_c is the cutoff frequency and μ is the free space permeability, respectively. The cutoff frequency is a function of the geometry of the waveguide and is equal to^[2]

$$f_{cTE_{nm}} = \frac{k_c}{2\pi\sqrt{\mu\epsilon}} = \frac{p'_{nm}}{2\pi a\sqrt{\mu\epsilon}}, \quad (8)$$

where p'_{nm} is the n^{th} positive root of $J'_m(x) = 0$, and J'_m is a Bessel function of the first kind of order m [3]. The values of the first few such roots are listed in Table 1.

Table 1 Values of p'_{nm} for TE modes of a circular waveguide

N	p'_{n1}	p'_{n2}	p'_{n3}
0	3.832	7.016	10.174
1	1.841	5.331	8.536
2	3.054	6.706	9.970

The finite conductivity of the steel pipe is another reason of the attenuation when the EM signal propagating inside the drilling pipe. The drilling pipe is treated as a cylindrical

waveguide. We assume the drilling pipe is in a cylindrical shape all the way from the top of the surface to the bottom of the well. Fig. 2^[2] shows the field lines for some of the lower order modes of a circular waveguide.

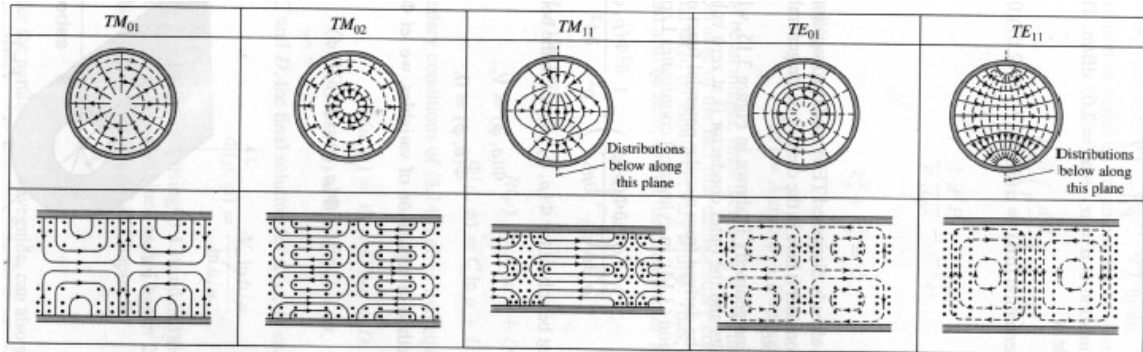


Fig. 2 Field lines for some of the lower order modes of a circular waveguide.

We choose TE_{11} mode for the wireless network in this project because TE_{11} mode has the lowest cutoff frequency. Given that the diameter of a drilling pipe is 4 inches and the conductivity is 1.4×10^6 S/m, the cutoff frequency for the TE_{11} mode of this cylindrical waveguide is 1.7 GHz. In order to match field lines of TE_{11} mode, different types of antenna have been designed and simulated for optimal selection.

2.1. Dipole Antenna

A dipole antenna can be made of a simple wire with a center-fed driven element. It consists of two metal conductors of rod or wire. The two metal conductors are oriented parallel and collinear with each other, with a small space between them. The dipole antenna is the simplest practical antennas from a theoretical point of view. A typical dipole antenna is made by two quarter wavelength ($\lambda/4$) conductors or elements placed back to back. The radio frequency voltage is applied to the antenna at the center, between the two conductors. A standing wave on an element of a quarter wavelength yields the greatest voltage differential. The larger the differential voltage is, the greater the current between the elements will be.

Assuming a sinusoidal distribution, the current impressed by this voltage differential is given by:

$$I = I_0 e^{i\omega t} \cos kl, \quad (9)$$

where ω is the angular frequency, $k = \frac{2\pi}{\lambda}$ is the wavenumber, and l is the length of the conductor, respectively.

The electric field of a radiating electromagnetic wave is given by:

$$E_\theta = \frac{-iI_0}{2\pi\epsilon_0 cr} \frac{\cos(\frac{\pi}{2} \cos \theta)}{\sin \theta} e^{i(\omega t - kr)}, \quad (10)$$

where E_θ is the far electric field of the electromagnetic wave radiated in the θ direction, ϵ_0 is the permittivity of vacuum, c is the speed of light in vacuum, r is the distance from the point on the conductor to where the electrical field E_θ is evaluated, respectively.

A dipole antenna model is built in CST Microwave Studio as shown in Fig. 3.

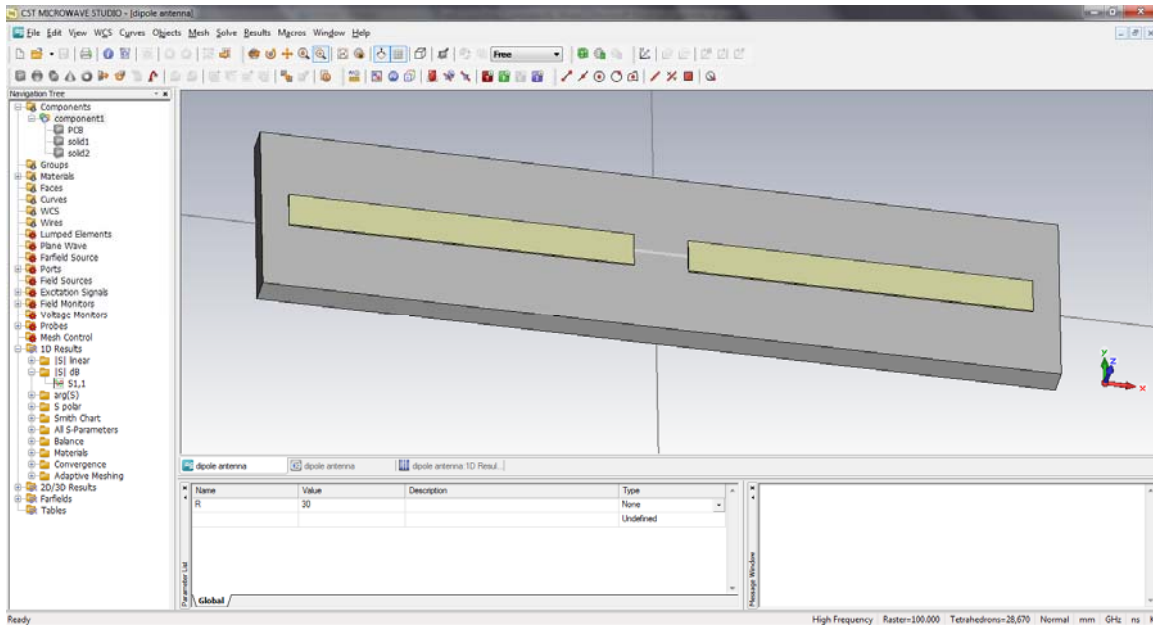


Fig. 3 The dipole antenna model in CST Microwave Studio

The dipole antenna is attached on a print circuit board (PCB). Considering that the operating frequency of the RF transceiver is 2.4 GHz, we design the antenna to resonant at the same frequency. The dipole antenna built in this model has a total length of 60 mm which is the half wavelength of a 2.4 GHz wave. The goal of the simulation is to find out the S11 response of the dipole antenna. S11 is the reflection coefficient see looking into port 1 when all other ports are terminated in matched loads. Since there is only one antenna built in this model, we do not need to consider about other ports. The simulation result of the S11 response is shown in Fig. 4. The result shows that the dipole antenna built in this model has a reasonable S11 response and the resonant frequency is at 2.4 GHz.

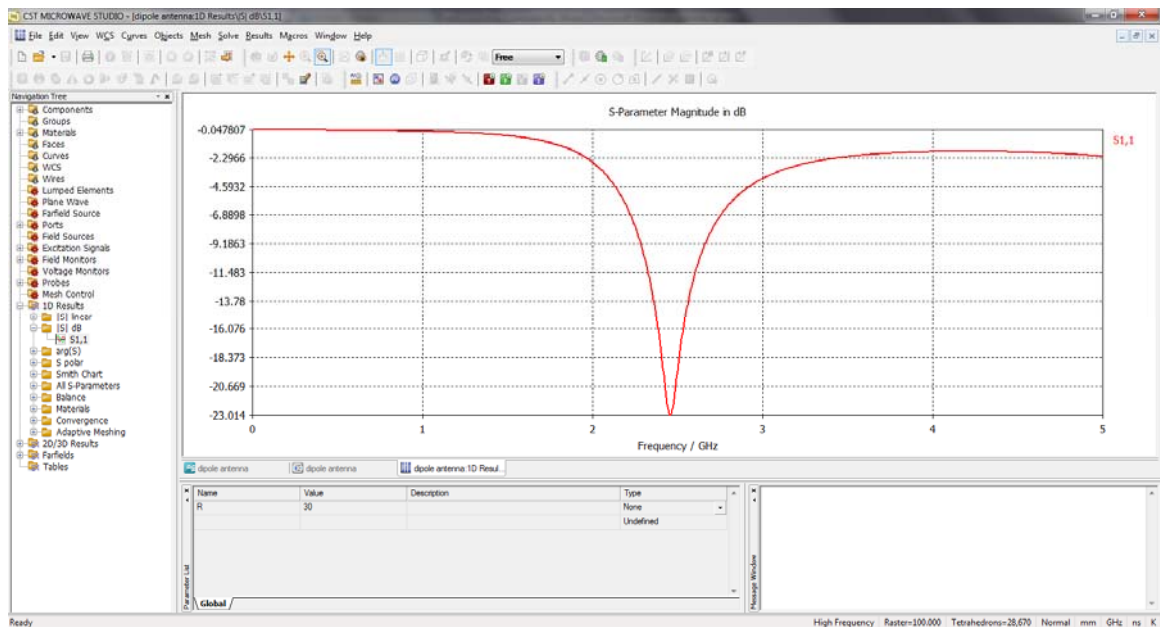


Fig. 4 S11 response of the dipole antenna in CST.

In order to transmit the signal from one to another, a number of antennas will be placed inside the drilling pipe. Having obtained the S11 response of the dipole antenna, the next step we need to do is to consider the coupling of these dipole antennas inside the pipe. Considering the radiation pattern of the dipole antenna (see Fig. 5), the best coupling would be achieved when two dipole antennas are facing one another.

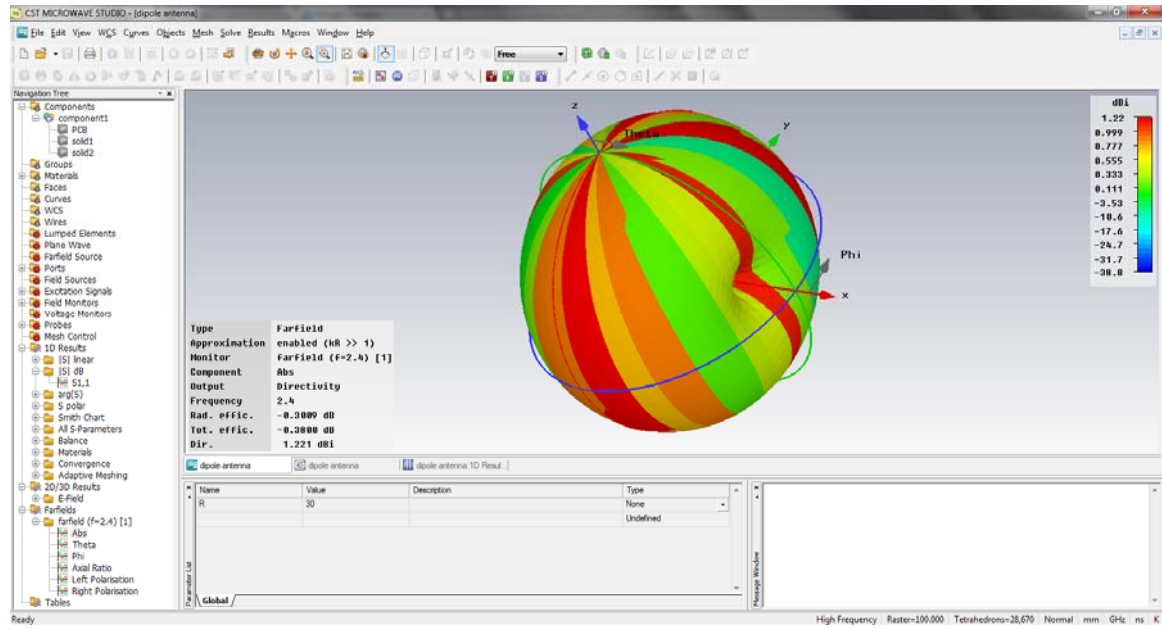


Fig. 5 Radiation pattern of the dipole antenna.

The second model of the dipole antenna is built as shown in Fig. 6. Two dipole antennas are placed 150 mm apart inside a metal pipe.

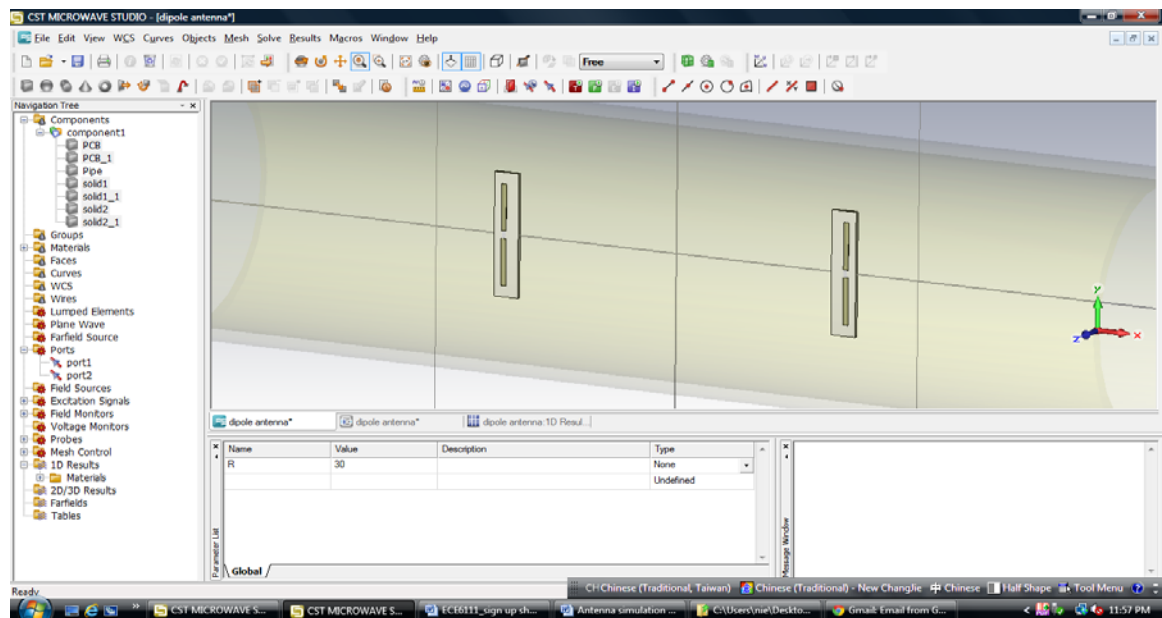


Fig. 6 Two dipole antennas inside a metal pipe.

The coupling of the two dipole antennas is determined by the S21 response. S21 is the transmission coefficient from port 1 to port 2. A reasonable S21 response would mean an effective radiation performance of the antennas. The S11 and S21 response of the second model are shown in Fig. 7 and Fig. 8.

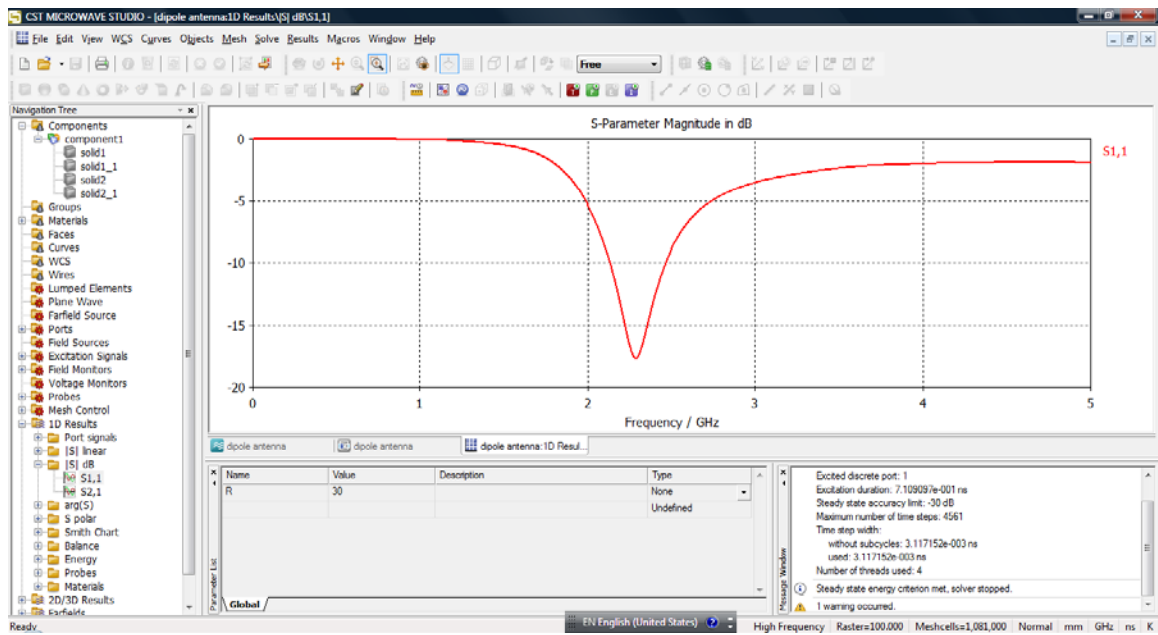


Fig. 7 S11 response of two dipole antennas.

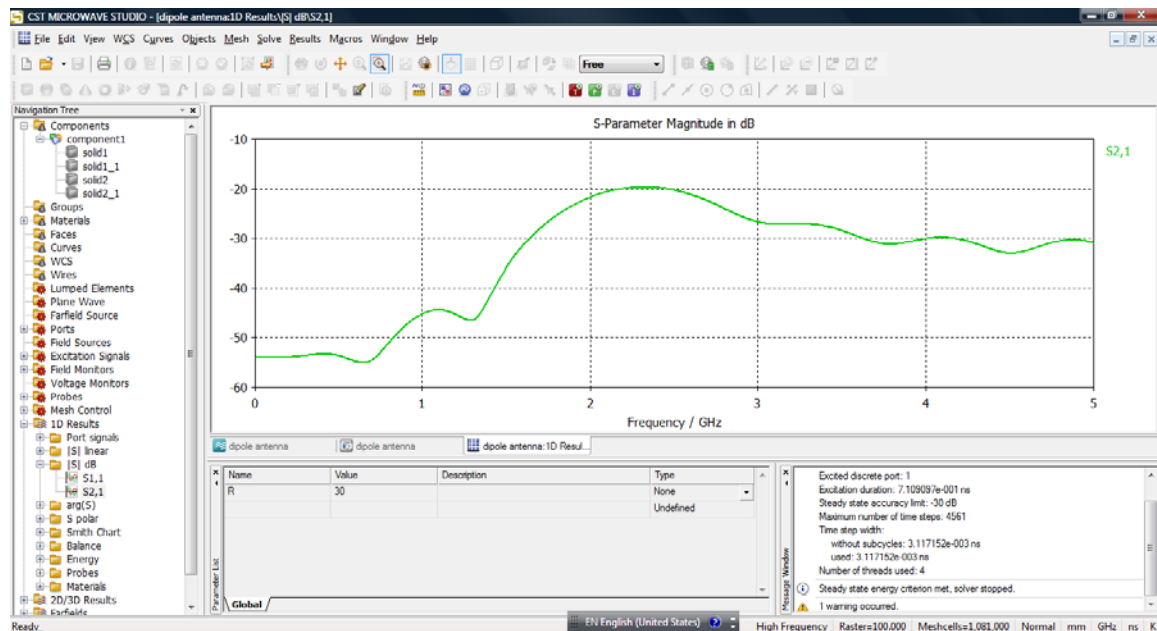


Fig. 8 S21 response of two dipole antennas.

As shown in the figures, the S11 and S21 response of the two dipole antennas are reasonable. The results have shown the efficiency of the dipole antenna. The only problem is the size of the dipole antenna. Considering that the diameter of the drilling pipe is about 4-inch, a dipole antenna with a length of 60 mm would be too large for our application. Placing a dipole antenna inside the pipe would probably block the drilling fluid. Therefore the dipole antenna becomes not practical for this project. Another type of antenna, that has efficient radiation performance but smaller size, is needed. The loop antenna becomes our next consideration.

2.2. Loop Antenna

A loop antenna is consisting of a loop of wire, or other electrical conductor with its ends connected to a balanced transmission line. The loop antenna is simple, inexpensive, and very versatile. It can take many different forms such as a square, rectangle, triangle, circle and many other configurations. The loop antenna is the most popular type because of its simplicity in construction and analysis. Most of the applications of loop antennas are in the HF (high frequency, 3-30 MHz), VHF (very high frequency, 30-300 MHz), and

UHF (ultra high frequency, 300-3,000 MHz) bands. The field pattern of the loop antenna is similar to that of a magnetic dipole antenna with a null perpendicular to the plane of the loop and with its maximum along the plane of the loop. As the overall length of the loop increases and its circumference approaches one free-space wavelength, the maximum of the pattern shifts from the plane of the loop to the axis of the loop which is perpendicular to its plane.

The circumference of an electrically large loop antenna is about a free-space wavelength ($C \sim \lambda$). The geometry for far-field analysis of a loop antenna is shown in Fig. 9.

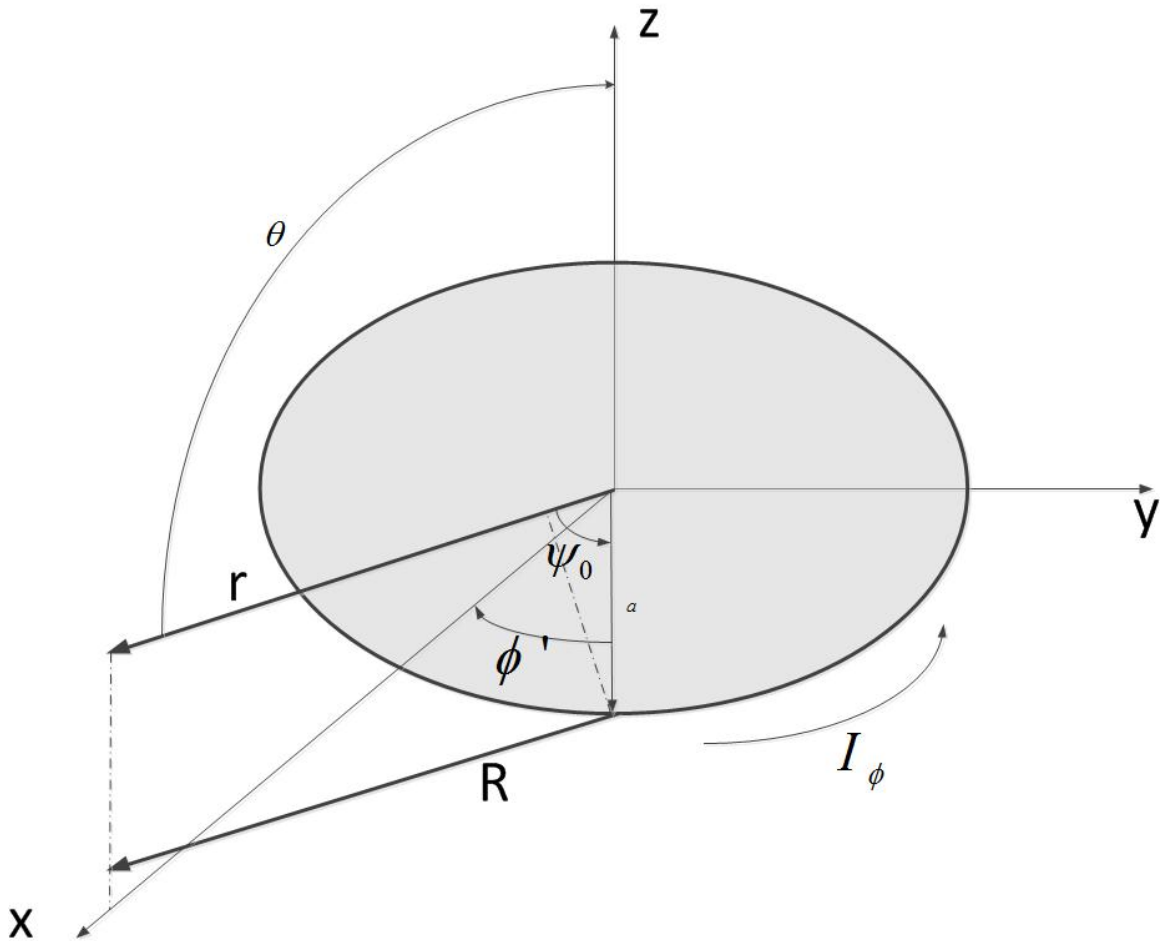


Fig. 9 Geometry for far-field analysis of a loop antenna.

The distance R can be approximated by:

$$R = \sqrt{r^2 + a^2 - 2ar \sin \theta \cos \phi'} \approx \sqrt{r^2 - 2ar \sin \theta \cos \phi'} \quad (11)$$

for $r \gg a$.

R can be reduced to:

$$R \approx r \sqrt{1 - \frac{2a}{r} \sin \theta \cos \phi'} = r - a \sin \theta \cos \phi' = r - a \cos \psi_0, \quad (12)$$

The electric potential at a certain point is given by:

$$A_\phi \approx \frac{a\mu I_0 e^{-jkr}}{4\pi r} \int_0^{2\pi} \cos \phi' e^{+jka \sin \theta \cos \phi'} d\phi' \quad (13)$$

It can be separated into two terms as:

$$A_\phi \approx \frac{a\mu I_0 e^{-jkr}}{4\pi r} \left[\int_0^\pi \cos \phi' e^{+jka \sin \theta \cos \phi'} d\phi' + \int_\pi^{2\pi} \cos \phi' e^{+jka \sin \theta \cos \phi'} d\phi' \right] \quad (14)$$

The second term within the brackets can be rewritten by making a change of variable of the form

$$\phi' = \phi'' + \pi \quad (15)$$

Therefore the equation (14) can be written as

$$A_\phi \approx \frac{a\mu I_0 e^{-jkr}}{4\pi r} \left[\int_0^\pi \cos \phi' e^{+jka \sin \theta \cos \phi'} d\phi' - \int_0^\pi \cos \phi'' e^{-jka \sin \theta \cos \phi''} d\phi'' \right] \quad (16)$$

Each of the integrals in (16) can be integrated by the formula

$$\pi j^n J_n(z) = \int_0^\pi \cos(n\phi) e^{+jz \cos \phi} d\phi \quad (17)$$

where $J_n(z)$ is the Bessel function of the first kind of order n .

Thus A_ϕ can be reduced to

$$A_\phi \approx \frac{a\mu I_0 e^{-jkr}}{4\pi r} [\pi j J_1(ka \sin \theta) - \pi j J_1(-ka \sin \theta)] \quad (18)$$

The Bessel function of the first kind and order n is defined by the infinite series

$$J_n(z) = \sum_{m=0}^{\infty} \frac{(-1)^m (z/2)^{n+2m}}{m!(m+n)!} \quad (19)$$

$$J_n(-z) = (-1)^n J_n(z) \quad (20)$$

When $n=1$

$$J_1(-z) = -J_1(z) \quad (21)$$

Thus the electric potential A_ϕ is given by

$$A_\phi \approx \frac{a\mu I_0 e^{-jkr}}{2r} J_1(ka \sin \theta) \quad (22)$$

The next step is to find out the electric field and magnetic field associated with the electric potential A_ϕ . According to Maxwell's equations and equation (22), the E- and H-fields are given by

$$E_r \approx E_\theta = 0 \quad (23)$$

$$E_\phi \approx \frac{ak\eta I_0 e^{-jkr}}{2r} J_1(ka \sin \theta) \quad (24)$$

$$H_r \approx H_\phi = 0 \quad (25)$$

$$H_\theta \approx -\frac{E_\phi}{\eta} = -\frac{akI_0 e^{-jkr}}{2r} J_1(ka \sin \theta) \quad (26)$$

where $\eta = 377 \text{ Ohms}$ is the wave impedance in free-space.^[1]

The model of a loop antenna built for our project is shown in Figure 2.9. The excitation signal is added at the bottom part of the loop antenna. The loop antenna needs to resonant at 2.4 GHz of which the wavelength is about 125 mm. According to the characteristic of the electrically large loop antenna, the circumference is about a free-space wavelength ($C \sim \lambda$). Thus, the radius of the loop antenna built in Fig. 10 is 20 mm, giving the loop antenna a relatively small size.

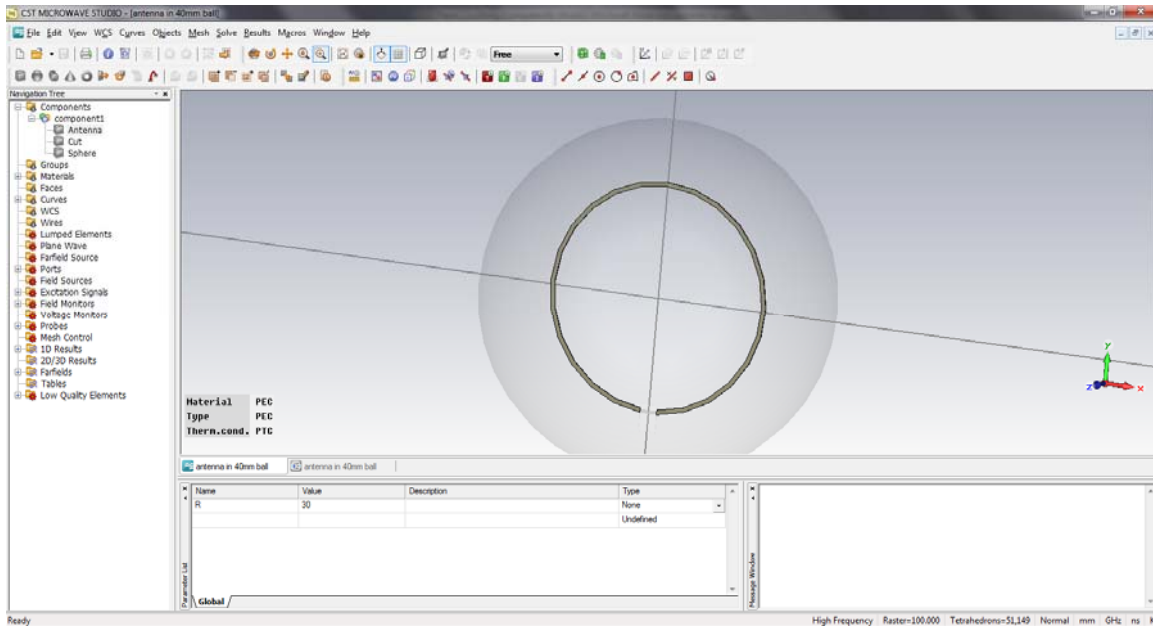


Fig. 10 The loop antenna built in CST Microwave Studio

The S11 response of the loop antenna is shown in Fig. 11.

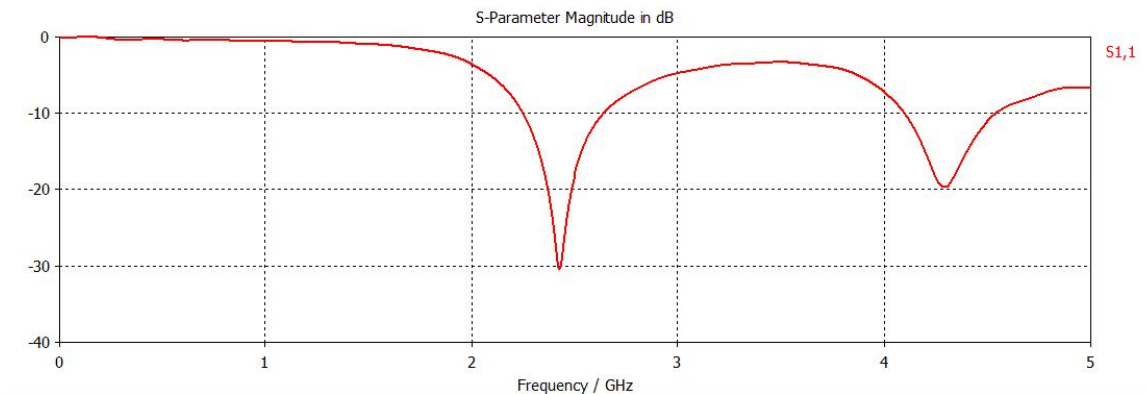


Fig. 11 S11 response of the loop antenna

The simulation result indicates a 2.4 GHz resonant frequency of the loop antenna, which is operating frequency of our transceiver. The manufactured loop antenna is shown in Fig. 12. The S11 response of the loop antenna measured by network analyzer is shown in Fig. 13.

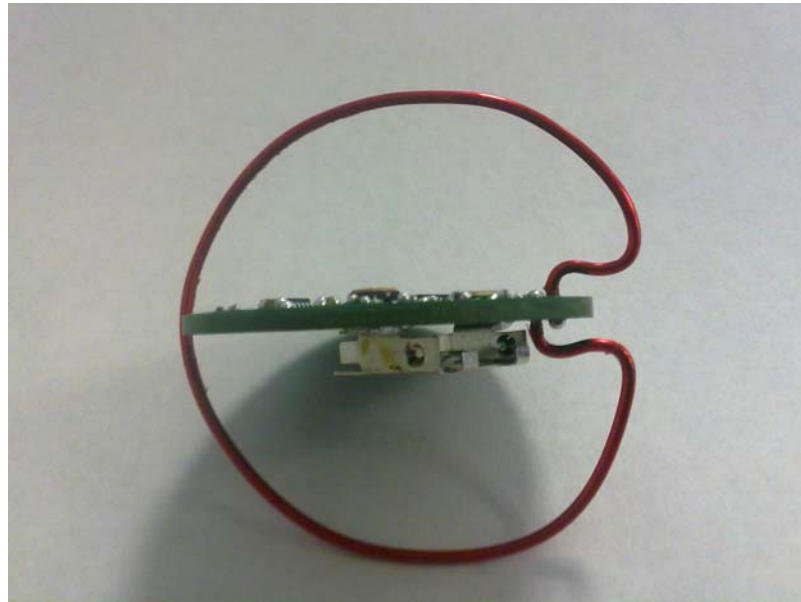


Fig. 12 Manufactured loop antenna.

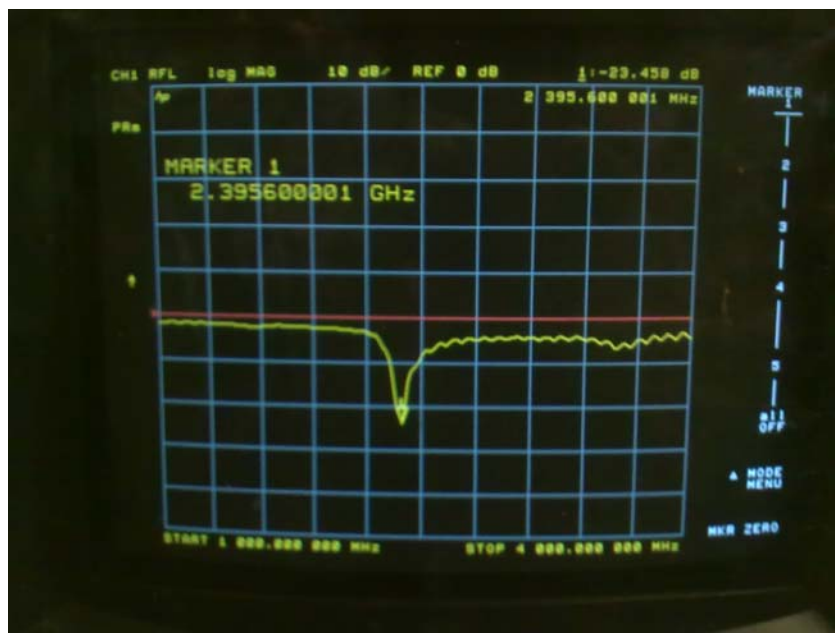


Fig. 13 Measure S11 response of the loop antenna on network analyzer

Based on the simulation results and lab measurements, a loop antenna has excellent radiation performance and small size. Thus, the loop antenna is chosen for our system.

3 Antenna System Design

The TI CC2510/CC2511 RF transceivers are chosen for this project. It operates at 2.4 GHz in a voltage range from 2.0V to 3.6V. The advantage of CC2510/CC2511 RF transceivers are the embedded microcontroller and the low current and power consumption. The receiving current consumption is 17.1 mA at 2.4 kbps and the transmitting current consumption is 16 mA at -6 dBm output power. The lowest power consumption at operating mode is 0.3 μ A in PM3. Compare to other RF transceivers, CC2510/CC2511 have a high sensitivity of -103 dBm at 2.4 kbps and their maximum data rate is up to 500 kbps. The block diagram of the CC2510/CC2511 RF transceiver is shown in Fig. 14.

Fig. 15 shows the top view of CC2511 pin-out. This chip has 17 general purpose input-output pins used for programming, debugging and testing. These pins are controlled by ports P0 (P0_0 to P0_5), P1 (P1_0 to P1_7) and P2 (P2_0, P2_1, P2_2). The 8051 microcontroller, the ADC and the RF front end of this chip run on two crystal oscillators. The 48.0 MHz crystal oscillator is connected to Pin 20 and Pin 21. And the 32.768 KHz crystal oscillator is connected to Pin 17 and Pin 18. For the CC2510 transceiver, a 26.0 MHz crystal oscillator is used instead of the 48.0 MHz crystal oscillator.

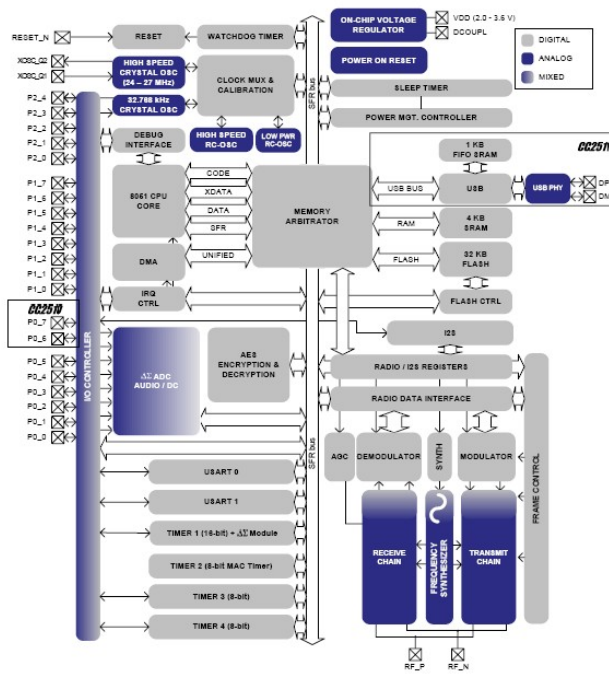


Fig. 14 Block diagram of the CC2511 transceiver (from TI website)

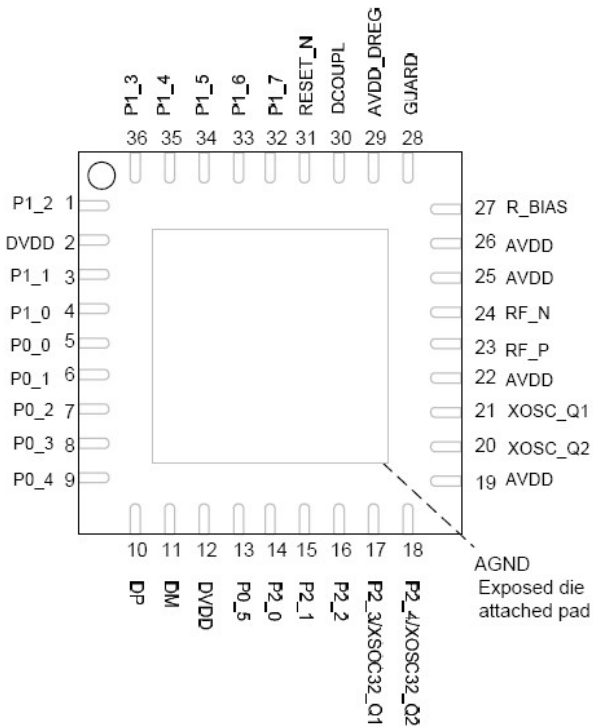


Fig. 15 Top view of CC2511 pin-out

Fig. 16 shows all the pins of the CC2511 transceiver and their descriptions.

Pin	Pin Name	Pin Type	Description
-	AGND	Ground	The exposed die attach pad must be connected to a solid ground plane
1	P1_2	D I/O	Port 1.2
2	DVDD	Power (Digital)	2.0 V - 3.6 V digital power supply for digital I/O
3	P1_1	D I/O	Port 1.1
4	P1_0	D I/O	Port 1.0
5	P0_0	D I/O	Port 0.0
6	P0_1	D I/O	Port 0.1
7	P0_2	D I/O	Port 0.2
8	P0_3	D I/O	Port 0.3
9	P0_4	D I/O	Port 0.4
10	DP	USB I/O	USB Differential Data Bus Plus
11	DM	USB I/O	USB Differential Data Bus Minus
12	DVDD	Power (Digital)	2.0 V - 3.6 V digital power supply for digital I/O
13	P0_5	D I/O	Port 0.5
14	P2_0	D I/O	Port 2.0
15	P2_1	D I/O	Port 2.1
16	P2_2	D I/O	Port 2.2
17	P2_3/XOSC32_Q1	D I/O	Port 2.3/32.768 kHz crystal oscillator pin 1
18	P2_4/XOSC32_Q2	D I/O	Port 2.4/32.768 kHz crystal oscillator pin 2
19	AVDD	Power (Analog)	2.0 V - 3.6 V analog power supply connection
20	XOSC_Q2	Analog I/O	Crystal oscillator pin 2
21	XOSC_Q1	Analog I/O	Crystal oscillator pin 1, or external clock input
22	AVDD	Power (Analog)	2.0 V - 3.6 V analog power supply connection
23	RF_P	RF I/O	Positive RF input signal to LNA in receive mode Positive RF output signal from PA in transmit mode
24	RF_N	RF I/O	Negative RF input signal to LNA in receive mode Negative RF output signal from PA in transmit mode
25	AVDD	Power (Analog)	2.0 V - 3.6 V analog power supply connection
26	AVDD	Power (Analog)	2.0 V - 3.6 V analog power supply connection
27	RBIAS	Analog I/O	External precision bias resistor for reference current
28	GUARD	Power (Digital)	Power supply connection for digital noise isolation
29	AVDD_DREG	Power (Digital)	2.0 V - 3.6 V digital power supply for digital core voltage regulator
30	DCOUPPL	Power decoupling	1.8 V digital power supply decoupling
31	RESET_N	DI	Reset, active low
32	P1_7	D I/O	Port 1.7
33	P1_6	D I/O	Port 1.6
34	P1_5	D I/O	Port 1.5
35	P1_4	D I/O	Port 1.4
36	P1_3	D I/O	Port 1.3

Fig. 16 Pin description of CC2511 (from TI website)

The schematic of the RF transceiver application circuit is shown in Fig. 17. Only a few external components are required for using the CC2510/CC2511 transceivers. The power supply has been properly decoupled using decoupling capacitors. Fig. 18 shows the layout of the board in OrCAD.

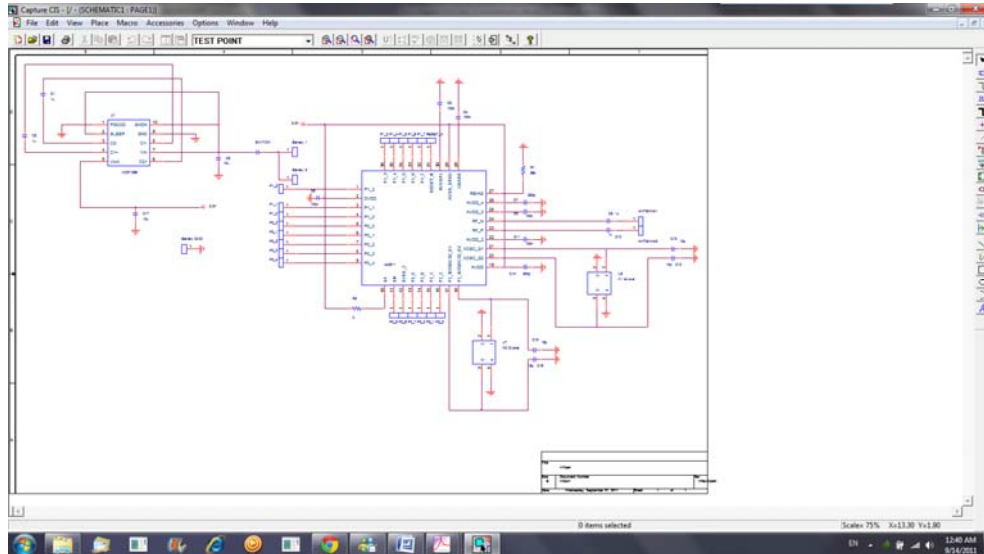


Fig. 17 Schematic of the application circuit designed in OrCAD Capture

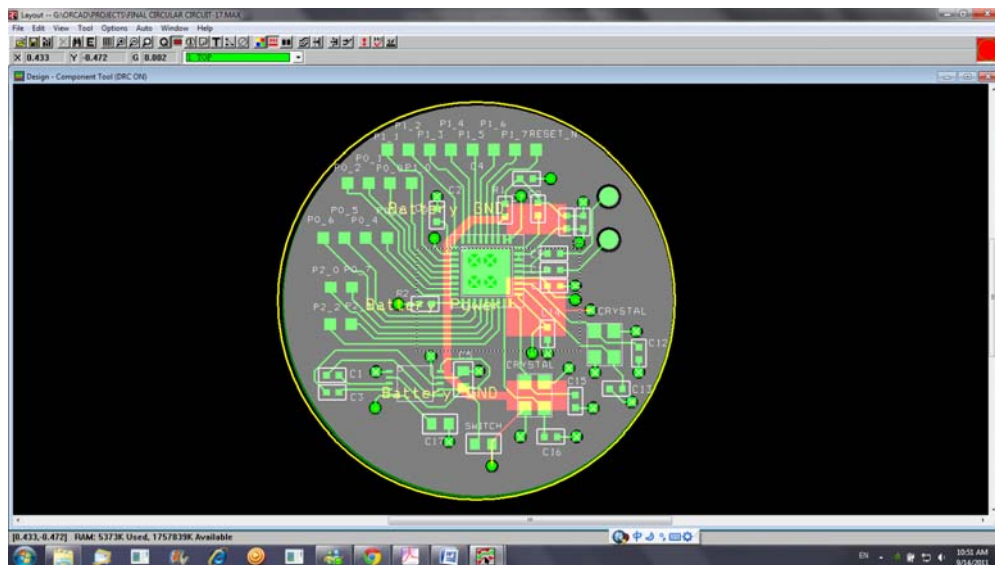


Fig. 18 The layout of the application circuit designed in OrCAD

The CC2510/CC2511 transceivers are powered up via the VDD pin and the power supply range is 2.0 V to 3.6V. The power will be supplied by 3V cell batteries. The

MCP1256 charge pump is included in the circuit to ensure the performance of the chip. The charge pump will generate a constant 3.3V output voltage to the CC2510/CC2511 transceivers from a 1.8V to 3.6V input. The schematic of the charge pump and its connection with the transceiver is shown in Fig. 19. Fig. 20 shows the manufactured board. The size of the board can be compared to a quarter coin in the figure.

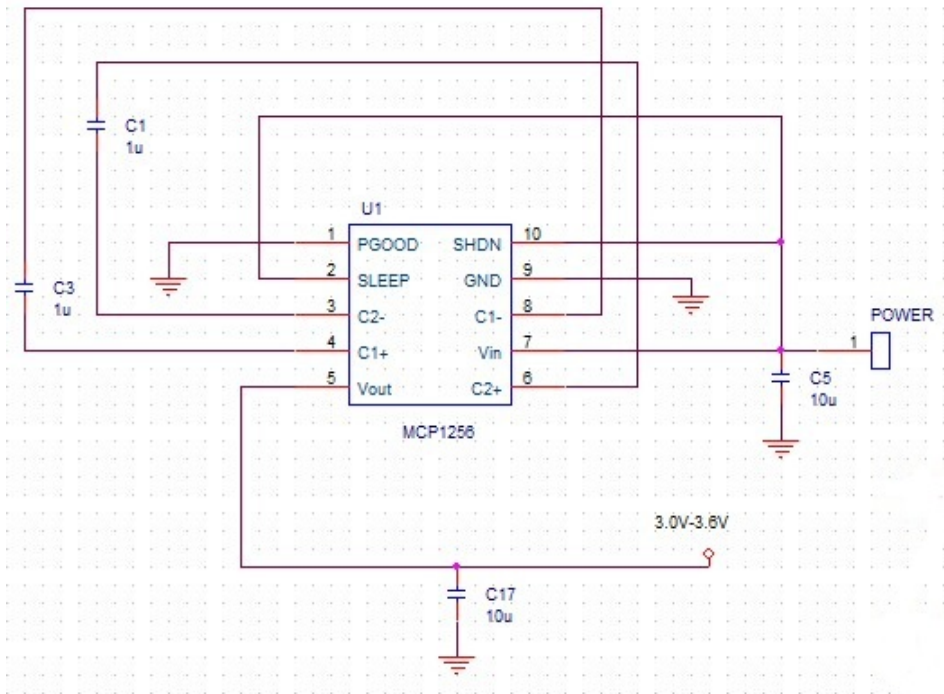


Fig. 19 Schematic of the charge pump.

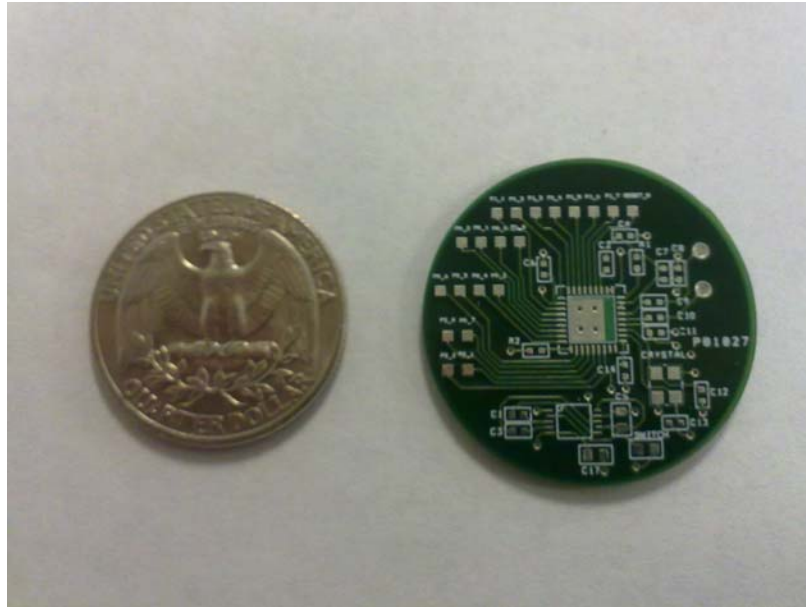


Fig. 20 The manufactured board based on the OrCAD layout.

Smart Flash Programmer provided by Texas Instrument is used for the programming of the RF transceiver. Fig. 21 shows the interface of the Smart Flash Programmer.

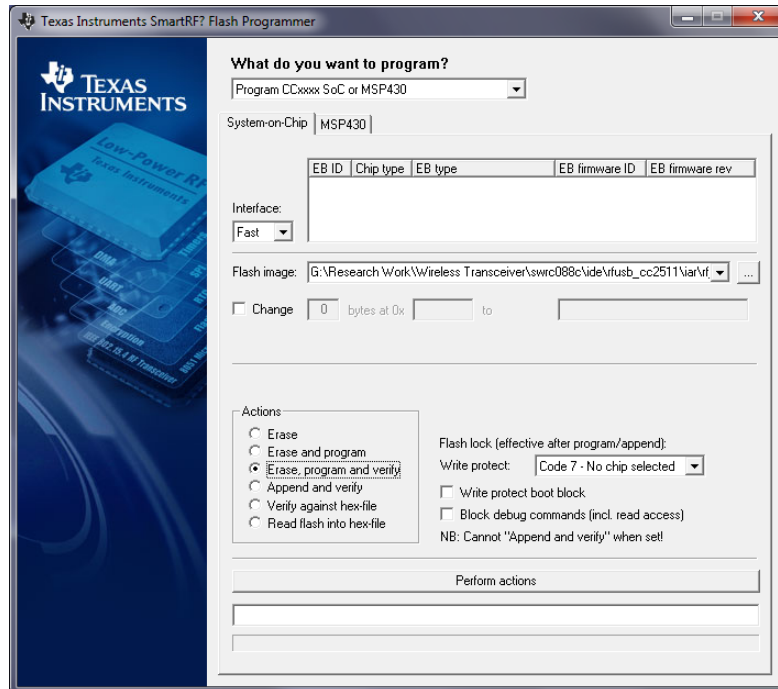


Fig. 21 Interface of Smart Flash Programmer.

The CC2510 evaluation kit, including the SmartRF04 evaluation board shown in Fig. 22, provided us with other hardware and software that are needed for programming the RF transceiver. The board is connected to computer through a CC Debugger for programming as shown in Fig. 23.

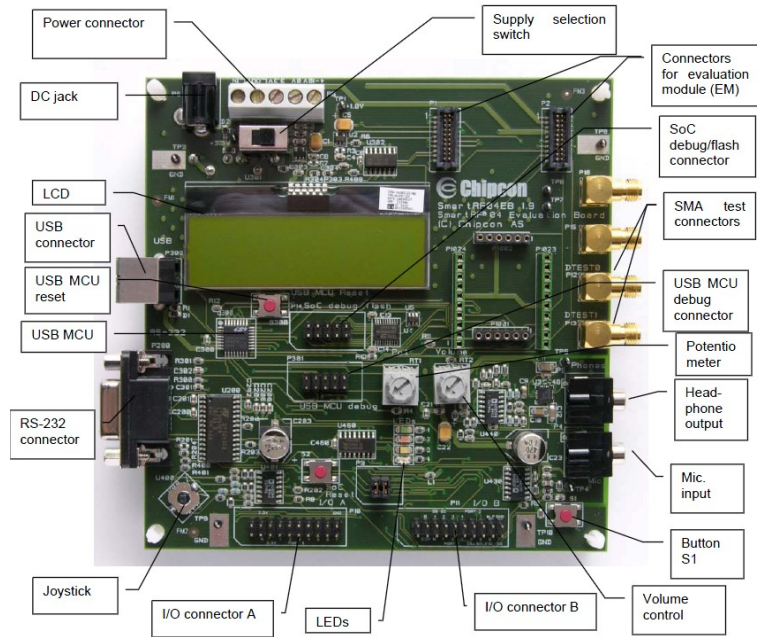


Fig. 22 SmartRF04 Evaluation Board.



Fig. 23 Programming the transceiver with CC Debugger.

4 Lab test and experimental results

4.1 Signal propagation inside a pipe

The first thing we want to make sure is that the signal can propagate inside a drilling pipe. As mentioned in the previous chapter, the pipe is treated as a lossy circular waveguide. The first experiment is to simulate a real MWD environment with a used drilling pipe. The schematic of this experiment is shown in Fig. 24.

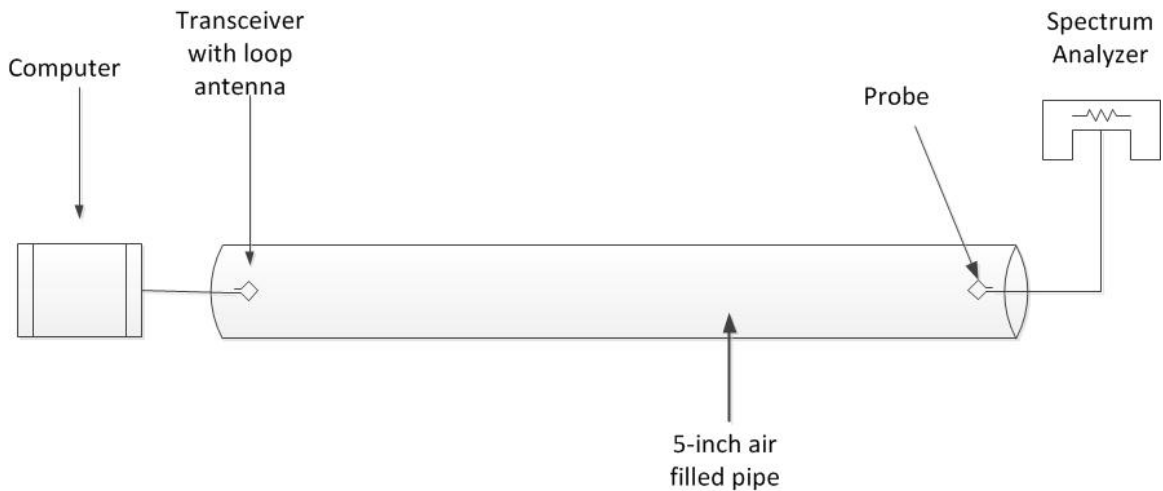


Fig. 24 Schematic of the signal propagation experiment.

A 5 feet long metal pipe is used in this experiment. The transceiver with the loop antenna is connected to the computer. It is placed at one end of the pipe. The spectrum analyzer (Hewlett-Packard E7403A) is put at the other end of the pipe to detect the received signal (see Fig. 25).



Fig. 25 Probing the electromagnetic wave inside a pipe.

The transceiver generates an electromagnetic (EM) wave. The input power of this EM wave is 1 mW. The received signal detected by the spectrum analyzer is shown in Fig. 26.

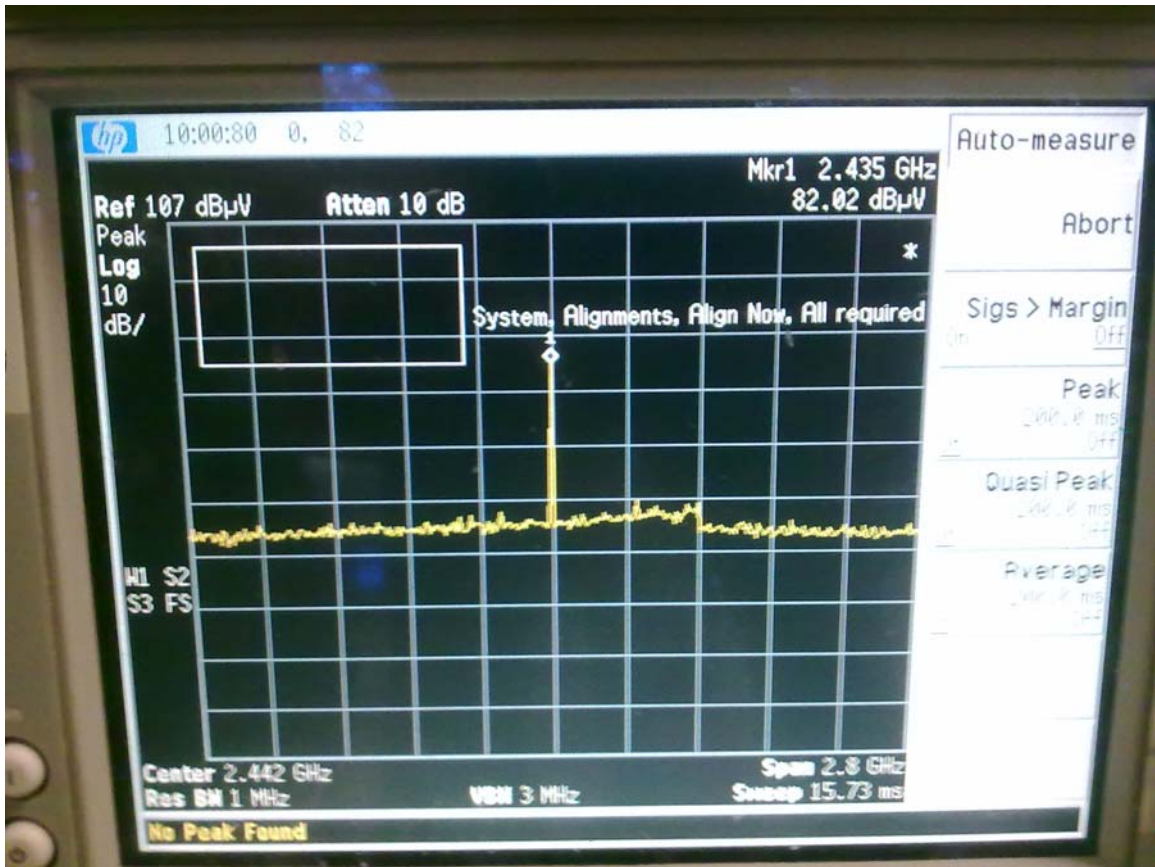


Fig. 26 Signal received by the spectrum analyzer.

The reference of the measurement is 107 dB μ V which equals to 1 mW. As shown in the figure, the received signal has a value of 82.02 dB μ V at 2.4 GHz, which is 0.0032 mW. The power attenuation of the received signal compared to the input signal is -24.95 dB.

The experiment results prove that the electromagnetic (EM) wave will propagate inside the drilling pipe when the frequency of the EM wave is greater than the cutoff frequency of the four inch pipe.

4.2 Packet error rate (PER) test in open air

The packet error rate (PER) test of data transmission between two transceivers has been performed. The first experiment with different data rates is tested in open air.

Table 2 Packet error rate at 2.4 kbps

Distance [m]	PER @2.4 kbps
1	0%
2	0%
3	0%
4	0%
5	0%
6	0%
7	0%
8	0%

Table 3 Packet error rate at 56 kbps

Distance [m]	PER @56 kbps
1	0%
2	0%
3	0%
4	0%
5	0%
6	0%
7	0%
8	0%

Table 4 Packet error rate at 180 kbps

Distance [m]	PER @180 kbps
1	0%
2	0%
3	0%
4	0%
5	0%
6	0%
7	2%
8	6%

Table 5 Packet error rate at 210 kbps

Distance [m]	PER @56 kbps
1	0%
2	1%
3	2%
4	5%
5	18%
6	37%
7	61%
8	92%

4.3 Packet error rate (PER) test inside a 5-inch pipe

The second experiment is to test the packet error rate inside a pipe. The pipe is shown in the previous picture. The length of the pipe is 5 inches. Different data rates are set. The result is shown in Table 6.

Table 6 Packet error rate inside a 5-inch pipe

Data rate [kbps]	Packet error rate
2.4	0%
56	0%
70	4%
90	10%
120	19%
150	41%
180	72%
210	100%

4.4 Three nodes relay network test

Three boards are used for the relay network test. These three nodes are transmitter, repeater and receiver. The boards are connected to the computer through RS232 serial adapters so that the information can be seen in hyper-terminal windows. The three devices used in this experiment are shown in Fig. 27.

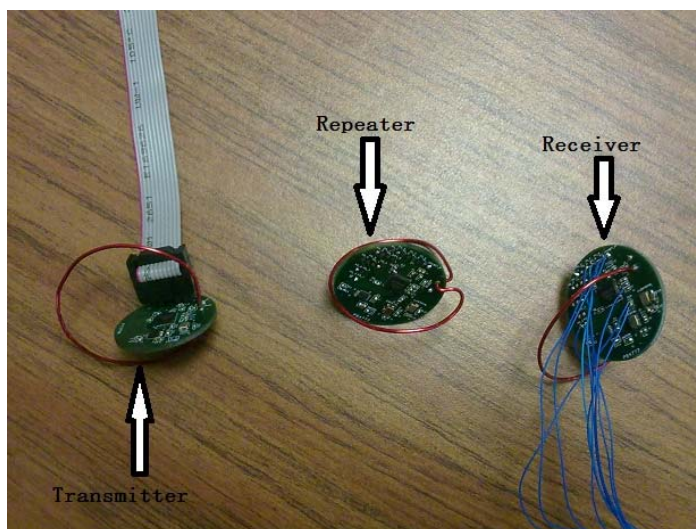


Fig. 27 Three nodes.

Once the transmitter is turned on, it starts to send continuous package data. The repeater receives the package data and then resend it to the next node. The receiver acquires the package data from the last repeater. The procedure is shown in Fig. 28. The windows from the left to the right represent the transmitter, the repeater and the receiver, respectively. Each device is distributed with a unique address so that it only receives data from one specified device and transmits it to another specified device. The results have proven that the repeater works effectively.

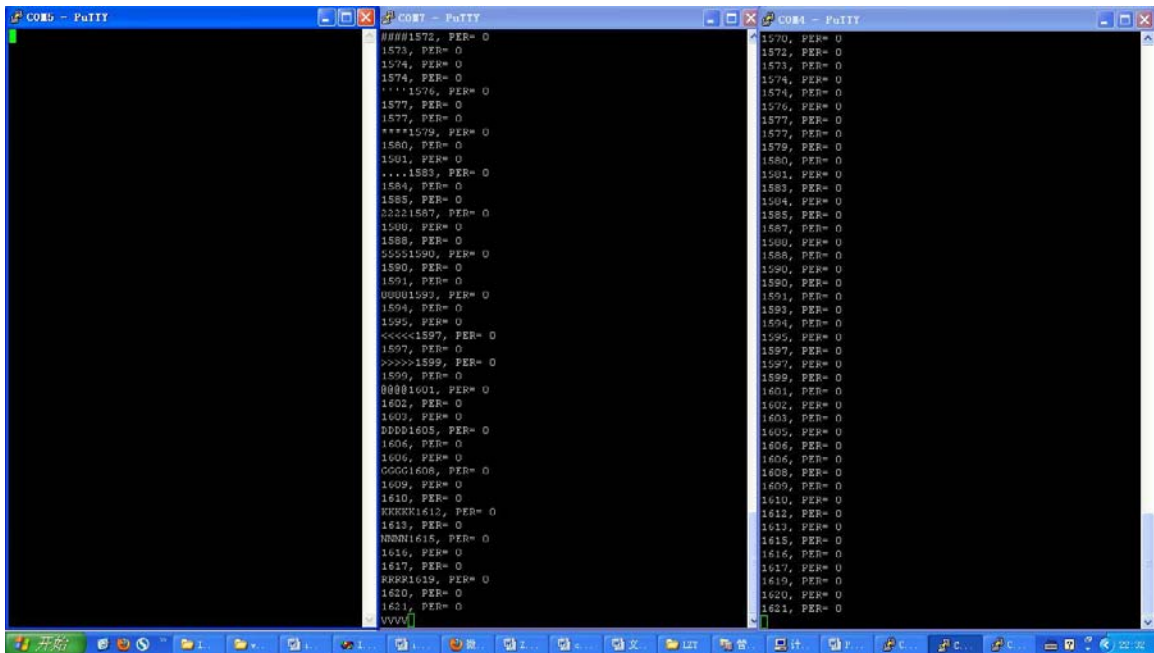


Fig. 28 Different ports of the three nodes.

5 Conclusion and future work

In this report, the wireless relay network that can be used in measurement-while-drilling (MWD) system is presented. The antenna system and the circuit system for the wireless network have been designed, manufactured and tested. The test result indicates the efficiency of the wireless relay network. Using small RF transceivers, the data rate of signal transmission can be improved up to 500 kbps. This method can provide a two-way communication between the downhole drilling tool and the surface control center.

For the whole wireless relay network, more models will be made to provide more nodes between two ends so that the packet error rate can be reduced and the transmission will be more accurate. The RF performance improvement of the repeater and the optimization of the wireless relay network are currently being studied.

References

- [1] Constantine A. Balanis, "Antenna Theory Analysis and Design," pp. 231-246, 2005.
- [2] David M. Pozar, "Microwave Engineering", pp. 117-126, 2005
- [3] Hamid Naseri, "Electromagnetic Telemetry in Measurement While Drilling with a Wireless Relay Network", PHD Dissertation, Department of Electrical and Computer Engineering, University of Houston, Houston, TX, May 2009.
- [4] A. C. Balanis, "Advanced Engineering Electromagnetics," pp. 728-731, 1989
- [5] Texas Instruments, data sheet of Low-Power SoC (System-on-chip) with MCU, memory, 2.4 GHz RF Transceiver, and USB
- [6] Texas Instruments, CC1111/CC2511 USB HW User's Guide.PDF
- [7] Digikey, data sheet of MCP1256 Charge Pump
- [8] J. P. Carcione, "A Telegraph equation for electric-telemetry in drill string," IEEE Transaction on Geosciences and Remote Sensing, vol. 40, pp. 1047-1053, 2002
- [9] L. C. Shen, "The Transmission-Line Model of an Insulated Antenna with a Two-Layer Eccentric Insulator," IEEE Transaction on Antennas and Propagation, vol. 24, pp. 895-896, Nov 1976
- [10] D. V. Ellis, "Well Logging for Earth Scientists," Elsevier Science Publishing Co., Inc., p 145, 1978
- [11] N. Brown, "Electromagnetic MWD telemetry system sets depth record offshore," Oil and Gas Journal, vol. 100, pp. 46-47, Sep 2002

APPENDIX A

List of Theses and Dissertations

The following are senior theses, master theses, and doctoral dissertations completed by the research staff of the Well Logging Laboratory.

- 1982** Shabbir A. Chowdhury
Investigation of Electrode Effects in the Measurement of Impedance of Water Saturated Rocks at Low Frequencies
(M. S. Thesis)
- Shey-Min Su
Measurements of Dielectric Constant and Conductivity of Petroleum Reservoir Rocks at Microwave Frequencies
(M. S. Thesis)
- 1984** Hardy X. J. Guo
Physical Modelling of Induction Logging in Dipping Beds
(M. S. Thesis)
- S. C. Frank Huang
Techniques for Measuring the Dielectric Properties of Samples Using Coaxial-Line and Insulated Antenna
(Ph. D. Dissertation)
- Shahryar Darayan
High-Temperature Electromagnetic Properties of Reservoir Rocks at UHF
(M. S. Thesis)
- 1985** Herzl Marouni
Dielectric Constant and Conductivity Measurement of Reservoir Rocks in the Range of 20-50 MHz
(M. S. Thesis)
- Gong Li
Physical Modelling of Induction Logging in Dipping Beds with a Large Borehole
(M. S. Thesis)
- 1986** Michel S. Bittar
Laterolog Scale Modelling Experiments
(M. S. Thesis)

Nancy S. Pollard
Computer Simulation of Induction Tool Resistivity Readings in Multiple Layer Formations
(Senior Thesis)

Kobina O. Eshun
A New Design for the WLL Induction Logging Model Facility
(Senior Thesis)

1987 Lee-Hwa Lue Wang
Inversion of Induction Logging Data in Horizontally Layered Formation
(M. S. Thesis)

Ming Huang
Modeling Medium Inhomogeneity in Induction Logging
(M. S. Thesis)

Xin Lin
Microwave Dipmeter
(M. S. Thesis)

1988 Kuang-Fu Han
Dielectric Constant Measurement of Saline Solution at 1.1 GHz
(M. S. Thesis)

Muhammad N. A. Ansari
Effect of Dissimilar Scale Factors for Length and Diameter on Shallow Laterolog Scale-Model Tool Response
(M. S. Thesis)

Kobina O. Eshun
A Laboratory Model of the Focused Induction Logging Sonde
(M. S. Thesis)

Chi-Ming Lam
Modelling the Electrode Well-Logging Sonde by the Method of Finite Elements
(M. S. Thesis)

Chia-Hsiang Lin
Conductivity Measurement at Low Frequencies Using a Digital Bridge
(M. S. Thesis)

- 1990** Yongdong He
Input Impedance of an Antenna and Its Application in Complex Permittivity
Measurement at High Frequencies
(Ph. D. Dissertation)
- Michael S. Bittar
Study of Resistivity Sondes by Scale Modeling and Three-Dimensional Finite
Element Method
(Ph. D. Dissertation)
- 1991** Xiaolu Zhao
Numerical Analysis of a TM_{010} Cavity for Dielectric Measurement
(M. S. Thesis)
- 1992** Chun-ta Chao
Welllog Simulator: Simulation for Induction Tool in Layered Medium
(M. S. Thesis)
- Yu-zhi Li
Monopole Antenna as a Probe for Measuring Dielectric Properties at 300-
1100 MHz
(M. S. Thesis)
- Tien-min Wang
Electrical Properties of Saline Solution and Contaminated Soils
(M. S. Thesis)
- 1993** Shahryar Darayan
Measurement of Dielectric Permittivity and Conductivity of Samples Using
Guarded Electrodes
(Ph. D. Dissertation)
- Ming Huang
Resistivity Measurement in Laboratory and Field Environments
(Ph. D. Dissertation)
- Yongchun Zhang
Induction Log Inversion and Cross-Hole Electromagnetic Tomography
(Ph. D. Dissertation)
- 1994** Jiazhi Chui
Simulation of Measurement-While-Drilling Tool in Cylindrical Media
(M. S. Thesis)

Liang (Linda) Lin
Simulation of Induction Tools in Dipping Beds
(M. S. Thesis)

Yongmin Zhang
A Time-Domain Modeling and Inversion Technique and Its Applications to
Electromagnetic Subsurface Sensing
(Ph. D. Dissertation)

1995 Qian Gu
Evaluation of Approximations Used to Simulate MWD Tools in Layered
Formations
(M. S. Thesis)

Xuhua Hu
Radial Resistivity Profile Invasion Using Array Induction Logs
(M. S. Thesis)

Xiaoning Zhang
Quick Look Inversion of Through Casing Resistivity Measurement
(M. S. Thesis)

1996 Rohit Gaikwad
Scale Modeling of the Through-Casing Resistivity Tool
(M.S. Thesis)

Feng Gao
A Scale Model of the Through-Casing Resistivity Measurement
(M.S. Thesis)

Jing Lin
Three Dimensional Finite-Element Mesh Generation and Interactive
Computer Graphic Visualization System
(M. S. Thesis)

Xiao-bing Wu
Inversion of Induction Logs in Dipping Beds
(Ph.D. Dissertation)

Ruilin Zhong
Simulation the Effects of Casing Corrosion on the Through-Casing
Resistivity Logs
(M. S. Thesis)

- Jiang Zhu
Modeling and Evaluation of MWD Resistivity Tool in Horizontal Well
(M. S. Thesis)
- 1997** Ji Fang
Algorithms for Inversion of Induction Logs in Dipping Bed
(M. S. Thesis)
- Xiang Tian
Numerical Simulations of Induction and MWD Logging Tools and Data
Inversion Method with X-Window Interface on a UNIX Workstation
(Ph.D. Dissertation)
- Yuanzheng Ming
Simulation of Through-Casing Resistivity Logging
(M. S. Thesis)
- Hongxu Wu
Theoretical Study of the Effective Dielectric Constant of 3D Mixtures with
Applications in Soil Water Content Measurement
(M.S. Thesis)
- 1998** Jingjing Sun
Simulation of Induction Logging in 2D Formation using the Born
Approximation
(M. S. Thesis)
- Shu Huang
Computer Simulation of Microwave Flow Meter
(M. S. Thesis)
- Long Wang
3-D Numerical Modeling of Induction Resistivity Tool for Well Logging
Using Finite Element Method
(Ph.D. Dissertation)
- 1999** Huage Zheng
Physical Modeling of an Automated Through-Casing Resistivity
Measurement System
(M. S. Thesis)

Hanming Wang
Finite Element Analysis of Resistivity Logging
(Ph.D. Dissertation)

2000 Yuan Hu
Simulation of Induction and MWD Logging in Wells with Varying Dip Angles
(M. S. Thesis)

Jian Li
2-D Inversion for Induction and MWD Logs
(Ph.D. Dissertation)

Ji Li
Modeling Electrode-type Logging Tools in 2-D Formations by Finite Element
Method
(M. S. Thesis)

Guoyu Hu
Two-dimensional Cross-well Forward Modeling and Inversion
(M. S. Thesis)

2001 Chatrpol Lertsirimit
Apparatus for Measuring Conductivity Tensor of Anisotropic Samples in the
Laboratory
(M. S. Thesis)

Chuanxiao Li
A Graphical Interface for Well-Logging Codes
(M. S. Thesis)

2002 Pei Jin
Laboratory Technique for Measuring Conductivity Tensor of Anisotropic
Samples
(M. S. Thesis)

Lili Zhong
Simulation of Multi-Component Induction Tool in Dipping Beds
(M. S. Thesis)

Wei Gao
3D Transmission Line Matrix Method and Application Interface
(M. S. Thesis)

2004 Lili Zhong

- Simulation of Tri-Axial Induction Tools in Dipping Anisotropic Beds
(Ph.D. Dissertation)
- Shanjun Li
Analysis of Complex Formations Using Computer Techniques
(Ph.D. Dissertation)
- Weishan Han
3D Finite Element Simulation Method of Induction and MWD Tools
(Ph.D. Dissertation)
- 2005** Jing Li
Electrical Property Measurement of Rocks in the Range of 10kHz –1.1GHz
(M.S. Thesis)
- 2006** Xueshen Yu
Inversion of Tri-Axial Induction Logs in Anisotropic Formation
(M.S. Thesis)
- 2007** David Navarro
Effects of Invasion Transient on Resistivity Time-Lapsed Logging
(M.S. Thesis)
- 2008** Asutosh Bhardwaj
1-D Inversion of Tri-axial Induction Logs in Anisotropic Medium
(M.S. Thesis)
- Yumei Tang
Modeling and Inversion of Multicomponent Induction Logs in Biaxial
Anisotropic Formation
(Ph.D. Dissertation)
- 2009** Li Zhong
Response of Induction and LWD Tools in Multiple Cylindrically Layered
Media
(M.S. Thesis)
- Jinjuan Zhou
Application of Finite Element Method in Solving Well Logging Problems
(Ph.D. Dissertation)

Hamid Naseri
Electromagnetic Telemetry in Measurement-While-Drilling with
a Wireless Relay Network
(Ph.D. Dissertation)

Mark Collins
Response of MWD Resistivity Tools in Eccentric Cylindrically Layered
Media
(M.S. Thesis)

2010

Chen Guo
Research on Ultra Wideband(UWB) Antenna and Radar Application
(Ph.D. Thesis)

Huaping Wang
Ground Penetrating Radar with Wireless Data Access and Control
(Ph. D. Thesis)

Wei Ren
The Portable Ground Penetrating Radar System Design
(Ph.D. Thesis)

Guoyu Hu, Analysis of Induction Tool Response to Fractures Using an
Improved 3D Finite Difference Method
(Ph.D Thesis)

2011

Yinan Xing
Road Profiling System using Non-contact laser Displacement Sensor
(M.S. Thesis)

El Emir Fouad Shehab
Low Frequencies and Numerical Evaluation of Permittivity of Digital Rocks at
High Frequency
(M.S. Thesis)

Zhijuan Zhang

1D Modeling and Inversion of Triaxial Induction Logging Tools in Layered
Anisotropic Medium

(Ph.D Dissertation)

APPENDIX B

List of Technical Paper Publications

The following are papers published in technical journals and symposium transactions by the research staff of the Well Logging Laboratory.

Papers Published in Technical Journals

1983

F.S.C. Huang and L. C. Shen, "Analysis of error due to presence of gaps in the measurement of rock samples in a coaxial Line," *Geophysics*, Vol.48, No.2, pp.206-212, February 1983.

1984

G. J. Zhang and L. C. Shen, "Response of a normal resistivity tool in a borehole crossing a bed boundary," *Geophysics*, Vol. 49, No. 2, pp. 142-149, February 1984.

D. Coope, L. C. Shen, and F. S. C. Huang, "The theory of 2 MHz resistivity tool and its application to measurement-while-drilling," *The Log Analyst*, Vol. XXV, No. 3, pp. 35-46, May-June 1984.

1985

L. C. Shen, W. C. Savre, J. M. Price and K. Athavale, "Dielectric properties of reservoir rocks and ultra high frequencies," *Geophysics*, Vol. 50, No. 4, pp. 692-704, April 1985.

L. C. Shen, "A Laboratory Technique for measuring dielectric properties of core samples at ultra high frequencies," *Society of Petroleum Engineers Journal*, pp. 502-514, August 1985.

L. C. Shen, and G. J. Zhang, "Electromagnetic field due to a magnetic dipole in a medium containing both planar and cylindrical boundaries," *IEEE Transactions on Geoscience and Remote Sensing*, Vol.23, No. 6, pp. 827-833, November 1985.

L. C. Shen, "Problems in dielectric-constant logging and possible routes to their solution," *The Log Analyst*, Vol. XXVI, No. 6, pp. 14-25, November-December 1985.

1986

R. H. Hardman and L. C. Shen, "Theory of induction sonde in dipping beds," *Geophysics*, Vol. 51, No. 3, pp. 800-809, March 1986.

1987

R. H. Hardman and L. C. Shen, "Charts for correcting the effect of formation dip and hole deviation on induction logs," *The Log Analyst*, Vol. 28, No. 4, pp. 349-356, July-August 1987.

D. P. Shattuck, Michel Bittar and L. C. Shen, "Scale modelling of the laterolog using synthetic focusing methods," *The Log Analyst*, Vol. 28, No. 4, pp. 357-369, July-August 1987.

L. C. Shen, H. Marouni, Y. X. Zhang and X. D. Shi, "Analysis of parallel-disk sample holder for dielectric permittivity measurement," *IEEE Transactions on Geoscience and Remote Sensing*, Vol. 25, No. 5, pp. 534-540, September 1987.

1989

M. Huang and L. C. Shen, "Computation of induction logs in multiple-layer dipping formation," *IEEE Transactions on Geoscience and Remote Sensing*, Vol. 27, No. 3, pp. 259-267, May 1989.

L. C. Shen, "Effects of skin-effect correction and three-point deconvolution on induction logs," *The Log Analyst*, Vol. 30, No. 4, pp. 217-224, July-August 1989.

1990

L. C. Shen, C. Liu, J. Korrinda and K. J. Dunn, "Computation of conductivity and dielectric constant of periodic porous media," *J. of Applied Physics*, Vol. 67, No.11, pp. 7071-7081, June 1990.

M. S. Bittar, D. P. Shattuck and L. C. Shen, "Laboratory study of the shallow laterolog in high and low contrast zones," *The Log Analyst*, Vol. 31, No.4, pp.189-197, 1990.

1991

K. F. Han, C. M. Butler, L. C. Shen, Y. D. He and M. A. Harris, "High-frequency dielectric permittivity of saline solution at elevated temperature," *IEEE Transactions on Geoscience and Remote Sensing*, Vol.29, No.1, pp. 48-56, January 1991.

C. Liu and L. C. Shen, "Response of electromagnetic-pulse logging sonde in axially-symmetrical formation," *IEEE Transactions on Geoscience and Remote Sensing*, Vol.29, No.2, pp. 214-221, March 1991.

C. Liu and L. C. Shen, "Numerical simulation of subsurface radar for detecting buried pipes," *IEEE Transactions on Geoscience and Remote Sensing*, Vol.29, No. 5, pp.795-798, September 1991.

L. C. Shen, "Theory of a coil-type resistivity sensor for MWD application," *The Log Analyst*, vol. 32, pp. 603-611, No.5, 1991.

1992

Y. D. He and L. C. Shen, "Measurement of complex permittivity of materials using a monopole antenna," *IEEE Transactions on Geoscience and Remote Sensing*, Vol.30, No.3, pp. 624-627, May 1992.

X. L. Zhao, C. Liu and L. C. Shen, "Numerical analysis of a TM₀₁₀ cavity for dielectric measurement," *IEEE Transactions on Microwave Theory and Techniques*, Vol.40, No.10, pp. 1951-1959, October 1992.

J. Li and L. C. Shen, "Numerical simulation of spherically focused log," *The Log Analyst*, Vol. 33, No. 6, pp. 495-499, 1992.

1993

C. Liu and L. C. Shen, "Dielectric constant of two-component, two-dimensional mixtures in terms of Bergman-Milton simple poles," *J. of Applied Physics*, vol. 73, no. 4, pp.1897-1903, 1993.

Jiang Li and L. C. Shen, "MWD resistivity logs in invaded beds," *The Log Analyst*, Vol.34, No. 2, pp. 15-17, 1993.

Jiang Li and L. C. Shen, "Vertical eigenstate method for simulation of induction and MWD resistivity sensors," *IEEE Transactions on Geoscience and Remote Sensing*, Vol.31, No. 2, pp. 399-406, March 1993.

C. Liu and L. C. Shen, "Dispersion characteristics of two-component, two-dimensional mixtures," *Modelling and Simulation in Materials Science and Engineering*, Vol. 1, pp. 723-730, 1993.

1994

Y. C. Zhang, L. C. Shen and C. Liu, "Inversion of induction logs based on maximum flatness, maximum oil, and minimum oil algorithms," *Geophysics*, pp. 1320-1326, 1994.

1995

M. Huang, C. Liu and L. C. Shen, "Monitoring the contamination of soils by measuring their conductivity in the laboratory using a contactless probe," *Geophysical Prospecting*, Vol. 43, pp 759-778, 1995.

M. Huang, C. Liu, L. C. Shen and D. Shattuck, "Laboratory conductivity measurement using a contactless coil-type probe," *The Log Analyst*, pp.82-90, May 1995.

Y. M. Zhang and C. Liu, "A space marching inversion algorithm for pulsed borehole radar in the time domain," *IEEE Transactions on Geosciences and Remote Sensing*, Vol. 33, No.3, pp.541-550, May, 1995.

M. S. Bittar, D.P. Shattuck and L.C. Shen, "Finite element modeling of the normal resistivity tool in azimuthally inhomogeneous formations," *Journal of Petroleum Science and Engineering*, Vol. 14, pp. 59-63, December, 1995.

1996

Y. M. Zhang, C. Liu and L. C. Shen, "The performance evaluation of MWD logging tools using magnetic and electric dipoles by numerical simulations," *IEEE Transactions on Geoscience and Remote Sensing*, Vol. 34, No. 4, pp. 1039-1044, 1996.

Y. C. Zhang, C. Liu, L. C. Shen, "An iterative algorithm for conductivity image reconstruction from crosswell EM measurements," *Geophysics*, Vol. 61, No. 4, pp. 987-997, 1996.

C. Liu and Q. Zou, "A simplified Fourier series expansion method for computing the effective dielectric constant of a two-component, three-dimensional composite material with geometric symmetry," *Modeling and Simulation in Materials Science*, Vol. 4, pp. 55-71, 1996.

S. Darayan, D. P. Shattuck, L. C. Shen and C. Liu, "Measurement of dielectric constant and conductivity of samples using guarded electrodes," *Radio Science*, Vol.31, No. 6, pp. 1417-1426, 1996.

Y. M. Zhang, C. Liu and L. C. Shen, "A TLM model of a borehole electromagnetic sensing system," *Journal of Applied Geophysics*, Vol. 36, pp. 77-88, 1996.

1997

C. Liu and H. X. Wu, "Computation of the effective dielectric constant of a two-component, three-dimensional composite materials using simple poles", *Journal of Applied Physics*, Vol. 82, No. 1, 1997.

1998

S. Graciet and L. C. Shen, "Theory and numerical simulation of induction and MWD resistivity tools in anisotropic dipping beds," *The Log Analyst*, Vol. 39, No. 1, pp. 24-37, 1998.

X. Tian, C. Liu and L. C. Shen, "A stable algorithm for simulation of array induction and measurement-while-drilling logging tools," *Radio Science*, Vol. 33, No.4, pp. 949-956, 1998.

S. Darayan, C. Liu, L. C. Shen, and D. Shattuck, "Measurement of electrical properties of contaminated soil," *Geophysical Prospecting*, Vol. 46, No. 5, pp. 477-488, 1998.

2000

H. M. Wang, L. C. Shen and G. J. Zhang, "Dual laterolog response in 3-D environments," *Petrophysics*, Vol. 41, No. 3, pp. 234-241, 2000.

L. C. Shen, "Comparison of modeling codes for resistivity and MWD instruments: part 1 1-D radial invasion," *Petrophysics*, Vol. 41, No. 3, pp. 242-245, 2000.

S. Graciet and L. C. Shen, "Finite difference forward modeling of induction tool in 3D geometry," *Petrophysics*, Vol. 41, No. 6, pp. 503-511, 2000.

J. Li and C. Liu, "A 3-D transmission line matrix method (TLM) for simulations of logging tools," *IEEE Transactions on Geoscience and Remote Sensing*, Vol. 38, No. 4, pp. 1522-1529, 2000.

2001

E. A. Badea, M. E. Everett, L. C. Shen and C. J. Weiss, "Effect of background fields on three-dimensional finite element analysis of induction logging," *Radio Science*, Vol. 36, No. 4, pp. 721-729, 2001.

H. M. Wang and L. C. Shen, "Dual laterolog responses in anisotropic crossing bedding formation," *Petrophysics*, Vol. 42, No. 6, pp. 624-632, 2001.

J. Li and C. Liu, "Noncontact detection of air voids under glass epoxy jackets using a microwave system", *Subsurface Sensing Technologies and Applications*, Vol. 2, No. 4, pp. 411-423, 2001.

M. E. Everett, E. A. Badea, L. C. Shen, G. A. Merchant and C. J. Weiss, "3-D finite element analysis of induction logging in a dipping formation," *IEEE Transactions on Geoscience and Remote Sensing*, Vol. 39, No. 10, pp. 2244-2252, 2001.

2002

L. C. Shen, "Comparison of modeling codes for resistivity and MWD instruments: part 2 1-D thin beds," *Petrophysics*, Vol. 43, No.1, pp. 20-25, 2002.

C. Liu, J. Li, Xinhua Gan, Huichun Xing and Xuemin Chen, "A new model for estimating the thickness and permittivity of subsurface layers from GPR data," *IEE Proceedings on Radar Sonar and Navigation*, Vol. 149, No. 6, 2002.

2003

Q. Zhang, X. Chen, X. Jiang and C. Liu, "A multi-frequency electromagnetic image system," *Computer-Aided Civil and Infrastructure Engineering*, Vol.18, 2003.

2004

Y. Zhang, L. Shieh, and C. Liu, "Digital PID controller design for multivariable analogue systems with computational input-delay," *IMA Journal of Mathematical Control and Information*, Vol.21, pp 433-456, 2004.

X. He, C. Liu, X. Chen and J. Li, "Simulation of a multi-frequency continuous-wave reconstruction technique for subsurface conductivity and dielectric-constant profiles," *Subsurface Sensing Technologies and Application*, Vol. 5, No. 3, pp. 99-120, July 2004.

J. Lin, C. Liu, J. Li and X. Chen, "Measurement of concrete highway rough surface parameters by an X-Band scatterometer," *IEEE Geoscience and Remote Sensing*, Vol. 42, No. 6, pp 1188-1196, June 2004.

2006

Richard C. Liu, "MWD telemetry with low-cost radios", *E&P Journal*, pp.111-112, May 2006.

H. Q. Zhou, L.S. Shieh, R. C. Liu and Q.G. Wang, "State-space PI controller design for linear stochastic multivariable systems with input delay," *The Canadian Journal of Chemical Engineering*, Vol. 84, No. 2, pp.230-238, April 2006.

2007

Chien-ping Kao, Jing Li, Huichun Xing, Ying Wang, Haobing Dong and Richard Liu, "Measurement of layer thickness and permittivity using a new multi-layer model from GPR data," *Transactions on Geoscience and Remote Sensing*, August 2007.

Dagang Wu, Ji Chen and Ce Liu, "Numerical evaluation of effective dielectric properties of three-dimensional composite materials with arbitrary inclusions using a finite-difference time-domain method," *Journal of Applied Physics*, 102, 2007.

2008

Dagang Wu, Ji Chen and Ce Richard Liu, "An efficient FDTD method for axially symmetric LWD environments," *IEEE Transactions on Geoscience and Remote Sensing*, Vol. 46, No. 6, June, 2008.

Lili Zhong, Jing Li, Ashutosh Bhardwaj, Liang C. Shen and Richard C. Liu, "Computation of triaxial induction logging tools in layered anisotropic dipping formations," *IEEE Transactions on Geoscience and Remote Sensing*, Vol. 46, No. 4, pp.1148-1163, April 2008.

2009

Y.P. Chang, L.S. Shieh, C.R. Liu, P. Cofie, "Digital modeling and PID controller design for MIMO analog systems with multiple delays in states, inputs and outputs," *Circuits Syst. Signal Process* Vol. 28, pp. 111-145, 2009.

2010

Chen Guo, Richard C .Liu. A Borehole Imaging Method Using Electromagnetic Short-Pulse in Oil Based Mud. *IEEE Geoscience and Remote Sensing Letters*, 2010, PP(99):856~860

Miao Luo, Ce Liu, and H.P. Pan, "Numerical Simulation on Dielectric Enhancement of Periodic Composite Media using a 3D Finite Difference Method," *The European Physical Journal Applied Physics*, 2010.

Xiaochun Nie, Ning Yuan and Richard Liu, "Simulation of LWD Tool Response

Using a Fast Integral Equation Method,” *IEEE Trans. on Geoscience and Remote Sensing*, Vol.48, No.1, pp.72-81, 2010.

Ning Yuan, Xiao Chun Nie and Richard Liu, “Response of a triaxial induction logging tool in a homogeneous biaxial anisotropic formation,” *Geophysics*, Vol.75, No.2, March-April, 2010

Chen Guo, Richard C. Liu, An-xue Zhang, “Design and Implement of a Shielded Antenna System for Ground Penetrating Radar Applications,” *Chinese Journal of Radio Science*, Vol.25, No.2, pp.221~226, 2010.

Papers Published in Conference Proceedings

1983

H. C. Shang and L. C. Shen, “A laboratory study of induction logs using physical modeling,” *SPWLA 24th Annual Logging Symposium*, June, 1983, Paper M, Calgary, Alberta, Canada.

1984

L.C. Shen, M. J. Manning, and J. M. Price, “Application of electromagnetic propagation tool in formation evaluation,” *SPWLA 25th Annual Logging Symposium*, June, 1984, Paper J, New Orleans, Louisiana.

1985

L. C. Shen, “Current problems in dielectric-constant logging and possible routes to their solution,” *SPWLA 26th Annual Logging Symposium*, June, 1985, Invited Paper, Dallas, Texas. The text was published in *The Log Analyst*, Nov. 1985.

1986

L. C. Shen and R. H. Hardman, “Effect of formation dip or hole deviation on induction logs,” *SPWLA 27th Annual Logging Symposium*, June, 1986, Paper I, Houston, Texas.

1987

L. C. Shen, “A parallel-disk sample holder for dielectric permittivity measurement in the 20-200 MHz range,” *SPWLA 28th Annual Logging Symposium*, June 1987, Paper J, London, England.

1988

L. C. Shen, "Effects of skin-effect correction and three-point deconvolution on induction logs," *SPWLA 29th Annual Logging Symposium*, June 1988, Paper M, San Antonio, Texas.

1991

L. C. Shen, "Investigation depth of coil-type MWD resistivity sensor," *SPWLA 32nd Annual Logging Symposium*, June 1991, Paper C, Midland, Texas.

1993

M. Huang, C. Liu, and L. C. Shen, "Laboratory resistivity measurement using a contactless coil-type probe," *SPWLA 34th Annual Logging Symposium*, June 1993, Paper JJ, Calgary, Alberta, Canada.

1997

S. Graciet and L. C. Shen, "Simulation of induction and MWD resistivity tools in anisotropic dipping beds," *SPWLA 38th Annual Logging Symposium*, June 1997, Paper M, Houston, TX.

1998

H. M. Wang, L. C. Shen, and G. J. Zhang, "Dual laterolog responses in 3-D environments," *SPWLA 39th Annual Logging Symposium*, May 1998, Paper X, Keystone, CO.

1999

H. M. Wang and L. C. Shen, "A three-dimensional mesh generation method for well-logging modeling," *Fifth SIAM Conference on Mathematical and Computational Issues in the Geosciences*, March 1999, San Antonio, Texas.

2001

L. C. Shen, "Simulation of electromagnetic logging tools," *2001 IEEE AP-S International Symposium and USNC/URSI National Radio Science Meeting*, July 2001, Boston, MA.

2003

Shanjun Li and L. C. Shen, "Dynamic invasion profiles and time-lapse electrical logs," *SPWLA 44th Annual Logging Symposium*, June 2003, Paper E, Galveston, TX.

2005

D. Wu, F. Yang, J. Chen and C. Liu, "MWD tool / small antenna analysis using cylindrical unconditional stable FDTD method," (invited) *Asian-Pacific Microwave Conference*, December, 2005.

2006

S.J. Li, C. Liu, L.C. Shen, H.M. Wang, J. Ouyang and G.J. Zhang, "Identification and evaluation of fractured tight-sand oil reservoir in deep zone of Bohai Gulf," *SPWLA Annual Conference*, Veracruz, Mexico June 4-7, 2006

Dagang Wu, Ji Chen and Ce Liu, "Numerical modeling of MWD electromagnetic responses using a unconditionally stable finite-difference time-domain (FDTD) method," *IEEE Geoscience and Remote Sensing Conference*, Denver, Colorado, July 31-August 4, 2006.

Dagang Wu, Rui Qiang, Ji Chen and Richard Liu, "Numerical evaluation of the effective dielectric property of multi-component three-dimensional mixtures using a finite-difference time-domain method," *in proceeding of SEG symposium*, 2006.

Yumei Tang, Tsili Wang, Bill Corley and James Morrison, "Interpreting fracture length from multi-array induction logs," *in proceeding of SEG symposium*, 2006.

Shanjun Li, Richard Liu and Liangchi Shen, "A new 3D electrode-type logging tool," *in proceeding of SEG symposium*, 2006.

Lili Zhong, L. C. Shen, Shanjun Li, Richard Liu, Michael Bittar and Guoyu Hu, "Simulation of triaxial induction logging tools in layered anisotropic dipping formations," *in proceeding of SEG symposium*, 2006.

2007

Dagang Wu, Ji Chen and Ce Liu, "Analysis of Three-dimensional composite materials with non-isotropic or biaxial anisotropic inclusions using a finite difference method," *IEEE Antenna and Propagation Symposium*, Hawaii, USA, June, 2007.

Jing Li and C. Richard Liu, "Complex dielectric measurement using TM₀₁₀ cylindrical cavity," *Progress in Electromagnetic Research Symposium*, Beijing, China, June 2007.

Jing Li, Xuesheng Yu, Lili Zhong and Richard C. Liu, "Frequency response of 1D tri-axial induction logging in different formations," *Progress in Electromagnetic Research Symposium*, Beijing, China, June 2007.

David Navarro, Shanjun Li, Richard C. Liu, Kishore K. Mohanty, Guoxin Li, Cancan Zhou and Changxi Li, "Invasion effects on time-lapsed array induction logs," *SPWLA 48th Annual Logging Symposium*, Austin, Texas, USA, June 3-6, 2007.

Yumei Tang, Tsili Wang, and Richard Liu, "Multicomponent induction response in a biaxially anisotropic formation," *SEG Annual Conference*, San Antonio, Texas, USA, August 2007.

2008

Xiaochun Nie, Ning Yuan and Richard C. Liu, "A 3-D Fast Integral Equation Method for Simulation of Induction Logging Response in Formations with Large Conductivity Contrasts," *2008 IEEE AP-S International Symposium and USNC/URSI National Radio Science Meeting*, San Diego, June 2008.

Hamid Naseri and Richard C. Liu, "Electromagnetic telemetry in measurement-while-drilling with a wireless relay network," *SEG 2008, Las Vegas, November 2008*.

Xiaochun Nie, Ning Yuan and Richard C. Liu, "Simulation of LWD Tool Response Using a Fast Integral Equation Method," *SEG 2008, Las Vegas, November 2008*.

2009

Ning Yuan, Xiaochun Nie and Richard C. Liu, "Dyadic Green's Function in a Homogeneous Biaxial Anisotropic Medium," *2009 IEEE AP-S International Symposium and USNC/URSI National Radio Science Meeting*, Charleston, South Carolina, June 2009.

Zhijuan Zhang, Ning Yuan and Richard Liu, "The effect of dip on 1-D simulation of triaxial induction tool in anisotropic layered formation," *SPWLA 50th Annual Logging Symposium*, Houston, Texas, USA, June 22-26, 2009.

Ning Yuan, Xiaochun Nie and Richard C. Liu, "Response of a triaxial induction logging tool in a homogeneous biaxial anisotropic formation," *Annual Meeting of Society of Exploration and Geophysicists*, 25-30, Oct., Houston, TX, U.S.A, 2009.

Xiao Chun Nie, Ning Yuan and Richard Liu, "Analysis of tilted-coil eccentric LWD tool response using a fast integral equation method," *Annual Meeting of Society of Exploration and Geophysicists*, 25-30, Oct., Houston, TX, 2009.

C. Guo and R. Liu, "Design of a shielded antenna system for ground penetrating radar applications," *2009 IEEE AP-S International Symposium and USNC/URSI National Radio Science Meeting*, Charleston, South Carolina, USA, June 2009.

Jing Li and C. Liu, "Simulation of a borehole radar in measurement while drilling (MWD) environments", *PIERS 2009*, Moscow, August 2009.

Hamid Naseri and Richard Liu, "Electromagnetic telemetry in measurement-while-drilling with small RF-transceivers," *Society of Geophysical Exploration, CPS/SEG Beijing 2009 Conference and Exposition*, Beijing China, April 2009.

Miao Luo and Ce Liu, "Numerical simulations of large dielectric enhancement in some rocks," *Society of Geophysical Exploration, CPS/SEG Beijing 2009 Conference and Exposition*, Beijing China, April 2009.

R. Zhong and R. Liu, "Development of a high resolution wireless distance measurement instrument," *2009 International Instrumentation and Measurement Technology Conference*, Singapore, May 5-7, 2009.

2010

Ning Yuan, Xiao Chun Nie, and Richard Liu, "Electromagnetic Field Response of Triaxial Induction Logging Tools in 1-D Multi-Layered Anisotropic Formations," accepted by *2010 IEEE AP-S International Symposium on Antennas and Propagation and 2010 USNC/URSI National Radio Science Meeting*, Toronto, ON, Canada, on July 11-17, 2010

Xiao Chun Nie, Ning Yuan and Richard Liu, "Simulation of Induction Logging Tools in Anisotropic Media Using a 3D Finite Difference Method," *Annual Meeting of Society of Exploration and Geophysicists*, 18-22, Oct., Denver, CO, 2010.

Guoyu Hu, Ingo M. Geldmacher, and Richard C. Liu, Effect of Fracture Orientation on Induction Logs: A Modeling Study, *SPE Annual Technical Conference and Exhibition*, Florence, Italy, 19-22, Sept., 2010, SPE 133802.

Chen Guo, Richard C.Liu, "EM Pulse Borehole Imaging System for Oil Based Mud," *IEEE International Symposium on Antennas and Propagation and USNC/CNC/URSI Meeting*, Toronto,Canada, July 11-17, 2010

Chen Guo, Richard C. Liu, "A 900MHz Shielded Bow-tie Antenna System for Ground Penetrating Radar," *XIII International Conference on Ground Penetrating Radar*, Lecce, Italy, 21-25 June 2010.

Chen Guo, Richard C. Liu, "An UWB EM Borehole Imaging System," *IEEE International Conference on Ultra-Wideband (ICUWB)* 2010.

C. P. Kao, Y. Cai, J. Li, R. Liu, "A Dielectric-Filled Ridged Horn Antenna Design for GPR Applications," *2010 IEEE AP-S International Symposium on Antennas and Propagation and 2010 USNC/URSI National Radio Science Meeting*, Toronto, ON, Canada, on July 11-17, 2010.

C. P. Kao, Y. Cai, J. Li, R. Liu, "Design a Meander Dipole Antenna for a Passive RFID System," *2010 IEEE AP-S International Symposium on Antennas and Propagation and 2010 USNC/URSI National Radio Science Meeting*, Toronto, ON, Canada, on July 11-17, 2010.

Huaping Wang, Ce Richard Liu, Wei Ren, Chen Guo, „A New Generation Ground Penetrating Radar with Wireless Data Communication–WGPR System," *4th International Conference on Environmental and Engineering Geophysics*, Chengdu, China, 2010.

A. Bhardwaj, Namrata, Richard Liu, "Parametric Inversion of Tri-axial Induction Logs in Anisotropic Media," *Third National Conference on Mathematical Techniques: Emerging Paradigms for Electronics and IT Industries (MATEIT)*, January 30-31, 2010, New Convention Centre, University of Delhi North Campus.

2011

Ning Yuan, Xiao Chun Nie, and Richard Liu, "Electromagnetic Field of Arbitrarily Oriented Coil Antennas in Complex Underground Environment," *2011 IEEE AP-S International Symposium on Antennas and Propagation and 2011 USNC/URSI National Radio Science Meeting*, July 3-8, 2011, Spokane, Washington, USA.